ABSTRACT

Title of Document: MULTISCALE MODELING OF ANISOTROPIC CREEP RESPONSE OF SnAgCu SINGLE CRYSTAL

Subhasis Mukherjee, PhD, 2015

Directed By: Prof. Abhijit Dasgupta, Department of Mechanical Engineering

The lack of statistical homogeneity in functional SnAgCu (SAC) solder joints due to their coarse grained microstructure, in conjunction with the severe anisotropy exhibited by single crystal Sn, renders each joint unique in terms of mechanical behavior. An anisotropic multiscale modeling framework is proposed in this dissertation to capture the influence of the inherent elastic anisotropy and grain orientation in single crystal Sn on the measured primary and secondary creep response of single crystal SnAgCu (SAC) solder. This study overcomes the intrinsic disadvantages of most of the existing studies, which assumes homogenized, macro-scale, isotropic behavior of these joint scale specimens, thereby making the models insensitive to the highly heterogeneous and anisotropic microstructure.

Modeling of microstructural deformation mechanisms in SnAgCu (SAC) solder interconnects requires a multiscale approach because of tiered microstructural heterogeneities. The smallest length scale (Tier 0) refers to the Body Centered Tetragonal (BCT) structure of the Sn matrix itself because it governs: (1) the associated dislocation slip systems, (2) edge and screw dislocation line tension (3) dislocation mobility and (4) intrinsic orthotropy of mechanical properties in the crystal principal axis system. Next higher length scale, Tier 1, consists of nanoscale Ag_3Sn intermetallic compounds (IMCs) surrounded by Body Centered Tetragonal (BCT) Sn to form the eutectic Sn-Ag phase. The next higher length scale (Tier 2) consists of micron scale lobes of Sn dendrites surrounded by eutectic Sn-Ag regions and

reinforced with micron scale Cu_6Sn_5 IMCs. Unified modeling of above two length scales provides constitutive properties for SAC single crystal. Tier 3 in coarse-grained solder joints consists of multiple SAC crystals along with grain boundaries. Finally, Tier 4 consists of the structural length scale of the solder joint.

Line tension and mobility of dislocations (Tier 0) in dominant slip systems of single crystal Sn is captured using elastic crystal anisotropy of body centered tetragonal (BCT) Sn and Stroh's matrix formalism. The anisotropic creep rate of the eutectic Sn-Ag phase of Tier I is then modeled using above inputs and the evolving dislocation density calculated for dominant glide systems. The evolving dislocation density history is estimated by modeling the equilibrium between five competing processes: (1) dislocation generation; (2) dislocation impediment due to forest dislocations; (3) recovery (by climb and diffusion) from forest dislocations; (4) dislocation impediment caused by back stress from pinning of dislocations at IMC particles; and (5) dislocation recovery due to climb/detachment from Ag_3Sn IMC particles. Of these mechanisms, the third and fifth mechanisms are modeled to be the rate governing mechanisms for anisotropic creep deformation processes for the Sn matrix and for the eutectic Sn-Ag alloy respectively. Orowan climb mechanism and dislocation detachment mechanism from nanoscale Ag_3Sn particles are found to be the rate controlling creep mechanisms in the eutectic Sn-Ag phase of SAC single crystal at low and high stress levels respectively.

The creep response of the eutectic phase (from Tier 1) is combined with creep of ellipsoidal Sn lobes at Tier 2 using the anisotropic Mori-Tanaka homogenization theory, to obtain the creep response of SAC305 single crystal along global specimen direction and is calibrated to experimentally obtained creep response of same SAC305 single crystal specimen. The Eshelby strain concentration tensors required for this homogenization process are calculated numerically for ellipsoidal Sn inclusions embedded in anisotropic eutectic Sn-Ag matrix. The orientations of SAC single crystal specimens with respect to loading direction are identified using orientation image mapping (OIM) using electron backscatter detector (EBSD) and then utilized in the model to estimate resolved shear stress along dominant slip directions.

The proposed model is then used for investigating into variability in transient and secondary creep response of Sn3.0Ag0.5Cu (SAC305) solder, which forms the first objective of the study. Transient creep strain rates along [001] direction of SAC305 single crystal #1 is predicted to be 1-2 orders of magnitude higher than that of along [100]/[010] direction. The proposed model is able to quantitatively capture the creep response of second SAC305 single crystal #2 and two bi-crystal specimens reasonably well. Parametric studies have also been conducted to predict the effect of changing orientation, aspect ratio and volume fraction of Sn inclusions on the anisotropic creep response of SAC single crystal. Predicted creep shear strain along global specimen direction is found to vary by a factor of (1-3) orders of magnitude due to change in one of the Euler angles (φ_1) in SAC305 single crystal #1, which is in agreement with the variability observed in experiments. The model is also able to capture the decrease in creep resistance of SAC305 single crystal, when the volume fraction of Sn inclusion in the SAC single crystal increases.

The second objective of this study focuses on characterization and modeling of creep constitutive response of new low-silver, lead-free interconnects made of Sn1.0Ag0.5Cu (SAC105) doped with trace elements namely, Manganese (Mn) and Antimony (Sb) using the above model. The proposed multiscale microstructural model is used to mechanistically model the improvement in creep resistance of above SAC105X solders due to addition of trace elements.

The third and final objective of this study is to use the above multiscale microstructural model to mechanistically predict the effect of extended isothermal aging on creep response of SAC305 solders.

Therefore, the proposed physics-based predictive model can capture the dominant load paths and deformation mechanisms at each length scale and is also responsive to the microstructural tailoring done by microalloying and the continuous microstructural evolution because of thermomechanical life-cycle aging mechanisms in solders.

MULTISCALE MODELING OF ANISOTROPIC CREEP RESPONSE OF SnAgCu SINGLE CRYSTAL

By

Subhasis Mukherjee.

Dissertation submitted to the Faculty of the Graduate School of the
University of Maryland, College Park, in partial fulfillment
of the requirements for the degree of
Doctor of Philosophy
2015

Advisory Committee:
Professor Abhijit Dasgupta, Chair
Professor Hugh Bruck
Professor Teng Li
Professor Patrick McCluskey
Professor Aris Christou (Dean's Representative)

Dedication

To

my father Mr. Pradip Kumar Mukhopadhyay and mother Mrs. Mitali Mukherjee for all their support, love and faith in me & Satarupa for her persistence with my crazy schedule and deadlines, and all my teachers.

Acknowledgements

It is hard to overstate my gratitude to my Ph.D. advisor Prof. Abhijit Dasgupta for giving me an opportunity to work with him and mentoring me as a researcher. It is difficult to be unaffected by his unfailing energy and enthusiasm which has always been a source of energy for me to deal with difficult and seemingly unyielding research problems. I am grateful to him for providing me with a research environment like a free intellectual playground to try out different ideas, nevertheless, all the guidance and support when I got lost after too much of play.

He helped me learn many skills and expanded my horizons in addition to my key dissertation requirements. My vocabulary is not enough to express my gratitude to Prof. Dasgupta for the innumerable subtle things that he taught me both explicitly and implicitly which helped me become a better researcher.

I would also like to thank Prof. Teng Li, Prof. Hugh Bruck, Prof. Patrick McCluskey, and Prof. Aris Christou for accepting to serve in my dissertation committee. Their valuable suggestions related to my dissertation helped me a lot during my Ph.D. I thank them for being very prompt and responsive about my dissertation needs despite of having unbelievably busy academic and research commitments of their own.

I would like to thank Prof. Thomas R. Bieler and Bite Zhou from Michigan State University for several insightful discussions on my dissertation and for their help in providing me critical experimental data, without which this work would not have been possible. I would also like to thank Prof. Toni Mattila from Aalto University, who helped me in providing an excellent summary on state of the art literature work in solder field and sharing his enriched experience/insights with me in this field. I would like to thank Prof. Sarah Penniston Dorland from Geology department at University of Maryland, for her guidance and support in allowing me to use the cross-polarized microscope.

My deepest gratitude goes to my family without whose support none of this could have been possible. I would like to thank my mother for her boundless love, patience and support. Values taught by my father and his wisdom helped me in making right choices in all aspects of my life including research.

I would like to thank my colleagues Cholmin Choi, Dr. Koustav Sinha, Jingshi Meng, Dr. Sandip Haldar, Ranjith Kumar, Dr. Preeti Chauhan, Dr. Gayatri Cuddalorepatta, Dr. Chandradip Patel, Dr. Sagar Chowdhury, Dr. Diganta Das, Ehsan Parsa, Ehsan Mirbhagheri, Dr. Dan Farley, Stuart Douglas, Qian Jiang, Josh Akman, David Leslie, Hannes Greve, Bhanu Sood, Anshul Srivastava, Hao Huang, Matt Ernst, Ed Habtour, Sandeep Menon, Jeami Hertzberger, Elviz George and other colleagues for their support, encouragement, and for creating an amicable work atmosphere in the laboratory.

I would also like to thank all the German Interns who have worked with me over the years as a part of their internship curriculum. Without their contribution and painstaking work with the microscale TMM specimens, this work would have never been possible.

I would like to thank more than 100 companies and organizations that support research activities at the Center for Advanced Life Cycle Engineering (CALCE) at the University of Maryland, College Park annually.

Last but not the least I would also like to thank the Mechanical Engineering administrative staff (Lita Brown, Penny Komsat, Lee Ellen Harper, and Amarildo DaMata) who were very helpful and prompt in helping me with administrative issues and thereby making my stay at the University of Maryland enjoyable and smooth.

Table of Contents

List of Tables

List of Figures

Chapter 1 : Introduction

Sn3.0Ag0.5Cu (SAC305) and Sn1.0Ag0.5Cu (SAC105) alloys form the focus of this study, which are currently being considered by microelectronics industry, owing to their low cost and similarity to near eutectic SAC387 (Sn3.8Ag0.7Cu) in terms of their microstructure and mechanical response. Owing to significant differences in microstructure and underlying deformation mechanisms, previous conclusions about Sn37Pb cannot be extrapolated to predict the mechanical behavior of SAC solders. For example, Sn37Pb alloy consists of large, soft, equiaxed Pb islands embedded in a polycrystalline Sn matrix [1] [Fig. 1.1], with grain boundary sliding (GBS) as the dominant creep mechanism. In comparison, the microstructure of SAC solder interconnects at microscale dimension is much more complex, consisting of phases of significantly different hardness and length scales. The microstructural length scales vary from dimensions of Ag_3Sn intermetallic compounds (IMCs) (nm) in the Sn-Ag eutectic region, which provide the dispersion creep strengthening [2], to structural length scale dimensions of Sn grains (mm) that contribute to the non-homogeneous behavior of micronscale SAC joints [Fig. 1.2][3][4]. The mechanical behavior of Pb-free SAC solder is heavily dependent on these microstructural features, such as anisotropic BCT (body centered tetragonal) Sn dendrites and IMC phases (of nm and μm dimensions) dispersed in the bulk and at the interface of the solder. Unlike Sn37Pb solder, hard nanoscale Ag_3Sn IMCs and micron scale Cu_6Sn_5 IMCs, that are embedded around soft Sn dendrites in SAC solders [5][6], cause dislocation glide and climb to be the dominant [2][6] mechanisms of creep deformation instead of grain boundary sliding. Because of the intrinsic anisotropy of the lattice structure of BCT Sn, which constitutes majority of SAC solder (e.g. 96.5 wt-% of Sn in SAC305 and 98.5 wt-% of Sn in SAC105), single crystal SAC solder joints are highly anisotropic. In the case of micron scale functional SAC solder joints; the coarse grain configuration also has an additional orientation dependent influence on the heterogeneous and anisotropic mechanical behavior as opposed to polycrystalline isotropic Sn-Pb solder joints [4][7]. As a result no two joints have similar grain structure and hence no two joints have similar anisotropic behavior in structural axes. This causes tremendous amount of joint-to-joint variability of mechanical behavior and hence, it is not cost-effective to attempt a purely empirical approach for a comprehensive

understanding of the dependence of the mechanical constitutive response of SAC solders on their microstructure. Furthermore, such empirical understanding cannot be easily extrapolated to other test conditions/solder material systems. Macro-scale phenomenological models developed so far also have several disadvantages since they are not explicitly connected to the intrinsic microstructural features and mechanisms. In order to obtain insights into the physics of the deformation process induced by each of the microstructural features, a multi-scale anisotropic modeling framework is needed, with the capability to capture the anisotropic and heterogeneous creep deformation mechanisms in micron scale joints, in terms of key microstructural features. There are three objectives for developing such a multiscale microstructural creep model for SAC solders.

The first objective is to explain piece to piece variability in constitutive creep response of SAC solders tested under identical loading conditions. The example material used in this part of the study is SAC305.

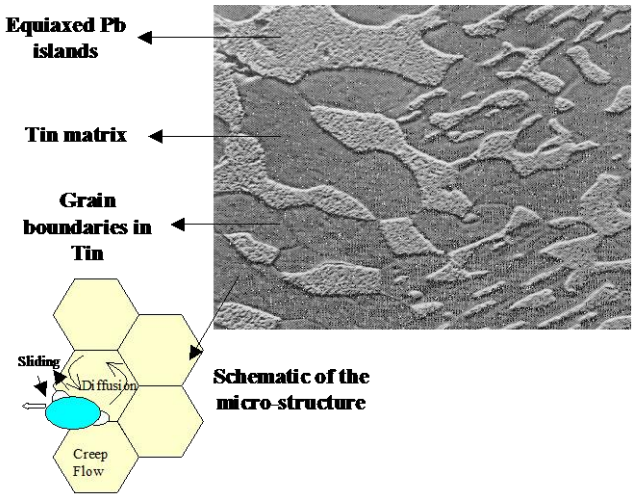

Figure 1.1: Typical microstructure of SnPb solders (Schematic adapted from Sharma, [1], cross-section image of SnPb solder from Lau, 1990)

The second objective is to explain the influence of the composition of SAC solders on the mechanical behavior, based on the composition-induced changes in the microstructure. The direct motivation comes from the commercial emergence of low cost hypoeutectic low-silver SAC solders (SAC105X) with addition of trace micro-alloying elements (X). The purpose of the micro-alloying is to reduce the amount of undercooling and hence refine the as-solidified microstructure of SAC105 solder joints to

obtain a more isotropic, homogeneous and stable behavior. Various trace elements (e.g. Mn, Sb, Bi, Zn, Ge, Ni, Ti, Cr, Co and Fe) have been added previously to SAC solder joints to improve their shear strength, drop durability, thermal cycling reliability etc. Some of the studies report improvement in mechanical response (especially drop durability) due to addition of these dopants but very few provide in-depth understanding of the effects of addition of these dopants on the microstructural features and the reasons behind the improvement in mechanical response. In particular, none of the studies in the literature have reported the effect of these added dopants on the creep resistance of SAC solder joints. Here, in the current study, the effect of two dopants, manganese (Mn) and antimony (Sb) on the creep resistance of SAC105 solder joints will be studied under constant force loading. The proposed multiscale microstructural model will be used in conjunction with quantitative microstructural information obtained from the microstructural investigation carried out on as-solidified microstructure of SAC105X solders, to explain the effect of such microalloying on the creep response of the solder alloy. In the third objective of this study, the effect of particle coarsening in SAC305 solder joints (induced by thermal aging) on the creep response of the solder alloy will be studied and modeled microstructurally, using the proposed multiscale mechanistic model.

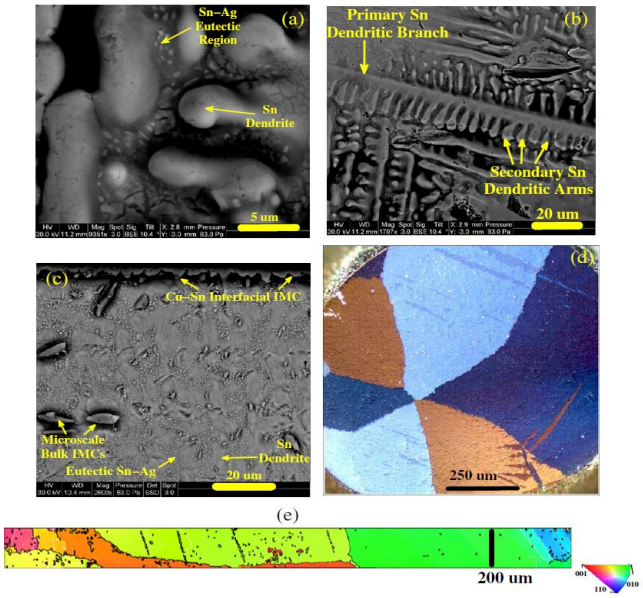

Figure 1.2: (a) 3D view of Sn dendrite (b) 2D view of Sn dendrite (c) Ag_3Sn and Cu_6Sn_5 IMCs and eutectic Sn-Ag phase in bulk solder (d) Coarse grained BGA SAC solder joint (e) OIM map of TMM solder joint] [8]

1.1.Background & Motivation

The motivation behind the multi-scale modeling of the anisotropic creep mechanisms of SAC solders to gain understanding of the scatter in their creep response is provided in Section 1.1.1. The motivation behind studying the effect of addition of trace micro-alloying elements (X) on the creep response of SAC105 solders is provided in Section 1.1.2. The motivation behind modeling the effect of particle coarsening on the creep constitutive response of SAC solders (e.g. SAC305) due to isothermal aging is provided in Section 1.1.3.

1.1.1. Multi-scale modeling of anisotropic creep response of SAC solder joints

There have been numerous studies conducted on the creep constitutive response of SAC solder interconnects. Most of the studies are phenomenological in nature and report a significant amount of scatter in the creep response. In one such study, the secondary creep strain rate of Sn3.9Ag0.6Cu alloy was studied at varying stress levels (2-40) MPa at varying temperatures (-25°C to 160°C) by Vianco et al. [9]. Significant variability in the creep curve shape, strain magnitude, and steady-state strain rate properties was observed, which was mainly attributed to differences in solder microstructure. Recently, another comprehensive review of the secondary creep response of SAC solder interconnects reported by Ma et al. [10] also pointed towards huge scatter in the secondary creep strain rate data reported by several authors [Fig. 1.3(a)]. Large discrepancies in the creep data are often acknowledged to be due to the differences in the microstructure of the tested samples, but unfortunately detailed investigation of this issue has not been adequately addressed in the literature. Another recent study by Rist et al. [11] also pointed towards significant scatter in the secondary creep rate of SAC387 solder tested at five different temperatures under varying stress levels [Fig. 1.3(b)]. In a separate study by Cuddalorepatta et al.[12], variation in the secondary creep rate of SAC305 solder was reported at three different temperatures [Fig. 1.4(a)]. Creep measurements for five different specimens of SAC305, fabricated using similar protocols, exhibited significant scatter in creep strain when tested at the same stress level (20 MPa) at 25°C [Fig. 1.4(b)]. In another study by the same author [13], variation in the primary creep strain history and the decay term was also reported [Fig. 1.5]. Significant variability (1-2 orders of magnitude in the case of primary creep response and secondary creep rate) exists in the viscoplastic

measurements of solders reported across different research groups. Such a large amount of scatter in the measurements has been mainly attributed in recent reports to the current solder interconnect length scales; because Pb-free solders such as SAC and Sn3.5Ag have very few Sn grains after reflow [Fig. 1.6(a)] Bogersen et al. [14]. Furthermore, single crystal Sn is known to exhibit significant anisotropy in their mechanical and thermal properties [Fig. 1.6(b)], shown by Bieler et al. [15]. The Young's modulus and CTE of Sn (the primary phase in SAC solders) are found to vary by a factor of 2-3 along the principal crystallographic directions. Therefore, microscale high-Sn Pb-free solder joints, such as SAC are expected to demonstrate significant piece to piece variability in their mechanical response in the as-fabricated state, depending on the crystallographic orientation distribution of the few Sn grains in a given joint [14][15][16][17].

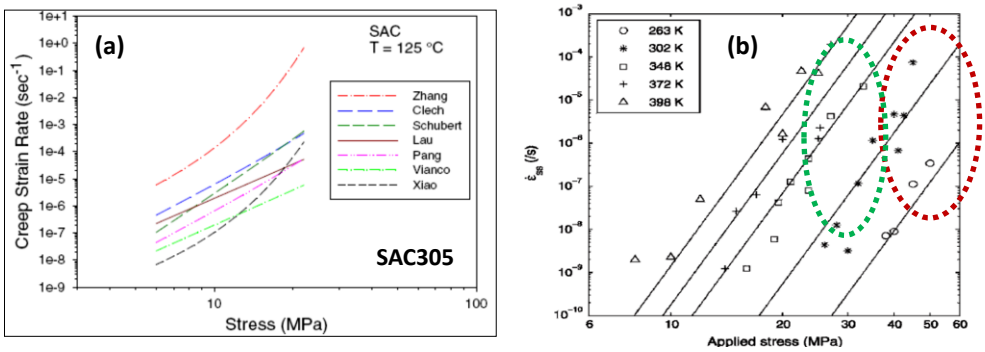

Figure 1.3: (a) Variability in creep data for SAC305 solder predicted by several authors [10] (b) Variability in secondary creep rate of SAC387 solder [11] (Dotted circle added in to emphasize the scatter)

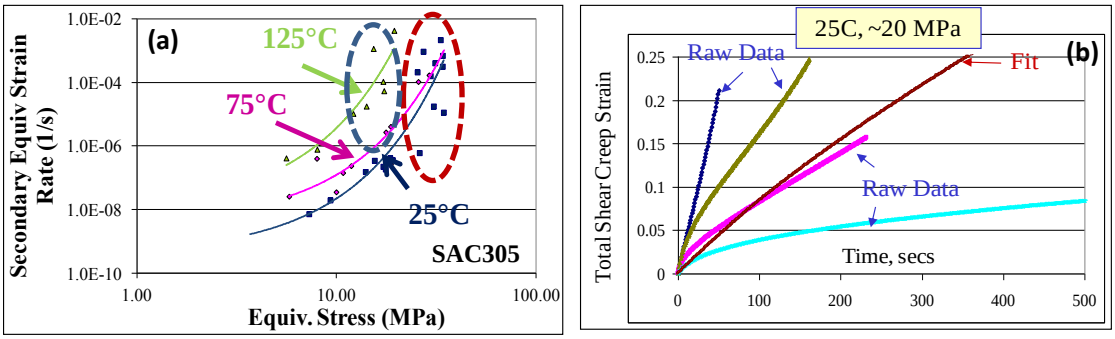

Figure 1.4: (a) Secondary equivalent creep rate for SAC305 specimens at three different temperatures [12] (Dotted circle shows the stresses at which the scatter is evident) (b) Variation in total shear creep strain for four as-cast SAC305 specimens loaded at 20 MPa tested at room temperature

This scatter was not evident or reported in previously widely used Sn-Pb solder interconnects because Sn-Pb solder interconnects are primarily polycrystalline joints, which cancels out the directionality dependence of properties, rendering the structure statistically homogeneous and isotropic.

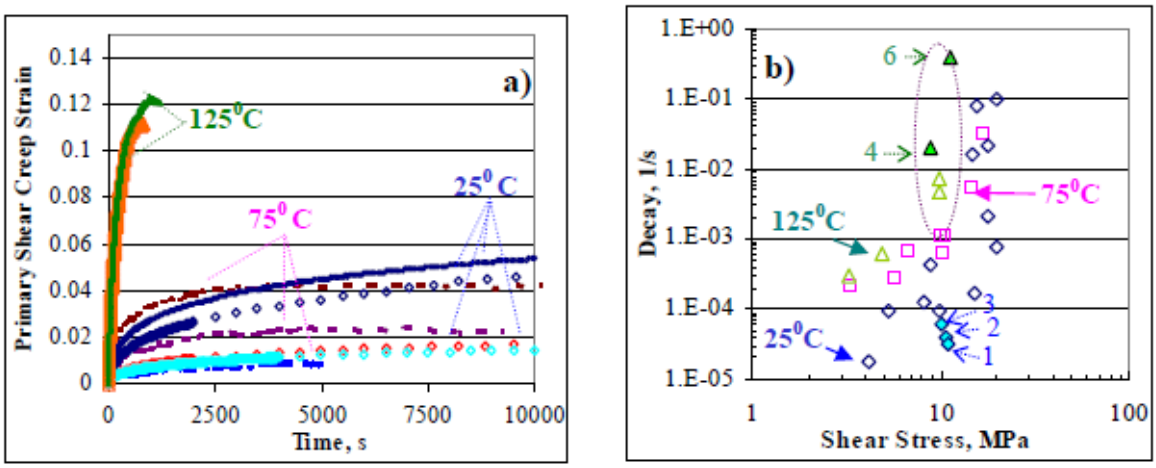

Figure 1.5: (a) Primary creep strain history at 10MPa across nine samples (b) Decay term of primary creep strain (Dotted circle shows the stresses at which the scatter is evident) [13]

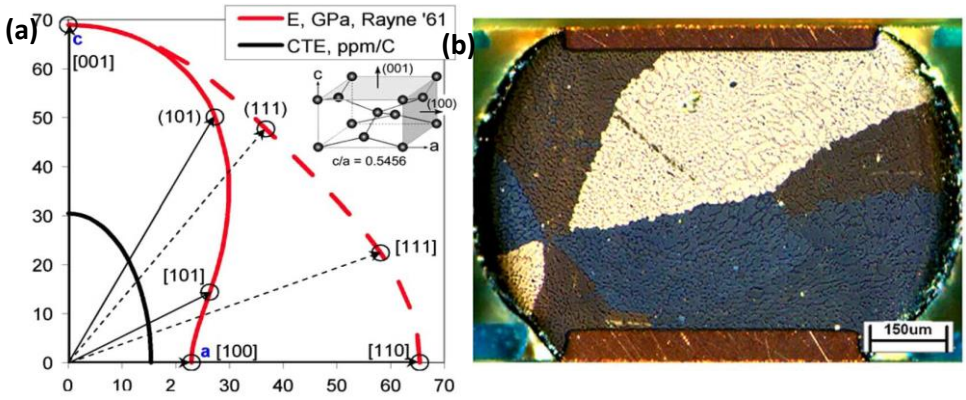

Figure 1.6: (a) Elastic modulus and CTE vary by a factor of (2-3) along principal crystallographic directions [15] (b) Cross-polarized image of BGA solder ball [17]

Hence, given this non-homogeneous coarse-grained microstructure of micron scale SAC solder joints and the associated anisotropy of Sn, it is important that the length scales and microstructure of the solder test specimen used for the study are comparable to the structural length scale of functional solder interconnects. The importance of specimen geometry is further supported by studies by Weise et al. [18] and Anderson et al. [19] that report significant differences in the mechanical response and

microstructure of bulk specimens versus micrometer-scale specimens, and material level tests versus assembly level solder joint tests. Therefore, as a part of this dissertation, the primary objective will be to use micron scale specimens, which will mimic the microstructural length scales of functional solder interconnects and develop a multi-scale modeling scheme, which can address the above unresolved issues. The proposed multi-scale model should have the ability to explain the piece-to-piece variability in the constitutive creep response of SAC305 solder.

1.1.2. Effect of addition of trace elements on creep response of SAC105 solder

The Sn-Ag-Cu (SAC) alloy family is considered to be one of the most favorable material systems as a replacement for eutectic tin-lead solder. However, there are still some shortcomings that need to be overcome. Numerous studies have revealed that additions of trace elements to SAC alloys provided a marked improvement in the microstructural features and the mechanical properties, and have attracted considerable attention. Kim et al. [20] reported that trace elements can form various IMC precipitates and reduce undercooling during solidification. Kang et al. [21] demonstrated that a small amount of Zn addition has the ability to reduce undercooling efficiently and suppress the formation of massive primary Ag_3Sn plates. Anderson et al. [22][23] proposed that adding Co and Fe can modify interfacial Cu-Sn compounds and increase the shear strength of joints plated with Cu. Kariya et al. [24] suggested that an addition of 0.05 wt.% Ni can enhance the low cycle fatigue endurance of flip-chip interconnections. Also, it has been reported that for Ni doped Sn-Ag solder joints plated with Cu, interfacial IMC was irregular $(Cu, Ni)_6Sn_5$ rather than scalloped Cu_6Sn_5 and did not show an observable change in thickness after long time aging [25]. Song et al. [26] found that trace element addition can effectively suppress the formation of the Ni-Sn-P phase between Ni_3P and interfacial compounds in SAC solder joints with Cu/ Ni(P)/ Au substrate. In addition to a reduced Ag content, a recent research [27] suggested that doping with either a small amount of Mn or Ti brings a pronounced improvement in drop test performance of SAC solder joints with electroplated Ni/Au surface finish. Also, Antimony has long been one of the candidate elements to be included as a minor alloying element in SAC solders. The Sn2.5Ag0.8Cu0.5Sb, also known as CASTIN™, is perhaps the most widely used Sb-containing alloy in the electronics industry. Due to the fact that Mn & Sb containing solders are still not very commonly used in the industry, many of the mechanical properties, such as

creep and mechanical cyclic fatigue in particular, of the Mn & Sb containing SAC solders are still unknown. Therefore, this study aims to experimentally investigate and theoretically model the effect of Mn and Sb dopants on the as-solidified microstructure and creep constitutive response of low Ag SAC (SAC105) alloy.

1.1.3. Effect of isothermal aging on creep response of SAC305 solder

Studying the effect of isothermal aging on the creep constitutive response of SAC solder interconnects has been one of the most popular areas of interest in the electronic packaging community. Several studies have demonstrated how the creep resistance of SAC solders decreases with increase in the isothermal aging duration and temperature. A comprehensive review of the effect of aging on the creep behavior of lead free solders (Sn3.0Ag0.5Cu and Sn4.0Ag0.5Cu) was presented by Ma et al. [28], where isothermal aging was conducted for varying durations (3 days, 6 days, 9 days, 21 days, 42 days, and 63 days) at room temperature (RT). For both the above alloys, RT aging affects both the steady state creep rate in the secondary creep region, and the elapsed time before tertiary creep and rupture. For the highest stress level considered, the creep strain rate increased by factors of 16X for Sn4.0Ag0.5Cu and 73X for Sn3.0Ag0.5Cu after 63 days of RT aging. In another study by the previous group [29], they also studied the effect of elevated temperature aging (80, 100, 125, 150 °C) on the creep resistance of Sn3.0Ag0.5Cu and Sn4.0Ag0.5Cu lead free solders. The samples were aged for various durations (0-6 months). Elevated temperature aging for longer durations was observed to drastically reduce the creep resistance of the above alloys. The decrease in creep resistance was hypothesized to be due to significant coarsening of second phase particles at high temperature, thus reducing the dispersion strengthening from the second phase particles. The same research group also extended their previous studies by including two more low silver alloys (Sn2.0Ag0.5Cu and Sn1.0Ag0.5Cu) and increasing the aging duration from 6 to 12 months [30]. As expected, the creep rates evolved more dramatically when the aging duration was increased. It was also observed that lowering of the silver content in SAC alloy leads to increase in the creep rates for all aging conditions. Similar observations have been also reported by Xiao et al. [31] for Sn3.9Ag0.6Cu which were aged at 180°C. All the above studies have been purely experimental and do not provide much insight into the physics of microstructural evolution occurring during isothermal aging at either room temperature or

high temperature. The proposed multiscale model will be used to explain the above observations based on underlying evolving microstructural features.

With the above motivations explained, the problem statement of this dissertation is now succinctly formulated below.

1.2. Problem Statement

Develop multiscale anisotropic mechanistic models to capture the effect of anisotropy of BCT Sn single crystal on the primary and secondary creep response of heterogeneous SAC joint scale interconnects and then use the above models in conjunction with experimentation and microstructural investigation to:

(i) understand the physics behind the variability in the creep response of SAC305 solder interconnects observed under identical loading conditions.

(ii) characterize the effects of micro-alloying with trace elements on the mechanical constitutive creep response of low silver content Sn1.0Ag0.5Cu (SAC105) solder.

(iii) understand the effects of isothermal aging on the constitutive creep response of Sn3.0Ag0.5Cu (SAC305) solder.

1.3.Literature Review

Literature review for the multi-scale modeling of anisotropic creep response of SAC solder is presented in Section 1.3.1. Literature review for studying the effect of addition of trace micro-alloying elements (X) on low cost hypoeutectic low-silver SAC (SAC105) solders will be provided in Section 1.3.2. Literature review for modeling the effect of particle coarsening on creep constitutive response of SAC305 due to isothermal aging will be provided in Section 1.3.3. In order to understand the gaps in the literature, a brief review of the multiscale modeling approach used in this dissertation has been discussed here. The microstructure can be classified into five distinct length scales, as shown in Figure 1.7 and discussed below.

The electronic subsystem of the printed wiring assembly (PWA) is the highest level of scale (Tier 5) relevant to interconnect stress modeling. This includes the geometry and materials of the printed wiring board (PWB) and the component that are soldered together, because these features govern the history of loads that will be generated on the solder joint during thermomechanical excursions. The solder joint is the means through which mechanical loads are transferred between the package (or component) and the PWB. Tier 4 represents the geometry of the solder joint itself and the architecture of the interfaces with the component and PWB (including the interfacial metallization and IMC layers) because this geometry governs the complex evolving boundary conditions imposed on the solder joint. In this study, the structure of interest at Tiers 4 and 5 is not a functional electronic assembly but rather a modified Iosipescu lap shear specimen [32] used for mechanical characterization. The next lower length scale (Tier 3) is the grain scale microstructure, typically consisting of one or several anisotropic Sn grains, either consolidated in a few large connected domains or intercalated over many smaller interconnected sub-domains, and sometimes in a truly polycrystalline arrangement. The grain boundaries are part of the Tier 3 micro-architecture because they play an important role in inelastic deformation mechanisms. The next lower length scale (Tier 2) focuses on the structure within individual grains, comprising of multiple tin dendrites formed during the solidification process, and surrounded by an eutectic Sn-Ag microconstituent that was the last to solidify. Embedded throughout this grain are additional micron scale intermetallic Cu_6Sn_5 precipitates that can be straight or branched structures of hexagonal cross-section. At this length scale, anisotropic composite models are effective for describing the load sharing between the Sn dendrites and the surrounding eutectic microconstituent. Tier 1 describes the details of the structure within the eutectic Sn-Ag microconstituent, consisting of a statistically homogeneous distribution of nanoscale Ag_3Sn ellipsoidal intermetallic particles embedded in a mono-crystalline tin matrix. The boundaries between the dendrites and the eutectic regions are sometimes low-angle grain boundaries (that sometimes recrystallize into high-angle grain boundaries during cyclic thermo-mechanical loading). At this length-scale, anisotropic models of dispersion strengthening due to dislocation interactions with interspersed particles that depend on spacing/size are appropriate. Tier 0 refers to the Body Centered Tetragonal (BCT) structure of the Sn matrix itself because it governs: (i) the associated dislocation slip systems needed for modeling in Tier 1, (ii) edge and screw dislocation line tension,(iii) dislocation mobility and (iv) intrinsic orthotropy of mechanical

properties in the crystal principal axis system. To model the anisotropic viscoplastic response of SAC single crystal, appropriate hierarchical models are needed for Tiers 0, 1, and 2, with relevant information being passed between each of these levels of scale efficiently to models at the next higher level.

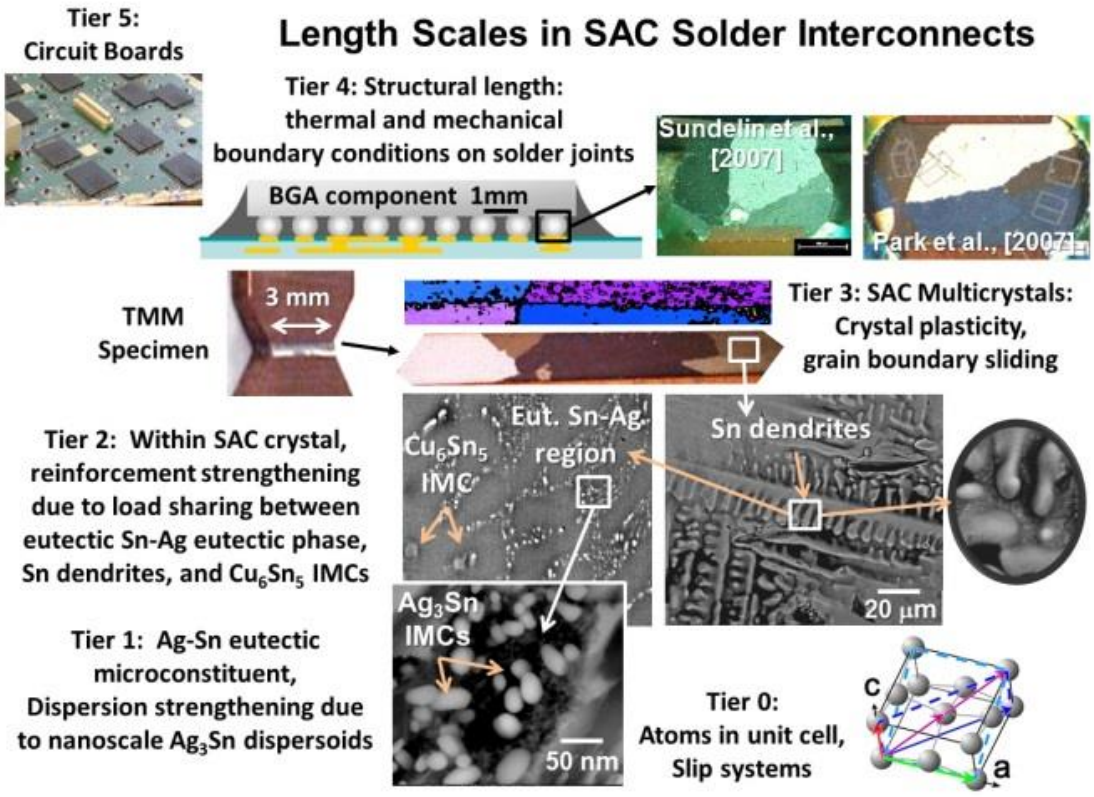

Figure 1.7: Multiple length scales (Tiers 0-5) in SnAgCu solder alloys

1.3.1. Multi-scale modeling of anisotropic creep response of SAC alloys

In Section 1.3.1.1, a background of the current state-of-art on the available macro-scale, phenomenological models for constitutive creep response is provided; a review of analytical and numerical modeling techniques to account for the effect of anisotropy on the creep response of coarse grained joint scale SAC solder specimens is given in Section 1.3.1.2. Since, several dislocation driven mechanisms will be addressed as a part of this study, a brief overview of dislocation mechanisms in materials systems is given in Section 1.3.1.3, with a major focus on dominant dislocation driven mechanisms for creep and plastic deformation. Since a multi-scale modeling strategy is adopted, a review of the available mechanistic models, both for solders systems and non-solder material systems,

are given in the Section 1.3.1.4. The literature review section will conclude by identifying the gaps (Section 1.3.1.5) in the existing multi-scale modeling literature in the context of addressing the critical influence of inhomogeneity and anisotropy on the constitutive creep response of SAC solder joints. The research objectives will be discussed in Section 1.3.1.6.

1.3.1.1.Review of macroscale empirical constitutive creep models

Since solder creep behavior is dependent on temperature, time and stress, and typically becomes important at $0.4T_m$ (where T_m is the absolute melting temperature of solder), majority of the macro scale models developed so far incorporate all three above independent variables – time, stress, temperature for describing the creep deformation behavior of solder alloys.

In the case of solders, secondary creep (also called steady state creep) has been extensively studied since it dominates the creep rupture life and creep-fatigue of the solders. Most popular models used for describing the secondary creep rate of solders are discussed below. Steady state creep strain rate is given below by Dorn's equation

$$\dot{\varepsilon}_c = \frac{AGb}{K_B T}\left(\frac{b}{d}\right)^p \left(\frac{\sigma}{G}\right)^n D_0 \exp\left(\frac{-Q}{RT}\right) \qquad (1)$$

where, $\dot{\varepsilon}_c$ is secondary creep strain rate, G is the shear modulus, A is a material constant, b is the Burgers vector, d is the grain size, p is the grain size exponent, D_0 is the diffusivity, n is creep stress exponent, Q is the activation energy, K_B is the Boltzmann constant, and T is temperature in Kelvin. From the above equation, it can be clearly seen that the steady-state creep strain rate is related to shear modulus, grain size, activation energy and the external loading conditions, such as temperature and applied stress. A decrease in grain size or an increase in service temperature or applied stress leads to a rise in the steady-state creep strain rate and a fall in the creep lifetime. This model cannot capture the contribution from the microstructural features at Tier 1 and 2 length scales discussed before. It can only handle Tier 3 (grain size only) length scale partly because it cannot model the effect the grain orientation or the effect of grain boundary.

Another popular model which has been extensively used for study of solder alloys is Weertman's power law constitutive model

$$\dot{\varepsilon}_c = A\sigma^n \exp(-\frac{Q}{RT}) \quad (2)$$

At high stress, this simple power law dependence on stress breaks down and the creep strain rate increases more quickly with applied stress. To provide a wider formulation for power law creep (low and medium stress level) and power-law breakdown (high stress level), double power-law and hyperbolic sine functions have been also widely used. The double power-law model can be expressed as follows:

$$\dot{\varepsilon}_c = A_1\sigma^{n_1} \exp(-\frac{Q_1}{RT}) + A_2\sigma^{n_2} \exp(-\frac{Q_2}{RT}) \quad (3)$$

Where, the first term in Equation. 3 corresponds to the creep behavior at low stress level, at which diffusion creep along grain boundaries is dominant, and the second term corresponds to the creep behavior at high stress level, where dislocation creep is dominant.. Q_1 and Q_2 are the activation energies of grain boundary sliding and dislocation climb, respectively. A_i and n_i are independent creep coefficients and exponents, respectively, for the two dominant mechanisms. The Garofalo steady-state creep model using the hyperbolic sine function has also been extensively used to model the power-law breakdown region, and is expressed as follows:

$$\dot{\varepsilon}_c = A[\sinh(\alpha\sigma)]^n \exp(-\frac{Q}{RT}) \quad (4)$$

Where, α is the stress multiplier, A, n, Q and T have the same meanings as in Equation. 1. Unlike in Equation 3, this model cannot address different activation energies for the two different dominant creep mechanisms (at low and high stress levels). Similarly, the creep coefficients and exponents for the two dominant creep mechanisms are interdependent.

The above steady-state creep models have been widely used to describe solder joint creep behavior for assessing electronic assembly reliability under thermal cycling loading conditions.

Majority of the constitutive models developed over the years for describing the creep deformation ignored the contribution of the primary creep and assumed that the secondary creep strain dominates over the primary creep strain in most problems of practical interest. In other words, most of the constitutive models like sine-hyperbolic Garofalo model, Dorn power law model, Weertman's model etc. ignore the contribution of primary creep and assume that the modeled material predominantly

exhibits secondary creep. However, testing of lead free solders has shown that this is not a good assumption when describing the behavior of these alloys. In order to account for the effects of primary creep on the reliability of the solder joints, a new model was proposed by Clech [33]. The model predicts total creep strain as the sum of primary and secondary creep strain.

$$\varepsilon_{creep} = \varepsilon_{sat}*(1-\exp(-K*\dot{\varepsilon}_{ss}*t)) + \dot{\varepsilon}_{ss}*t \qquad (5)$$

Where, ε_{sat} is primary saturated strain, K is a rate constant for exponential decay of primary strain and $\dot{\varepsilon}_{ss}$ is the steady state strain rate for a given stress and temperature. Clech showed that depending on stress and temperature, the primary creep can last from 10 seconds to 100 minutes, and steady-state creep appears to last from 1 minute to 100 minutes. The duration of the primary creep stage can be significant in comparison to the duration of test time encountered during accelerated thermal cycling profiles. Constitutive models that do not account for primary creep will underestimate the total creep strain. The above readings are in agreement with another work by Plumbridge [34], where he showed that assumption of steady state creep as the only stage of creep can result in significant underestimation (~100X) of creep life.

Bhate et al. [35] used a time hardening creep model to describe the evolution of creep strain with time under the application of constant stress at a given temperature. The form given below in Equation 6, chosen based on classical description of rate dependent behavior, is also used in commercial finite element packages.

$$\varepsilon_{cr} = K*\sigma^{n}*t_{p}*\exp(\frac{-Q_1}{RT}) + B*\sigma^{m}*t_{s}*\exp(\frac{-Q_2}{RT}) \qquad (6)$$

Where, first term in the equation accounts for the primary creep and the second term correspond to secondary creep regime. According to above authors, the time hardening model is more accurate than the Anand model, since it takes into account the primary creep regime which can be of significant duration depending on stress and temperature. Another study by Cuddalorepatta et al. [36] also investigated into thermomechanical response of solder under accelerated thermal cycling conditions using the generalized-exponential model for primary creep (Equation 7).

$$\frac{\epsilon_{sat} - \epsilon_p}{\epsilon_{sat}} = \exp(-d*t) \; ; \; \varepsilon sat = C_1*\sigma^{C}{}_2 \; ; \; d = C_3*\sigma^{C}{}_4*\exp(-Q/RT) \qquad (7)$$

Where, ϵ_p = equivalent primary creep, ϵ_{sat} = equivalent primary saturated creep, d = decay term, C_1, C_2, C_3, and C_4 are material constants.

All these above macro scale models are phenomenological in nature and do not explicitly take into account the underlying physical mechanisms while predicting the creep response of materials and therefore, they are suitable only for addressing the properties of isotropic homogeneous materials within the experimental range. In the current study, the limitations of the above models will be overcome by developing a mechanistic model to model the anisotropic primary and secondary creep response of heterogeneous solder interconnects by taking into account the physics of the underlying dominant microstructural deformation mechanisms.

1.3.1.2. Review of analytical and numerical models to investigate the effect of anisotropy on reliability of solder interconnects

Sn has a body-centered tetragonal structure with lattice parameters of a = b (0.5632 nm) and c (0.3182 nm), which is highly anisotropic with c/a ratio of 0.546. At 30°C, the coefficients of thermal expansion in the principal directions are $\alpha_{[100]} = \alpha_{[010]}$ = 16.5ppm/°C and $\alpha_{[001]}$ = 32.4ppm/°C. At high temperatures, the values change substantially, for example at 130°C, $\alpha_{[100]} = \alpha_{[010]}$ = 20.2ppm/°C and $\alpha_{[001]}$ = 41.2ppm/°C. The elastic modulus of single crystal Sn varies by a factor of 3 on the (101) plane (between the [100] and [001] directions).

Matin et al. [37] reported that anisotropy in thermal expansion and elastic properties of Sn induce significant stresses at Sn-grain boundaries (Fig. 1.8(a)) during thermal cycling. Fatigue damage was shown to occur in a mechanically unconstrained Sn-rich solder under thermal cycling between 293K and 353K. The micro-cracks were found to be localized mainly along high grain boundaries. A combination of experiments using orientation imaging microscopy and numerical methods was used to find a strong correlation between large stresses caused at grain boundaries and thermomechanical anisotropy of Sn. Zhao et al. [38] also studied the effect of anisotropy of Sn elastic properties and thermal expansion on Sn whisker growth during temperature cycling (-55°C - 85°C), using

computational modeling. The grain structure was explicitly captured in the model by using the Voronoi cell method (Fig. 1.8(b)). Sn elasticity of each grain was modeled using the elastic stiffness matrix of Sn single crystal. The crystal orientations were assigned to the grains according to the information collected by X-ray diffraction (XRD).

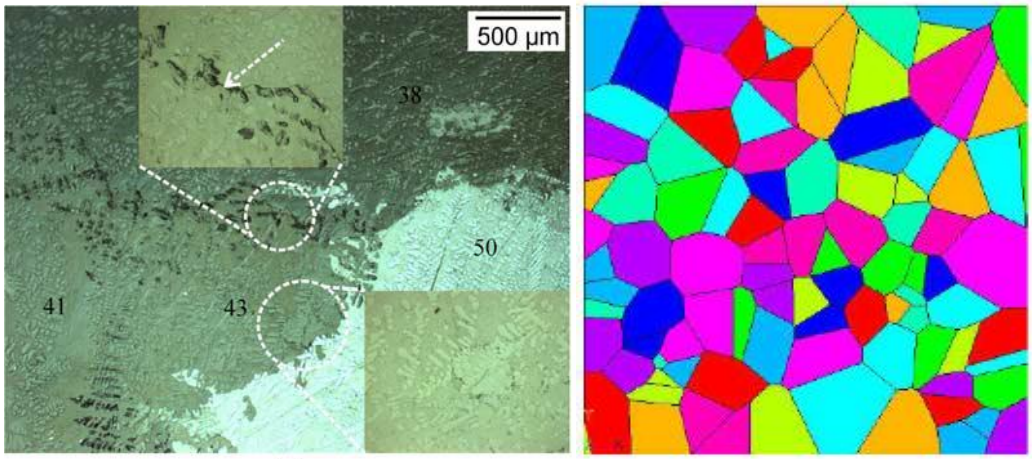

Figure 1.8: (a) Stress concentration at grain boundaries of BCT Sn grains [37] (b) Typical grain pattern (Vornoi diagram) generated replicating XRD image of actual solder joint structure [38]

The stress along with the strain energy density distributions in grains were calculated using finite element methods, for different grain structures of Sn microstructure. The effect of Sn plasticity was explored using a simple bilinear isotropic hardening stress–strain relation because anisotropic plastic properties were not available during the study. Creep response was not addressed in this study. The strain energy density criterion was selected to predict Sn whisker growth driving force. Strain energy density was found to be highest in the Sn grains with high angle grain boundaries due to significant anisotropy in elastic and CTE properties of Sn grains. In another study by Subramanian et al. [39], the CTE mismatch at the interface of Sn grains was found to be significantly higher compared to bulk solder-IMC interface or IMC-Cu pad interface, due to inherent anisotropy of the Sn phase (Fig. 1.9). Significant stresses that can develop from thermal excursions in Sn based solders can cause extensive grain boundary sliding and grain boundary decohesion. The coalescence of such cracks in the highly constrained region of the solder near the solder/IMC interface, can develop into catastrophic cracks that can degrade the mechanical integrity of the solder joint.

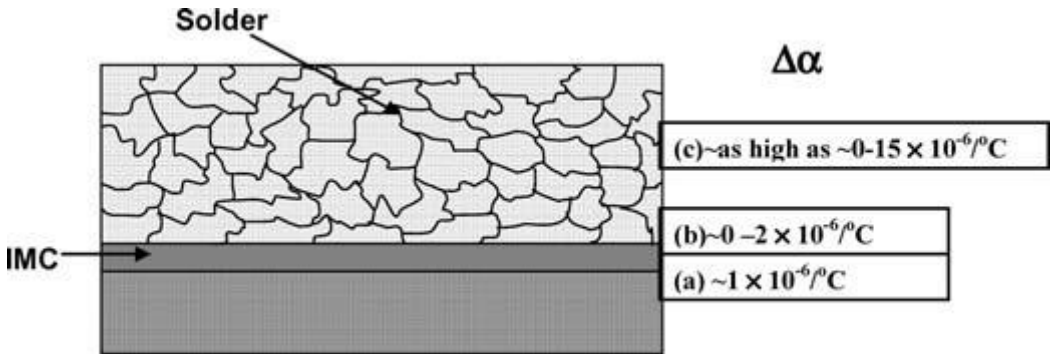

Figure 1.9: Schematic showing CTE mismatches in different regions of the solder joint [39]

Telang et al. [40] characterized the microstructure and crystal orientation of Sn phase in single shear lap Sn3.5Ag solder joint specimens. They found that solder joints are typically made up of at most a few dominant grain orientations, having low angle boundaries, implying a single or multicrystalline rather than a polycrystalline texture. The OIM maps from two opposite sides of a joint showed that the same crystal orientation is highly probable throughout the joint, implying that surface OIM scans are probably representative of the interior of the joint. The dominant orientations obtained after solidification from several specimens indicated some preferred orientations that may be a consequence of rapid crystal growth in [110] directions that are aligned with the heat flow direction. They hypothesized that lack of orientations with the [001] c-axis in the plane of the joint might have resulted from the large difference in thermal expansion between tin in the [001] direction and the copper substrate. A three-dimensional elasto-viscoplastic damage model has been used to investigate the possible influence of the mechanical and thermal anisotropy of Sn on fatigue damage by Ubachs et al. [41]. They modeled the elastic behavior and the thermal expansion coefficients as anisotropic, whereas the viscoplastic and damage behavior were considered to be isotropic. The simulations showed stress and viscoplastic strain concentrations at grain boundaries, dependent on the misorientation between the grains and their orientation with respect to the grain boundary. A consistent agreement was found between the numerically obtained strain distribution field and the experimentally observed damaged areas (Fig. 1.10). The authors concluded that anisotropy indeed plays an important role in determining

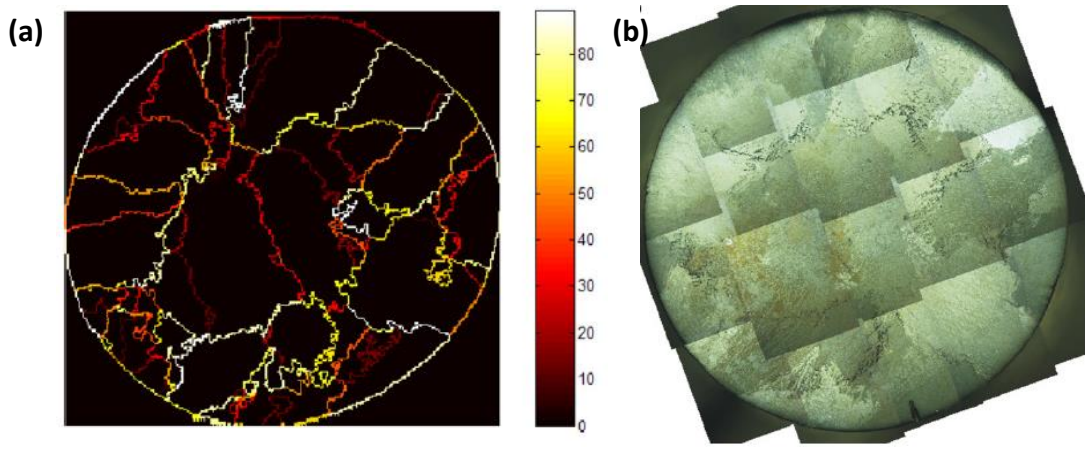

Figure 1.10: (a) Misorientation angles between the [001] crystal axes (b) Optical micrograph of SAC specimen after 1000 thermal cycles between 293 and 353 K [41]

the thermal fatigue life of SAC solders. In another study by Park et al. [42] a multigrained solder interconnect was modeled to study the effect of anisotropy on thermal cycling reliability of the joint. They used a global-local approach where the global model addressed the entire assembly of the component, substrate and interconnects; while the local model addressed an individual interconnect in much greater detail. Solder material properties used in the assembly level global model were considered to be homogenous and isotropic. Anisotropic elastic material properties of tin were used in the numerical local model of the single multi-grained interconnect. Stress concentrations were observed at the grain boundaries, depending on the orientation of the connected grains, their interfaces, and the orientation mismatches between the adjoining grains. Comparison of the numerical results with the experimental observations indicated a reasonable agreement with the strain distribution. The results (Fig. 1.11) showed higher strain localization not only along the pad-solder interfaces but also along the grain boundaries. Those were the primary areas of energy consumption during fatigue loading.

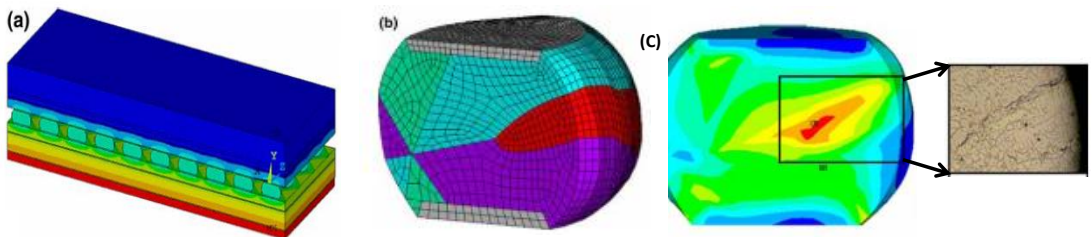

Figure 1.11: (a) Flip-chip plastic ball grid array package (b) Finite element mesh and 3D detailed FEA of each grain (c) von Mises strain at 100°C obtained from FEA and optical micrograph of regions with maximum plastic strain accumulated after 35 cycles of -45°C to 125°C [42]

In another recent study by Zamiri et al. [43], crystal plasticity analysis was used to evaluate stress and strain resulting from a 165°C temperature change in a single-crystal joint using two simplified geometries appropriate for realistic solder joints.

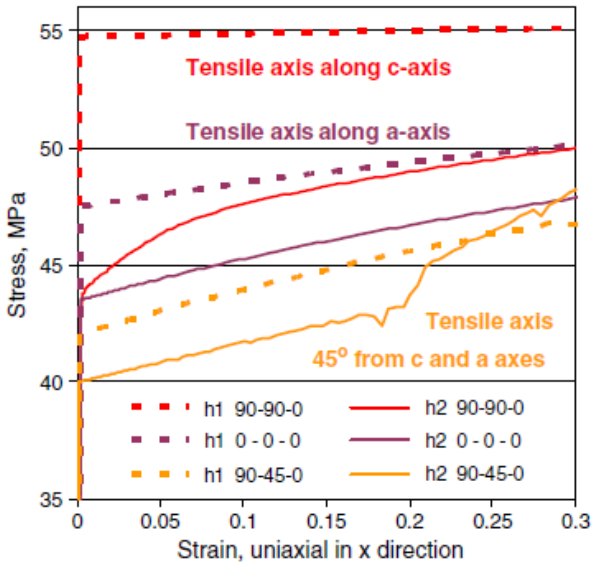

Figure 1.12: Uniaxial stress strain curves for two hardening cases studied using crystal plasticity parameters for Bunge Euler angle Sn orientations indicated in legend [43]

Phenomenological flow models for ten slip systems were estimated based upon semi quantitative information available in the literature, along with known anisotropic elastic property information (Fig. 1.12). The results showed that the internal energy of the system is a strong function of the tin crystal orientation and geometry of the solder joint. The internal energy (and presumably the likelihood of damage) is highest when the crystal c-axis lies in the plane of the substrate, leading to significant plastic deformation. When the a-axis is in the plane of the interface, deformation due to a 165°C temperature change is predominantly elastic.

As evident from the above studies, majority of the studies have focused on anisotropy present in elastic properties and CTE of Sn grains in their approach while modeling the thermal cycling reliability of SAC solder interconnects. None of the studies considered the anisotropic creep properties, which is

one of the most important properties, since these solder materials demonstrate significant amounts of creep deformation even at room temperature. The main reason that previous authors have not been able to use anisotropic creep properties of SAC solder interconnects in their studies is because creep properties of single crystal SAC solders are not available in literature. Also, the microstructural length scales in the above studies are limited to Sn grains and contributions from smaller features such as Sn dendrites and bulk IMCs are not explicitly captured in their creep constitutive models of SAC solder.

1.3.1.3.Overview of dislocation mechanisms in SAC material systems

The overview of dislocation mechanisms has been consolidated from basic dislocation theory textbooks and selected review articles [Hull, 1986], [Ashby and Frost, 1988], [Hirth, 1990], [Rosler and Arzt, 1989], [Herztberg, 1999], [Brehm, 2002], [Blum, 2002], and [Ovidko, 2002, 2004].

The driving force for dislocation nucleation in solders is believed to be due to local stresses generated during the reflow of the material. Under high strain rate loading conditions (and low temperatures), the material response is dominated by plasticity in phenomenological terms. At the micro-scale, the underlying physical mechanism is dislocation slip. The dislocations also multiply at various sources by various methods, under above loading conditions in order to accommodate the large plastic strains generated during inelastic deformation. Two mechanisms of importance that contribute to the regenerative multiplication of dislocations are Frank-Read type sources, and multiple cross glide. For further understanding of the multiplication of dislocations the reader is referred to Hull [1986], Hirth [1990], and Lardner [1974]. The characteristic velocity of these dislocations has a power-law dependence on the applied stress. However, if impurities or intermetallics (which serve as obstacles) are encountered, dislocations become pinned, causing a bowing of the dislocation line. Due to this pinning mechanism, higher stresses are required to drive the dislocation slip, and the bowing of the dislocations leads to what is known as Orowan hardening. This explains the phenomenological process of work hardening seen in tensile testing of material where a higher stress is required to drive deformations (strains) after yielding. This phenomenon is quantitatively modeled in dislocation theory by the bowing of Orowan loops. Dislocations can also be pinned due to the interaction with other sessile dislocations in the path of moving dislocation. This leads to the formation of jogs and kinks, each being distinguished based on the type of interacting dislocations (edge or screw). It should be

noted that dislocation stress fields experience not only short range interactions (leading to jogs and kinks), but also long range interactions.

Once the dislocation motion is obstructed, the physical mechanisms that help detach the pinned dislocations explain the creep deformation observed in the empirical formulations. Thus the mechanisms for subsequent motion of the trapped dislocations requiring energy are termed as "*non-conservative"* processes. The motion of dislocations in the plasticity context is also understood based on dislocation dipoles.

During creep deformation, the dislocations trapped around the particles move past the obstacles by dislocation climb and detachment. However, both of these processes require thermal activation and hence creep occurs at high homologous temperature. The rate at which the dislocations detach from the particles governs the creep deformation and is dependent on the available thermal energy available to overcome the athermal detachment stress. A quantitative formulation of this stress is given by Rosler et al. [44].

There are also other competing creep mechanisms. Along with the climb process, diffusion processes also occur under thermal activation. For example, the prismatic loops formed can either shrink or grow based on the diffusion of the vacancies. The dislocation loops formed by breaking up of dislocation dipoles can either be vacancy or interstitial loops and leads to rearrangement of material around the dislocation core. This contributes to stress relaxation phenomena observed empirically in creep conditions. Examples of such diffusion processes are pipe diffusion, volume self-diffusion etc.

Under cyclic loading, dislocations pile up at grain boundaries or particles and create enough energy to open a crack. This forms the basis of plasticity dominated fatigue damage. On the other hand, in creep dominated damage, the dislocation climb and glide contribute to local stress concentrations, which act as critical sites of void nucleation. Void growth followed by interlinkage leads to creep failure.

The active mode of deformation can be understood based on Ashby's deformation mechanism maps as a function of stress and temperature for the material under study. In addition to the above mechanisms, polycrystals also experience grain boundary sliding during creep deformation. As the homologous temperature is higher than 0.5 in most applications for SAC solder, the creep deformation is significant and cannot be ignored. This is true for both SnPb and Pb-free solders

even at room temperature (the homologous temperature for Sn37Pb is 0.65 and for Sn3.0Ag0.5Cu is 0.61). In the case of dispersion hardened materials such as SAC solder, the intermetallics particles serve as obstacles to the path of dislocation glide. The interaction between the particle and dislocation can be either attractive or repulsive. The dislocations upon reaching the particle has two options either change its slip plane by cross-slip or climb or move in the same path by moving through or bulging around the particle. When the dislocation cuts through the particle it is termed as "cutting mechanism". In the case where it wraps itself around the particle and moves ahead leaving behind loops called Orowan loops.

These two methods largely depend on the line tension of the dislocations and the strength of the particle. If temperature is high enough, then climb dominates even if the stresses are lower than the Orowan stresses. Assuming that the particles are strong enough and do not permit the cutting by the dislocations, then dislocation loops are left behind by the passing dislocation. When the back stress formed from the Orowan loops balances the applied stress, then the deformation is in equilibrium. However, this occurs only at low temperatures. However at high temperatures, these loops attain energy to climb and self-annihilate, thereby allowing deformation again. For a steady state of deformation, it is logical to see that the formation of loops should equal the disappearance of the loops.

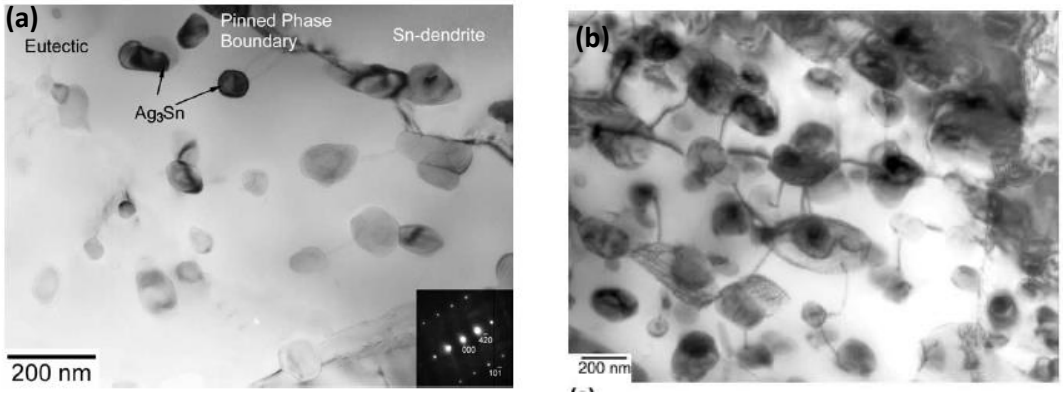

Figure 1.13: (a) Pinning of dislocation by Ag_3Sn in Sn3.5Ag (b) Pinning of dislocation by Ag_3Sn after creep deformation [45]

Weise et al. [45] reported from experimental testing that the creep deformation in eutectic SAC solder is dominated by dislocation climb. Chen et.al [46], found (for temperatures between 298 K and 398 K), that dominant creep mechanism was dislocation climb aided by lattice diffusion at lower stresses while at higher stresses combined dislocation glide and climb occurred. Similar observations were made by Dutta et al. [47], Kerr et al. [48] (shown in Fig. 1.13), Mathew et.al [49], and Ochoa et.al. [50], for Sn3.5Ag. Furthermore, Ochoa [50] found that grain boundary sliding was found to have a significant contribution to total creep strain in Sn3.5Ag bulk solder specimen. Mathew et al. [49] found that the creep mechanism between $0.58 < T_h < 0.8$, was dominated by dislocation climb. Hence, dislocation climb and detachment is found to be the primary creep mechanisms in SAC solder. The high secondary creep stress exponents of SAC solder reported in the literature [12] support the hypothesis that dislocation climb over obstacles is the dominant rate governing creep mechanism in SAC solder. Furthermore, TEM studies conducted by Artz et al. [51] on dispersion strengthened materials such as aluminum and titanium alloys suggest that dislocation climb occurs in multiple stages: approach, climb and detachment. A strong attractive interaction between dislocation and the obstacle is observed in post climb phase of the dislocation and the detachment of the departing dislocation rather than climb is seen to be rate limiting mechanisms for deformation (Fig. 1.14) [8]. The above mechanism was also evident in other studies by Kerr and Dutta et al. [48][46] that captured the contributions of the eutectic Sn-Ag phase and nanometer dimension IMC length scales. However, the model assumed that the behavior is dictated only by the dispersion strengthening of nanoscale Ag_3Sn IMCs in the Sn-Ag eutectic region. Thus the load sharing between the Sn matrix in the eutectic region and the Sn dendrites was not addressed in the above studies.

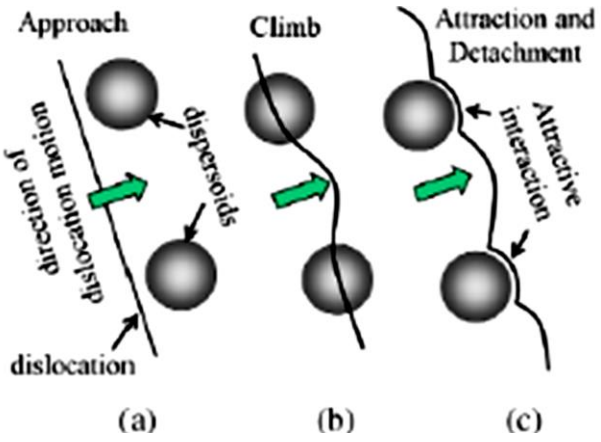

Figure 1.14: Schematic of dislocation climb and detachment of a single dislocation (a) while approaching the obstacle, (b) during climb over obstacle, and (c) experiencing attractive interaction with obstacle after climb and eventually departing form the particle (detachment)

1.3.1.4.Review of available mechanistic models for viscoplastic creep response

The mechanistic or physical models of creep constitutive response available in literature are discussed here. Gaps in the current literature are pointed out in Section 1.3.1.5. The microstructural length scales in SAC solder joints vary from nanometer-sized Ag_3Sn intermetallics in Sn-Ag eutectic region to the structural dimensions of Sn grains (~ mm), that contribute to non-homogeneous behavior of macroscale SAC joints. In the case of microscale SAC solder joints; the grain configurations have an additional influence on the constitutive response. The microstructure of Sn dendrites and IMCs is dependent on various parameters like manufacturing profile, loading history and weight fraction of Ag and Cu in SAC alloys [8]. Therefore, comprehensive understanding of the influence of each of these microstructural features through purely experimental parametric studies is both costly and time consuming. Moreover, such experimental understanding of the constitutive response based on empirical models cannot be extrapolated to other test conditions or other material systems. In order to obtain insights into the physics of deformation induced by each of these microstructural features, mechanistic modeling framework, that captures the dominant creep mechanisms in terms of key microstructural features, is needed.

Dutta et al. [47] suggested that the creep response of Sn-Ag solders is controlled by the behavior of the eutectic structure which consists of Ag_3Sn IMC particles embedded in a Sn matrix. The total creep rate of Sn-3.5Ag solder was written as the sum of two mechanisms, which occur simultaneously (i.e. in parallel with each other).

$$\dot{\varepsilon}_T = \dot{\varepsilon}_{gc} + \dot{\varepsilon}_{pc} \tag{8}$$

Where, $\dot{\varepsilon}_{gc}$ is the strain rate due to glide-climb mechanism (where either viscous glide or climb is rate controlling) and $\dot{\varepsilon}_{pc}$ is the strain rate due to particle limited climb. The glide-climb mechanism

dominates the observed creep behavior at low stresses, whereas the particle-limited climb mechanism dominates at high stresses shown in Fig. 1.15.

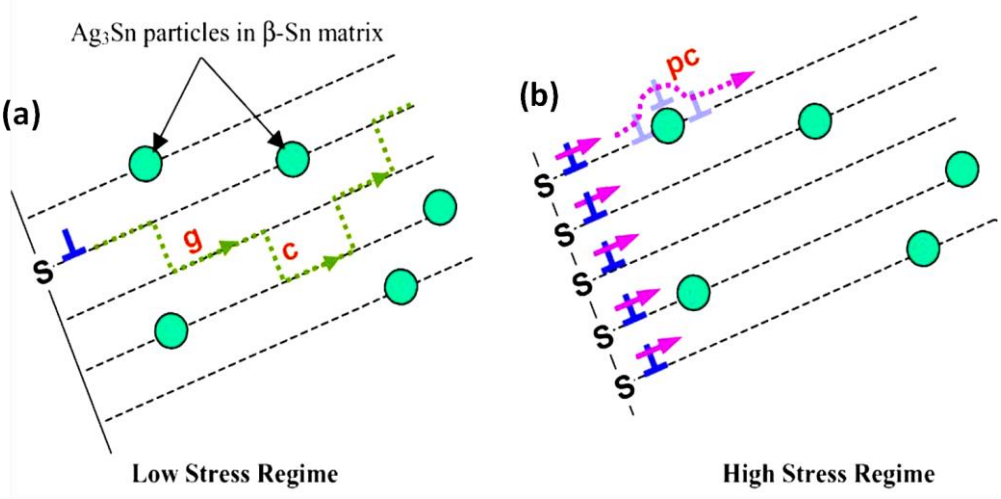

Figure 1.15: A pictorial summary of operative creep mechanisms in Sn-Ag. (a) The overall deformation of the "composite" microstructure is controlled by the behavior of the eutectic, which deforms via glide-climb ("g" and "c") at low stresses (b), and by particle- limited climb ("pc") at high stresses

Gong et al. [52] utilized above microscale dislocation climb detachment models to capture the creep response of nanoscale Ag_3Sn IMCs based on the work of Kerr et al. and Dutta et al. However, the model assumes that the behavior is dictated only by the dispersion strengthening of nanoscale Ag_3Sn IMCs in the Sn-Ag eutectic. Only the eutectic Sn-Ag region is modeled, without any load sharing of other scales. Most of the microscale models reviewed this far on constitutive modeling account for the nanoscale Ag_3Sn IMCs or the eutectic Sn-Ag region and assumes that the contribution of the Sn dendrites is negligible. In another study, Chawla et al. [53] reviewed the literature on analytical and numerical techniques available to model the heterogeneous microstructure of multiphase solder materials. Models presented in their review in 2007, mostly simplify the heterogeneous microstructure of multiphase solder materials. They first came up with a novel methodology that addressed the critical link between microstructure and deformation behavior, by using two-dimensional (2D) and three-dimensional (3D) virtual microstructures as the basis for a robust model to simulate damage caused by deformation. Their model was unable to capture all the dominant physical mechanisms during the deformation process because homogenized properties were considered for different phases in the

solder during FEA analysis. These simplifications definitely make modeling and analysis more efficient and straightforward, but fail to accurately predict the effective properties and local damage behavior which are inherently dependent on the microstructure of SAC solder. Another interesting study by Pei et al. [54] evaluated the effective creep properties of Pb-free SnAg solders using homogenization methods for the measured properties of individual phases (eutectic Sn-Ag phase and Sn dendritic phase). However, this technique does not utilize mechanistic equations to capture individual IMC phase properties and thus lacks the predictive capability for extrapolating the creep response to other microstructural states of SAC solder. Studies involving mechanistic modeling to capture the physics of the underlying viscoplastic creep mechanisms of SAC solder are very limited in the literature. Furthermore, studies that provide the influence of the Sn dendrites, micron-scale IMCs and the eutectic Sn-Ag region (lower length scales) on the creep behavior are required. To address the above issues, Cuddalorepatta et al. [8] proposed an isotropic mechanistic secondary creep model based on Rosler and Artz's dislocation detachment model [55]–[58] for SAC solders that captured the two lowest length scales (Tier 1 and Tier 2 described in Figure 1.7) . The smallest length scale modeled was that of nanoscale IMCs via analytical dislocation creep models, and the largest length scale was that of the Sn dendritic colonies (~μm). Since secondary creep measurements show much less sensitivity than primary creep, to the coarse-grained anisotropic Sn microstructure in the Sn3.0Ag0.5Cu specimens [12], geometric modeling of the Sn grains and grain boundaries was not necessary. Furthermore, isotropic modeling was considered to be adequate when developing analytical formulation of the creep deformation at the two lowest length scales. The response of the eutectic Sn-Ag region is evaluated by assuming Sn as the matrix and IMCs of nanometer dimension Ag_3Sn as inclusions. At the second level, the effective creep properties of SAC composite are evaluated by considering the load sharing between the eutectic Sn-Ag region embedded with micron scale Cu_6Sn_5 IMCs as the matrix and the micron scale softer pure Sn dendrites as the inclusions. The model accounted for motion of a single dislocation and inherently assumed that an attractive interaction exists between the dislocation and the nanometer dimension Ag_3Sn IMC dispersoids after climb into Sn matrix based on previous studies. The eutectic Sn-Ag shear creep rate was taken to be due to a combination of the Sn matrix shear creep rate and the Ag_3Sn IMC dispersion-hardening shear creep rate. Effect of Sn dendritic colonies is taken into account by using self-consistent homogenization

schemes (SCM) from micromechanics theories used in composite materials. The Sn dendrite lobes are assumed to be spherical shaped inclusions (with effective isotropic properties) and are hence accounted for only through their volume fractions in Eshelby's tensor. The sum of the volume fractions of the reinforced Sn-Ag eutectic region and Sn dendrites, which constitute the primary phases in SAC alloy, is taken to be equal to unity.

Although the model proposed by Cuddalorepatta et al. [59] provides theoretical insights into the effects of key microstructural features and detachment creep mechanism on the secondary creep behavior, it is still an isotropic model and cannot capture the anisotropic creep behavior of SAC single crystals. This becomes important in primary creep since experiments reveal that the single-crystal anisotropy and the grain structure have very strong influences on primary creep behavior. Furthermore, anisotropy introduced by the non-spherical shape of dendritic lobes also becomes important. Hence studies that address the impact of the experimentally observed non spherical Sn dendritic configurations on the measured creep response are necessary. The sensitivity of the model to the nanoscale IMCs is extremely high. In its present form, the above model only provides a "dilute approximation" since it does not explicitly account for the interactions between neighboring dislocation fronts at high dislocation densities. Furthermore the dislocation density used in Cuddalorepatta's study is based on a hypothetical assumption that all the slip planes in BCT Sn are completely saturated with dislocations when the creep deformation advances to the secondary creep regime. The dislocation density in all dominant slip systems of Sn is thus considered to be extremely high (~1E21 m^{-2}). This uniform saturation assumption of all dominant slip systems is the mechanistic underpinning in Cuddalorepatta's study for justifying the use of the isotropic model.. Therefore, experimentally observed anisotropic primary and secondary creep behavior of solder alloy cannot be modeled with Cuddalorepatta's model because of its inherent limitations. All these above limitations will be addressed as a part of the anisotropic model developed in this dissertation to explain the variability observed in creep response of SAC305 solder interconnects of varying grain structures.

1.3.1.5.Gaps in the literature

While the previous cited studies in the literature provide several insights into relationship between the mechanical behavior and microstructure of the SAC material systems for microscale and bulk solder joints, there are several unresolved new research issues.

1. Microscale SAC solder mechanical properties exhibit significant anisotropy in the as-fabricated state, due to the coarse-grained microstructure and the anisotropy of single crystal Sn. There are no studies that have provided mechanics-based predictive capability to estimate the primary or secondary creep constitutive behavior of such joints based on microstructural morphology, although several studies have pointed towards significant anisotropy in elastic and plastic properties of BCT Sn.
2. The coarse-grained morphology and the single-grain anisotropy together result in every joint having a unique creep response in the global loading axes. This result in significant scatter observed in primary and secondary creep response and this needs to be understood from the microstructural standpoint. The huge variability in primary creep measurements is significantly larger than that observed for secondary creep and also needs to be explored by considering the evolution of dislocation density in primary slip systems of Sn by modeling simultaneously dislocation generation, impediment by forest dislocations and Ag_3Sn particles and dislocation recovery from particles and forest dislocations in dominant slip systems during the creep process. Dislocation density used in a past study by Cuddalorepatta et al. [8] is based on a hypothetical assumption that all the slip planes in BCT Sn are completely saturated with very high dislocation density (~1E21 m^{-2}) when the creep deformation advances to the secondary creep regime. This assumption makes the secondary creep response isotropic and needs to be re-examined in light of the joint-to-joint variability observed in creep response of solder joints.
3. There has been no study which focuses on anisotropic evolution of dislocation density during primary and secondary creep regime along dominant slip systems. This needs to be modeled by explicitly modeling multiple creep recovery mechanisms (particularly dislocation climb and detachment mechanisms) observed in dispersion strengthened materials e.g. SAC alloys.

4. The detachment of dislocations climb during secondary creep is captured in the literature [59], [60] using dilute concentration approximation (i.e. the model considers only the interaction of a single dislocation with the Ag_3Sn IMC). Interactions between neighboring dislocation fronts need to be accounted for, to handle non-dilute dislocation densities.

5. One of the key parameters of the dislocation detachment model, relaxation parameter (k) [61], [62] (ratio of line tension of dislocation at particle-matrix interface to that in matrix only) used to capture the strong attractive interaction between dislocation and nanoscale particle during the post-climb phase, has been previously modeled as a function of stress and temperature and calibrated against experimental observations of secondary creep rates. However, authors think it is a fundamental property of the material and should have a constant value. The magnitude of k governs how strongly the detachment mechanism contributes to the overall creep rate.

6. SAC alloy is treated as a composite consisting of soft pure Sn dendrite inclusions embedded in a dispersion-strengthened and reinforcement-strengthened Sn-Ag eutectic "matrix". The effective properties of this composite have been obtained in the literature using simple isotropic self-consistent homogenization micromechanics theories [63]. There are no studies that have provided ways to predict the anisotropic viscoplastic properties of SAC single crystals along principal crystallographic directions, based on the time-dependent anisotropic creep response of the individual micro-constituents such as ellipsoidal Sn dendrites and the anisotropic creep properties of the eutectic Sn-Ag phase.

7. The Sn dendritic geometry needs to be extended to handle dendrite lobes of different types of non-spherical geometries because this contributes to the anisotropy of the creep response. Past studies [59] were restricted to spherical lobes of the Sn dendrites.
8. The microstructure of Sn dendrites, nanoscale Ag_3Sn IMCs, and Cu_6Sn_5 IMCs are known to evolve as a function of aging time and temperature, with significant effect on the constitutive response. However, there is no mechanistic predictive capability in the literature to predict the effect of this microstructural evolution on the primary and secondary creep response of solder interconnects. Hence the practice of utilizing the as-fabricated mechanical properties for modeling

the behavior of solder throughout the entire service life is questionable and needs to be investigated.

9. There has been no microstructural bottom-up study in the literature which provides a pro-active way to predict the solder response for any morphology, rather than having to empirically (and parametrically) determine it for every microstructural combination encountered in different solder alloys. Such an empirical approach available in the literature is prohibitively slow and expensive for today's product development cycle time.
10. Effect of the addition of trace elements e.g. Mn and Sb on the creep response of low silver SAC solder has not been explored. There has been no mechanistic modeling study to predict the effect of micro-alloying on creep response of SAC alloys.

1.3.1.6.Objectives of the Dissertation

In the current study, the anisotropic creep properties (transient as well as steady-state creep) of SAC single crystals will be predicted based on the underlying dislocation driven mechanisms. The reasons behind the large amount of pice-to-piece varability observed in primary and secondary creep response of SAC305 will be addressed from the microstructural standpoint. To this end, the line tension of dislocations in dominant slip systems of tetragonal BCT Sn medium will be calculated and used as an input for modeling the secondary and primary creep response of Sn and of the eutectic Sn-Ag region in SAC solder. Primary creep response will be explored by replacing constant dislocation density models with the evolution of dislocation density in primary slip systems of anisotropic Sn during primary and secondary creep process. The dilute-concentration assumed for dislocation densities in existing models of creep in dispersion strengthened eutectic Sn-Ag phase, will be refined by including the interactions between neighboring dislocations when the dislocation concentration becomes high. . The anisotropic effect of highly ellipsoidal Sn dendrites will also be modeled in the current study using anisotropic composite micromechanics homogenization theories. The proposed multi-scale model will be capable of modeling both primary and secondary creep behavior of SAC solders and explaining the piece to piece variability measured in the constitutive primary and secondary creep response of SAC305 solder.

1.3.2. Effect of addition of trace elements on creep response of SAC105 solder

Addition of trace amounts of a fourth micro-alloying additive can have a wide range of different effects on various physical properties of SAC solders. The quaternary phase diagram of these alloys are quite complex. One of the major problems encountered in SAC alloys is the large amount of undercooling of β-Sn phase during solidification, which contributes to the formation of large intermetallics during the solidification process. Addition of trace amounts of Mn, Ti, Co, and Ni as a fourth micro-alloying element has been found to reduce the amount of undercooling in SAC solders considerably from 25°C to almost (4-5)°C by forming heterogeneous solidification nuclei as reported in literature [20]. These dopants are introduced primarily to modify (a) the morphology of the intermetallic compound layers both in the bulk solder and at the interface between the solder and copper pads and/or, (b) the solidification behaviour and/or, (c) the mechanical properties of the bulk solder. Antimony has been for a long time one of the candidate elements to be included as a minor alloying element in SAC solders. The Sn2.5Ag0.8Cu0.5Sb, also known as CASTIN™, is perhaps the most widely used Sb-containing alloy in the electronics industry. The primary reason for adding Sb in SAC solders is its effect on the strength of the alloy: the ultimate tensile strength (UTS) of the Sn3.5Ag0.7Cu solder alloy was increased by about 15% (Fig. 1.16 (a)) at strain rate of 1E-4 s^{-1} as the Sb content was increased to the range of 1-2 wt.-% percent [64]. Addition of Sb up to 3.0 wt.-% in Sn3.5Ag0.7Cu does not produce new phases and, instead, Sb dissolves in the Sn-rich phase to form solid solution as well as Cu_6Sn_5 and Ag_3Sn phases by substituting Sb in the Sn sub lattice as $Cu_6(Sn, Sb)_5$ and $Ag_3(Sn, Sb)$ [65][66][67]. Thus, Sb affects mechanical properties of the solder primarily through solid solution strengthening. In another study by Park et al. [68] lead free SAC solder with 0.5 wt.-% Sb addition showed significant improvement in drop test reliability on ENIG surface finish (Fig. 1.16 (b)). Adding a small amount of Sb enhances the drop test reliability on ENIG surface finish by the suppression of P-rich Ni layer growth. However, creep performance of Sb containing SAC solder is still not well characterized, which is very important for improved thermal cycling reliability.

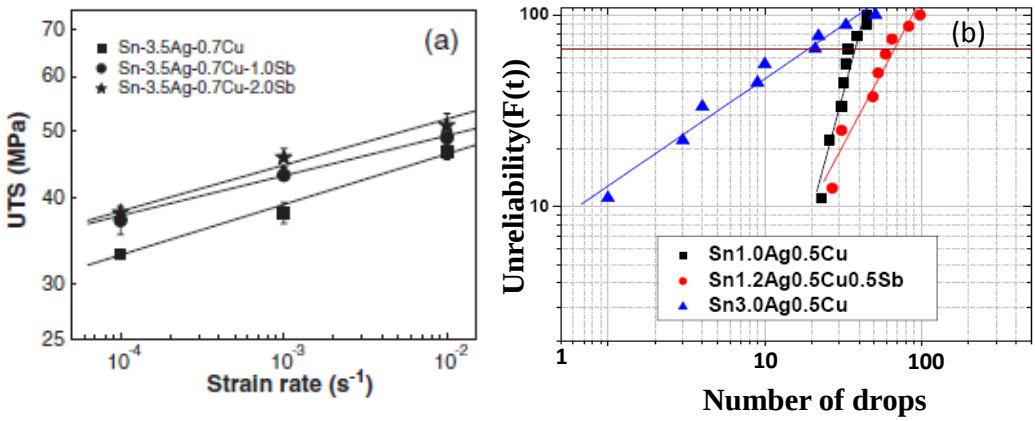

Figure 1.16: (a) UTS of SAC357 solder increases by 15 % due to addition of (1-2) weight % of Sb at strain rate of 1E-4/s [62] (b) Sn1.2Ag0.5Cu0.5Sb shows best drop durability performance among all three solders in BGA packages with ENIG finish [61]

Reports on improved drop reliability with the introduction of trace amount of Mn have also made it an interesting new minor alloying element for SnAgCu solders. Liu et al. have made an extensive reliability evaluation with BGA component boards assembled with different solder alloys, including the Sn1.0Ag0.5Cu0.05Mn [69][70]. Their studies show that, compared to SAC105, the drop reliability improves (Fig. 1.17(a)) by about (10-50) % depending on the pre-test treatment used in the study and thermal cycling reliability by about (10-40) %. Liu and Lee have reported earlier that drop reliability improves only up to about 0.13 wt.-% percent Mn in SAC105, after which drop reliability degrades with further increase in Mn concentration [71]. Improved performance under the ball impact shear test has also been reported due to the addition of Mn [72]. The effects of Mn addition in SAC interconnection microstructures seem to be quite subtle but the impact on solidification is more significant. Addition of Mn does not significantly affect the average thickness or morphology of the interfacial intermetallic layers but differences have been identified between the bulk microstructures of SAC and SAC-Mn solders [73][74][75]. The solid state solubility of Mn in SAC solder is quite small and Mn reacts with Sn to form a new phase even at very low Mn concentrations, as evidenced by the observations that even the addition of (0.15 - 0.8) wt.-% Mn in SAC105 solder introduced fine particles in the bulk solder, most likely those of $MnSn_2$, whose amount and size increase rapidly with increasing Mn content [69][72]. Lin et al. [75] studied SAC105Mn0.15 and SAC105Mn0.5 and found that the yield strength, UTS and elastic modulus of the low silver compositions slightly decreased even

with the addition of 0.15 wt.-% Mn in the SAC105 solder but the ductility improved (Fig. 1.17 (b)). Due to the fact that Mn containing solders are still very little used in the industry, many of the mechanical properties, such as creep properties in particular, of the Mn containing SAC solders are still unknown.

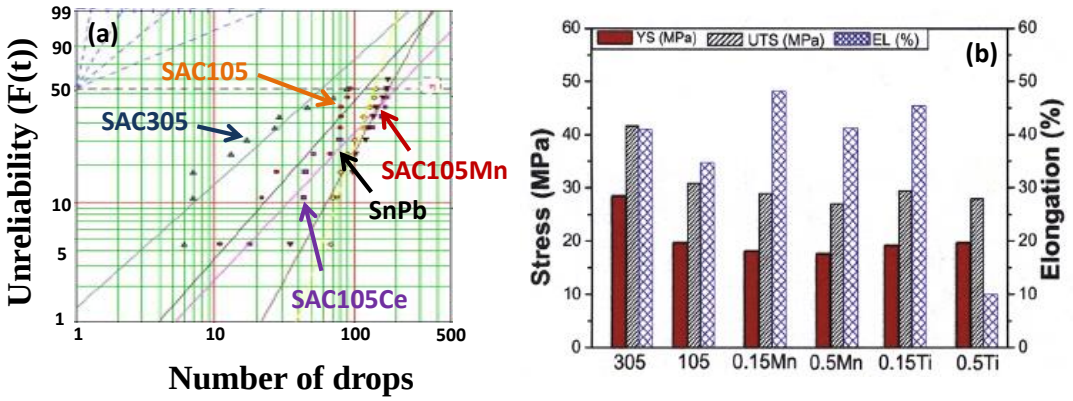

Figure 1.17: (a) Addition of 0.05 wt.-% Mn improves drop durability of low silver content SAC105 solder [66] (b) Improvement in ductility of SAC solder due to addition of 0.15 wt.-% Mn [72]

1.3.2.1. Gaps in the literature

1. Viscoplastic creep response of SAC105X solders has not been investigated before.
2. Mechanistic modeling of the secondary creep response of SAC105X due to addition of trace elements (X) and their subsequent effects on the as-cast microstructure has not been explored.
3. Piece to piece variability in constitutive creep response of SAC105X solders have not been explored using dislocation density models and grain orientation data from orientation image mapping of individual SAC105X solder joints using EBSD detector.

1.3.2.2. Objectives of the Dissertation

1. Conduct microstructural investigation on as-solidified doped SAC105 solders and quantifying the microstructural differences between doped SAC105 and undoped SAC105.
2. Characterize the grain morphology (size and orientation) of SAC105X solder alloys to investigate if additions of trace elements make the solder joints polycrystalline, thereby aiding in obtaining a more isotropic mechanical response.

3. Conduct creep tests at varying stress levels (2-15 MPa) to investigate the steady-state creep resistance of SAC105X solders compared to SAC105.
4. Predict the secondary creep constitutive response of these new solders as a function of varying stress levels using a microstructural multiscale model proposed in the first objective and compare the model predictions with the experimental results.

1.3.3. Effect of isothermal aging on creep response of SAC305 solder

The effect of isothermal aging on the creep constitutive response of SAC solder interconnects has been an important topic of interest in the electronic packaging community because solder interconnects experience significant amount of thermal exposure during the life-cycle. Several studies have demonstrated how the creep resistance of SAC solders decreases with the increase in steady state aging duration and temperature. A comprehensive review of the effect of aging on the creep behavior of lead free solders (Sn3.0Ag0.5Cu and Sn4.0Ag0.5Cu) was presented by Ma et al. [28], where isothermal aging was conducted for varying durations (3 days, 6 days, 9 days, 21 days, 42 days, and 63 days) at room temperature (RT). For both the above alloys, RT aging affects both the strain rate in the secondary creep region, and the elapsed time before tertiary creep and rupture. For the highest stress level considered, the creep strain rate increased by factors of 16X for Sn4.0Ag0.5Cu and 73X for Sn3.0Ag0.5Cu during the 63 days of RT aging. The aging effects were similar for the two lead free alloys. However, the data clearly show that Sn4.0Ag0.5Cu creeps less than Sn3.0Ag0.5Cu for the same stress levels and aging conditions. In another study by the previous group [29], they also studied the effect of elevated temperature aging (80, 100, 125, 150°C) on the creep resistance of Sn3.0Ag0.5Cu and Sn4.0Ag0.5Cu lead free solders. The samples were aged for various durations (0-6 months). Elevated temperature aging for longer durations was observed to drastically reduce the creep resistance of the above alloys. The decrease in creep resistance was hypothesized to be due to significant coarsening of second phase particles at high temperature, thus reducing the dispersion strengthening from the second phase particles. The same research group also extended their previous studies by including two more low silver content alloys (Sn2.0Ag0.5Cu and Sn1.0Ag0.5Cu) and increased the aging duration from 6 to 12 months [30]. As expected, the creep rates evolved more dramatically when

the aging temperature was increased. It was also observed that lowering of the silver content in SAC alloy leads to increase in the creep rates for all aging conditions. Similar observations have been also reported by Xiao et al. [31] for Sn3.9Ag0.6Cu and Sn37Pb alloys which were aged at 180°C. Additionally a research conducted by Chauhan et al. [76] provides the relation between isothermal aging and the thermal cycling reliability of select Sn-based solders. The Sn-based solders with 3%, 1%, and 0% silver content that have replaced tin-lead are studied and compared against tin-lead solder. The activation energy and growth exponents of the Arrhenius model for the intermetallic growth in the solders are provided. An aging metric to quantify the aging of solder joints, in terms of phase size in the solder bulk and interfacial intermetallic compound thickness at the solder-pad interface, is established in the study. All the above studies have been purely experimental and do not provide much insight into the physics of microstructural evolution occurring during isothermal aging at either room temperature or high temperature. A microstructural coarsening model is required which can predict the creep response of isothermally aged SAC solder based on underlying physical mechanisms.

1.3.3.1. Gaps in the literature

All the above studies have been purely experimental and do not provide much insight into the physics of microstructural evolution occurring during isothermal aging at either room temperature or high temperature and its effect on the creep response of these alloys. An adaptive microstructural coarsening model is required to explain the above results based on the underlying physical mechanisms. Previously, Dutta et al. [77] used a semi-empirical Ansell-Weertman model to explain the effect of coarsening of Ag_3Sn particles on the steady state creep behavior of SAC alloys. While this approach is convenient and easy to implement, it does not address any other microstructural features except for Ag_3Sn particles.

1.3.3.2. Objectives of the Dissertation

The current study adopts a detailed mechanistic model to capture more detailed microstructural aspects of solders including size and spacing of Ag_3Sn IMC particles, size and area fraction of Cu_6Sn_5 IMC particles, and area fraction of pro-eutectic Sn dendritic lobes. The model takes into account the interactions of dislocations with nanoscale Ag_3Sn particles in the eutectic phase and considers the Orowan looping and dislocation detachment to be rate controlling mechanisms operating in parallel.

Saturated dislocation density, a critical parameter in the model, is not assumed constant; rather it evolves with applied stress and temperature. Saturated dislocation density during secondary stage of creep is estimated as the equilibrium saturation between three competing processes: (1) dislocation generation; (2) dislocation impediment caused by back stress from pinning of dislocations at IMCs; and (3) dislocation recovery due to detachment from IMCs. The above model has been utilized to understand the effect of isothermal aging on secondary creep response of SAC solder alloys.

1.4. Scope of Dissertation

The scope of the dissertation is as follows. Experimental specimen and test setup will be discussed briefly in Chapter 2. In Chapter 3, effect of micro-alloying Mn and Sb into low silver content SAC105 solders on its creep response will be experimentally evaluated and discussed in terms of microstructural features. In Chapters 4 and 5, multiscale modeling of the anisotropic transient creep response of SAC single crystals will be presented. In Chapter 6, multiscale modeling of the anisotropic steady state creep response of SAC single crystals will be presented. In Chapter 7, multiscale modeling of the effect of aging on secondary creep response of SAC305 solder joints will be presented. In Chapter 8, multiscale modeling of the effect of micro-alloying Mn and Sb on secondary creep response of SAC105 solder joints will be presented. Finally, the dissertation will end with a review of summary & conclusions, limitations & future work and contributions in Chapter 9.

Chapter 2 : Experimental Test Setup and Test Specimen

The experimental test setup used for conducting the material level tests in this study is discussed in this chapter. The setup has been used in previous dissertations for characterization of several lead based and lead free solders [78], [79]. Detailed description of the test system is provided in the dissertation of Haswell [79], and additional improvements to the design and calibration of the system are provided in dissertation of Zhang [78]. A brief description is provided in the current dissertation for completeness. A brief description of the test specimen is provided in Section 2.1 and brief description of the test setup is provided in Section 2.2.

2.1. Test Specimen

The test specimen used for this work is a simple, notched lap shear specimen similar to that proposed by Iosipescu [80], which produces a very uniform stress field in the specimen gage zone due to the 90°notch angles [81]. Copper is used in the current study to mimic the pad finish. Hence the results are applicable to solder behavior on OSP finish. As shown in Figure 2.1, the specimen is similar to that of a modified lap shear specimen and the solder joint is typically between 180 -200 µm wide, 3.0 mm long and approximately 1mm thick. The specimen is originally 1.5mm thick and reduced to a thickness of approximately 1mm thickness after fabrication by using standard grinding and polishing procedures.

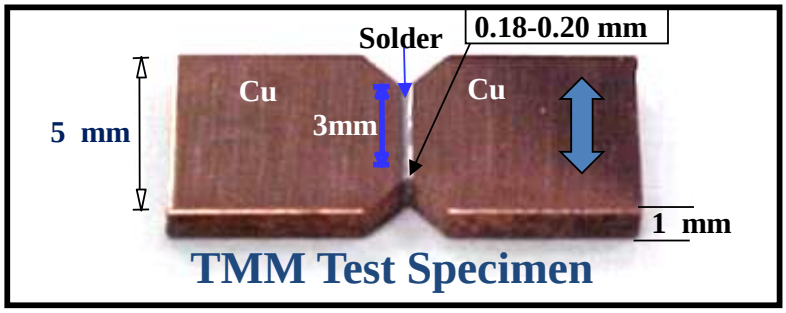

Figure 2.1: Modified Iosipescu TMM shear specimen

The final specimen is prepared for characterizing the microstructure of the specimen using optical microscopy. This step is crucial to understand the influence of the microstructure on measured mechanical response. The specimen is prepared by manual soldering to produce specimens with repeatable microstructures similar to those seen in functional solder interconnects. The fabrication

methodology used for the fabrication of the TMM specimens mimics typical solder reflow procedures used in functional microelectronics. The procedure includes a slow preheat time, soldering time and post soldering cool down phases. Further details on the fabrication process of the specimens can be found elsewhere [78], [79]

The copper platens are manufactured using electron discharge machining (EDM) to produce repeatable geometric dimensions and features with tight tolerances. Prior to soldering the copper platens, the soldering surface is prepared using grinding procedures to obtain a smooth, oxide free soldering surface. The grinding is conducted on seven pairs of copper platens in a batch grinding fixture. Grinding is conducted using 1200 grit sandpaper, in order to produce a flat, planar and uniform wetting surface. Because of the geometric variability of the platens, selective assembly is used by manually inspecting the dimensions and pairing the copper platens accordingly. Matching pairs are then placed in matching positions on the grinding fixture and then cleaned using isopropyl alcohol (IPA) and rosin flux. Each copper platen is first cleaned with IPA and a soft bristle brush. The copper platens are dipped in flux and placed on a hot plate at ~ 132°C for approximately 30 seconds to activate the flux. The platens are then cleaned with IPA and the cleaning process is repeated thrice, or as needed, to obtain a clean surface on the soldering face of the platens. The prepared copper platens are then assembled in an alignment fixture and the soldering region gap between the platens is established using a shim to generate solder joints of ~ 180 μm height.

The soldering procedure followed in the current dissertation is strictly controlled to be consistent with that followed by Haswell [103], Zhang [94], and Cuddalorepata [82], in order to facilitate comparisons of the mechanical behavior of the various solder compositions tested with the current methodology. The prepared specimens are then conditioned for 100 hours at approximate 80% of absolute melting temperature (or 0.8 homologous temperature).

Each specimen is then individually characterized, i.e. the geometric parameters and microstructural features are recorded. In particular, the void densities, intermetallic layer at the interface and fillets are examined. Specimens with high void content, weak interfacial bonding between the copper and the solder, and other unusual microstructural features (pre-existing cracks) and joint geometries (skewed, asymmetric solder joints) are rejected. Please refer to [78], [79] for more details on the fabrication process of the specimens.

2.2. Test Setup

The experiments in this study are conducted using a custom built test setup, Thermo-Mechanical-Microscale (TMM) setup, designed by Haswell to conduct monotonic tests for constitutive properties as well as for cyclic durability tests, at temperatures up to 150°C [79]. Test setup is shown in Fig. 2.2. Mechanical tests are conducted in closed loop displacement control using a lead-zirconate-titanate (PZT) piezoelectric stack actuator, which is capable of driving displacements up to 90 µm. The actuator is connected to the shaft holding the grips through flexible link and low friction, Frelon™-lined linear bushing. Testing is conducted in shear mode. The flexible link and bushing hence aid in preventing bending loads to the brittle actuator during specimen installation and test loading.

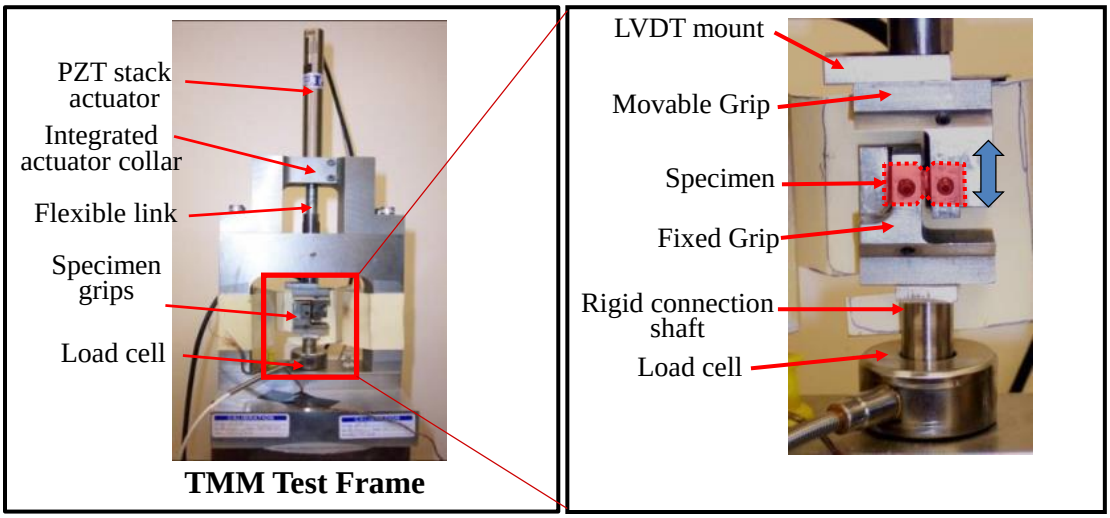

Figure 2.2: TMM (Thermo-mechanical microscale) test setup

Close loop displacement control is achieved using a capacitive gage that measures the displacement across the grips. A Keithley data acquisition card with a 16-bit digital-to-analog and analog-to-digital converter is used to collect test data as well as provide a feedback control signal to the PZT actuator. The effective positional resolution is approximately ±10 nm. The force in the system is measured by a 445N capacity miniature tension/compression load cell with the effective resolution of 0.1N.

The specimen is held securely in the grips using stainless steel wedges and set screws.

Insulating 'ultem' blocks are placed below and above the copper regions of the specimens. A properly installed specimen results in the solder region aligned in line with the loading axis of the setup. The capacitive gage measures the displacement of the grips, load train and the solder material. Thus the

load train compliance is used to isolate the solder deformation from the measured total displacement. The load train compliance has been previously measured by Haswell using digital image correlation methods and was found to be 0.044 μm/N. The control algorithm adjusts the input displacement according to the load train compliance value specified. The setup is capable of conducting tests at elevated temperatures (up to 150°C) using pressurized air. Please refer to dissertations of Haswell [79], Zhang [78], and Cuddalorepatta [82] for more details on test setup.

Chapter 3 : Multiscale Modeling of the Effect of Micro-alloying Mn and Sb on the Viscoplastic Response of SAC105 Solder

Abstract

This study investigates time-dependent viscoplastic response of two relatively new SAC105-X solders – i] SAC105-05Mn (Sn1.0Ag0.5Cu (SAC105) doped with 0.05 wt-percent Mn) and ii] SAC105-55Sb (SAC105 doped with 0.55 wt-percent Sb) using a custom built thermo-mechanical micronscale (TMM) testing machine. These two compositions were chosen based on their improved drop durability response reported in the literature. Results show that the addition of Mn or Sb increases the creep resistance of SAC105 solder by one to two orders of magnitude at tested stress levels (2-20) MPa. The effect of microalloying on the microstructure is characterized using optical image processing by quantifying the size, volume fraction, and inter-particle spacing of both nanoscale Ag_3Sn intermetallic compounds (IMCs) and micronscale Cu_6Sn_5 IMCs. The addition of Mn as a fourth alloying element promotes homogeneous distribution of micronscale Cu_6Sn_5 IMCs, thereby reducing their size and interparticle spacing as compared to that of in SAC105. Furthermore, the volume fraction of nanoscale Ag_3Sn IMCs in the eutectic component is higher in SAC105-05Mn compared to that of in SAC105, and the volume fraction of Sn dendrites in the as-solidified microstructure is lower in SAC105-05Mn. On the other hand, addition of Sb doesn't change the size and spacing of the Cu_6Sn_5 particle, but promotes formation of uniformly sized Sn dendritic lobes, homogeneously distributed in the whole solder joint. Moreover, Sb also forms solid solution with Sn and strengthens the Sn matrix in SAC105-55Sb itself. Neither Mn nor Sb refines the average Sn grain size in SAC105 solder joint. The effects of these microstructural changes (obtained using image processing) on secondary creep constitutive response of SAC105 solder interconnects are then modeled using a mechanistic multiscale creep model. The mechanistic phenomena modeled include: i] dispersion strengthening and reinforcement strengthening provided by nanoscale Ag_3Sn IMCs and micronscale Cu_6Sn_5 IMCs respectively; and ii] load sharing between primary Sn dendrites and the surrounding eutectic Sn-Ag structure. The current model is isotropic and is intended for modeling secondary creep behavior, where the effect of

anisotropy of body centered tetragonal Sn matrix is relatively weak. The modeling approach therefore uses a directional average of the creep along preferred slip systems and orientations in anisotropic Sn grains present in coarse grained SAC105 solder joints. The above mechanistic model is able to capture the trends in secondary-creep constitutive response of the above alloys fairly accurately and explain the improvement in creep resistance of SAC105 due to the addition of Mn and Sb. The original draft of this chapter is a journal paper which has been accepted in Journal of Electronic Materials.

3.1. Introduction

As SnPb solders have been replaced with environmentally friendly lead-free alternatives, the reliability of lead-free solder interconnections has been a much researched topic over the past decade. When solder alloys to replace SnPb were developed, the lead-free alternatives were evaluated primarily based on their suitability in the existing assembly processes. Since that time, it has become clear that the replacement alloys are completely different from SnPb alloys, and they consist of mostly Sn and a small fraction of hard precipitates (whereas SnPb has a large fraction of Pb, which is a much softer phase than Sn). Furthermore, Sn based solders tend to have large grains, or are single crystals. Recent work has investigated the influence of large grains on microstructural evolution and reliability [83]–[88].

Another important emphasis of solder research and development has shifted from processing issues to tailoring the microstructure and mechanical properties of the solder interconnections for specific use conditions by adding trace microalloying elements and optimizing their compositions. The Ag content of SnAgCu (SAC) solders has gained much attention over the past few years not only because of the constant pressure to reduce costs but also because it affects the reliability of solder interconnections. When the Ag content is high (~ 3.0 wt-%), the strength and durability under thermo-mechanical loading is high, while lower Ag content (~ 1 wt %) improves ductility and durability under shock/drop loading [89]–[91].

Addition of fourth alloying elements can have a wide range of different effects on the physical properties of solders. The quaternary phase diagram of these alloys are quite complex. One of the major problems encountered in SAC alloys is large amount of undercooling during solidification which contributes to formation of large intermetallics during the solidification process. Addition of

Mn, Ti, Co, and Ni as a fourth alloying element can reduce the amount of undercooling in SAC solders considerably from 25°C to almost 5°C by providing heterogeneous nucleation sites [92]. These dopants are introduced primarily to modify (a) the morphology of the intermetallic compound layers both in bulk solder and at interface between solder and copper pads and/or, (b) the solidification path, and/or (c) the mechanical properties of the bulk solder.

Antimony (Sb) has long been one of the important minor alloying elements in SAC solders. The Sn2.5Ag0.8Cu0.5Sb, also known as CASTIN™, is perhaps the most widely used Sb-containing alloy in the electronics industry. The primary reason for adding Sb in SAC solders is its effect on the strength of the alloy: the ultimate tensile strength (UTS) of the Sn3.5Ag0.7Cu solder alloy was increased by about 15 % (at strain rate of 10E-4/sec) as the Sb content was increased from 1 - 2 wt-% [93]. Addition of Sb up to 3.0 wt-% in Sn3.5Ag0.7Cu solder ends up forming solid solution in both Sn-rich phase, Cu_6Sn_5 and Ag_3Sn phases by substituting for Sn in the Sn sub lattice as $Cu_6(Sn, Sb)_5$ and $Ag_3(Sn, Sb)$ [94], [95]. Amagai studied the effect of small amounts of Sb in SnAg (Sn3.0Ag vs. Sn3.0Ag0.3Sb on Cu pads) and did not observe any difference in the thickness of the intermetallic layers [96]. Li et al. extended their investigation to varying Sb concentrations (Sn3.5Ag0.7CuxSb, where x = 0, 0.2, 0.5, 1.0, 1.5, or 2.0). They found that Sb actually decreases the size of Cu_6Sn_5 precipitates and the thickness of the intermetallic layers, but the effect becomes detectable only with times more than about 4 minutes in the liquid state (1 wt-% Sb concentration resulted in the smallest thickness of the intermetallic layers) [97]. However, the effect of adding a trace amount of Sb on the bulk microstructural features of SAC solder and its subsequent creep constitutive properties have not been explored.

Reports on improved drop reliability with the introduction of trace amounts of Mn have made it an interesting microalloying element for SAC solders. Liu et al. made an extensive evaluation of reliability using ball grid array (BGA) component boards assembled with different solder alloys, including the SAC105-0.05Mn [98], [99]. Compared to SAC105, their studies show that the drop reliability is improved by about (10-50) % depending on the pre-test treatment used in the study, and thermal cycling reliability by about (10-40) %. However, Liu and Lee reported earlier that drop reliability is improved only up to addition of about 0.13 wt-percent Mn in SAC105, and reliability

decreased with a further increase in Mn concentration [100]. Improved performance under the ball impact shear test has also been reported due to the addition of Mn [101]. Kim et al. also studied SAC305 with 0.1Mn [92], [102], where they did not observe a change in yield strength, UTS or elastic modulus, however the ductility increased considerably [92].

The effects of Mn addition in SAC microstructure seem to be quite subtle but the impact on solidification is more significant. The solid state solubility of Mn in SAC solder is quite small and Mn reacts with Sn to form a new phase even with very low Mn concentrations, as evidenced by the observations that even (0.1-0.15) wt-% Mn in SAC105 solder introduced fine particles in the bulk solder, most likely those of $MnSn_2$, whose amount and size increase rapidly with increasing Mn content [98]–[100]. Lin et al. studied SAC105 with 0.15Mn and 0.5Mn, where the yield strength, UTS and elastic modulus decreased slightly and the ductility improved, even with the addition of 0.15 wt-% Mn. They saw small primary $MnSn_2$ particles squeezed between the Sn cells/dendrites with the 0.15Mn composition. This observation indicates that that the $MnSn_2$ is possibly the primary phase during solidification. Formation of these small crystals prior to solidification of the primary Sn-rich phase, in particular, could help it to solidify more rapidly by providing heterogeneous nucleation sites for the remaining liquid. Due to the fact that Mn containing solders are still under development, many of the mechanical properties, such as creep and mechanical fatigue properties in particular, of the Mn containing SAC solders are unknown. Here, in this paper effect of addition of trace amount of Mn (0.05 wt-%) on creep properties of SAC105 solder is being explored.

Most of the above studies have been purely experimental and do not provide much quantitative insight into the effect of underlying changes in the microstructure of SAC-X solder on their improved mechanical properties. The current study employs a multiscale mechanistic model to capture the effect of the microstructural changes quantitatively due to addition of trace elements (Mn and Sb in this study) on improved mechanical properties (time-dependent viscoplastic response in this study) of SAC (SAC105 in this study) solder. Improvement in experimentally measured creep resistance of SAC105 solder due to addition of above two trace elements is reported in Section 2. Both qualitative and quantitative insights into the effect of Mn and Sb addition on the morphology of bulk IMCs in as-cast SAC105 solder joints are discussed in Section 3. In Section 4, the framework for multiscale modeling is discussed. In Section 5, multiscale modeling prediction of secondary creep strain rate due to addition

of trace amount of Mn is discussed. Finally, the paper concludes in Section 6 with a brief summary of the most important findings from the study.

3.2. Experimental Setup and Creep Test Results

The constitutive creep response of SAC105, SAC105-05Mn, and SAC105-55Sb alloys has been measured using a custom built thermo-mechanical micro scale (TMM) test system. The test setup used in this work has been described in more detail elsewhere [103]. The specimen configuration used in the current work is shown schematically in Figure 3.1. The specimen is a modified version of the notched lap shear specimen developed by Iosipescu [104]. The advantage of this specimen configuration is that the stress distribution in joint volume is quite uniform because of the notches [105]. The specimen fabrication involves soldering two notched copper platens together with the solder of interest. The solders used in this study are variants of SAC105: (i) undoped (SAC105); (ii) doped with 0.05 weight percent of Mn (SAC105-05Mn); and (iii) doped with 0.55 weight percent of Sb (SAC105-55Sb). Complete details of the fabrication procedure are presented elsewhere [103].

The fabricated specimens in this study have a nominal solder joint height of about 180 μm. This dimension is of the same length scale as typical functional solder interconnects found in electronic assemblies. The specimens were deformed in pure shear mode. Prior to characterization, all specimens are pre-aged for 100 h at $0.8T_m$ (~121-127^{0}C), to stabilize the microstructure and to relax residual stresses that are developed during soldering or during subsequent mechanical grounding and fine polishing steps. There are no significant changes observed in the distribution of Ag_3Sn and Cu_6Sn_5 IMCs before and after the above preconditioning treatment.

The TMM test system is schematically depicted in Figure 3.2. The system is primarily comprised of three components; namely a piezoelectric stack actuator, a linear variable displacement transducer (LVDT) (not shown in schematic, it's located underneath the specimen grips) and a load cell. The specimen is loaded in the steel grips that are attached to the piezoelectric actuator via an extension shaft and a flexible link. The piezoelectric actuator applies the specified load on the specimen in closed-loop control. The LVDT measures the relative displacement of the grips and the displacement of the solder joint is extracted from the measured displacement by taking into account the load train

compliance and the load cell measures the load. Complete details of the test procedure are presented elsewhere [106].

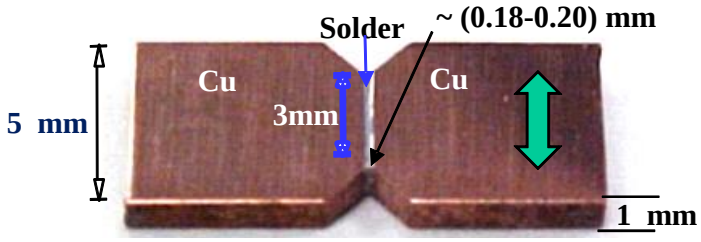

Figure 3.1: TMM test specimen

Using the above test specimen and test setup, viscoplastic creep tests were conducted for the three SAC alloys at varying shear stress levels (2-15) MPa at room temperature and compared against each other. Figure 3.3 shows the effect of addition of trace elements on the creep strain history of low silver content (SAC105) solder at one of the studied stress level (15 MPa) at room temperature. The creep

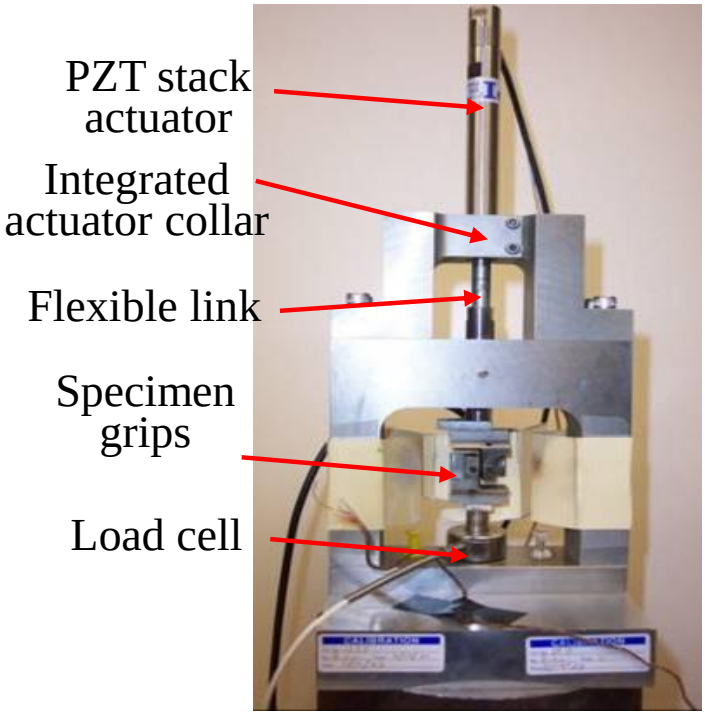

Figure 3.2: TMM test system

resistance of SAC105 increases with addition of minor amounts of Mn and Sb. Using the creep strain data, the secondary creep region is identified by identifying the minimum strain rate, asshown in Figure 3.4. Addition of trace amounts of managanese and antimony improves the creep resistance of

SAC105 solder by one to three orders of magnitude at the measured shear stress levels. More details about these creep tests are presented elsewhere [107].

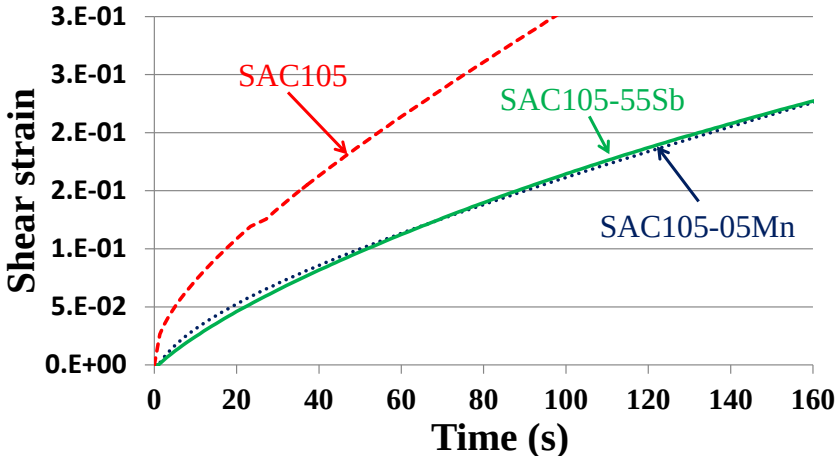

Figure 3.3: Effect of trace element addition: Comparison of creep strain history of SAC105-05Mn, SAC105-55Sb & SAC105 at 15MPa at room temperature

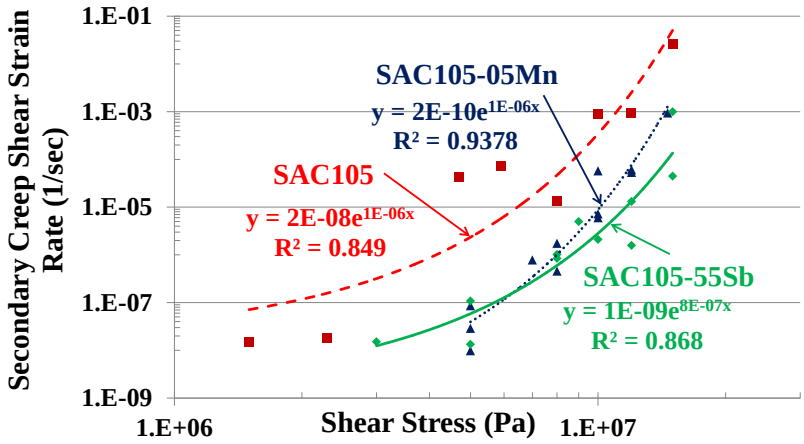

Figure 3.4: Comparison of secondary creep strain rate of SAC105-05Mn, SAC105-55Sb, and SAC105 at room temperature

3.3. As-solidified Microstructure Characterization

The microstructure of typical SAC solder interconnects can be broadly classified into four distinct length scales [108], as shown in Figure 3.5. The structural length scale (characteristic dimensions of the entire interconnect structure) forms the highest length scale (Tier 4), and features of interest at this

length scale are the actual physical dimensions and geometry of the joint. Tier 4 features also include the adjacent metallization layers (Cu in this study) being soldered to the SAC solder, and the intermetallic layers separating the metallization from the solder materials. The next lower length scale (Tier 3) is the average grain size, since a coarse-grained joint typically consists of a few highly anisotropic Sn grains and grain boundaries. The next lower length scale (Tier 2) considers the structure within individual grains consisting of many tin dendrites within each Sn grain that are surrounded by the eutectic Sn-Ag component that solidifies last. Embedded throughout this grain are micron scale Cu_6Sn_5 intermetallic rods. Finally, the lowest length scale (Tier 1) describes the structure of eutectic Sn-Ag matrix, which is a particulate composite consisting of a statistically homogeneous distribution of nanoscale, ellipsoidal Ag_3Sn intermetallic particles embedded in a pure mono-crystalline tin matrix. While not shown in Figure 3.5, we also consider a Tier 0, which looks at the pure tin crystal structure. At this length scale, we consider individual dislocation slip systems that contribute to the deformation mechanisms needed for modeling in Tier 1, atomistic scale effects related to mobility and line tension of single dislocation and dislocation structure/core relaxation interactions.

Sn grain texture of the as-fabricated undamaged micronscale SAC105 & SAC105-05Mn lap shear solder joints are investigated using cross-polarized microscope. Both SAC105-05Mn and SAC105 solder joints are predominantly coarse grained, as evident from cross-polarized microscope (XPM) images (Figures 3.6 and 3.7).

Furthermore, orientation imaging microscopy (OIM) reveals that these SAC105X specimens contain only a few highly anisotropic Sn grains across the joint. OIM measurements compliment XPM or focused ion beam (FIB) analysis for quantifying grain orientation, crystallographic orientation variations such as subgrain orientation gradients within grains. Figures 3.8 and 3.9 show the inverse pole figure maps (IPF) from the OIM study on two different SAC105Mn and SAC105Sb TMM joints respectively. The tetragonal unit triangle combined with overlaid prisms facilitates identification of crystallographic orientations and orientation.

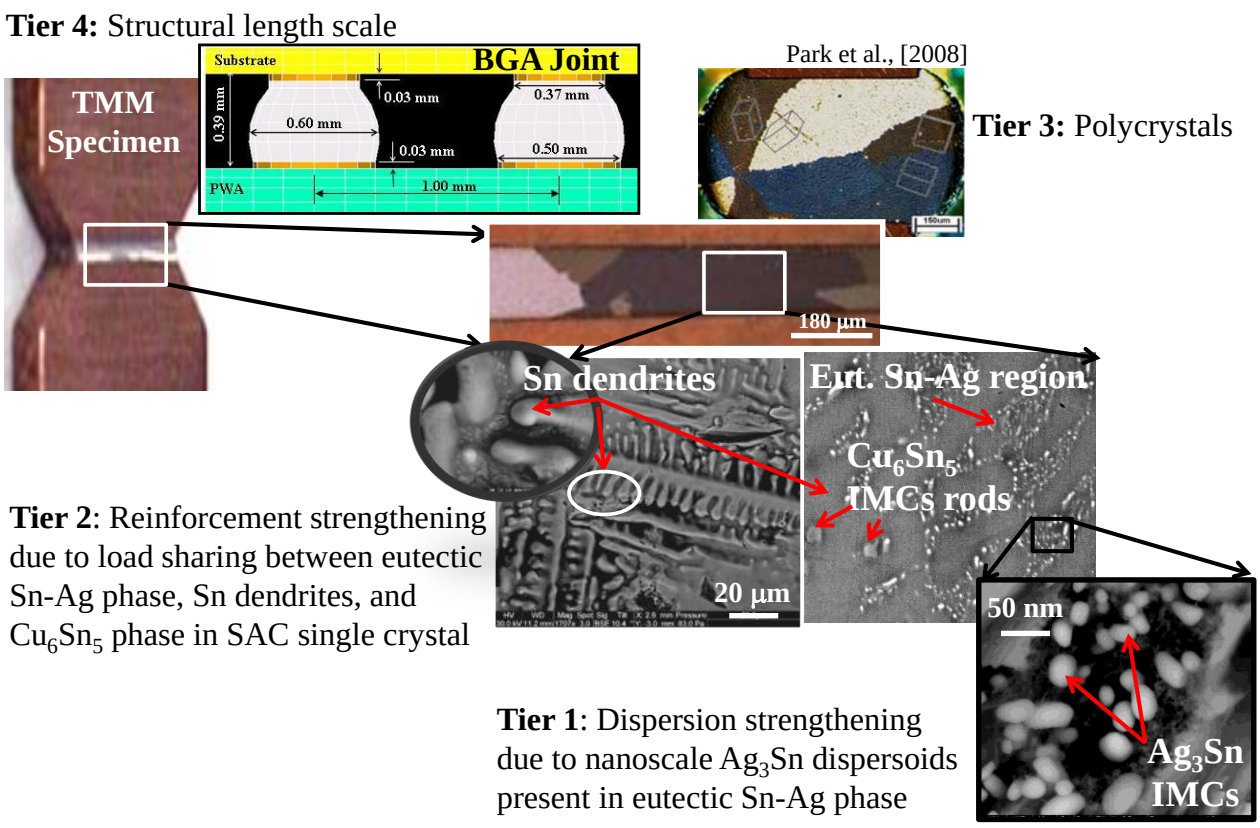

Figure 3.5: Multiple length scales in SAC solder alloy

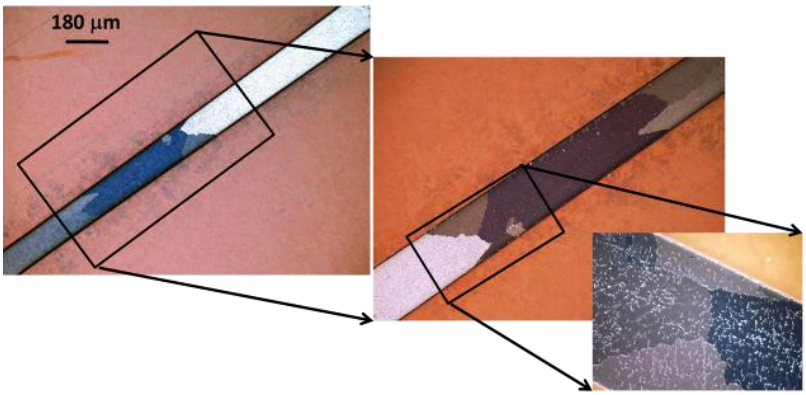

Figure 3.6: Cross-polarized images of as cast solidified SAC105-05Mn solder joint

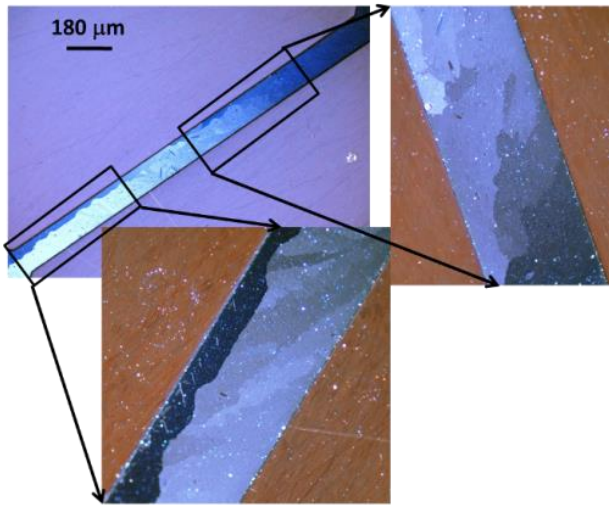

Figure 3.7: Cross-polarized images of as cast solidified SAC105 solder joint

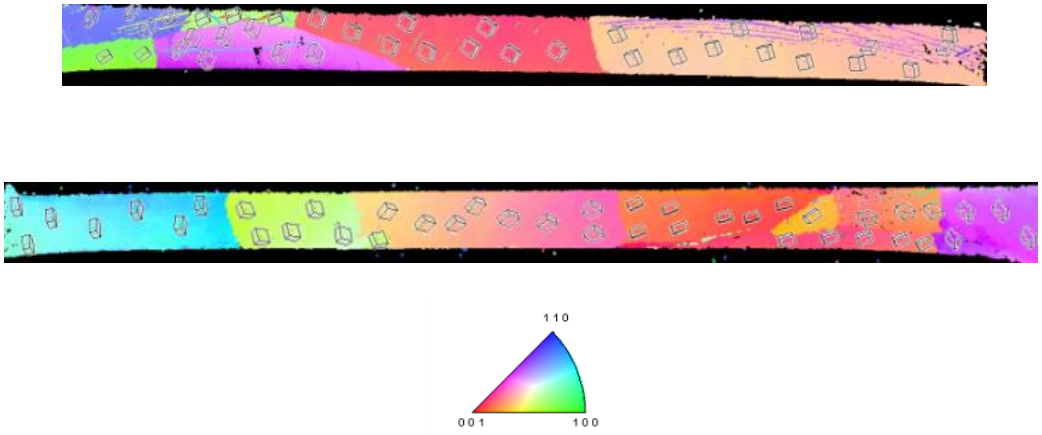

Figure 3.8: Orientation image maps of two as-solidified SAC105Mn TMM joints. The tetragonal unit triangle for relating the IPF colors (100 IPF) with respect to the sample normal/vertical direction as shown next to specimen.

Figure 3.9: Orientation image maps of two as-solidified SAC105Sb TMM joints. The tetragonal unit triangle for relating the IPF colors (100 IPF) with respect to the sample normal/vertical direction as shown next to specimen.

gradients in the maps. Apart from the four specimens shown here, additional specimens were analyzed that also had the similar coarse-grained structure. Therefore, addition of trace amounts of Mn or Sb do not produce fine grains in SAC105 solder joints. Formation of new phases in SAC105X alloys due to addition of trace amounts of Mn and Sb were also investigated using synchrotron X-ray diffraction. The experiments were conducted in beam line 6-ID-D at the Advanced Photon Source at Argonne National Laboratory, IL using a monochromatic X-ray beam with wavelength of about 0.12Å. 2-D diffraction patterns show concentric rings of scattering peaks corresponding to the various d-spacing in the crystal lattice (d-spacing in a crystal lattice refers to planar spacing of adjacent planes). The different peaks correspond to particular diffraction planes from the different crystal structures present in the sample. The positions and the intensities of the diffraction peaks are used for identifying the underlying structure (or phase) of the material.

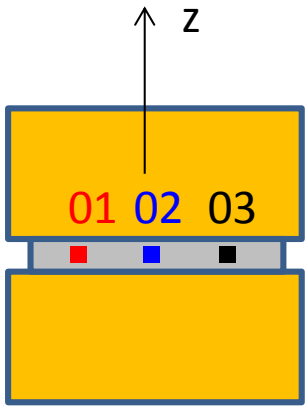

Figure 3.10: Locations on SAC solder joint for diffraction pattern imaging using X-ray diffraction

A schematic of the TMM specimen used for the above experiment is shown in Figure 3.10. Three square boxes (red, blue and black) correspond to three different locations on the solder joint connecting two Cu platens, where from diffraction patterns were captured. The specimen was rotated about the vertical z-axis from -22.5 deg to 22.5 deg while the diffraction patterns were recorded in 58 frames to capture all the patterns possible from the diffractive volume. Figure 3.11 shows the diffraction patterns of a SAC105Sb specimen at three different locations at 0 deg sweep (initial state of the specimen). The scattered spots show that the illuminated volume was not a polycrystal, as only one or a few orientations are present through the thickness. The fact that the spots are streaked implies that the crystals are bent, or have many low angle boundaries.

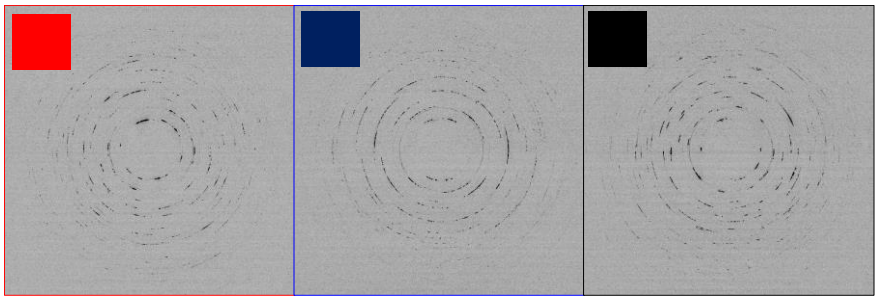

Figure 3.11: Diffraction patterns for three locations at 0 deg sweep in SAC105Sb solder joint

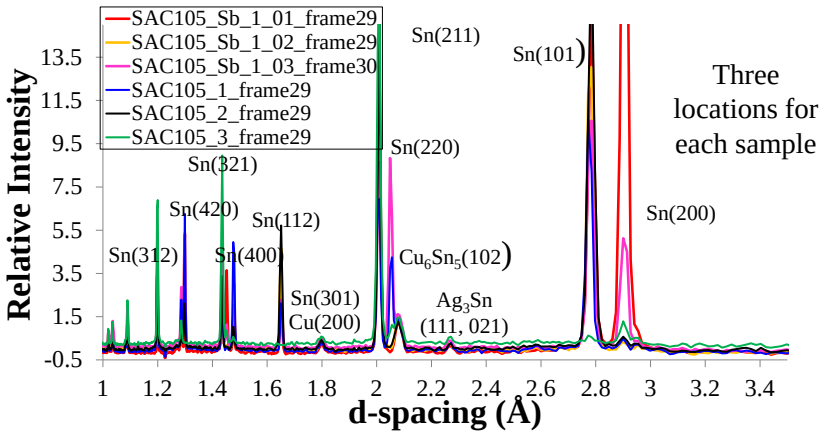

Figure 3.12: Diffraction peaks for three locations in SAC105 and SAC105Sb

Figure 3.12 & 3.13 show the diffraction peak intensities at three locations for two specimens (SAC105 and SAC105Sb) & (SAC105 and SAC105Mn) respectively. Due to the multi-crystal microstructure, the peak intensities vary considerably for each particular pattern, due to the fact that only a couple Sn grain orientations are present. In contrast, the small crystals of Cu substrate, Cu_6Sn_5, and Ag_3Sn

provide uniformly similar peak intensities that represent their volume fraction, Compared to SAC105 samples, there are no apparent peaks from Sn-Sb or Sn-Mn intermetallics in the sampled volume, indicating that if they are there, the volume fraction is very small, less than ~1%. No separate peak or change in location of peak intensity was observed in Figures 3.12 & 3.13, indicating no formation of new phase in SAC105-55Sb or SAC105-05Mn. Peak intensities of Sn (200) in SAC105Sb corresponding to 2.9A d-spacing is higher in SAC105Sb compared to that of SAC105 due to change in size and orientation of grains. Similar observations are also found for SAC105Mn as evident in Figure 3.13. This analysis suggests, there were no obvious differences in the Tier 3 grain structure of SAC105 due to addition of trace amounts of Mn and Sb. Because the solder joint area consists of several different grain orientations, the effect of a particular grain orientation cannot be extracted from

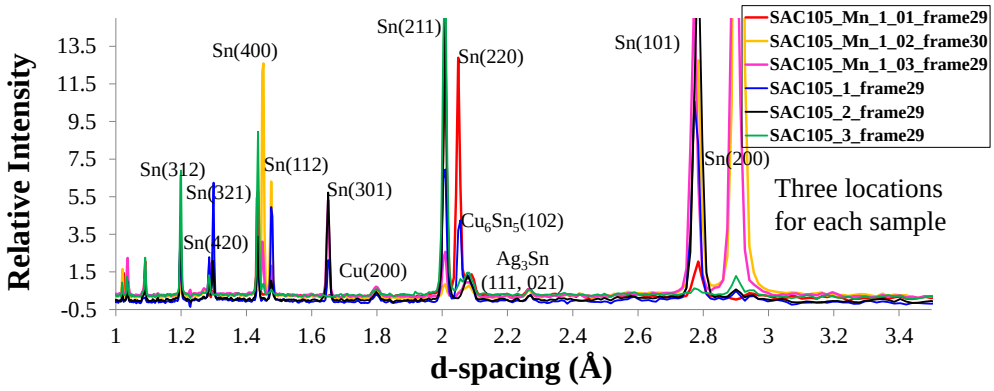

Figure 3.13: Diffraction peaks for three locations in SAC105 and SAC105Mn

these data, because the effects of heterogeneous slip behavior of Sn is homogenized. Therefore, the improvement in creep resistance of SAC105-X solder (compared to that of SAC105) must be due to changes in Tier 1 and Tier 2 scale structures within a single Sn grain, and this provides the justification for focusing on mechanisms relevant to Tiers 1 and 2.

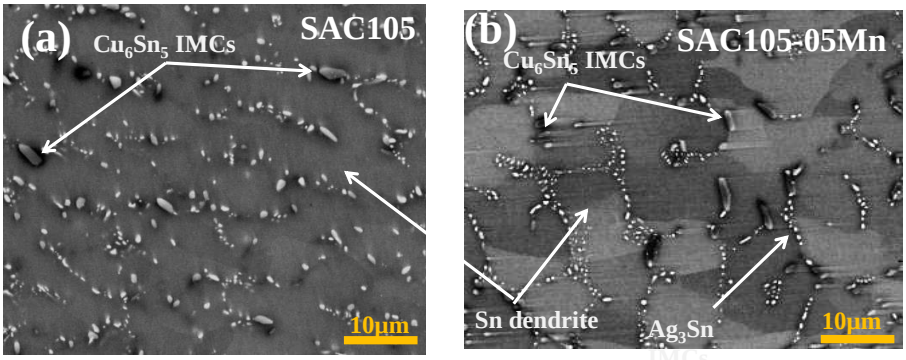

Figure 3.14: As cast solidified microstructure of (a) SAC105 & (b) SAC105-05Mn solders

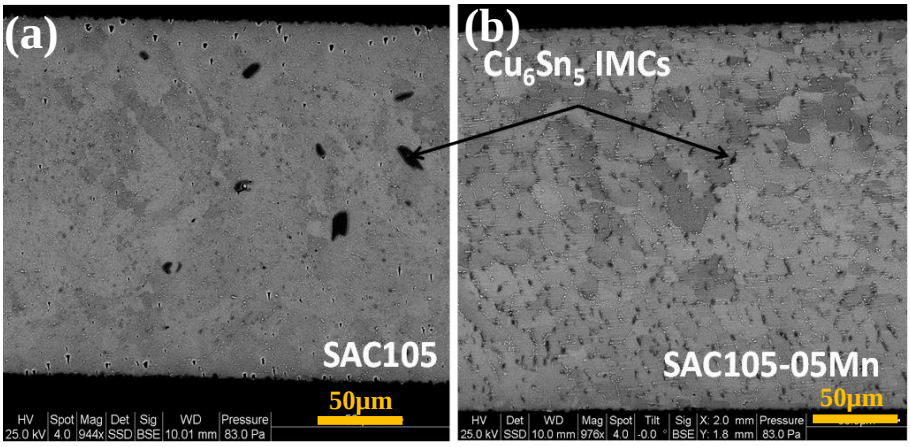

Figure 3.15: Difference in size and distribution of Cu_6Sn_5 IMCs in (a) SAC105 & (b) SAC105-05Mn solders

Figure 3.14 compares environmental backscatter scanning electron microscope (ESEM) images of the as-solidified Tier 1 & 2 microstructures for SAC105 and SAC105-05Mn. The eutectic component is comparatively more clustered in SAC105Mn than in SAC105. Also, micronscale Cu_6Sn_5 IMCs in SAC105-05 Mn solder are found to be smaller in size and more homogeneously distributed in SAC105-05Mn solder compared to the larger rods of the primary Cu_6Sn_5 phase observed in SAC105 (refer to Figure 3.15). These microstructural features are quantitatively captured using image processing and used as inputs to the microstructural model described in Section 3.4. Ag_3Sn and Cu_6Sn_5 IMCs are selected separately for measurement of sizes as shown in Figure 3.16 using the threshold tool, which can separately pick the two above IMCs due to major difference in their average size.

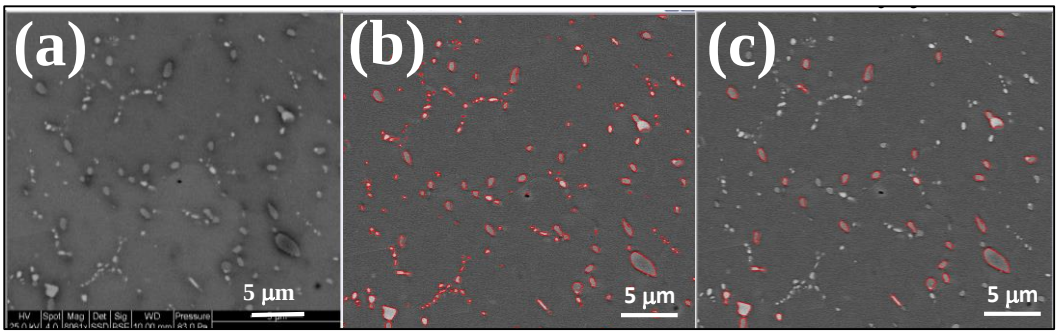

Figure 3.16: Measurement of size of (b) Ag_3Sn and (c) Cu_6Sn_5 IMCs in as-cast solidified (a) SAC105 TMM solder joint

The volume fraction of the eutectic component of the microstructure (Sn and Ag_3Sn IMCs) is captured by selecting the eutectic component in multiple locations separately. The volume fraction of primary Sn dendrites is calculated by subtracting the volume fraction of the eutectic component (shaded in white, refer to Figure 3.17 (c)) from the total volume of the solder joint captured in Figure 3.17.

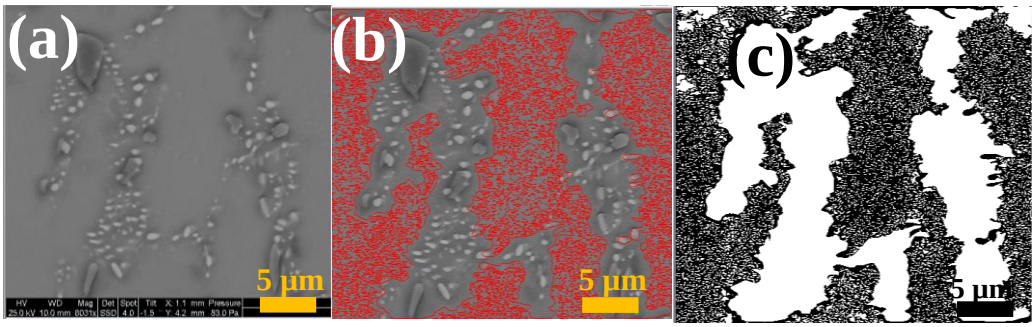

Figure 3.17: Measurement of volume fraction of primary Sn dendrites using segmentation techniques in SAC105 solder joint

Figure 3.18 compares the as-solidifed Tier 1 & 2 microstructures of SAC105 and SAC105-55Sb. The eutectic component is more clearly defined in SAC105Sb than in SAC105, making the Sn dendrite lobes more uniform in size and evenly distributed across the SAC105Sb solder joint.

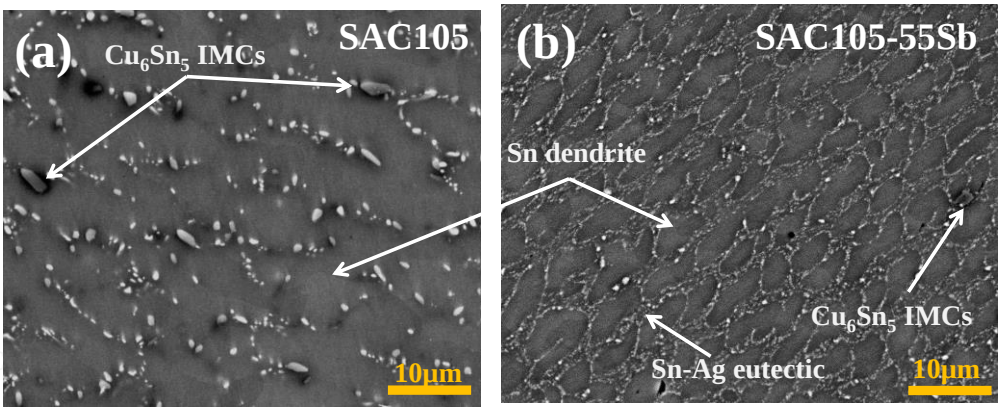

Figure 3.18: As solidified microstructure of (a) SAC105 & (b) SAC105-55Sb solders

As shown in Figure 3.19, Sb is also found to dissolve in the Sn-rich phase solid solution. Thus, addition of Sb affects creep properties of the SAC105 solder not only through dispersion hardening but also through solid solution strengthening. Similar techniques were used to quantify the size and volume fraction of the IMC precipitates in SAC105-55Sb solder (refer to Figure 3.20). The volume fraction of the primary Sn dendritic phase is calculated by subtracting the sum of the volume fraction of eutectic component and the micronscale Cu_6Sn_5 from unity. Table 1 provides a summary of the measurement of different microstructural parameters in as-solidified SAC105 and SAC105-X solder joints obtained using image processing via Image-Pro Plus software.

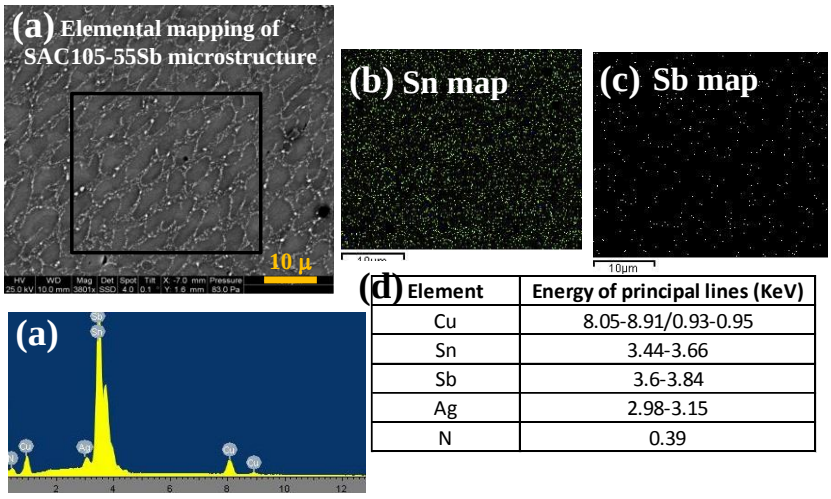

Element	Energy of principal lines (KeV)
Cu	8.05-8.91/0.93-0.95
Sn	3.44-3.66
Sb	3.6-3.84
Ag	2.98-3.15
N	0.39

Figure 3.19: As cast solidified microstructure of SAC105Sb; (a) Elemental mapping of SAC105-55Sb bulk microstructure (b) Elemental Sn map (c) Elemental Sb map (d) Energy of principal lines of elements

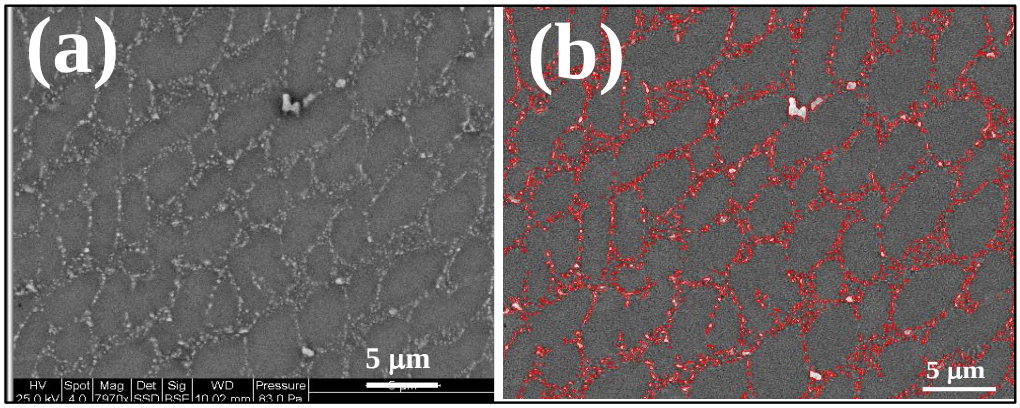

Figure 3.20: Measurement of size of (b) Ag_3Sn and Cu_6Sn_5 IMCs in as-cast solidified (a) SAC105-55Sb TMM solder joint

The volume fraction of Ag_3Sn IMCs in the eutectic component is higher in SAC105-55Sb and SAC105-05Mn by 8 % and 2 % respectively compared to that of SAC105. This is in agreement with the earlier qualitative observation of more clustered eutectic component in SAC105-X compared to that of SAC105.

The volume fraction of Cu_6Sn_5 IMCs in SAC105-05Mn in a unit representative volume element (RVE) is higher by 7 % compared to that of SAC105. This is due to addition of trace amounts of Mn, which promotes heterogeneous nucleation of Cu_6Sn_5 IMCs thereby resulting in reduced spacing between them. Size of Cu_6Sn_5 IMCs is higher by 150 % in SAC105 compared to that of SAC105-05Mn solder. This is also a consequence of the formation of primary Cu_6Sn_5 IMCs which can grow larger because of the higher undercooling observed in SAC105 alloys **[109]**. Also, the volume fraction of primary Sn dendrites in an unit RVE is higher in SAC105 solder compared to that of in other two alloys. Since the sum of the volume fractions of the primary Sn dendritic phase, eutectic component, and micronscale Cu_6Sn_5 phase is constant and is equal to unity, the volume fraction of eutectic component can be deduced from the data given in Table 3.1. In summary, addition of trace amounts of Mn & Sb contribute to significant microstructural changes in Tier 1 and 2 microstructure of SAC105 . Tier 3 features remain largely unaffected. The microstructural parameters obtained in Table 3.1 using image processing have been used in conjunction with the multiscale creep model

(discussed next in Section 4) to predict the steady state secondary creep response of the above solder alloys.

Figure 3.21: Microstructural parameters in as-solidified SAC105 and SAC105X solder joints obtained using image processing

Solders	Size of Ag_3Sn r (m)	Volume fraction of Ag_3Sn f_{Ag3Sn}	Size of Cu_6Sn_5 R_{rein} (m)	Volume fraction of Cu_6Sn_5 (f_{rein})	Volume fraction of primary Sn dendrites (f_{incl})
SAC105	2.50E-08	0.0480	4.55E-06	0.0300	0.83
SAC105-05Mn	2.70E-08	0.0490	1.84E-06	0.0322	0.74
SAC105-55Sb	2.55E-08	0.0516	1.15E-06	0.0160	0.75

3.4. Multi-scale Modeling Framework

Due to the complex multiscale microstructure of SAC solders shown in Figure 3.5, the constitutive creep response of SAC solders is highly dependent on factors such as its composition and prior isothermal aging. As demonstrated in Section 3, only Tiers 1 and 2 microstructures need to be quantified, because the microstructural features in these two length scales are more sensitive to the effects of micro alloying. The modeling approach is described in detail elsewhere [108] and is summarized here for continuity.

In Tier 1, nanoscale Ag_3Sn IMCs provide dispersion-strengthening via dislocation climb and detachment in the Sn-Ag eutectic region. The creep strengthening of the eutectic component due to these particles is modeled using Rosler's athermal detachment model for dislocation climb [110], which is based on energy considerations of the mechanics of climb around particles. In this study, the nanoscale Ag_3Sn IMC particles are modeled as spherical inclusions in the path of dislocations moving through the Sn matrix. Reinforcement strengthening from micronscale Cu_6Sn_5 IMC further contributes to creep strengthening of the eutectic component by reducing the effective magnitude of stress in the material. These micronscale Cu_6Sn_5 IMCs are more effective in pinning dislocations when they are homogeneously distributed in the Sn matrix with a smaller mean interparticle spacing, as observed in the case of SAC105-05Mn.

The net shear creep rate of the eutectic component $\dot{\gamma}_{eut\ Sn-Ag\_rein}$ was derived **[108]** from the assumption that the time taken by the dislocation to traverse through a unit cell of the reinforced eutectic component is the sum of the time taken to taken to travel over the reinforced Sn matrix phase and Ag_3Sn dispersion IMC phase particle:

$$\frac{1}{\dot{\gamma}_{eut\ Sn-Ag\_rein}} = \frac{1}{\dot{\gamma}_{mat\_rein}} + \frac{1}{\dot{\gamma}_{disp-IMC\_rein}} \qquad (1)$$

where, $\dot{\gamma}_{disp-IMC\_rein}$ is given by:

$$\frac{\dot{\gamma}_{disp-IMC\_rein}}{\dot{\gamma}_0} = \exp\left(\frac{-G_{det}b^2r\left[(1-k)\left(1-\frac{\tau}{\tau_d}\right)\right]^{1.5}}{\mathrm{K_B}T}\right) \qquad (2)$$

where, b (0.32 nm) is Burger's vector for Sn; G_{det} (26.5-(12.6*T/505.1)) GPa is the line tension factor of dislocation in Sn; r is the average radius of Ag_3Sn IMCs (Table 1); k_B is the Boltzmann constant; T is the temperature in Kelvin (298 K); k is the relaxation parameter (ratio of the line tension of the climbing dislocation at the particle matric interface versus that in the Sn matrix) [108]. Readers are referred to reference [108] for more details on relaxation parameter (k). Athermal detachment stress (τ_d) is given by:

$$\tau_d = \frac{G_{\mathrm{det}}b}{2\lambda}\sqrt{1-k^2} \qquad (3)$$

The reference strain rate ($\dot{\gamma}_0$) is:

$$\dot{\gamma}_0 = \frac{6\lambda\rho}{b}\left[D_{0L}\exp\left(-\frac{Q_L}{RT}\right) + D_{0H}\exp\left(-\frac{Q_H}{RT}\right)\right] \qquad (4)$$

where, ρ (~1E21) [108] is the saturated dislocation density during secondary stage of creep.

and the particle spacing of Ag_3Sn IMCs (λ) is given by:

$$\lambda = r\left(\frac{\pi}{6f_{Ag_3Sn}}\right)^{\frac{1}{2}} \qquad (5)$$

where, f_{Ag3Sn} (Table 1) is the volume fraction of Ag_3Sn IMCs.

and the creep rate ($\dot{\gamma}_{mat\_rein}$) of the Sn matrix is given by:

$$\dot{\gamma}_{mat\_rein} = A_L\left(\frac{\tau/\Lambda}{G_{Sn}(T)}\right)^{n_L}\exp\left(-\frac{Q_L}{RT}\right) + A_H\left(\frac{\tau/\Lambda}{G_{Sn}(T)}\right)^{n_H}\exp\left(-\frac{Q_H}{RT}\right) \qquad (6)$$

where, G_{Sn} is the shear modulus of Sn; subscripts "L" and "H" refer to low and high stress levels (more than 10 MPa) respectively; D_0 is the diffusivity constant (1E-4 m^2/sec); Q is the activation energy (Q_L = 31 KJ/mol/K, Q_H = 69 KJ/mol/K); n is the power law exponents (n_L = 6 and n_H = 11); R is the universal gas constant [108].

To account for the solid solution strengthening of Sn matrix due to addition of Sb in SAC105-55Sb, these equations has been modified to capture effects of both solid solution strengthening [111] and reinforcement strengthening.

$$\dot{\gamma}_{mat-rein} = \frac{\pi(1-\nu)k_B T D_{eff}}{6e^2 c b^3 G_{Sn}} \left(\frac{\tau}{\Lambda G_{Sn}}\right)^3 \qquad (7)$$

where, D_{eff} is effective diffusivity; c (0.55) is weight percent of solute Sb in Sn solvent, e (3E-12 m) is difference in atomic radius between solute and solvent.

$$\text{Where, } D_{eff} = D_L + 200 D_p \left(\frac{\tau}{G_{Sn}}\right)^2 \qquad (8)$$

where, D_L (6.33E-21 m^2/s) is lattice diffusion co-efficient; D_p (8.64E-13 m^2/s) is pipe diffusion co-efficient [111].

and the strengthening co-efficient Λ is given by:

$$\Lambda = 1 + 2*\left(2 + \frac{l_{rein}}{R_{rein}}\right)\left(f_{rein}\right)^{1.5} \qquad (9)$$

where, l_{rein} (20 μm) [108], R_{rein}, and f_{rein} are the length; and the radius and volume fraction of hexagonal micronscale Cu_6Sn_5 IMCs obtained from Table 1 using image processing.

In Tier 2, the SAC alloy model is treated as a composite consisting of soft pure spherical Sn dendritic inclusions embedded in dispersion- and reinforcement-strengthened isotropic eutectic Sn-Ag matrix. The model uses averaged isotropic properties for Sn in the dendritic lobes. The effective creep properties of the SAC composite are obtained using a composite micromechanics homogenization scheme which takes into account the volume fractions of the primary Sn dendrites & the eutectic component. The net shear creep rates of the above two microstructural components are obtained from Tier 1 at different stress levels. The secondary creep properties of this effective medium approximation (EMA) are defined in terms of viscosity using a closed-form equation derived by Nemat Nasser et al.

[112] for spherical-shaped inclusions in isotropic medium. The effective creep properties of SAC composite are obtained as follows:

$$\mu_{eff} = \frac{1/5}{\left(\frac{f_{incl}}{3\mu_{eff} + 2\mu_{incl}}\right) + \left(\frac{f_{matrix}}{3\mu_{eff} + 2\mu_{matrix}}\right)} \quad (10)$$

where, f (Table 1) refers to the volume fraction and μ (from Tier 1 calculations) refers to the viscosity of the material ($\tau/\dot{\gamma}$). The subscripts "*eff*", "*matrix*", and "*incl*" refer to the SAC composite, Sn-Ag eutectic matrix reinforced with micrometer scale Cu_6Sn_5 IMCs, and the primary Sn dendritic inclusions, respectively. Above homogenization model captures the non-linear phenomenon using a step wise linear scheme.

3.5. Multi-scale Modeling Results and Discussions

The performance of the multi-scale modeling framework proposed in Section 4 in predicting the secondary creep response of SAC105 and SAC105-X solder composites as a function of the microstructural features tabulated in Table 1, is described next. Since the above model is isotropic, it cannot capture the variation in creep properties due to difference in orientation of multiple grains (Tier 3) in these coarse grained joints. However, the secondary creep response of SAC solders is probably more sensitive to the Tier 1 and 2 as-cast microstructures (early in the life of a solder joint), so the model discussed in Section 4 can be used to provide quantitative trends about the creep response of as-fabricated low silver content SAC solder joints. The secondary creep strain rate of the reinforced Sn matrix (Sn matrix reinforced with Cu_6Sn_5 particles) for all three materials are plotted in Figure 3.21. The reinforced Sn matrix in SAC105-05Mn is predicted to be slightly more creep resistant than that of other two solders due to the smaller size and reduced spacing of Cu_6Sn_5 IMCs, whereas the reinforced Sn matrix in SAC105-55Sb is (5-6) orders of magnitude more creep resistant compared to that of SAC105 due to solid solution strengthening of Sn matrix because of addition of Sb. The secondary creep shear strain rates of reinforced eutectic component in three low SAC solders are calculated using Equations (1-9) and shown in Figure 3.22. The predicted steady state secondary creep resistance of reinforced eutectic component in SAC105 solder is lower than that of in SAC105-X solders up to shear stress levels of 10MPa (Eq. 1-2) by one order of magnitude. Above 10 MPa, secondary creep

resistance of SAC105-55Sb and SAC105-05Mn is higher than that of SAC105 by 2-3 orders of magnitude respectively, which is in strong agreement with the experimental data. This is due to relatively similar size of nanoscale Ag_3Sn IMCs but higher volume fraction of Ag_3Sn IMCs in the eutectic component (refer to Table 1) compared to that of in SAC105, resulting in smaller interparticle spacing between Ag_3Sn paerticles. The experimentally observed higher creep resistance is also due to the reduced size and reduced spacing of micronscale Cu_6Sn_5 IMCs in SAC105-05Mn solder (refer to Table 3.1) and solid solution strengthening of the Sn matrix due to Sb in SAC105-55Sb as compared to that of SAC105. Also, there is a cross-over point observed in the model predictions between the secondary creep rate predictions of the eutectic component in SAC105-05Mn and SAC105-55Sb around shear stress level of 10 MPa (eq. 9-10). SAC105-05Mn is found to be more creep resistant compared to SAC105-55Sb below shear stress levels of 10 MPa, whereas the trend is reversed above 10 MPa.

This observation is also in agreement with the experimental trends. Micronscale Cu_6Sn_5 IMCs are effective in pinning dislocations only at lower stress levels but becomes ineffective in providing creep resistance at high shear stress levels of above 10 MPa. Above 10 MPa, reduced spacing between Ag_3Sn IMCs and solid solution strengthening of Sn matrix in SAC105-55Sb make it more creep resistant compared to that of SAC105-05Mn.

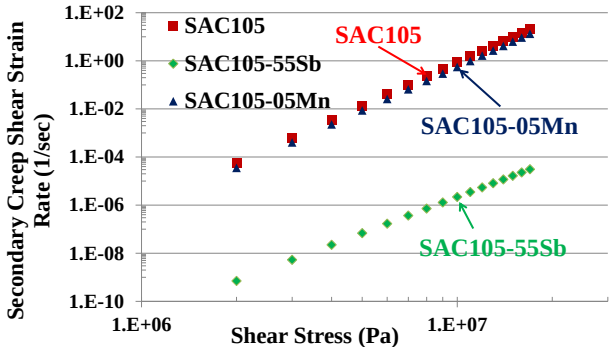

Figure 3.22: Secondary steady state creep response of Sn matrix reinforced with Cu6Sn5 particles in SAC105, SAC105-05Mn and SAC105-55Sb solder

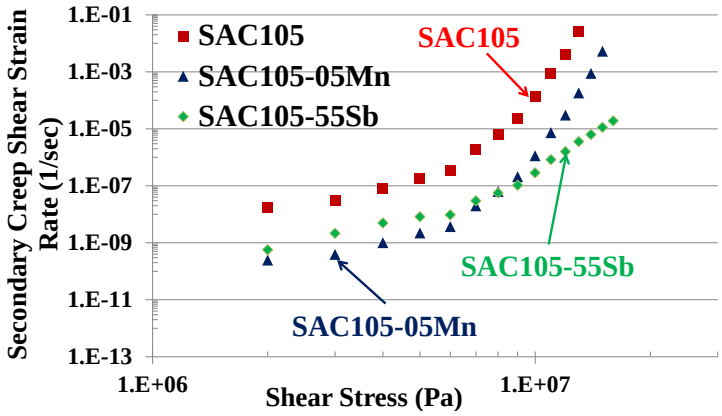

Figure 3.23: Secondary steady state creep response of reinforced eutectic component in SAC105, SAC105-05Mn and SAC105-55Sb solder

Furthermore, model predictions (for Tier 1) shown in Figure 3.22 have been extended to Tier 2 modeling scheme, to capture the secondary creep properties of SAC solder composites using the composite micromechanics homogenization theory as formulated in Equation 10. For modeling simplicity, the SAC composite is assumed to be composed of spherical isotropic Sn dendrites embedded in reinforced eutectic Sn-Ag matrix, although Sn dendrites are elliptical in shape as found in the microstructural as-cast images.

The resulting secondary shear strain rates of all three solders due to the load sharing between eutectic component and primary Sn dendrites are plotted in Figure 3.23. Load sharing between eutectic component and primary Sn dendrites does not change the stress exponents of the curves obtained for eutectic component but only contributes to a parallel shift in the creep curves of the SAC solder composites. Compared to the dispersion strengthening in the eutectic component, the load-sharing by the dendritic inclusions appears to have a weakening effect on the creep properties of the alloy. This observation is expected given the higher creep resistance of the eutectic component compared to the softer Sn dendrites and is in agreement with experimental data [113]. This proposed multiscale model captures the secondary creep response of SAC105 and SAC105-X solder composites reasonably well and is in good agreement with the experimental data except for SAC105-55Sb, where the model over predicts its creep resistance particularly above shear stress level of 10 MPa.

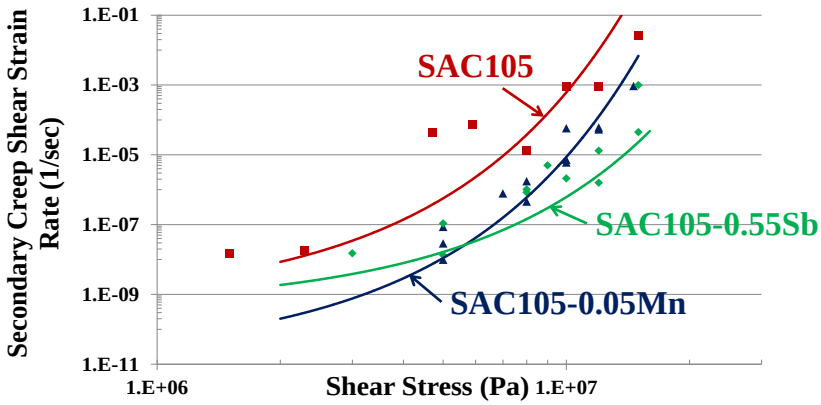

Figure 3.24: Secondary steady state creep response of SAC105, SAC105-05Mn and SAC105-55Sb solder composites

3.6. Summary and Conclusions

Mechanistic models of dislocation climb and detachment are used to capture the effect of additions of trace amounts of Mn or Sb on the viscoplastic properties of SAC105. The creep properties are affected via dispersion-strengthening in the eutectic component of low silver content SAC solders. These microscale models are combined at the next larger length scale (that of Sn dendrites and eutectic Sn–Ag colonies), with traditional micromechanics-based homogenization schemes, to capture the load-sharing between the eutectic component and Sn dendrites, to predict the creep strain rates of SAC solder composites. The addition of trace amounts of Mn does not refine the grain structure in SAC105 solder joints, confirmed using orientation image mapping and does not form any new phase in SAC105-05Mn joint, confirmed using synchrotron diffraction analysis. The volume fraction of the Ag_3Sn IMCs in the eutectic component is higher in SAC105-05Mn alloys compared to that in SAC105. Addition of trace amount of Mn also resulted in reduced spacing between micronscale Cu_6Sn_5 IMCs because the addition of Mn promoted homogeneous distribution of micronscale Cu_6Sn_5 IMCs. This leads to a smaller Cu_6Sn_5 size and reduced interparticle spacing in SAC105-05Mn compared to that in SAC105. The volume fraction of primary Sn dendrites in an unit RVE is also found to be higher in SAC105 solder compared to that in SAC105-05Mn alloy. The secondary creep resistance of SAC105 solder is predicted to be (1-2) orders of magnitude lower than that of SAC105-05Mn solder, which is in good agreement with experimental data. This is because the strengthening co-

efficient is higher in case of SAC105-05Mn compared to that of SAC105, since it is inversely proportional to the size and directly proportional to the volume fraction of Cu_6Sn_5 IMCs in SAC solder.

The reinforced Sn matrix in SAC105-55Sb is (5-6) orders of magnitude more creep resistant compared to that of SAC105 due to solid solution strengthening of Sn matrix by Sb. The solid solution strengthening of the Sn matrix due to the addition of Sb coupled with the higher volume fraction of Ag_3Sn IMCs in the eutectic component explain the observed higher creep resistance of SAC105-55Sb compared to that of SAC105. The proposed multiscale model captures the secondary creep response of SAC105 and SAC105X solder composites reasonably well and is in agreement with the experimental data except for SAC105-55Sb, where the model over predicts its creep resistance particularly above shear stress level of 10 MPa.

3.7. Limitations and Future Work

The proposed mechanistic framework provides valuable insights into the effect of microalloying on the secondary creep behavior of SAC105 alloys. However, the model is based on certain simplifying assumptions and requires further improvement in order to extend the accuracy and capability for modeling the creep behavior (particularly the transient creep response). Sn dendrites are modeled as soft spherical inclusions, however Sn dendritic inclusions are actually elliptical in shape. Hence Eshelby's tensor, which represents the geometric parameters of the inclusions, should take into account the inclusion aspect ratio, not only the effect of volume fraction of Sn dendrites in the SAC alloy. Furthermore, the high dislocation density used in the current study (please refer to [108] for details) is based on a hypothetical assumption that all the slip planes in transversely isotropic Sn matrix are completely clogged with dislocations when the creep deformation advances to the secondary creep regime. The current model uses a dilute approximation and assumes that the interaction between neighboring dislocation fronts are negligible. The mechanics of climb of several dislocations (as opposed to a single dislocation) over particles with the associated interaction effects expected in SAC materials needs to be investigated. Finally, the current model makes no distinctions about which slip system dislocations move on, which is reasonable when dislocation mobility is limited by departure

side pinning by dispersions. Hence, the model is useable for predicting the early part of solder joint life, before Ostwald ripening causes the eutectic component of the microstructure to disappear. This model appears to provide reasonable predictions (at least for explaining qualitative trends) for coarse-grained joints but starts to fall apart as the contribution of grain boundary effects starts to increase during loading-induced dynamic recrystallization in thermal cycling conditions.

3.7. Acknowledgements

The authors would like to thank more than 100 companies and organizations that support research activities at the Center for Advanced Life Cycle Engineering (CALCE) at the University of Maryland, College Park annually. The authors would also like to acknowledge and express their appreciation for the assistance with metallographic cross-sectional analysis provided by Bastian Gebauer and Michael Hartmann, summer interns from University of Mannheim, Germany. Thomas R. Bieler and Bite Zhou also acknowledge the support from a NSF GOALI grant 1006656. Use of the Advanced Photon Source was supported by the US Department of Energy, Office of Science, Office of Basic Energy Sciences, under Contract No. DE-AC02-06CH11357.

Chapter 4 : Multiscale Modeling of the Anisotropic Transient Creep Response of Single Crystal SnAgCu Solder – Part I

Abstract

The lack of statistical homogeneity in functional SnAgCu (SAC) solder joints due to their coarse grained microstructure, in conjunction with the severe anisotropy exhibited by single crystal Sn, renders each joint unique in terms of mechanical behavior. A mechanistic multi-scale modeling framework is proposed in this study to predict the influence of composition and microstructure on the anisotropic transient creep response of single crystal SnAgCu (SAC) solder. For convenience, this framework is presented in two parts based on two length scales (termed Tiers 1 and II). Tier I consists of single-crystal eutectic Sn-Ag alloy, with nanoscale Ag_3Sn particles embedded in a single-crystal Sn matrix and is presented in this paper. Tier II consists of single crystal SAC solder which is composed of Sn dendrites surrounded by the eutectic Sn-Ag phase of Tier I and is presented in Part II of this two-part paper. The Tier I anisotropic transient creep model is based on dislocation mechanics. The Tier II model uses the results of Tier I as an input and is based on anisotropic composite micro-mechanics.

In Tier I, creep deformation is governed by dislocation impediment and recovery at nanoscale Ag_3Sn particles, with recovery being the rate controlling mechanism. Dislocation climb and dislocation detachment at the Ag_3Sn particles are proposed to be the competing rate controlling recovery mechanisms. Line tension and mobility of dislocations in dominant slip systems of single crystal Sn are estimated based on the elastic crystal anisotropy of body centered tetragonal (BCT) Sn. The anisotropic transient creep rate of the eutectic Sn-Ag phase of Tier I is then modeled using above inputs and the evolving dislocation density calculated for dominant glide systems during the transient stage of creep. The evolving dislocation density history is estimated by modeling the equilibrium between five competing processes: (1) dislocation generation; (2) dislocation impediment due to forest dislocations; (3) recovery (by climb and diffusion) from forest dislocations; (4) dislocation impediment caused by back stress from pinning of dislocations at IMC particles; and (5) dislocation recovery due to climb/detachment from Ag_3Sn IMC particles. Of these mechanisms, the third and fifth mechanisms

are modeled to be the rate governing mechanisms for anisotropic transient creep deformation processes for the Sn matrix and for the Ag_3Sn IMC particles, respectively, for the eutectic Sn-Ag alloy. These creep calculations are performed for the three dominant slip systems in a given Sn BCT crystal. The dominant slip systems are determined based on the dislocation mobility and on the orientation angle between the crystal principal axes and the loading direction. Transient creep rate is predicted to be highest along (110)0.5[1-11] slip system and lowest along (100)[0-11] system because of the difference in resolved shear stress and average initial resolved velocity along the slip systems in the modeled single crystal SAC305 specimen for the loading direction [0.67 0.46 -0.59] along the crystal axis. Transient creep strain along one of the facile slip systems (110)[001] is predicted to increase by (1-2) orders of magnitude as the interparticle spacing between nanoscale IMCs increases by a factor of three. Similarly, increase in the volume fraction of nanoscale Ag_3Sn IMCs is predicted to decrease the transient creep rates along (110)[001]. These results will be used in Part II, along with anisotropic micromechanics theories, to predict the transient creep response for Tier II microstructure. The original draft of this chapter is a journal paper and will be submitted to Acta Materiala and part of the paper has been accepted at ICEP, 2013 (International Conference on Electronic Packaging) at Osaka, Japan.

Keywords: Creep, anisotropy, dislocation density, BCT Sn, SAC solder, dislocation detachment, Orowan looping

4.1. Introduction

The hypo-eutectic SnAgCu (SAC) alloys chosen to replace eutectic Sn-Pb contain approximately 97 weight percent of Sn, and display very different physical and mechanical behavior than the well characterized Sn-Pb system [114]–[121]. The nature of solidification in SAC alloys often leads to solder joints comprised of very large, highly anisotropic Sn grains [117]–[119]. Thus, the microstructure of most functional SAC solder joints is coarse-grained with 1-6 grains in the joint. Without the micron scale inclusions of relatively soft Pb that are found in eutectic Sn-Pb solder alloys, the mechanical properties of these Sn based Pb-free solder materials are dominated by those of Sn. Because the thermomechanical properties of Sn exhibit large anisotropy, the thermomechanical response of SAC solder joints depends greatly on the size and orientation of the few Sn grains [114]–[127]. The lack of statistical homogeneity in these microscale SAC joints due to its coarse grained

microstructure, in conjunction with the severe anisotropy exhibited by single crystal Sn, renders each joint unique in terms of anisotropic mechanical behavior [128]–[135]. There is significant evidence in the literature that micron-scale high-Sn SAC solder joints exhibit significant piece to piece variability in their mechanical response under identical load conditions in the as-fabricated state [130], [133], [136]–[138]. For example, the steady state creep strain rate of a SAC solder reported by several authors can be seen to vary by orders of magnitude when tested at similar stress levels (refer to Figure 4.1).

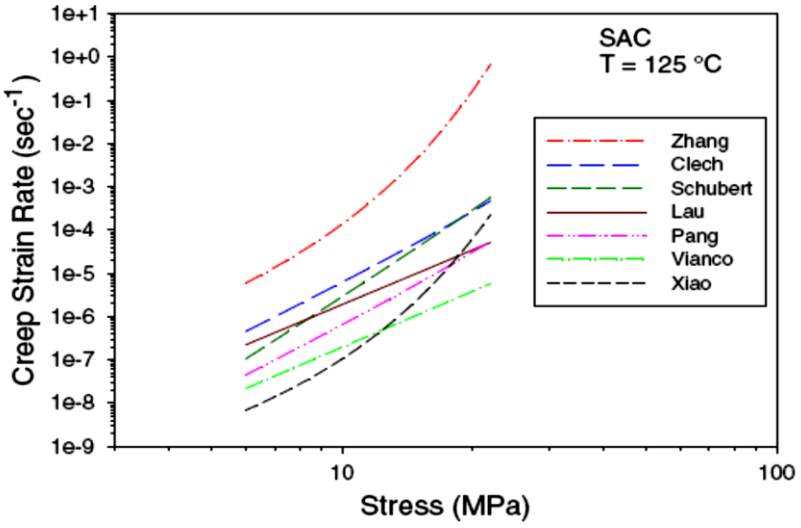

Figure 4.1: (3-4) orders of magnitude variability observed in steady state secondary creep strain rates in SAC305 solder alloy tested at 125°C [139]

Creep measurements conducted on microscale SAC305 solder specimens in a study conducted by Cuddalorepatta et al. [140] also show significant piece-to-piece variability in the creep behavior of identical test specimens tested under identical loading conditions (refer to Figure 4.2). Primary creep strains observed for four specimens tested at the same shear stress level (20 MPa) at room temperature varies considerably. Microstructural analysis of these microscale SAC305 solder specimens revealed [140] that in spite of using consistent fabrication protocols, these specimens exhibit a non-repeatable

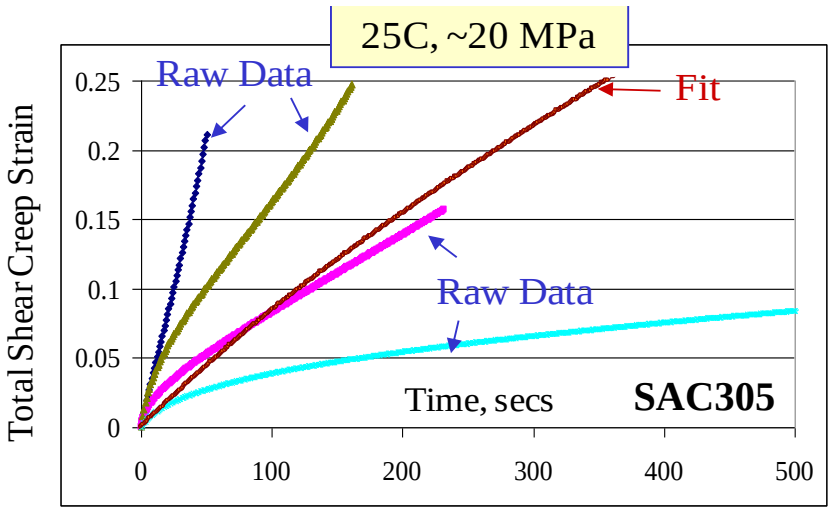

Figure 4.2: Variability observed in transient creep response observed in five different SAC305 solder joints tested under identical loading conditions (Creep test conducted at 20 MPa at 25°C) **[140]**

coarse-grained Sn microstructure, similar to that seen in SAC joints in functional microelectronics (refer to c-axis grain orientation maps of a PBGA joint in Figure 4.3). In order to understand the effects of anisotropic Sn properties and of grain orientation on the variability of creep response of these SAC solder interconnects, a multiscale modeling approach is proposed where the microstructure can be classified into five distinct length scales, as shown in Figure 4.4 and discussed below.

The electronic subsystem of the printed wiring assembly (PWA) is the highest level of scale (Tier 5) relevant to interconnect stress modeling. This includes the geometry and materials of the printed wiring board (PWB) and the component that are soldered together, because these features govern the history of loads that will be generated on the solder joint during thermomechanical excursions. The solder joint is the means through which mechanical loads are transferred between the package (or component) and the PWB. Tier 4 represents the geometry of the solder joint itself and the architecture of the interfaces with the component and PWB (including the interfacial metallization and IMC layers) because this geometry governs the complex evolving boundary conditions imposed on the solder joint. In this study, the structure of interest at Tiers 4 and 5 is not a functional electronic assembly but rather a modified Iosipescu lap shear specimen [32] used for mechanical characterization. The next lower length scale (Tier 3) is the grain scale microstructure, typically consisting of one or several anisotropic Sn grains, either consolidated in a few large connected domains or intercalated over many smaller

interconnected sub-domains, and sometimes in a truly polycrystalline arrangement. The grain boundaries are part of the Tier 3 micro-architecture because they play an important role in inelastic deformation mechanisms.

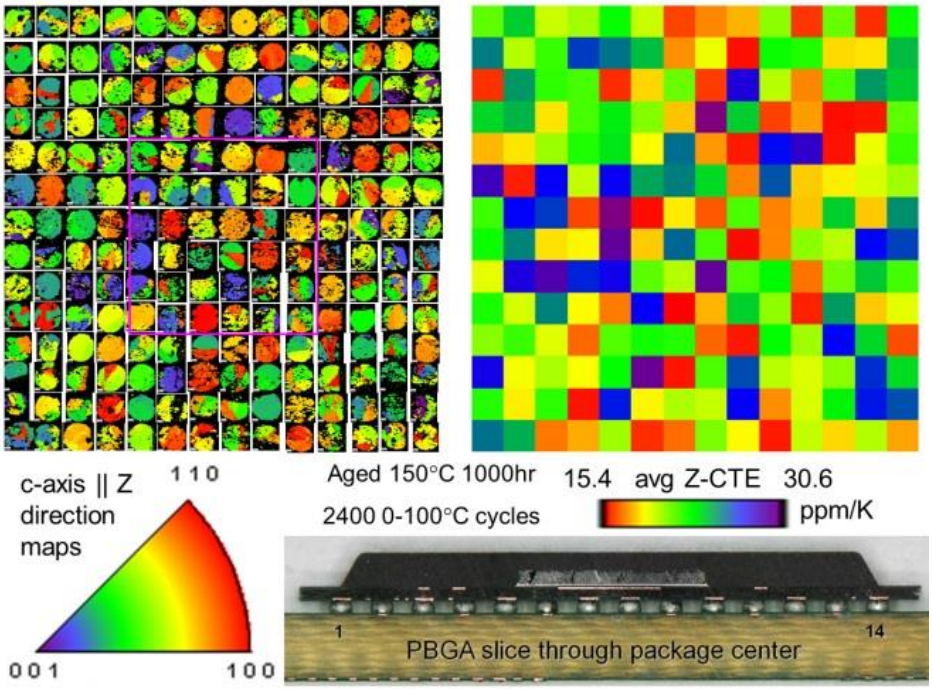

Figure 4.3: Measurements of 196 joints mid plane show random orientations with a mix of single crystals and tri-crystals. The correlated c-axis map and average CTE map show low (red) to high (purple) expansion coefficients in the normal direction [141]

The next lower length scale (Tier 2) focuses on the structure within individual grains, comprising of multiple tin dendrites formed during the solidification process, and surrounded by a eutectic Sn-Ag microconstituent that was the last to solidify. Embedded throughout this grain are additional micron scale intermetallic Cu_6Sn_5 precipitates that can be straight or branched structures of hexagonal cross-section. At this length scale, anisotropic composite models are effective for describing the load sharing between the Sn dendrites and the surrounding eutectic microconstituent. Tier 1 describes the details of the structure within the eutectic Sn-Ag microconstituent, consisting of a statistically homogeneous distribution of nanoscale Ag_3Sn ellipsoidal intermetallic particles embedded in a mono-crystalline tin matrix. The boundaries between the dendrites and the eutectic regions are sometimes low-angle grain boundaries (that sometimes recrystallize into high-angle grain boundaries during cyclic thermo-

mechanical loading). At this length-scale, anisotropic models of dispersion strengthening due to dislocation interactions with interspersed particles that depend on spacing/size are appropriate. Tier 0 refers to the Body Centered Tetragonal (BCT) structure of the Sn matrix itself because it governs: (i) the associated dislocation slip systems needed for modeling in Tier 1, (ii) edge and screw dislocation line tension (refer to section 4.3.1),(iii) dislocation mobility (refer to section 4.3.2), and (iv) intrinsic orthotropy of mechanical properties in the crystal principal axis system. Since, Sn has a body centered tetragonal structure, highly anisotropic thermomechanical properties of BCT Sn have been reported before by Bieler et al. [128] as a function of crystal direction (refer to Figure 4.5). The coefficient of thermal expansion increases by a factor of 2–3 from a to c direction, and the elastic modulus varies by a factor of 3 on the (101) plane (between the [100] and [001] directions).

To model the anisotropic viscoplastic response of SAC single crystal, appropriate hierarchical models are needed for Tiers 0, 1, and 2, with relevant information being passed between each of these levels of scale efficiently to models at the next higher level. This paper addresses the anisotropic modeling work needed at Tiers 0 and 1 to predict transient creep rates of the monocrystalline Sn-Ag eutectic alloy along the principal crystal directions. In Part II of this two-part paper, transient creep rates predicted at Tier I will be used in conjunction with the predicted transient creep rates along principal crystallographic directions of single crystal pure Sn dendrites, to predict the anisotropic transient creep response of single crystal SAC solder materials (Tier II model).

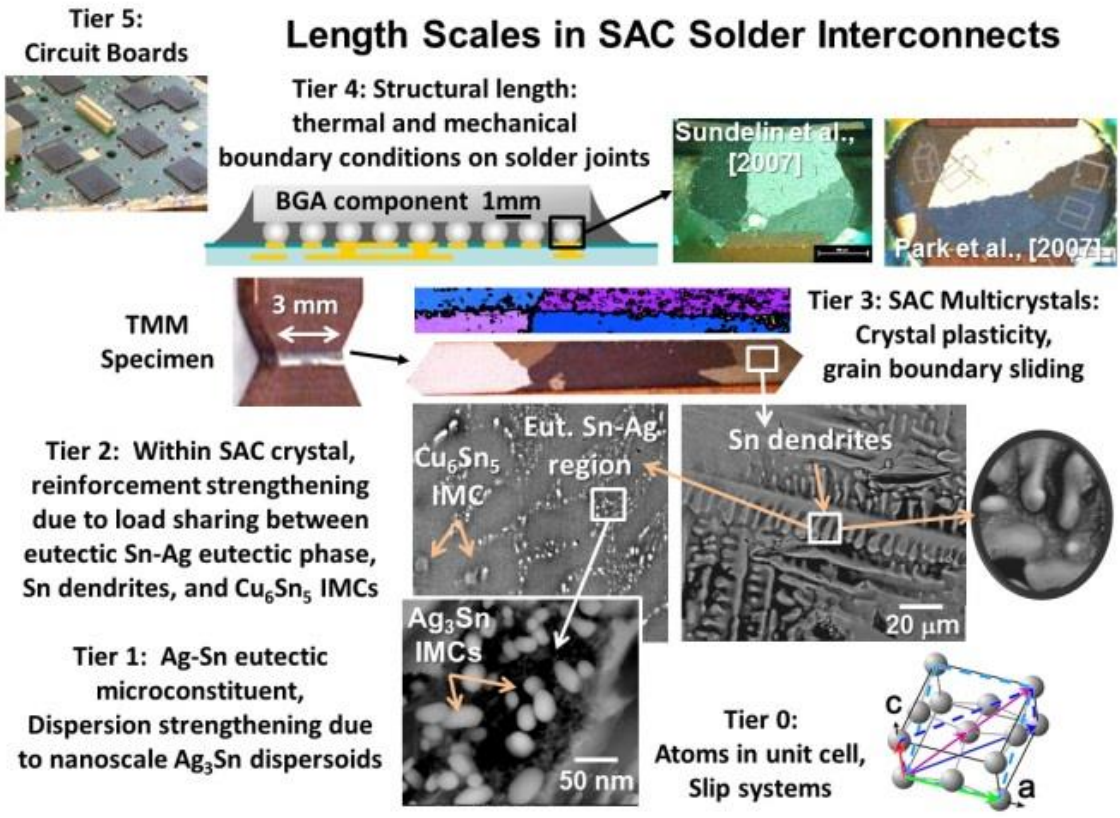

Figure 4.4: Multiple length scales (Tiers 0-5) in SnAgCu solder alloys

Studies involving mechanistic modeling to capture the physics of the underlying viscoplastic creep mechanisms at different length scales of SAC solder are very limited in the literature. Transmission electron microscopy (TEM) studies suggest that the presence of nanoscale IMCs of Ag_3Sn serve as obstacles to pin the motion of dislocations [142]. High secondary creep stress exponents (~ 9) of SAC solder measured in the literature [140], [142], [143] support the hypothesis that dislocation creep over obstacles is the dominant rate-governing creep mechanism in SAC solders. Furthermore, TEM studies conducted on other dispersion-strengthened materials such as aluminum and titanium alloys [144], [145], suggest that dislocation creep occurs in multiple stages: approach, climb and detachment. A mechanistic, multiscale, isotropic modeling framework for SAC solders was proposed by Cuddalorepatta et al. [59], which provided an average isotropic representation of the mechanisms for steady state creep response at Tiers 1 & 2 length scales. At the Tier 1 length scale, nanoscale Ag_3Sn particles in the eutectic region provide dispersion strengthening by impeding the movement of dislocations. The rate limiting process for dislocation motion was considered to be dislocation

detachment mechanism based on the works of Rösler and Arzt [60], and implemented for a constant uniform dislocation density. This model has been modified and improved in the current study to capture the anisotropic transient viscoplastic behavior observed in SAC solder alloys. The main improvements include the capability to address: (i) the evolution of dislocation density; (ii) the evolution of the average dislocation velocity; (iii) anisotropy of mechanical properties of BCT tin, which is highly orthotropic in the principal crystal directions.

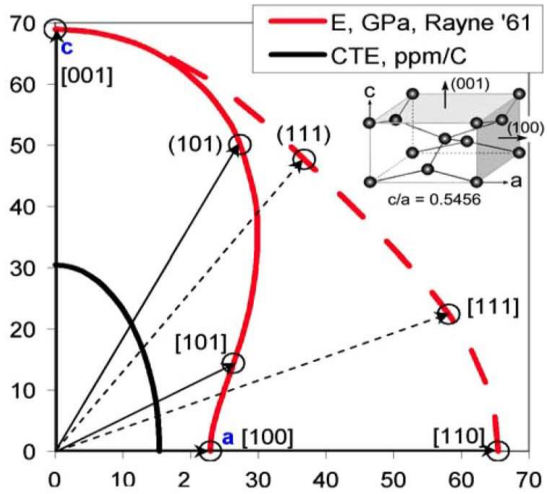

Figure 4.5: Radial from origin to curve is Young's modulus of BCT Sn in GPa; Solid and dashed red lines correspond to (101) & (111) slip planes respectively **[128]**

To capture the effect of the anisotropy present in BCT Sn structure, individual slip systems present in Sn are explicitly considered in this study. Line tension and drag-coefficients (inverse of mobility) of edge dislocations in dominant slip systems of single crystal Sn is captured using fundamental elastic crystal anisotropy calculations. Line tension and drag-coefficients of screw dislocations are (1.5-2) times lower than that of edge dislocations depending on slip systems. Screw dislocations have not been considered for calculations here because screw dislocations don't undergo dislocation climb rather it cross-slips to favorable slip planes. Since, the stacking fault energy for pure Sn is low (which promotes formation of dislocation partials), the probability of cross-slip phenomena in pure Sn is low; however authors believe cross-slip should be modeled in future for completeness. Drag coefficients of edge dislocations in dominant slip systems of Sn are then used to calculate the initial average velocity of the edge dislocation before individual dislocations are impeded and pinned by forest dislocations and by nanoscale Ag_3Sn particles. The anisotropic transient creep response of eutectic Sn-Ag phase, one of the

primary phases in SAC systems, is then modeled using above inputs and the evolving dislocation density calculated for dominant glide systems during the transient stage of creep. Dislocation density used in the model reported in [59] was based on a hypothetical assumption that all slip planes in BCT Sn are completely saturated with dislocations during the secondary stage of creep and a high value of dislocation density (1E21/m^2) was assumed. However, this number has no physical basis and in this study a new method has been proposed where dislocation density evolution during the transient stage are estimated by modeling five competing processes: (1) dislocation generation; (2) dislocation impediment due to pinning by forest dislocation on intersecting slip systems; (3) recovery from forest dislocations by dislocation climb; (4) dislocation impediment caused by back stress from pinning of dislocations at Ag_3Sn IMC particles; and (5) dislocation recovery due to climb/detachment from IMCs. Also, one of the key parameters of the dislocation detachment model is the relaxation parameter ('*k*'), [59], [60], [146] used to capture the attractive interaction between the dislocation line and the nanoscale particle during the post-climb detachment phase. In the previous model [34] this parameter was an empirical function of stress and temperature and was calibrated against experimental observations. However, in the present study '*k*' is treated as a fundamental material property and has been estimated by taking into account the fundamental configuration of a dislocation attached to a particle.

Therefore, the primary objective of this paper is to propose mechanistic model which can capture the anisotropy of transient creep in single crystal eutectic Sn-Ag phase based on the heterogeneous morphology of nanoscale Ag_3Sn IMC particles embedded in a pure single-crystal Sn phase. Anisotropic transient creep response of eutectic Sn-Ag phase and Sn phase obtained along dominant slip systems of Sn from this study are then utilized to capture the homogenized anisotropic creep response of SAC single crystal in Tier 2 length scale and will be reported in Part II of this two-part paper. As stated earlier, the microstructural heterogeneity and anisotropy addressed in the developed models are key to understanding the variability in transient creep response of coarse-grained SAC solder tested under similar loading conditions.

4.2. Modelling Approach

As seen in Figure 4.4, at the Tier 1 length scale, nanoscale Ag_3Sn IMCs result in dispersion-strengthening of the Sn matrix. The creep strengthening of the Sn matrix phase due to these particles and the effective properties of the eutectic Sn-Ag phase are modeled by capturing dislocation impediment by the nanoscale IMCs and subsequent recovery by two competing mechanisms: Orowan's climb model [147] and Rosler's detachment model [60], [146]. Diffusional creep via grain boundary sliding is not relevant at the Tier 1 and 2 length scales since the focus is on single crystal behavior.

The Orowan climb mechanism for dispersion creep strengthening is modeled without threshold stress, using a formulation originally proposed by Ansell and Weertman [147]. As illustrated in Figure 4.6, in this mechanism, dislocations bypass the Ag_3Sn particles accumulated at Sn dendritic boundaries by bowing between them. Orowan loops form around the equator of these Ag_3Sn particles and the resulting backstress prevents further dislocations from passing through and can eventually inhibit all deformation. However, under creep loading, these loops can be gradually eliminated because their line tension promotes shrinkage and annihilation by diffusion assisted climb to the poles of the particle. In this scenario, the overall creep rate is controlled by the interfacial climb rate of these Orowan loops piled up against the particle at Sn dendrite boundaries.

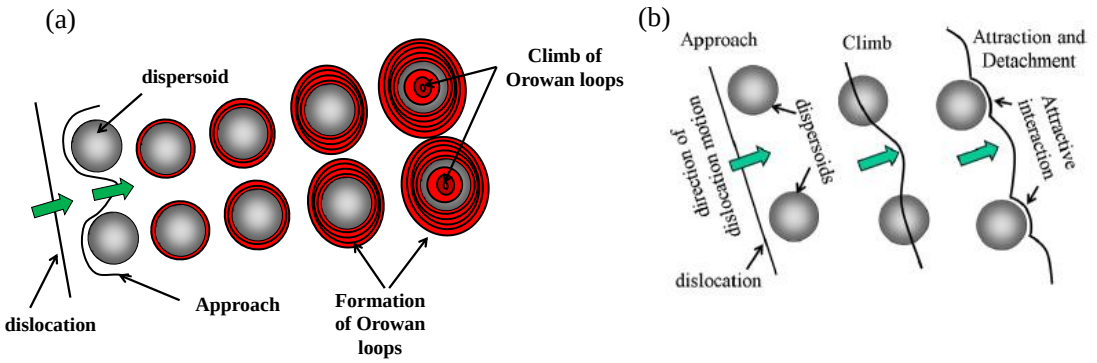

Figure 4.6: Recovery of dislocations from nanoscale Ag_3Sn dispersoids by (a) Orowan climb mechanism and (b) dislocation detachment mechanism (Tier 1 in Figure 4.7)

The other competing recovery mechanism modeled here is dislocation detachment, where strong attractive interaction between the climbing dislocation and the particle is observed in the post-climb

phase of the dislocation [148], [149]. Detachment of the departing dislocation, rather than climb, is seen to be the rate limiting creep deformation mechanism. Therefore, contributions from both Orowan climb mechanism and dislocation detachment mechanism have been modeled in this study as dislocation recovery mechanisms from the nanoscale Ag_3Sn particles. Of these two mechanisms, the one that contributes to faster visco-plastic flow of dislocations in the material is the one that governs the effective creep rates. Flowchart of the bottom up multi-scale modeling approach is provided in Figure 4.7. Tiers 0 and 1 are modeled in this Part I of the manuscript and Tier 2 is modeled in Part II of the manuscript. Author will keep referring to this flowchart (Figure 4.7) throughout this paper to make it easy for the reader.

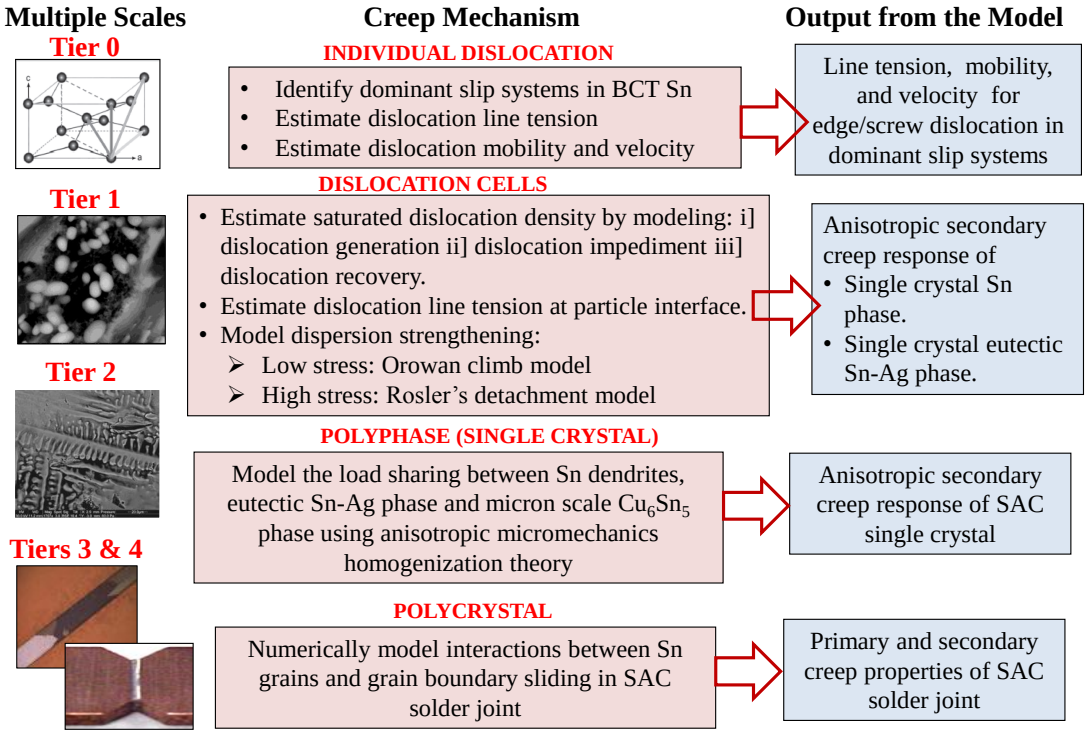

Figure 4.7: Flowchart for multiscale modeling

The governing equations for both mechanisms are illustrated below. The net shear creep rate in the eutectic Sn-Ag region $(\dot{\gamma}^{i}_{\text{eut-Sn-Ag}})$ is formulated in terms of the creep rate on each of the dominant slip systems in the crystal. The creep rate for the i^{th} slip system is derived from the assumption that the time taken by the dislocation to traverse through a unit cell of the eutectic Sn-Ag phase is the sum of

the time taken to travel over Sn matrix micro-constituent and the Ag_3Sn IMC micro-constituent (Tier 1 in Figure 4.7):

$$\frac{1}{\dot{\gamma}^{i}_{eut-SnAg}} = \frac{f_{mat}}{\dot{\gamma}^{i}_{mat}} + \frac{f_{disp-IMC}}{\dot{\gamma}^{i}_{disp-IMC}} \qquad (1)$$

where $\dot{\gamma}^{i}_{disp-IMC}$ for the Orowan climb mechanism is given by [147] [Figure 4.6 (a)]:

$$\dot{\gamma}^{i}_{disp-IMC} = \gamma_1 \frac{\pi \rho^{i}_{ins} \lambda^2 K_i b_i D}{k_B T} \frac{b_i}{d} \left(\frac{\tau^{i}_{eff}}{G_i}\right)^2 \qquad (2)$$

and $\dot{\gamma}^{i}_{disp-IMC}$ for the Rosler detachment mechanism is given by [60] [Figure 4.6 (b)]:

$$\frac{\dot{\gamma}^{i}_{disp-IMC}}{\dot{\gamma}^{i}_{0}} = \gamma_1 \exp\left(\frac{-K_i b_i^{\,2} r[(1-k_i)(1-\frac{\tau^{i}_{app}}{\tau^{i}_{d}})]^{\frac{3}{2}}}{k_B T}\right) \qquad (3)$$

All the terms in Equations 1-3 are described below. The subscripts and superscripts *i* refer to the i^{th} slip system; $f_{disp\text{-}IMC}$ (=1-f_{mat}) refers to the volume fraction of Ag_3Sn in the eutectic Sn-Ag phase; b_i is Burger's vector for the i^{th} slip system in Sn; K_i is the line tension factor of pure edge dislocation for the i^{th} slip system in the Sn matrix; r (=25 nm) and λ (=80 nm) are the average radius and interparticle spacing of Ag_3Sn IMCs (obtained from image processing) [59]; d is the average pro-eutectic Sn dendrite size (10 - 20 μm) (obtained from image processing) [59], k_B is Boltzmann's constant (1.38E-23 $m^2kg/s^2/K$); T is the temperature in Kelvin (298 K); τ^{i}_{eff} is the instantaneous effective shear stress along the i^{th} slip system due to the evolving dislocation density (derivation is discussed in Section 4.3.3); $\dot{\gamma}^{i}_{0}$ is the reference strain rate (as shown in Equation 10, the reference strain rate is directly proportional to the instantaneous dislocation density), τ^{i}_{d} is the thermal detachment stress along the i^{th} slip system (refer to Equation 8); D is the effective diffusivity (refer to Equation 9); G_i is the shear modulus along the i^{th} slip direction considered in orthotropic BCT Sn [150]; ρ^{i}_{ins} is the instantaneous dislocation density in the neighborhood of the Ag_3Sn phase in the i^{th} slip system during the transient creep stage.

This dislocation density (Tier 1 in Figure 4.7) is estimated by modeling three competing processes: (1) dislocation generation; (2) dislocation impediment from pinning of dislocations at IMCs; and (3) dislocation recovery due to climb/detachment from IMCs (complete derivation is discussed in Section 4.3.3), k_i (Tier 1 in Figure 4.7) is the relaxation parameter (ratio of the line tension of the dislocation when attached to the particle surface to the line tension when the dislocation is free in the Sn matrix). The relaxation parameter is calculated from Ashby et al. [151]. The driving force used in in Rosler's detachment model (Equation 3) is the applied resolved shear stress τ_{app}, while in Orowan's climb model the driving force is the net effective shear stress τ_{eff}; where τ_{eff} accounts for the back-stress from net dislocation impediment and pileup stresses. The reason for not using τ_{eff} in the detachment model is because the detachment rate is a function of the ratio of the driving stress to the detachment stress τ_d and this ratio is considered to be insensitive to dislocation density, to a first order approximation. In other word, the pileup backstress on the detaching dislocation is assumed to alter both the applied stress and the thermal detachment stress by the same amount. Therefore, it has been assumed that the ratio of effective driving stress to effective thermal detachment stress will be very close to the ratio of initial applied stress to initial thermal detachment stress.

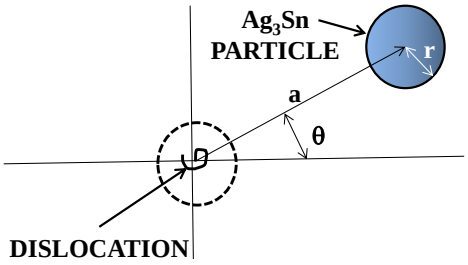

Figure 4.8: Relaxation parameter calculation, Ashby et al. [151]

Relaxation parameter (k_i) of a detaching dislocation in the i^{th} slip system is given by [151]:

$$E^{i}_{el} / 2r = (1-k_i)K_i b_i^2 \qquad (4)$$

where E^{i}_{el} for edge dislocation (Equation 4) is given by [40]

$$E^{i}_{el} = -\frac{a^3}{6\pi}\frac{G_i b_i^2}{r^2}\frac{1}{(1-\nu)^2}\{\frac{2}{3}A_i(1+\nu)(1-2\nu)\times\sin^2\theta + B_i(1-\frac{(2+4\nu-4\nu^2)}{3}\sin^2\theta)\} \qquad (5)$$

where a is the distance between the center of the particle and the dislocation core, θ is the angle between the equatorial line through the dislocation core and the line connecting the center of

dislocation and the particle, G_i is shear modulus of the Sn matrix along the i^{th} slip direction, ν is Poisson's ratio, and A is a function of the bulk moduli of the particle and matrix, and B is a function of shear moduli of particle and matrix (refer to Equations 6 and 7) [151].

$$A_i = -\frac{\Delta K_i}{\frac{1}{3}(\frac{1+\nu}{1-\nu})\Delta K_i + K_i}; \Delta K_i = K_I - K_i \qquad (6)$$

$$B_i = -\frac{\Delta G_i}{\frac{2}{15}(\frac{4-5\nu}{1-\nu})\Delta G_i + G_i}; \Delta G_i = G_I - G_i \qquad (7)$$

where K_I and G_I are the bulk modulus and shear modulus, respectively, of Ag_3Sn particle [152], and K_i and G_i are bulk and shear moduli, of Sn along the principal direction and i^{th} slip direction respectively. At the point of detachment of the dislocation from the particle, a is equal to r and θ is equal to zero (refer to Figure 4.8), which provides an estimate of 0.94-0.98 for the relaxation parameter (k_i), depending on the slip system.

The thermal detachment stress (τ^i_d) in Equation 3 is given by:

$$\tau^i_d = \frac{K_i b_i}{2\lambda}\sqrt{1-k_i^2} \qquad (8)$$

and the effective diffusivity (D) in Equation 2 for dislocation (Orowan) climb is given by:

$$D = D_0[\exp(-\frac{Q_L}{RT}) + \exp(-\frac{Q_H}{RT})] \qquad (9)$$

D_0 is the diffusivity constant (1E-4 m^2/sec); Q is the activation energy (Q_L = 31 KJ/mol/K, Q_H = 69 KJ/mol/K) [59]; R is the universal gas constant. Subscripts "L" and "H" refer to low and high stress levels, respectively.

The reference strain rate ($\dot{\gamma}_0$) in Equation 3 is given by:

$$\dot{\gamma}^i_0 = \frac{6\lambda\rho^i_{ins}}{b_i}[D_{0L}\exp(-\frac{Q_L}{RT}) + D_{0H}\exp(-\frac{Q_H}{RT})] \qquad (10)$$

where ρ^i_{ins} is the instantaneous dislocation density at a transient stage of creep in i^{th} slip system (derived in Section 4.3.3).

The creep rate ($\dot{\gamma}^{i}_{Sn}$) of the Sn matrix (Equation 1) is modeled by modeling two competing recovery mechanisms [153] for the recovery of dislocations from forest dislocations by (i) climbing over the impeding dislocation through the formation of jogs/kinks (Figure 4.9 (a)) and (ii) mass transport diffusion mechanism through the Sn lattice (Figure 4.9 (b)).

$$\dot{\gamma}^{i}_{Sn-C} = \frac{A_c D_c^{\,i} G_i b_i}{k_B T} \left(\frac{b_i}{\lambda_i}\right)^2 \left(\frac{\tau^{i}_{eff}}{G_i}\right)^2 \qquad (11)$$

$$\dot{\gamma}^{i}_{Sn-MD} = \frac{A_{MD} D_{MD}^{\,i} G_i b_i}{k_B T} \left(\frac{b_i}{d}\right)^2 \left(\frac{\tau^{i}_{eff}}{G_i}\right)^2 \qquad (12)$$

where A_C and A_{MD} are model constants for dislocation climb and mass diffusion mechanisms; $D_c^{\,i}$ is the diffusivity for climb process; $D_{MD}^{\,i}$ is the diffusivity for mass diffusion process (D_L + 200 D_P $(\tau/G_i)^2$); where D_L= 6.3E-22 m^2/s is the lattice diffusivity co-efficient; D_P (=8.64E-13 m^2/s) is the pipe diffusion co-efficient [154]; G_i is shear stiffness; λ_i is the spacing between the dislocations (inversely proportional to the square root of instantaneous dislocation density); ρ^{i}_{ins} is the instantaneous dislocation density in the Sn phase in the i^{th} slip system during the transient creep stage and is estimated by modeling three competing processes: (1) dislocation generation; (2) dislocation impediment caused by forest dislocations (complete derivation is discussed in Section 4.3.3) and (3) dislocation recovery either by climb from forest dislocation through formation of jogs/kinks(refer to Figure 4.8 (a)) and/or by mass diffusion process through Sn lattice (refer to Figure 4.8 (b));

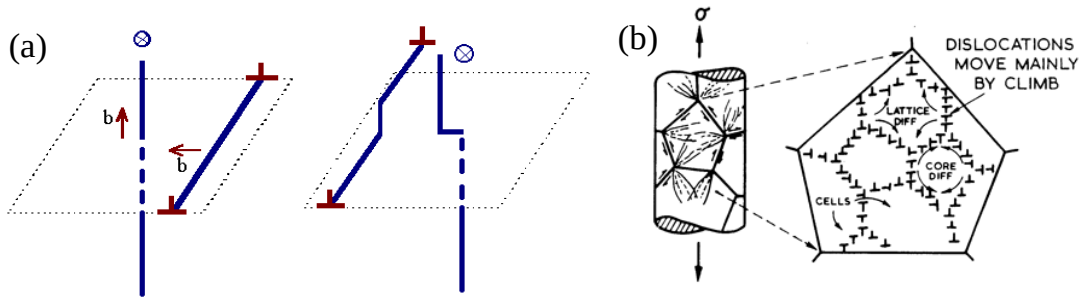

Figure 4.9: Dislocation recovery mechanism in pure Sn phase (a) by climb through formation of jogs and kinks in edge and screw dislocations respectively and (b) mass diffusion (lattice and pipe diffusion) transport through the Sn lattice in a single crystal [155]

d is Sn dendrite size (10-20 μm). Coble creep (grain boundary creep) mechanism is not modeled because this study is concerned with the creep mechanism in single crystal Sn. Transient creep rates obtained in this paper for eutectic Sn-Ag phase and for pure Sn phase, along individual slip systems will be used to predict the anisotropic transient creep response of single crystal SAC crystal using micromechanics anisotropic homogenization theory in Part II of this two-part paper.

4.3. Estimation of Model Inputs (Tier 0 in Figure 4.7)

The proposed modeling framework relies on the estimation of several fundamental parameters to capture the anisotropic creep behavior exhibited by SAC single crystal alloy (treated mechanistically here as a particulate viscoplastic composite with a dispersion strengthened matrix). This section presents the approach and calculation of these parameters (Tier 0 parameters) in Section 4.3.1 (line tension); Section 4.3.2 (mobility) and Section 4.3.3 (dislocation density evolution), which are used as inputs to the above model (Tier 1) to calculate the anisotropic creep strain rate of the eutectic Sn-Ag phase and of the pure Sn dendritic phase (Tier 1). Euler angles of single crystal SAC305 specimen obtained using orientation image mapping via EBSD (electron backscatter diffraction) and the co-ordinate transformation tensor derived to resolve the applied shear stress along the slip systems will be presented in Section 4.3.4.

4.3.1. Line tension factor (K) for a dislocation in anisotropic single crystal BCT Sn

The matrix of stiffness constants of the 4/mmm class of the tetragonal system to which β tin belongs is:

$$C_{ij} = \begin{pmatrix} C_{11} & C_{12} & C_{13} & 0 & 0 & 0 \\ C_{12} & C_{11} & C_{13} & 0 & 0 & 0 \\ C_{13} & C_{13} & C_{33} & 0 & 0 & 0 \\ 0 & 0 & 0 & C_{44} & 0 & 0 \\ 0 & 0 & 0 & 0 & C_{44} & 0 \\ 0 & 0 & 0 & 0 & 0 & C_{66} \end{pmatrix}$$

These elastic constants have been measured by a number of authors; the most reliable data appear to be those of Rayne and Chandrasekhar [122]. There are six independent elastic constants, compared with only two for an isotropic material. Four ratios may therefore be used to describe the elastic anisotropy. These are $A = C_{44}/C_{66}$; $B = C_{33}/C_{11}$; $C = C_{12}/C_{13}$ and $D = 2C_{66}/(C_{11} - C_{22})$, all of which are unity in the

case of elastic isotropy. Over the temperature range from 4.2 to 500 K, these ratios have the following ranges: 0.96<A<0.89, 1.24<B<1.23, 1.69<C<1.54, and 2.26>D>13.57, for pure BCT Sn [9].

Table 4.1: Dominant Sn slip systems observed in Sn (Rank 1 denotes most facile slip system) [156]

SLIP SYSTEMS	SLIP SYSTEMS		RANK
	PLANE	DIR	
1	{100}	[001]	7
2	{110}	[001]	1
3	{100}	[010]	8
4	{110}	1/2[1-11]	2
5	{110}	[1-10]	4
6	{100}	[0-11]	3
7	{001}	[010]	6
8	{001}	[110]	10
9	{011}	[0-11]	5
10	{211}	[0-11]	9

Thus, β tin shows considerable shear anisotropy, the stiffness modulus for shear in [110] direction on (110) planes being much less than that for shear in [100] or [001] directions on {010} planes. Because of this elastic anisotropy the stress state and resulting slip process is different in every single crystal solder joint in electronic assemblies. To understand the slip behavior of Sn in SAC solder joints, relative operation of different slip systems (Tier 0 in Figure 4.7) was analyzed in 196 joints with different orientations by Bieler et al. [141] and correlated with the c-axis orientation. Using the result from Bieler et al. [156], [157] active slip systems in SAC solder considered here for this study are ranked in Table 4.1.

The elastic field of a straight edge dislocation line in an anisotropic crystal was treated theoretically first by Eshelby et al. [158]. For anisotropic elasticity, the determination of line tension factor (K) requires numerical approaches, and can be evaluated by using either the sextic formalism proposed by Eshelby et al. [158] or the integral formalism proposed by Barnett et al. [159]. Eshelby's sextic formalism method was modified by Stroh [160] and expressed with a matrix formalism, a form amenable to numerical computation. Stroh's method has been adapted in this study to calculate the line tension of pure edge and screw dislocations in single crystal BCT Sn.

The line tension, or energy per unit length of a dislocation, is given by Kb^2, where K is the line tension factor, and is dependent on the elastic constants of the crystal and slip systems in the single crystal. Several authors have previously reported elastic constants for BCT Sn. Here in this study, elastic constants of Sn from Rayne et al. [122] have been used for calculation of line tension factor of straight dislocation lines in BCT Sn, using MATLAB. Line tension factor (Tier 0 in Figure 4.7) of straight edge/screw dislocation lines in BCT Sn using Stroh's matrix formalism formulated in MATLAB is plotted in Figure 4.10 at 298 K. The governing equations for calculation of line tension factor for edge and screw dislocations in anisotropic Sn matrix are provided in the Appendix A4.7.1.

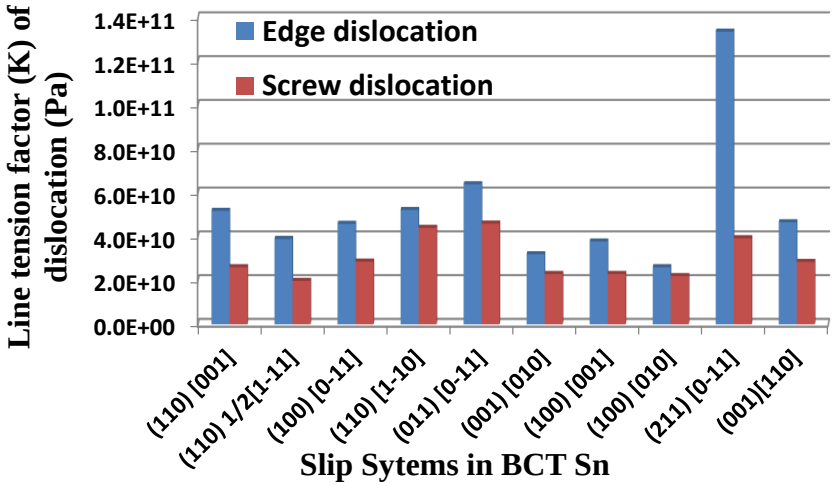

Figure 4.10: Line tension factor of dislocations in anisotropic BCT Sn at 298 K

Line tension factor values of edge/screw dislocations obtained for different slip systems in Sn are in agreement with the mobility along slip systems of Sn reported in literature [127]. For example, slip systems (211)[0-11] & (011)[0-11] are reported to be difficult systems whereas slip systems (110)[001] & (110)1/2[1-11] are reported to be the facile systems, which is in strong agreement with the line tension values calculated above using the modified Stroh formalism. Here in this study, to reduce the computational burden, all subsequent calculations are done for edge dislocation in three most facile slip systems (slip systems # 2, 4 & 6 ranked in Table 1) in eutectic Sn-Ag phase.

4.3.2. Intrinsic mobility of dislocation in pure BCT Sn (without any back stress from any obstructions)

In order to capture the evolution of dislocation density in dominant slip systems of single crystal Sn, which will be discussed next in Section 4.3.3, the velocity of a single edge dislocation in anisotropic Sn (Tier 0 in Figure 4.7) should first be estimated from fundamental principles. Velocity (v_0) of a single dislocation in an anisotropic medium (assuming there is no particle or forest dislocation or grain boundaries to exert any back stress on it or impede its motion) is given by [161]:

$$v_0{}^i = \frac{\tau^r{}_i b_i}{B_i} \qquad (13)$$

where, subscript "i" refers to the i^{th} slip system; τ^r_i is applied resolved shear stress along the i^{th} slip system; b_i is Burger's vector along the i^{th} slip system; B_i is viscous drag co-efficient along the i^{th} slip system. Viscous drag co-efficient of an edge dislocation is given by [162]:

$$B_i = \frac{\eta b_i}{C_i^t} \qquad (14)$$

where, c_i^t is transverse sound wave velocity along the i^{th} slip systems in Sn medium; and $c_i^t = (G_i/\tilde{\rho})^{0.5}$; where G_i is the shear modulus along the i^{th} slip direction of Sn and $\tilde{\rho}$ is the mass density of Sn, η is the thermal energy density of Sn. Thermal energy density of Sn can be calculated using Equation 15, where

$$\eta = \tilde{\rho} * C_p * (T - T_D) \qquad (15)$$

C_p is specific heat capacity; T_D is Debye temperature for Sn (200 K); T is the test temperature in Kelvin. The viscous drag coefficient and mobility (inverse of drag-coefficient) calculated for the three selected slip systems using the above equations are shown in Figure 4.11 at 298 K.

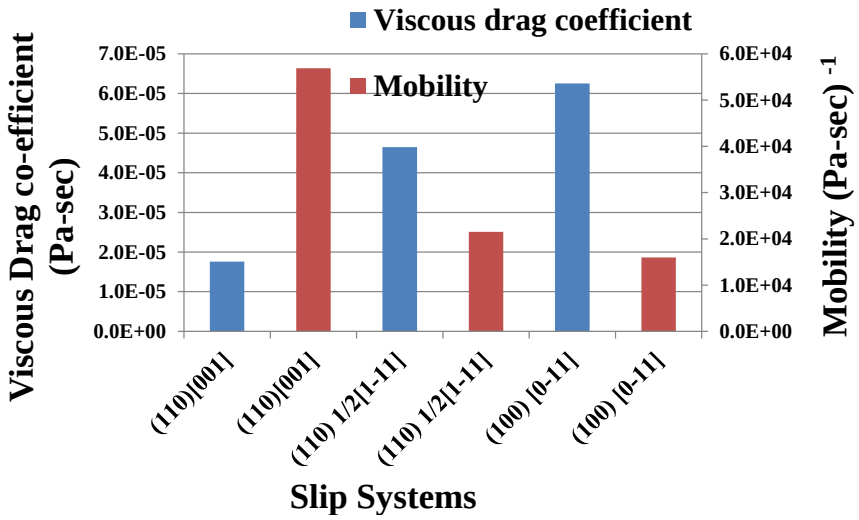

Figure 4.11: Mobility calculations for the three most facile slip systems in anisotropic BCT Sn at 298 K

(110)[001] & (100)[0-11] systems are found to be the most facile and most difficult system, respectively, at two different temperatures in single crystal Sn out of the three selected slip systems. The initial velocity of individual dislocations in above three slip systems in anisotropic The creep rate of Sn can now be calculated using the above results and Equation 13, and will be used next as input to the analytical model developed for capturing the transient dislocation density during creep deformation process in Section 4.3.3.

4.3.3. Dislocation density evolution in dominant slip systems of SAC solder

Instantaneous dislocation density (ρ_i^{ins}) and average velocity (v_i^{ins}) (Tier 1 in Figure 4.7) are estimated in the Sn-Ag eutectic phase and in the Sn matrix, by modeling relevant competing processes that govern the availability of mobile disclocations. As discussed earlier, in the Sn-Ag eutectic phase the three competing processes are: (1) dislocation generation; (2) dislocation impediment caused by pinning of dislocations at the Ag_3Sn IMC particles; and (3) dislocation recovery from IMCs in Ag_3Sn phase due to climb/detachment. In the Sn matrix, the three competing processes are: (1) dislocation generation; (2) dislocation impediment by forest dislocations in the pure Sn matrix phase; and (3) dislocation recovery due to climb over forest dislocation and mass diffusion transport through Sn lattice. As an approximation, cross slip mechanisms have been ignored. Molecular dynamics

simulations need to be carried out in future to estimate the activation energy which can be incorporated into the dislocation models.

For Ag_3Sn IMC phase, dislocation density (ρ_i) evolution rate in i^{th} slip system is modeled by:

$$\dot{\rho}_i(t) = v_0^i k_i \rho_i \tau_i^{eff} \quad (16)$$

where the instantaneous effective stress (τ_i^{eff}) for the i^{th} slip system at Ag_3Sn IMC particles is given by:

$$\tau_i^{eff} = \tau_i^r - \frac{\zeta G_i b_i n_i}{\lambda} + \frac{\beta \zeta G_i b_i n_i}{\lambda} \quad (17)$$

where the instantaneous number of dislocations pinned by Ag_3Sn IMC is given by:

$$n_i = (1 - f_{disp-IMC})(\pi / 6 f_{disp-IMC})^{(2/3)} \rho_i \lambda^2 \quad (18)$$

Evolution of dislocation density in the i^{th} slip system is incrementally modeled by a time-stepping technique:

$$\rho_i(t + \Delta t) = \rho_i(t) + \dot{\rho}_i(t) \times \Delta t \quad (19)$$

First term of Equation 17 denotes dislocation generation, second term denotes dislocation impediment by nanoscale Ag_3Sn IMCs, and third term denotes recovery by dislocation climb/detachment from the particle; v_0^i is the initial resolved velocity of edge dislocation along i^{th} slip system; k_i ($=1/\alpha_1 K_i b_i$) is a model constant for the slip system; where K_i, b_i are the line tension factor and Burgers vector for edge dislocation in i^{th} slip system; α_1 (5E8) is a model constant to calibrate the model predictions to the experimental observation; τ_i^r is the resolved shear stress along the i^{th} slip system; G_i and b_i is shear modulus and Burgers vector, respectively, for the i^{th} slip system; ζ (=0.1) is the precipitate hardening calibration parameter; β (=0.5) is calibration parameter for dislocation recovery from precipitate by climb/detachment; $f_{disp-IMC}$ is the volume fraction (=0.05) of Ag_3Sn dispersoids in eutectic Sn-Ag phase. Evolution of creep strain rate during transient creep stage is modeled by using instantaneous effective stress (Equation 17) and instantaneous dislocation density (Equation 19) and Equations 2 and 3 for competing dislocation recovery mechanisms.

For Sn phase, dislocation density evolution is modeled by:

$$\dot{\rho}_i(t) = v_0^i k_i \rho_i \tau_i^{eff} \quad (20)$$

where instantaneous effective stress in Sn phase is given by:

$$\tau_i^{eff} = \tau_i^{r} - \alpha G_i b_i \sum_j \sqrt{C_{ij}\rho_j} + \xi \alpha G_i b_i \sum_j \sqrt{C_{ij}\rho_j} \qquad (21)$$

First term of Equation 21 promotes dislocation generation, second term is a back stress term that comes from dislocation impediment by forest dislocations, and the third term denotes recovery by dislocation climb from the forest dislocation; α is a forest hardening calibration parameter lying between 0.1 and 2 [163]; ξ (=0.5) is a forest hardening recovery parameter; C_{ij} (=0.01) is a constant capturing the interactions between i^{th} and j^{th} slip system; G_i is the shear modulus along i^{th} slip direction. As a first approximation, the interaction parameters (C_{ij}) are all assumed to be 0.01 to capture interactions between all the slip systems in this study and need to be calibrated in future by simulating SAC single crystal experiments using simulations based on discrete dislocation dynamics (DDD). Model constants used for calculations are summarized in Table 4.2. This model was first employed to predict the dislocation density evolution in one of the slip systems (110)[001] (soft slip system #2 in Table 1) for a constant applied shear stress level (10 MPa) to model the evolution of dislocation density due to dislocation generation, precipitate hardening, dislocation recovery from precipitates in Ag_3Sn phase. Initial dislocation density in Sn phase is assumed to be 5E9 m^{-2} [164]; which was experimentally estimated by Duzgun et al. where they studied the initial dislocation density in pure Sn single crystal specimens using the Bridgman method [165]. Initial dislocation density in Sn-Ag phase is assumed to be 5E11 m^{-2} since the dislocation density in the eutectic Sn-Ag phase is bound to be higher than that of pure Sn phase since most of the dislocations are entangled surrounding the nanoscale Ag_3Sn precipitates in eutectic Sn-Ag phase. Near the Ag_3Sn particles (Figure 4.12), dislocation generation rate dominates over precipitate hardening rate initially and then as more and more dislocations get pinned by dislocations, precipitate hardening rate starts dominating and dislocation density evolution rate reaches steady state when summation of dislocation generation and dislocation recovery rate becomes equal to that of precipitate hardening rate. As discussed before, cross-slip mechanisms for dislocation recovery have been ignored in this study and should be explored in future work. Now, this model is used to calculate the evolution of dislocation density during the transient creep stage for the first three slip systems.

4.3.4. Orientation image maps and co-ordinate transformation matrices

The second-order coordinate transformation tensor used for converting quantities from the loading coordinate system (superscripts s) to crystal coordinate system (superscript c) is given by:

$$g_{ij}^{s\to c} = g_{\varphi_2}.g_{\phi}.g_{\varphi_1} \quad (22)$$

$$= \begin{bmatrix} \cos\varphi_2 & \sin\varphi_2 & 0 \\ -\sin\varphi_2 & \cos\varphi_2 & 0 \\ 0 & 0 & 1 \end{bmatrix} \begin{bmatrix} 1 & 0 & 0 \\ 0 & \cos\phi & \sin\phi \\ 0 & -\sin\phi & \cos\phi \end{bmatrix} \begin{bmatrix} \cos\varphi_1 & \sin\varphi_1 & 0 \\ -\sin\varphi_1 & \cos\varphi_1 & 0 \\ 0 & 0 & 1 \end{bmatrix} \quad (23)$$

$$g_{ij}^{s\to c} = \begin{bmatrix} \cos\varphi_1\cos\varphi_2 - \sin\varphi_1\cos\phi\sin\varphi_2 & \sin\varphi_1\cos\varphi_2 + \cos\varphi_1\cos\phi\sin\varphi_2 & \sin\phi\sin\varphi_2 \\ -\cos\varphi_1\sin\varphi_2 - \sin\varphi_1\cos\phi\cos\varphi_2 & -\sin\varphi_1\sin\varphi_2 + \cos\varphi_1\cos\phi\cos\varphi_2 & \sin\phi\cos\varphi_2 \\ \sin\varphi_1\sin\phi & -\cos\varphi_1\sin\phi & \cos\phi \end{bmatrix} \quad (24)$$

$$\overleftrightarrow{\tau}_{crystal} = \overleftrightarrow{g} \begin{bmatrix} 0 & \tau_{sample} & 0 \\ \tau_{sample} & 0 & 0 \\ 0 & 0 & 0 \end{bmatrix} \overleftrightarrow{g}^T \quad (25)$$

$$\overleftrightarrow{\tau}_{slipsystem} = \overleftrightarrow{a}\,\overleftrightarrow{\tau}_{crystal}\,\overleftrightarrow{a}^T \quad (26)$$

where $\overleftrightarrow{a}$ is the second order coordinate transformation tensor comprising of direction cosines between crystal axes ([h k l], [u v w] and [h k l]×[u v w] (cross product of loading plane normal and loading direction)) and individual slip system axes ([n_1 n_2 n_3], [b_1 b_2 b_3] and [n_1 n_2 n_3]× [b_1 b_2 b_3] (cross product of slip plane normal and slip direction)), respectively.

Table 4.2: Tier 0 and Tier 1 model constants

Model Parameters	Units	(110)[001]	(110)0.5[1-11]	(100)[0-11]	Reference
Burgers vector (b)	m	3.18E-10	4.42E-10	6.64E-10	[40]
Shear modulus	GPa	21.9	7.4	23.4	[40]
Boltzmann constant	$m^2kgs^{-2}K^{-1}$	1.38E-23			Matweb
Temperature	Kelvin	298			Present Study
Lattice diffusion coeffieciet	m^2/s	6.33E-22			[43]
Pipe diffusion coefficicent	m^2/s	8.64E-13			[43]
Ag_3Sn particle radius	nm	25			[34]
Ag_3Sn interparticle spacing	nm	80			[34]
Sn dendrite major diameter	microns	50			[34]
k_r (Relaxation parameter)		0.9484	0.9811	0.941	Present Study
Volume fraction of Ag_3Sn in eutectic Sn-Ag		0.05			[34]
Poisson's ratio		0.35			[34]
Ag_3Sn Young's Modulus	GPa	99			[42]
Debye tempearature for Sn	Kelvin	200			Matweb
Mass density of Sn	Kg/m^3	7.37E+03			Matweb
α_1 (Dislocation density calibration parameter)		5.00E+08			Present Study
ζ (Precipitate hardening parameter)		0.1			Present Study
β (Recovery parameter)		0.5			Present Study
α (Forest hardening parameter)		1			Present Study
ξ (Forest recovery parameter)		0.5			Present Study
Initial dislocation density in Sn phase	m^{-2}	5.00E+09			[52]
Initial dislocation density near Ag3Sn phase	m^{-2}	5.00E+11			Present Study
γ_1 (Model constant for Ag_3Sn phase)		5	5	0.1	Present Study
A_c and A_{MD} (model constants for Sn phase)		1.00E+07	7	3.00E+05	Present Study

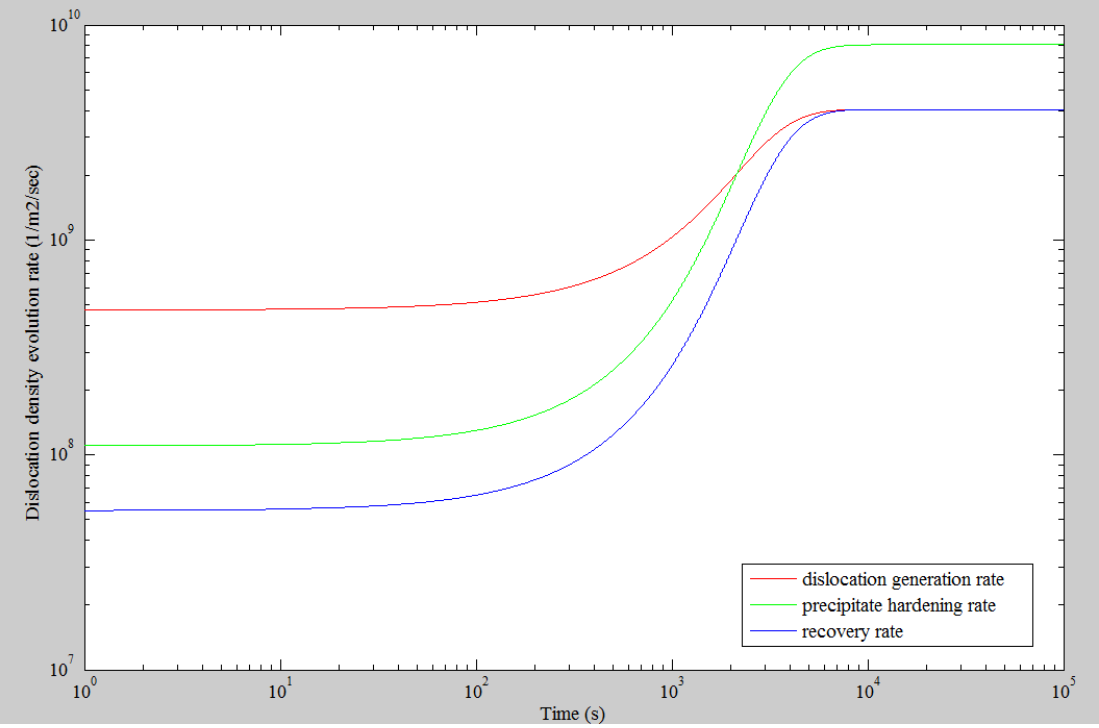

Figure 4.12: Dislocation density evolution during transient creep stage in slip system #2 (110)[001] in Ag_3Sn phase in eutectic Sn-Ag phase due to three competing mechanisms

4.4. Results & Discussions

The above proposed model has been calibrated for illustrative purposes based on the measured creep behavior of a single-crystal SAC305 specimen. Ideally, more calibration tests are needed, but single-crystal specimens are difficult to produce. Future studies should focus on better model calibration. Model predictions for the anisotropic transient creep rates in eutectic Sn-Ag phase and pure Sn phase will be presented in this paper. In Part II of this manuscript, the anisotropic creep rates along dominant slip systems of eutectic Sn-Ag phase and pure Sn phase will be combined using micromechanics homogenization theory to obtain the anisotropic creep properties of SAC single crystal. These results will be calibrated based on the experimental observations. The Euler angles of single crystal SAC305 specimen obtained using orientation image mapping via EBSD (electron backscatter diffraction) and the co-ordinate transformation tensor derived to resolve the applied shear stress along the slip systems will be presented in Section 4.4.1. Dislocation density evolution in the dominant slip systems in Ag_3Sn phase and pure Sn phase will be presented in Section 4.4.2. Anisotropic transient creep rates near Ag_3Sn particles, in the pure Sn phase and in the eutectic Sn-Ag phase in the SAC305 single crystal will be presented in Section 4.4.3. Finally in Section 4.4.4, the effect of the volume fraction of the Ag_3Sn phase and the effect of interparticle spacing between nanoscale Ag_3Sn IMCs on the anisotropic transient creep response of eutectic Sn-Ag phase will be presented.

4.4.1. Orientation Image Map and Euler Angle of Single Crystal SAC305 Specimen

An inverse pole figure map of SAC305 single crystal is presented in Figure 4.13. The misorientation angle between the sub grains in the single crystal is mostly less than 10°; therefore this SAC305 solder joint can be approximately considered as a single crystal. Euler angles of the joint at four different locations are presented, average of which will be used to convert the applied shear stress from global (sample) co-ordinate system to the crystal co-ordinate system and then further to individual slip system co-ordinate system.

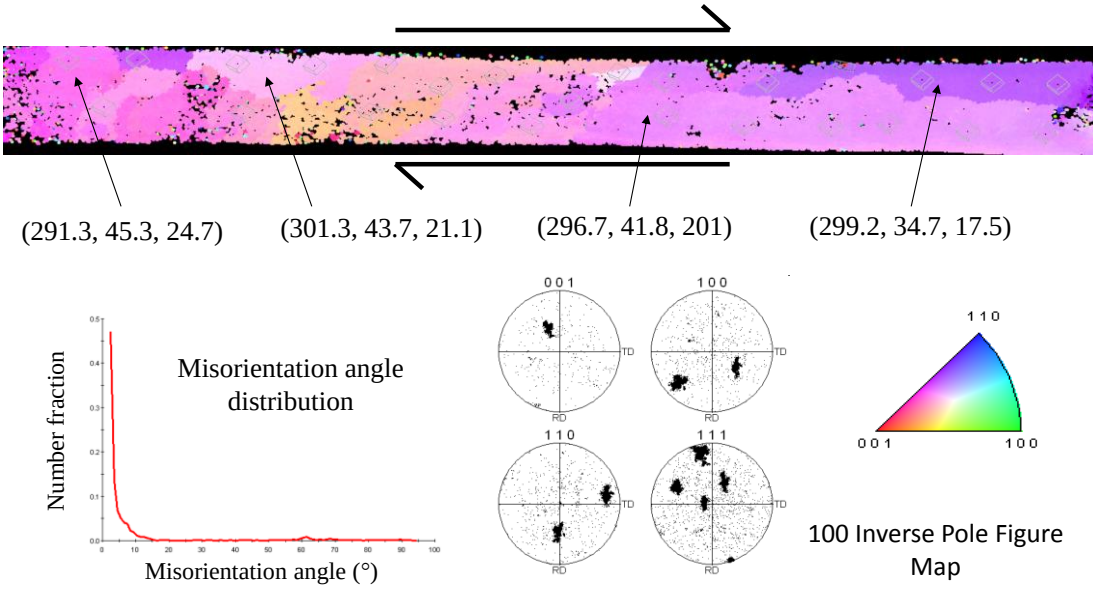

Figure 4.13: Inverse pole figure [100] map for SAC305 single crystal. Numbers inside parenthesis at four different locations of the joint refer to the Euler angles (φ_1, ϕ, φ_2), needed to convert the physical quantities from global co-ordinate system to crystal co-ordinate system

Applied in-plane shear stress (τ_{12}) along global specimen direction in SAC305 single crystal in the experiment is 10 MPa at room temperature. The resolved shear stress after performing above two co-ordinate transformations (from structural axes to crystal principal axes and then from crystal axes to slip system axes) is found to be 5.3 MPa along (110)[001] slip system; 6.7 MPa along (110)0.5[1-11] slip system; and 3.81 MPa along (100)[0-11] slip system. Average resolved initial velocity (based on Equation 13) is found to be 54.5 m/s along (110)[001] slip system; 39.9 m/s along (110)0.5[1-11] slip system; and 40.5 m/s along (100)[0-11] slip system.

4.4.2. Dislocation density evolution prediction in slip systems near Ag_3Sn particles and in pure Sn region in eutectic Sn-Ag phase

Rate of increase in dislocation density under the applied 10 MPa stress at RT is highest along (110)0.5[1-11] because of higher resolved shear stress along this slip direction and lowest along (100)[0-11] slip system because of lower resolved shear stress along global specimen direction in SAC305 single crystal (refer to Figures 4.14 and 4.15). Next, the transient dislocation density history calculated in this section are used to calculate the anisotropic transient creep rates near the Ag_3Sn IMC

particles using Equations 2 and 3 and in the Sn region using Equations 11 and 12, as described below in Section 4.4.3.

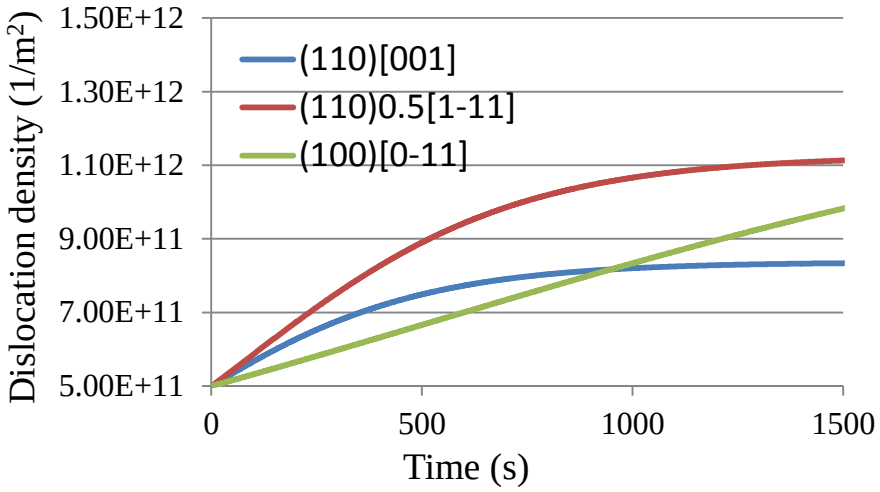

Figure 4.14: Dislocation density evolution in Ag_3Sn phase in an unit cell of eutectic Sn-Ag phase in SAC305 single crystal at 10 MPa shear stress level at RT

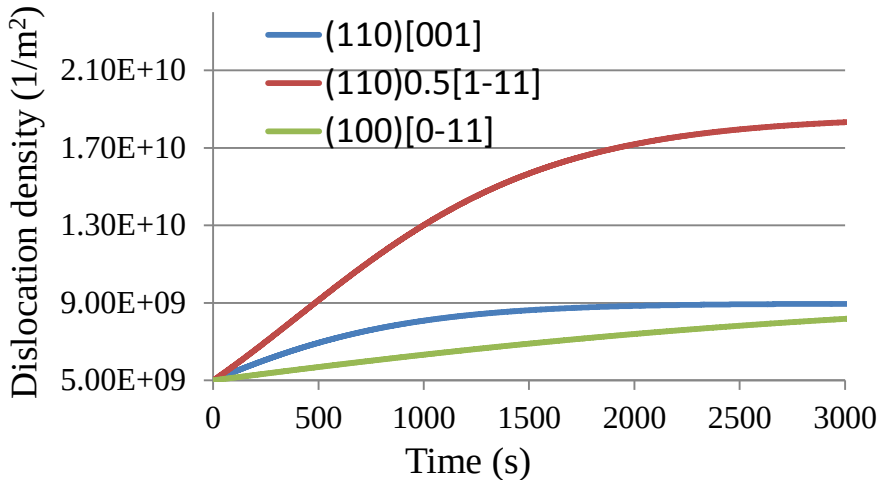

Figure 4.15: Dislocation density evolution in Sn phase in an unit cell of eutectic Sn-Ag phase in SAC305 single crystal at 10 MPa shear stress level at RT

4.4.3. Anisotropic transient creep rate predictions near Ag_3Sn particle & Sn region in eutectic Sn-Ag phase

Anisotropic transient creep rates along three dominant slip systems are calculated using Equation 2 for the Orowan climb mechanism and Rosler's dislocation detachment mechanism near the Ag_3Sn particles embedded in the eutectic Sn-Ag phase and plotted in Figure 4.16 and Figure 4.17, respectively.

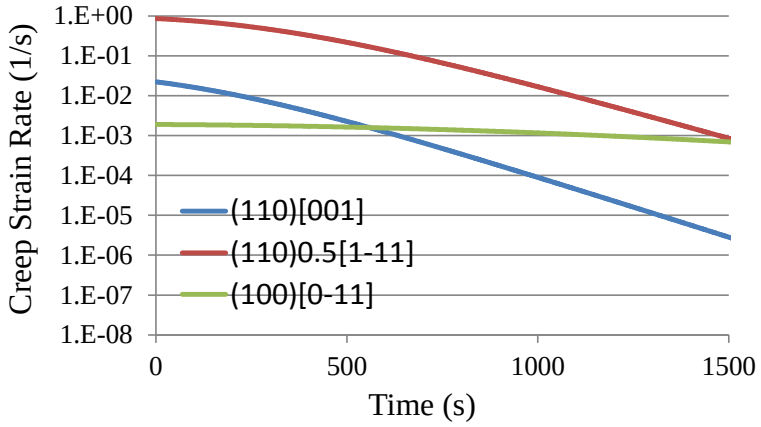

Figure 4.16: Anisotropic transient creep rates near Ag_3Sn particles in a unit cell of eutectic Sn-Ag phase in SAC305 single crystal due to dislocation loop climb (Equation 2) at 10 MPa shear stress level at RT

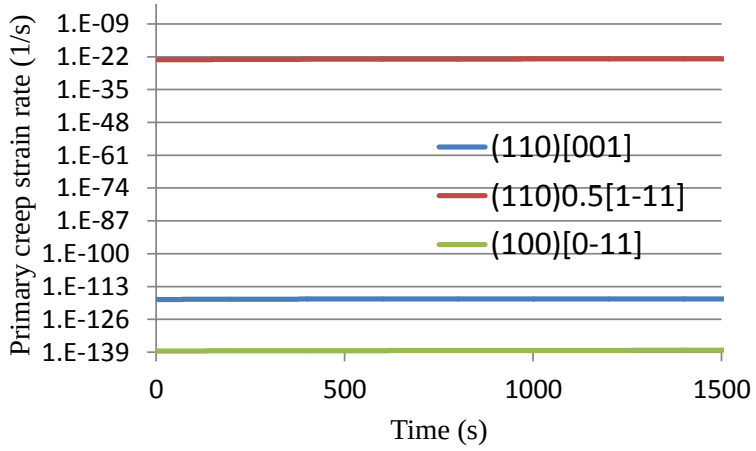

Figure 4.17: Anisotropic transient creep rates near Ag_3Sn particles in a unit cell of eutectic Sn-Ag phase in SAC305 single crystal due to dislocation detachment (Equation 3) at 10 MPa shear stress level at RT

Since, Orowan climb mechanism and dislocation detachment mechanism compete in parallel and the faster process dominates the rate controlling creep mechanism, transient creep strain rate over time is summed together to calculate the transient creep strain rate near the Ag_3Sn particles. Anisotropic transient creep rates along dominant slip systems for pure Sn phase are modeled using the climb and mass transport models and then summed up to predict the effective anisotropic transient creep rates along slip system. These results are plotted in Figure 4.18. The creep strain is predicted to be highest along the (110)[001] slip system and lowest along the (110)0.5[1-11] system.

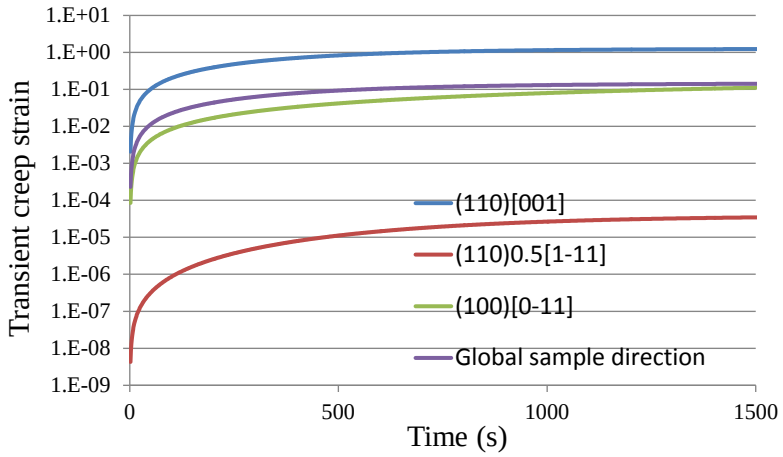

Figure 4.18: Anisotropic transient creep response in Sn phase in SAC305 single crystal (summation of creep strain due to dislocation climb and mass diffusion mechanism) at 10 MPa shear stress level at RT

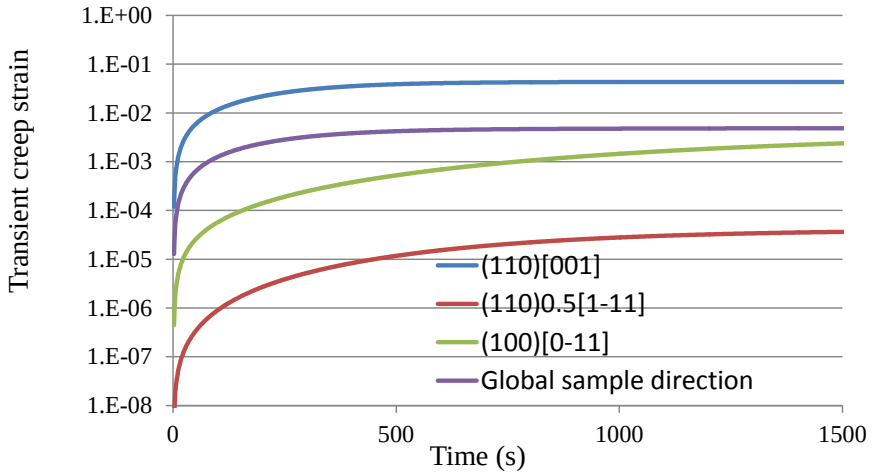

Figure 4.19: Anisotropic transient creep response in a unit cell of eutectic Sn-Ag phase in SAC305 single crystal at 10 MPa shear stress level at RT

Anisotropic transient creep rates along dominant slip systems for eutectic Sn-Ag phase is modeled using Equation 1 and plotted in Figure 4.19. The transient creep rate is predicted to be highest along the (110)[001] slip system and lowest along the (110)0.5[1-11] system.

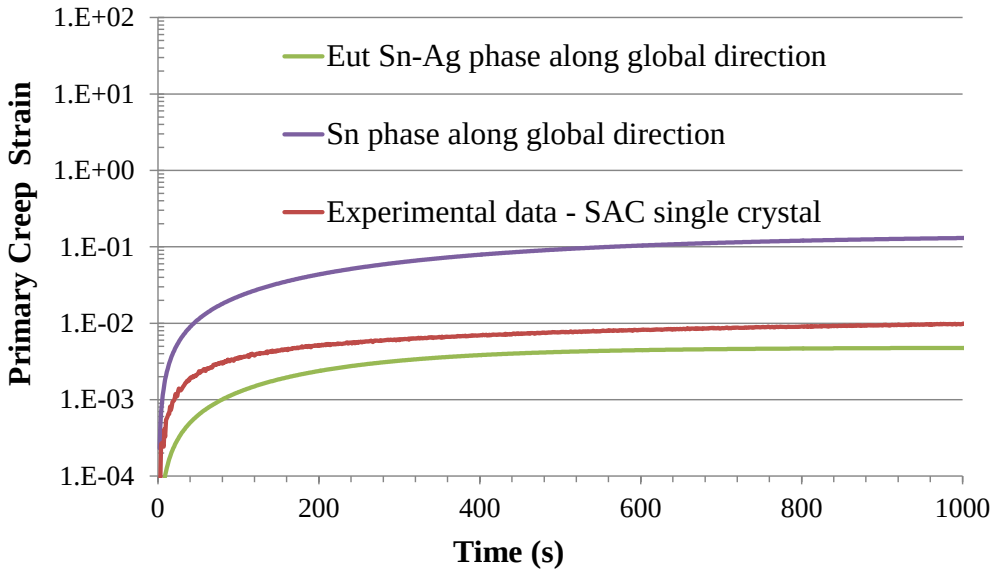

Figure 4.20: Anisotropic transient creep strain in Sn phase, eutectic Sn-Ag phase in SAC305 single crystal along global specimen direction at 10 MPa shear stress level at RT

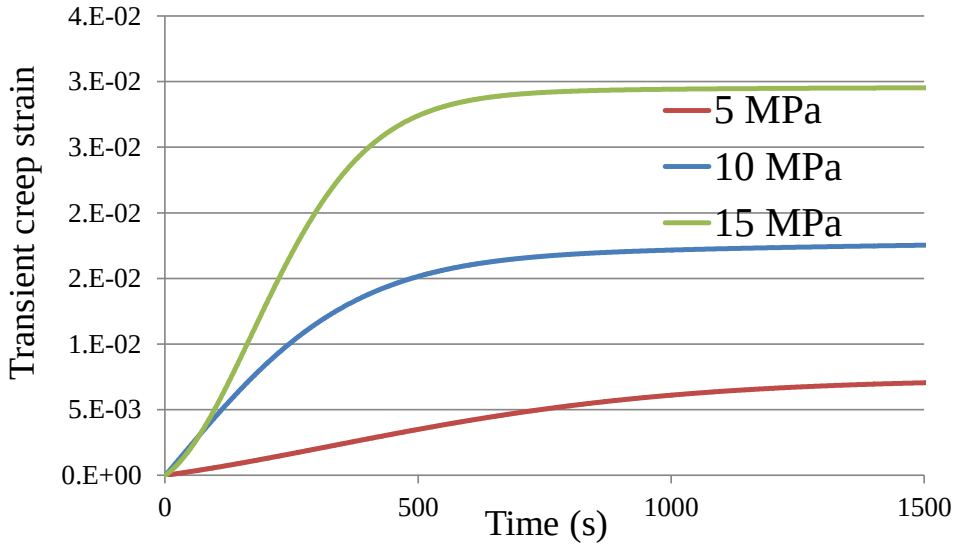

Figure 4.21: Anisotropic transient creep strain in eutectic Sn-Ag phase in SAC305 single crystal along global specimen direction for different stress levels at RT

Anisotropic transient creep rates for eutectic Sn-Ag phase and pure Sn phase along the specimen global direction (same as the loading axis system) are calculated and plotted against the experimental creep response for SAC single crystal in Figure 4.20. Anisotropic transient creep rates for the eutectic Sn-Ag phase along the global specimen direction are calculated for varying stress levels at room temperature and are plotted in Figure 4.21. The results predict the correct trend of increasing creep strain with increasing stress level. Unfortunately, the results cannot be compared yet to experimental results because the test data are for single crystal SAC305 solder but not for eutectic Sn-Ag phase. In Part II of this two-part series, the anisotropic creep response of eutectic Sn-Ag phase and pure Sn phase obtained along dominant slip systems of Sn will be utilized to capture the anisotropic creep response of SAC single crystal in Tier 2 length scale. The Tier II calculations will use micromechanics based on a fully anisotropic Eshelby tensor and Mori-Tanaka homogenization theory and will be calibrated to experimentally measured creep rates. The Tier II results will then be compared to experimental results in Part II of this two-part paper.

4.4.4. Effect of volume fraction and interparticle spacing of Ag_3Sn IMCs in eutectic Sn-Ag phase

In this section, the effects of varying volume fraction and interparticle spacing of nanoscale Ag_3Sn IMCs on anisotropic transient creep rates along (100)[0-11] slip system of eutectic Sn-Ag phase are explored. This parametric understanding is important because thermal aging of SAC solders causes continuous evolution and coarsening of the eutectic phase, resulting in increase of both the average particle size as well as the average interparticle spacing [76].

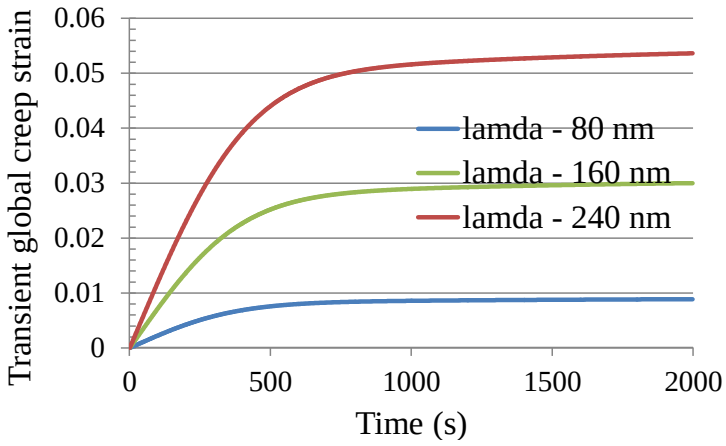

Figure 4.22: Effect of isothermal aging on transient creep strain in a unit cell of eutectic Sn-Ag phase in SAC305 single crystal along global specimen direction at 10 MPa shear stress level at RT

Transient creep rates along one of the slip systems is predicted to increase by (1-2) orders of magnitude as the interparticle spacing between nanoscale IMCs increases by a factor of three (refer to Figure 4.22), which is in agreement with experimental observation [166]. Similarly, with increase in volume fraction of nanoscale Ag_3Sn IMCs, transient creep rates are predicted to decrease (refer to Figure 4.23), which is also in agreement with experimental observation [166]. This is because increase in volume fraction of Ag_3Sn IMCs in a unit cell of eutectic Sn-Ag phase results in an increase in the number of particles impeding the motion of dislocations, thereby reducing the creep strain rate.

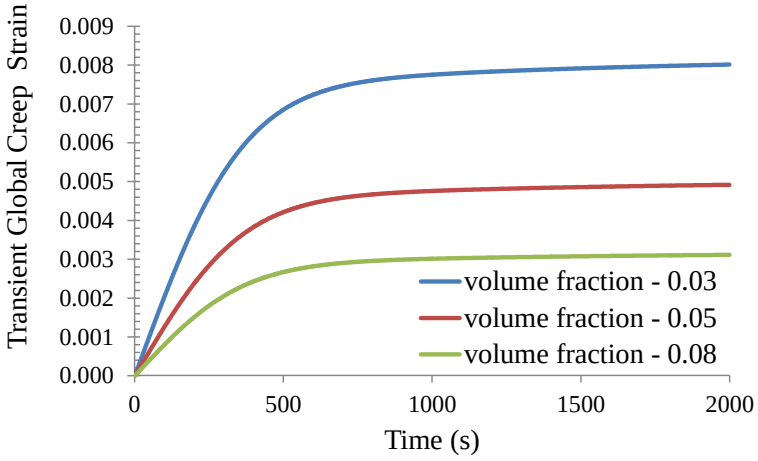

Figure 4.23: Effect of volume fraction of Ag_3Sn IMCs on transient creep strain in a unit cell of eutectic Sn-Ag phase in SAC305 single crystal along global specimen direction at 10 MPa shear stress level at RT

4.5. Summary and Conclusions

An anisotropic dislocation density based modeling framework is proposed in this study to capture the influence of the inherent elastic anisotropy of single crystal BCT Sn on the predicted anisotropic transient creep response of Sn-Ag eutectic alloy, which forms one of the two constituents of Sn-Ag-Cu (SAC) solders. Within this eutectic phase, the creep deformation is determined by the impediment due to nanoscale Ag_3Sn particles and by the creep in the surrounding Sn matrix.

The rate governing mechanisms for the creep deformation due to Ag_3Sn nanoscale IMC particles in the Sn-Ag phase are the recovery processes of the dislocations that are trapped by the Ag_3Sn particles in the Sn-Ag eutectic phase. The competing recovery mechanisms considered here are dislocation loop climb (Orowan climb) and dislocation detachment (Rosler detachment). Line tension and mobility of edge dislocations in dominant slip systems of single crystal anisotropic BCT Sn are modeled using Stroh's matrix formalism for modeling anisotropic elastic problems. Screw dislocations have not been considered for calculations here because screw dislocations don't undergo dislocation climb rather it cross-slips to favorable slip planes. Since, the stacking fault energy for pure Sn is low (which promotes formation of dislocation partials), the probability of cross-slip phenomena in pure Sn is low; however author believes cross-slip should be modeled in future for completeness. The anisotropic transient creep rate of the eutectic Sn-Ag phase is then modeled using above inputs and transient dislocation density calculated for dominant glide systems during the transient primary stage of creep. The transient dislocation density in the vicinity of the Ag_3Sn particles is estimated as the equilibrium between three competing processes: (1) dislocation generation; (2) dislocation impediment caused by back stress from pinning of dislocations at IMCs; and (3) dislocation recovery due to climb/detachment from IMCs in Ag_3Sn phase. For the pure Sn matrix, the anisotropic transient creep rates along dominant slip systems are modeled with dislocation climb and mass transport diffusion as the dominant competing recovery mechanisms. Transient dislocation density in the Sn phase is estimated as the equilibrium between three competing processes: (1) dislocation generation; (2) dislocation impediment from forest dislocations; and (3) dislocation recovery due to climb from forest dislocations in the Sn phase.

Transient creep rate is predicted to be highest along the (110) [001] slip system and lowest along the (110)0.5[1-11] system because of the difference in resolved shear stress and average initial resolved

velocity along those slip systems. Transient creep rates along one of the slip systems is predicted to increase by (1-2) orders of magnitude as the interparticle spacing between nanoscale IMCs increase by a factor of three, which is in agreement with experimental observations. Similarly, with increase in volume fraction of nanoscale Ag_3Sn IMCs, transient creep rates is predicted to decrease which is also in agreement with experimental observation.

4.6. Appendix

4.6.1. Dislocation line tension calculation in anisotropic BCT Sn :

An elastically distorted region around a dislocation produces extra strain energy. Due to the large strain within the dislocation core's radius (around 1~2 b (burgers vector)), the axioms of continuum elasticity are not applicable any more within this range. Thus, the total energy can be divided into

$$E_{total} = E_{elastic\ strain} + E_{core} \quad \text{(A1.1)}$$

The elastic strain energy per unit length for an isotropic material can be expressed as [167]:

$$E_{elastic\ strain} = \frac{\mu b^2(1-\nu\cos^2\theta)}{4\pi(1-\nu)}\ln\left(\frac{R}{r_o}\right) \quad \text{(A1.2)}$$

Where, μ is the shear modulus; b is the Burgers vector; ν is the Poisson's ratio; θ is the angle between the dislocation and the Burgers vector; R is the outer radius of integration; r_o is the dislocation core radius. For isotropic elasticity,

$$K = \frac{\mu(1-\nu\cos^2\theta)}{(1-\nu)} \quad \text{(A1.3)}$$

is defined as the energy factor of a dislocation. Then Equation A1.2 can be rewritten as:

$$E_{elastic\ strain} = \frac{Kb^2}{4\pi}\ln\left(\frac{R}{r_o}\right) \quad \text{(A1.4)}$$

For anisotropic elasticity, the determination of K requires numerical approaches, and can be evaluated by using either the sextic formalism of Eshelby et al. [168][169] or the integral formalism of Barnet et al. [170][171]. Here in this study, Eshelby's sextic eigen value formalism is adapted for calculation of line tension of a dislocation in an anisotropic medium. Here, a short summary of the sextic eigen value formalism is given as follows.

The basic equation of linear relation between the stresses σ_{ij} and the strains e_{ij} can be written in terms of the fourth rank tensor C_{ijkl}:

$$\sigma_{ij} = C_{ijkl}\, e_{kl} \quad \text{(A1.5)}$$

Where, i, j, k and l all take values from 1 to 3 and Einstein summation convention is implied over repeated subscripts. Strains e_{kl} can be expressed in terms of displacements (u_{ij}) as:

$$e_{kl} = \frac{1}{2}\left(\frac{\partial u_k}{\partial x_l} + \frac{\partial u_l}{\partial x_k}\right) \quad \text{(A1.6)}$$

Substituting Equation A1.6 into Equation A1.5, the stresses can be written in terms of the displacements:

$$\sigma_{ij} = C_{ijkl}\frac{\partial u_k}{\partial x_l} \quad \text{(A1.7)}$$

In the case of no body forces, substituting Equation A1.7 into static equilibrium equation, we can get:

$$C_{ijkl}\left(\partial^2 u_k\right)/\,\partial x_j\,\partial x_l) = 0 \quad \text{(A1.8)}$$

In the study of Eshelby et al. [168], the axis x_3 was taken to be parallel to the dislocation line, which means that the elastic state is independent of x_3. Therefore, the standard form of solutions for Equation A1.8 can be shown to be:

$$u_k = A_k\, f(x_1 + p x_2) \quad \text{(A1.9)}$$

Where, p and A_k are constants. Substituting Equation A1.9 into Equation A1.8, we have

$$(C_{i1k1} + C_{i1k2}\,p + C_{i2k1}\,p + C_{i2k2}\,p^2)\,A_k = 0 \quad \text{(A1.10)}$$

The Equations A1.10 have a nonzero solution for the A_k only if *p* is such that the determinant of their coefficient is zero, i.e.

$$|C_{i1k1} + C_{i1k2}\,p + C_{i2k1}\,p + C_{i2k2}\,p^2| = 0 \quad \text{(A1.11)}$$

Equation A1.11 can be expanded in the following form to get the sextic characteristic equation. The characteristic equation of the resulting matrix shown below has to be solved to obtain the values of p and subsequently A_k

$$[C_{1111} + (C_{1112}+C_{1211})p + C_{1212}p^2]\,[C_{2111} + (C_{2112}+C_{2211})p + C_{2212}p^2]\,[C_{3111} + (C_{3112}+C_{3211})p + C_{3212}p^2]$$
$$[C_{1121} + (C_{1122}+C_{1221})p + C_{1222}p^2]\,[C_{2121} + (C_{2122}+C_{2221})p + C_{2222}p^2]\,[C_{3121} + (C_{3122}+C_{3221})p + C_{3222}p^2]$$
$$= 0$$
$$[C_{1131} + (C_{1132}+C_{1231})p + C_{1232}p^2]\,[C_{2131} + (C_{2132}+C_{2231})p + C_{2232}p^2]\,[C_{3131} + (C_{3132}+C_{3231})p + C_{3232}p^2]$$
$$\text{(A1.12)}$$

Solving the roots of a sextic equation is numerically challenging and time consuming. Stroh proposed a way of solving the above problem as a Eigen value problem. For an anisotropic medium whose elastic

stiffness constants C_{ijkl} are relative to e_1-e_2-e_3 natural crystal basis, let x denote a position from origin O, a mutually orthogonal right hand basis m-n-t was chosen to solve the above problem. Thus,

$$x = (m*x, n*x, t*x)^T \quad \text{(A1.13)}$$

Assuming,

(i) $b_j = 0$; i.e. there is no body force

(ii) the solution of u is independent of x_3, i.e. invariant along the dislocation line

Stroh suggested a displacement field of the form,

$$u_k = A_k f(m*x+pn*x) \quad \text{(A1.14)}$$

where A is a constant vector, p is a constant and f is an arbitrary analytical function. Plugging in this trial solution into Equation A1.10, we get

$$\{C_{ijkl} (m_i+pn_i) (m_l+pn_l)\} f'' A_k = 0 \quad \text{(A1.15)}$$

The case of $f''=0$, gives a constant strain field for dislocations, which is impossible.

Therefore, $$\{C_{ijkl} (m_i+pn_i) (m_l+pn_l)\} A_k = 0 \quad \text{(A1.16)}$$

A nontrivial solution for A exists only if

$$||C_{ijkl} (m_i+pn_i) (m_l+pn_l)|| = 0 \quad \text{(A1.17)}$$

where || || stands for the determinant. The resulting characteristic equation is a sixth order polynomial equation in p with real coefficients. The general solution to the displacement field can be written as a linear combination of the six solutions corresponding to p_{α}.

$$u_k = \sum D_\alpha A_{k\alpha} f(m.x + p_\alpha n.x) \quad \text{(A1.18)}$$

where D_α are coefficients determined by the boundary conditions of the elastic problem under consideration. To sum up, solving for p enables solving for A; while coefficients D_α are dependent on p_α and the boundary conditions.

To solve the above problem, there are two possible approaches: 1] Matrix formalism and 2] Integral formalism. Here, the matrix formalism is used. Equation A1.16 can be rewritten as:

$$\{C_{ijkl} (m_i+p_\alpha n_i) (m_l+p_\alpha n_l)\} A_{k\alpha} = 0 \quad \text{(A1.19)}$$

The basic idea is to convert Equation A1.19 into an eigen value problem, which is easier to solve than the sixth order polynomial. A new variable, vector L is introduced,

$$L_{j\alpha} = -n_i C_{ijkl} (m_l+p_\alpha n_l) A_{k\alpha} \quad \text{(A1.20)}$$

Alternatively, we can write, $L_{j\alpha} = \frac{1}{p_\alpha} m_i C_{ijkl} (m_l + p_\alpha n_l) A_{k\alpha}$ (A1.21)

$A_{k\alpha}$ and $L_{k\alpha}$ are also unique by using the normalization condition;

$$2A_{k\alpha}L_{k\alpha} = 1 \quad \text{(A1.22)}$$

Now using the following notation, $(ab)_{jk} = a_i C_{ijkl} b_l$ and applying it to Equations A1.20 and A1.21, we get

$$(nm)_{jk} A_{k\alpha} + L_{j\alpha} = - p_\alpha (nn)_{jk} A_{k\alpha} \quad \text{(A1.23)}$$

$$(mm)_{jk} A_{k\alpha} = - p_\alpha (mn)_{jk} A_{k\alpha} + p_\alpha L_{j\alpha} \quad \text{(A1.24)}$$

In terms of six dimensional matrices it becomes,

$$\begin{Bmatrix} (nm) & I \\ (mm) & 0 \end{Bmatrix} \begin{Bmatrix} A_\alpha \\ L_\alpha \end{Bmatrix} = p_\alpha \begin{Bmatrix} (nn) & 0 \\ (mn) & I \end{Bmatrix} \begin{Bmatrix} A_\alpha \\ L_\alpha \end{Bmatrix} \quad \text{(A1.25)}$$

Where, $$\begin{Bmatrix} A_\alpha \\ L_\alpha \end{Bmatrix} = \begin{Bmatrix} A_{k\alpha} \\ L_{k\alpha} \end{Bmatrix} = \begin{Bmatrix} A_{1\alpha} \\ A_{2\alpha} \\ A_{3\alpha} \\ L_{1\alpha} \\ L_{2\alpha} \\ L_{3\alpha} \end{Bmatrix} \quad \text{(A1.26)}$$

Multiplying both sides of Equation A1.25 by

$$-\begin{Bmatrix} -(nn)^{-1} & 0 \\ -(mn)(nn)^{-1} & -I \end{Bmatrix}$$

And noting that, $-\begin{Bmatrix} -(nn)^{-1} & 0 \\ -(mn)(nn)^{-1} & -I \end{Bmatrix} \begin{Bmatrix} (nn) & 0 \\ (mn) & I \end{Bmatrix} = \begin{Bmatrix} I & 0 \\ 0 & I \end{Bmatrix}$; we obtain the following eigen equation:

$$\mathbf{N}\xi_\alpha = p_\alpha \xi_\alpha \quad \text{(A1.27)}$$

Where, $$\mathbf{N} = -\begin{Bmatrix} (nn)^{-1}(nm) & (nn)^{-1} \\ (mn)(nn)^{-1}(nm) - (mm) & (mn)(nn)^{-1} \end{Bmatrix}$$

$$\xi_\alpha = \begin{pmatrix} A_\alpha \\ L_\alpha \end{pmatrix} \quad \text{(A1.28)}$$

Therefore, p and **A** can be derived by solving the above Eigen value problem. And the line tension of the dislocation can be solved by solving for Eigen values of one of three useful matrices (**Q**, **B**, **S**) [172] given by Stroh, which depend on the values of the A and L matrices. Line tension of dislocations can be calculated by solving the eigen values of B matrix, whose expression is given by:

$$B_{js} = \text{real}(\sum \pm L_{j\alpha} L_{s\alpha}) \quad \text{(A1.29)}$$

Where '+' is used for $\alpha = 1, 2, 3$ and '-' is used for $\alpha = 4, 5, 6$.

Eigen values of B matrix gives the value of line tension factor of edge/screw dislocation in anisotropic matrix.

Chapter 5： Multiscale Modeling of the Anisotropic Transient Creep Response of Single Crystal SnAgCu Solder

Part II: Reinforcement Strengthening due to Sn-Ag Phase

Abstract

Many researchers have demonstrated that micron scale high-Sn SAC solder joints exhibit significant piece to piece variability in their mechanical response under identical load conditions in the as-fabricated state due to coarse grained structure and the anisotropy of Sn. A multiscale mechanistic modeling approach was proposed in Part I this two-part paper, where anisotropic transient creep rates of the eutectic Sn-Ag phase (Tier 1) and the pure Sn phase were modeled along the dominant slip systems of the Sn grain in a single crystal of SAC solder material. The creep response of the eutectic phase (from Tier 1) is combined with the creep response of Sn lobes at Tier 2, using the anisotropic Mori-Tanaka homogenization theory in this paper, to obtain the transient creep response of a SAC305 single crystal along global specimen directions. This model has been calibrated using experimentally obtained transient creep response of a SAC305 single crystal specimen. The Eshelby strain concentration tensors required for this homogenization process are calculated numerically for ellipsoidal Sn inclusions embedded in transversely isotropic eutectic Sn-Ag matrix. The above multiscale calibrated model is then used to predict (i) the transient creep response of another SAC305 single crystal specimen and (ii) the effect of orientation (by changing one of the Euler angles) on the transient creep response of SAC305 single crystal. The grain orientation of above two SAC single crystal specimens (with respect to loading direction) were identified with orientation image mapping and then utilized in the model to estimate the resolved shear stress along the dominant slip directions. Parametric studies have also been conducted to predict the effects of the volume fraction, aspect ratio, and orientation of ellipsoidal Sn inclusions on the anisotropic transient creep response of SAC single crystals. The original draft of this chapter is a journal paper and will be submitted to Acta Materiala

and part of the paper has been accepted at USNCTAM, 2014 (United States National Congress on Theoretical and Applied Mechanics) at East Lansing, MI.

Keywords: Creep, anisotropy, BCT Sn, SAC single crystal, Eshelby tensor, ellipsoidal inclusion, Mori-Tanaka homogenization

5.1. Introduction

Because of the anisotropic elastic and thermal properties of Sn, the thermomechanical response of lead free SAC solder joints depends greatly on the size and orientation of its Sn grains [114]–[127]. Significant literature exists that demonstrate that micron scale high-Sn SAC solder joints exhibit significant piece to piece variability in their mechanical response under identical loading conditions in the as-fabricated state [130], [133], [136]–[138]. This is because the microstructure evolution of tin based solder is not well understood because no other metal other than tin has the squashed diamond cubic body centered tetragonal structure of Sn, with its unusual deformation characteristics. Second, tin crystal properties are very anisotropic, with a CTE twice as large in the <c> as the <a> direction. Also, the elastic properties differ by as much as a factor of 5 at the higher temperatures expected in service (refer to Figure 5.1).

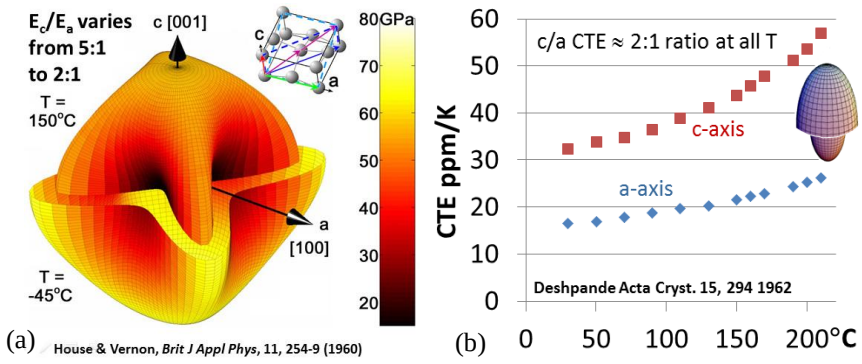

Figure 5.1: Anisotropic properties of BCT Sn crystal: (a) Directional variation of elastic stiffness at two different tempertures (b) Temperature dependent CTE along two principal crystal orientations [173], [174]

Tin expands the most in the stiffest direction, leading to a strong driving force for heterogeneous deformation. The small joint volume and a high entropy of transformation often requires 30°C of

undercooling to form a critical nucleus, resulting in either large single crystals or large twinned grains with rotational periodicity [175], which amplifies the anisotropic properties in the joint. These anisotropic features make the evolution of stress and microstructural defects arising from mechanical and thermal boundary conditions in tin complex, yet important, because they provide the localized driving force for recovery, recrystallization, grain boundary mobility, damage nucleation, crack formation and propagation, and ultimately the end of life of electronic interconnects. The anisotropy of Sn has been masked by the relatively soft properties of Pb for hundreds of years because of the use of SnPb solders [131], [176], [177]. Thus, isotropic material models have been adequate for Sn-Pb solders, showing that failure is more likely with higher strain energy that occurs in the corner joints. However, failures have been reported for Sn based alloys near the center of packages, and correlated to the orientation of the tin crystal as first documented in [128]. Figure 5.2 shows EBSP (Electron Back Scatter Pattern) mapping of an interior row, showing that cracks occurred preferentially in joints where the c-axis was nearly parallel to the interface. These 'red' joints, whose c-axis is parallel to the interface, undergoes more deformation (which leads to cracking), because CTE of Sn along c-axis is two times that of along a-axis. In contrast, 'blue/purple' joint orientations with the c-axis nearly perpendicular to the interface show the least amount of cracking [178], [179]. This tensile/compressive damage mode arising from the anisotropic CTE does not occur in Sn-Pb joints, and because a statistical analysis of all joints in a package show that crystal orientations are nearly randomly distributed, vulnerable (red) joints can be located anywhere.

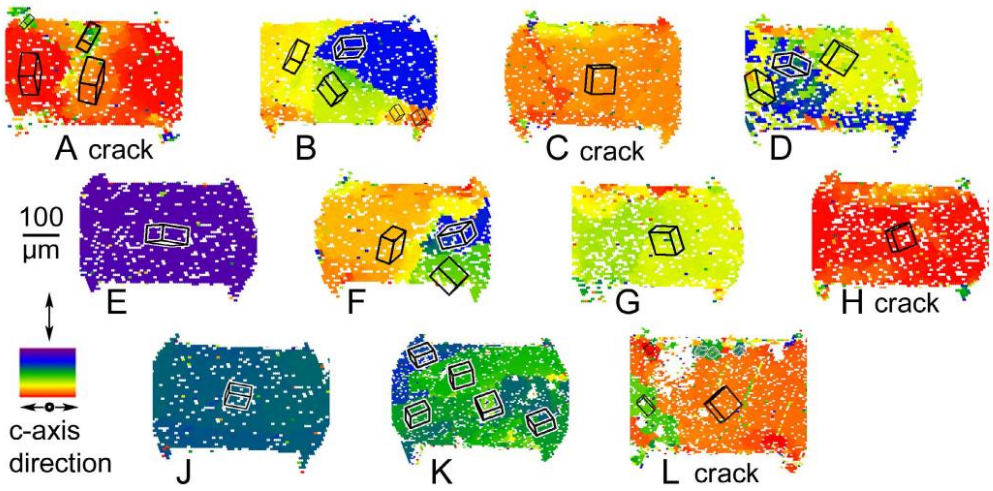

Figure 5.2: "Red" orientations with the c-axis nearly parallel to the board are most susceptible to cracking. Cracked joints in the 9x11 array after 2500 thermal cycles are indicated in the package joint layout.

A full understanding of the effect of anisotropy of Sn and grain orientation on the thermomechanical response of these SAC solder interconnects requires a detailed insight into not only the elastic and thermal properties of Sn, but also of the anisotropic viscoplastic properties of SAC solder joints. A multiscale modeling approach was proposed in Part I of this two part paper, where the SAC microstructure was classified into four distinct length scales, as shown in Figure 5.3. Tier 4 represents the complex evolving boundary conditions imposed on the actual physical geometry of the solder join including the interfacial metallization that creates the intermetallic bond between the solder and the component. In our study, the structure is a modified Iosipescu lap shear specimen. The next lower length scale (Tier 3) is the grain scale microstructure, typically consisting of an anisotropic single crystal or a few Sn grains and grain boundaries.

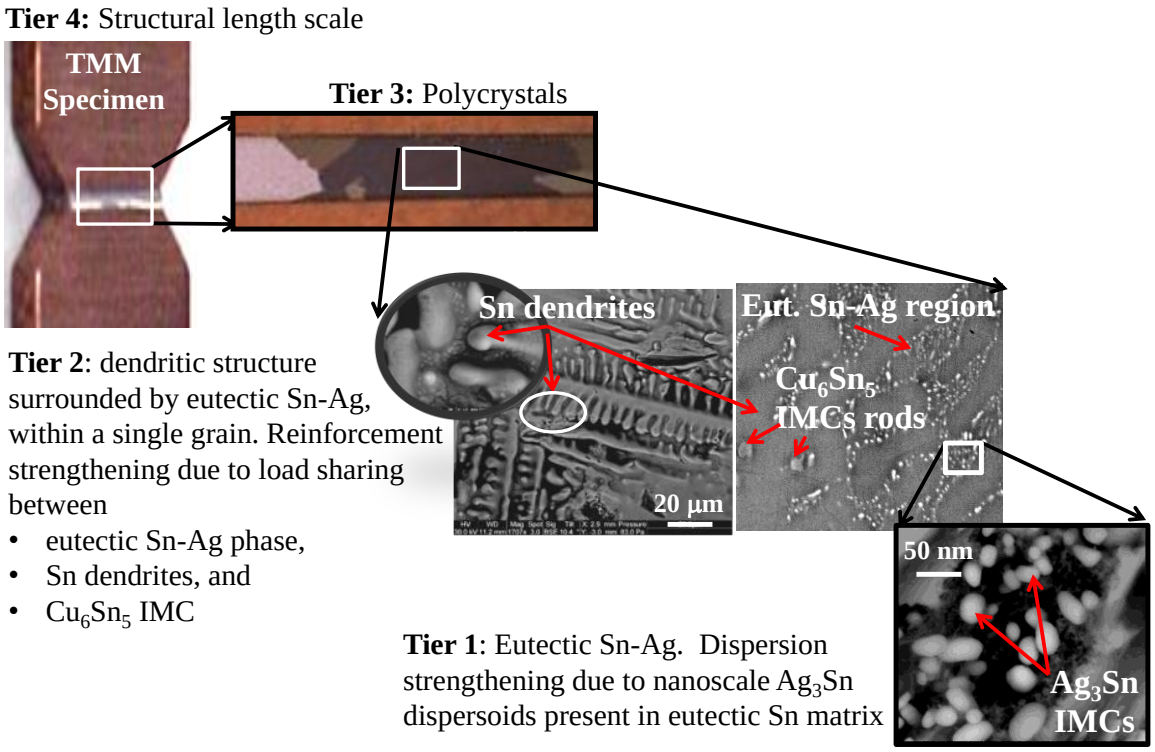

Figure 5.3: Multiple length scales (Tiers 0-5) in SnAgCu solder alloys

The next lower length scale (Tier 2, which is the focus of this paper) focuses on the structure within individual grains, comprising of multiple tin dendrites formed during solidification, that are surrounded by a eutectic Sn-Ag microconstituent that was the last to solidify. Embedded throughout this grain are additional micron scale intermetallic Cu_6Sn_5 precipitates. At this length scale, anisotropic composite models are effective. Tier 1 (focus of Part I of this two-part paper) describes the structure of the eutectic Sn-Ag microconstituent consisting of a locally homogeneous distribution of nanoscale Ag_3Sn intermetallic particles embedded in a mono-crystalline tin matrix. The behavior at Tier I was described in Part I with anisotropic models of dislocation interactions with particles that depend on spacing/size.

Effect of anisotropy of BCT Sn on Tier 0 and 1 viscoplastic responses of eutectic Sn-Ag phase and pure Sn phase in SAC single crystal was captured in Part I of this two-part paper. The anisotropic transient creep response of SAC single crystal is predicted in this paper using anisotropic micromechanics Mori-Tanaka homogenization techniques, based on the transient Tier I creep rates predicted in Paper I along dominant slip systems in (i) single crystal eutectic Sn-Ag phase; and (ii) pure Sn dendrites.

A mechanistic multiscale modeling framework was earlier proposed by Cuddalorepatta et al. [59], which can capture the physics of average isotropic steady state creep response at Tier 2 length scale. At the length-scale of dendritic colonies (~50 μm), the alloy is treated as a composite consisting of soft pure Sn dendrite inclusions and hard Cu_6Sn_5 IMC inclusions embedded in a dispersion-strengthened Sn-Ag eutectic 'matrix'. The properties of the Sn-Ag eutectic phase were obtained from the Tier 1 isotropic formulation [59]. The effective properties of this composite were obtained by using self-consistent homogenization schemes from micromechanics theories. The resulting creep properties (viscosity) were obtained by using the effective medium approximation (EMA). Sn dendrites were assumed to be spherical shaped inclusions with effective isotropic properties. The effect of the dendrites was accounted only through their volume fraction. The effective viscosity has been derived for spherical shaped inclusions by Nemat Naseer et. al [63], and was used in [59] to predict the isotropic homogenized creep response of SAC305 solder composite. Although, the model in [59] can predict the isotropic steady state behavior of the material it cannot capture the anisotropic transient and steady state creep response of SAC single crystal. Moreover, the Sn dendrites are modeled as soft

spherical inclusions. Hence Eshelby's tensor, which represents the geometric parameters of the inclusions, is independent of the inclusion dimensions and the effect of Sn dendrites is included only via their volume fraction in the SAC alloy. However, since the experimentally observed Sn dendritic configuration is non spherical, its impact on the measured creep response needs to be captured.

To overcome these limitations, the anisotropic creep response of the eutectic phase (Tier 1 response from Part I of this two-part paper) is combined with the creep response of the Sn lobes (from Tier 1 from Part I of this two-part paper) at Tier 2 using the anisotropic Mori-Tanaka homogenization theory in this paper, to obtain the transient creep response of SAC305 single crystal along principal crystallographic directions. The Eshelby strain concentration tensors required for this homogenization process are numerically evaluated for ellipsoidal Sn inclusions embedded in an anisotropic eutectic Sn-Ag matrix. The above multiscale model is calibrated using the experimentally observed transient creep response of one of the SAC305 single crystal specimens. The above multiscale calibrated model is then used to predict the transient creep response in another SAC305 single crystal specimen and the effect of orientation (by changing one of the Euler angles) on the transient creep response of SAC305 single crystal. The orientations of above two SAC single crystal specimens with respect to the loading direction were identified with orientation image mapping and then utilized in the model to estimate the resolved shear stress along the dominant slip directions. In Section 5.2, the modeling approach will be discussed; in Section 5.3, Eshelby tensor calculation for ellipsoidal inclusion embedded in anisotropic matrix will be discussed; and finally in Section 5.4, the anisotropic transient creep rates of SAC single crystal will be predicted and calibrated against the experimental observation. The manuscript will conclude with parametric studies to predict the effect of volume fraction, aspect ratio, and orientation of ellipsoidal Sn inclusions on the anisotropic transient creep rates of one of the tested SAC single crystal specimen.

5.2. Modelling Approach

In Tier 2 length scale, anisotropic transient creep rates of eutectic Sn-Ag phase and Sn inclusion along three dominant slip systems are being utilized to predict the anisotropic creep rates of SAC single crystal along principal crystallographic directions. For an ellipsoidal inclusion embedded in a general

anisotropic material Eshelby tensor $\overset{\Leftrightarrow}{S}$ has to be determined numerically. For a composite with the inclusion phases characterized by the index i, and the matrix phase characterized by index 0, the effective viscosity of the single crystal composite is given in Mori Tanaka homogenization method by:

$$\overset{\Leftrightarrow}{V} = \overset{\Leftrightarrow}{V_0} + \sum_{i=1}^{2} c_i (\overset{\Leftrightarrow}{V_i} - \overset{\Leftrightarrow}{V_0})[c_0 \overset{\Leftrightarrow}{S} \overset{\Leftrightarrow}{V_0}^{-1} (\overset{\Leftrightarrow}{V_i} - \overset{\Leftrightarrow}{V_0}) + \overset{\Leftrightarrow}{I}]^{-1} \qquad (1)$$

Where,

$\overset{\Leftrightarrow}{V}$ = Effective viscosity of the composite RVE;

$\overset{\Leftrightarrow}{V_0}$ = viscosity of the matrix (eutectic Sn-Ag phase) in unit RVE;

$\overset{\Leftrightarrow}{V_i}$ = viscosity of the inclusion (Sn inclusion) and Cu_6Sn_5 IMC in unit RVE;

$\overset{\Leftrightarrow}{S}$ = Eshelby tensor of the ellipsoidal Sn inclusion and cylindrical Cu_6Sn_5 inclusion (cross-section is assumed to be elliptical) embedded in anisotropic medium;

$\overset{\Leftrightarrow}{I}$ = identity tensor;

c_i & c_0 $(1 - c_i)$ = volume fraction of Sn (0.55 in SAC305; obtained using image processing) and Cu_6Sn_5 (0.03 in SAC305; obtained using image processing) inclusion and matrix in the composite RVE.

The inclusion problem described by Eshelby (1957) [180] is as follows: A region (inclusion) in an infinite, homogeneous, isotropic, and liner elastic medium (matrix) undergoes a change in shape and size. Under the constraint of the matrix, the inclusion has an arbitrary homogeneous strain. The definition of eigenstrain ε^*, summarized by Mura (1987) [167], can be regarded as the strain state that the inclusion will enter if we remove the constraints of the matrix. Eshelby referred to this as stress-free strain. In Mura [167], an inclusion is defined as subdomain Ω in a domain D, and eigenstrain $\varepsilon_{ij}^*(x)$ is given in Ω and zero in D-Ω. The elastic moduli in the inclusion Ω and the matrix D-Ω are the same. The displacement u_j, strain ε_{ij}, and stress σ_{ij} for both the inclusion and matrix are expressed [167] as

$$u_i(x) = -C_{kjmn}\int_{\Omega} \varepsilon^*(x')G_{ij,k}(x-x')dx' \quad (2)$$

$$\varepsilon_{ij}(x) = -\frac{1}{2}\int_{\Omega} C_{klmn}\varepsilon_{mn}{}^*(x')(G_{ik,lj}(x-x') + G_{ijk,li}(x-x'))dx'; \quad (3)$$

$$\sigma_{ij}(x) = -C_{ijkl}\int_{\Omega} C_{pqmn}\varepsilon_{mn}{}^*(x')(G_{kp,ql}(x-x')dx' + \varepsilon_{kl}{}^*(x) \quad (4)$$

where C_{ijkl} is the stiffness tensor; G_{ij} is Green's function; and **x** is the position vector; and **x'** denotes the position of a point source. For an ellipsoidal inclusion embedded in an isotropic material, Green's function is given by Mura [167]

$$G_{ij}(x-x') = \frac{1}{16\pi\mu(1-\nu)|x-x'|}\left((3-4\nu)\delta_{ij} + \frac{(x_i - x_i')(x_j - x_j')}{|x-x'|^2}\right) \quad (5)$$

Assuming the eigenstrain in the inclusion is constant, we can take ε* out of the integrals of Equations 2-4. Eshelby [180]–[182] derived solutions for the interior and exterior field of such an inclusion. One of Eshelby's prominent results is that the strain and stress fields within the inclusion are uniform.

$$\varepsilon_{ij} = S_{ijkl}\varepsilon_{kl}^* \quad (6)$$

where S_{ijkl} is the fourth order Eshelby tensor [167].

However, there is no closed form analytical solution available for Eshelby's tensor for ellipsoidal inclusions embedded in anisotropic material, so this tensor has to be numerically evaluated. For a general anisotropic material, the Eshelby tensor (S) is given by the following surface integral, parameterized on the surface of a unit sphere (Mura 1987) [167]

$$S_{ijkl} = \frac{1}{8\pi}L_{mnkl}\int_{-1}^{+1} d\zeta_3 \int_0^{2\pi}\{G_{imjn}(\xi') + G_{j\min}(\xi')\}d\omega \quad (7)$$

where

$$G_{ijkl}(\xi') = \xi_k'\xi_l' N_{ij}(\xi')/D(\xi') \quad (8)$$

$$\xi_i^{'} = \zeta_i / a_i; \zeta_1 = (1-\zeta_3^2)^{1/2}\cos(\omega); \zeta_2 = (1-\zeta_3^2)^{1/2}\sin(\omega); \zeta_3 = \zeta_3 \quad (9)$$

$$D(\xi') = \varepsilon_{mnl} K_{m1} K_{n2} K_{l3}; N_{ij}(\xi') = \frac{1}{2}\varepsilon_{ikl}\varepsilon_{jmn} K_{km} K_{\ln}; K_{ik} = L_{ijkl}\xi_j^{'}\xi_l^{'} \quad (10)$$

where, ε_{ijk} is the permutation tensor and L_{ijkl} are the components of the stiffness tensor of the anisotropic material. In this work, a numerical scheme for the evaluation of S_{ijkl} is used [183] based on Equation (7). The double integration is performed using the Gaussian quadrature formula:

$$S_{ijkl} = \frac{1}{8\pi}\sum_{p=1}^{M}\sum_{q=1}^{N} L_{mnkl}\{G_{imjn}(\omega_q, \zeta_{3p}) + G_{j\min}(\omega_q, \zeta_{3p})\}W_p W_q \quad (11)$$

where, M and N refer to the points used for integration over ζ_3 and ω, respectively, and W_p, W_q are the corresponding Gaussian weights.

5.3. Results: Calculation of Eshelby Tensor

Analytical solutions are available for Eshelby tensor for ellipsoidal inclusions embedded in transversely isotropic material. These analytic solutions for Eshelby tensor are compared to the numerical results from Equation 11 for isotropic and transversely isotropic materials [167]. A parametric numerical study was first conducted by varying the number of Gauss points for N from 3 to 500 and M=2 to explore the convergence of the S tensor components over the domain.

Figure 5.4 illustrates that all components of S tensor are stable after N=20; therefore M= 2 and N= 20 is used for all further calculations and verification purposes.

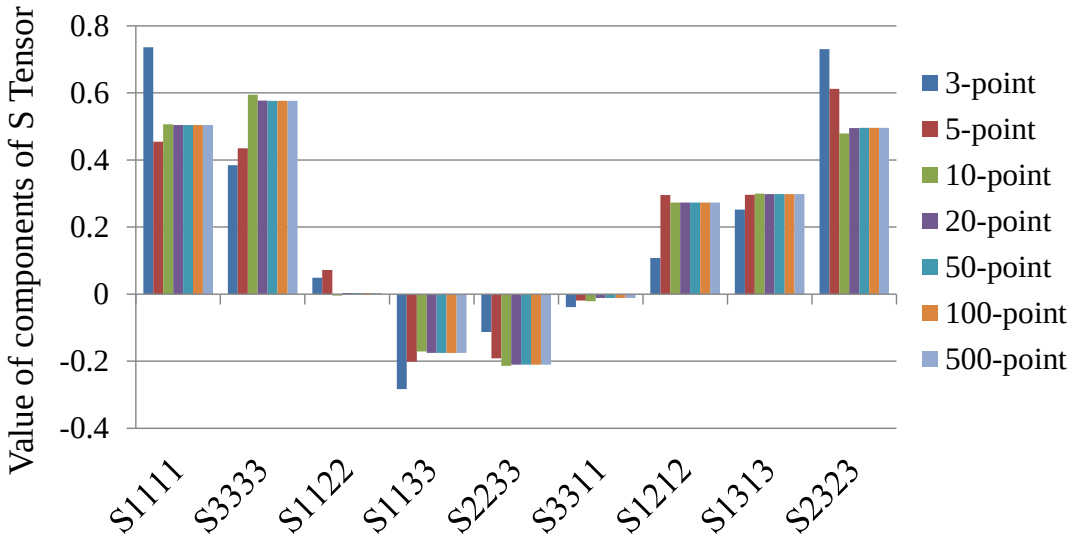

Figure 5.4: Variation of Eshelby tensor components with increase in number of Gauss points in numerical quadrature calculations

Different components of Eshelby tensor for both needle shaped and disk shaped inclusions embedded in isotropic matrix are numerically evaluated and compared against the respective closed form solutions provided by Mura [167]. The numerical results are found to agree well with the analytical results, as illustrated in Tables 5.1 and 5.2.

Table 5.1: Components of Eshelby tensor calculated for needle shaped inclusions embedded in isotropic matrix

	Numerical (code)	**Analytical (Mura book) [32]**
S1111	0.6516	0.6785
S1133	0.2792	0.2143
S3311	0	0
S3322	0	0
S3333	0	0
S1212	0.3484	0.3214

Table 5.2: Components of Eshelby tensor calculated for thin disk shaped inclusions embedded in isotropic matrix

	Numerical (code)	**Analytical (Mura book)**
S3311	0.4286	0.4286
S3322	0.4286	0.4286
S3333	1	1
S2323	0.5	0.5
S1313	0.5	0.5
S1212	0	0

Different components of Eshelby's strain concentration tensor for spherical and ellipsoidal inclusions embedded in an isotropic matrix are numerically evaluated and compared against the closed form solution obtained from Mura [167] and Withers et al. [184]. Once again, the numerically calculated Eshelby tensor is found to agree with the closed form analytical solution for spherical inclusions embedded in transversely isotropic matrix (refer to Figure 5.5). The components of the Eshelby tensor are also calculated for ellipsoidal inclusions with varying aspect ratio embedded in transversely isotropic medium and compared with the analytical solution (Figure 5.6) obtained from Withers et al. [184]. Once again the numerically calculated S tensor components are found to agree well with the closed form analytical solution. Details of the closed form analytical solution for an ellipsoidal inclusion embedded in a transversely isotropic matrix are presented in the Appendix at the end of this Chapter.

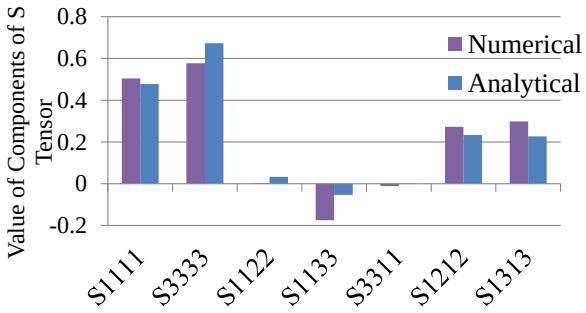

Figure 5.5: Components of Eshelby tensor calculated for spherical inclusions embedded in transversely isotropic matrix

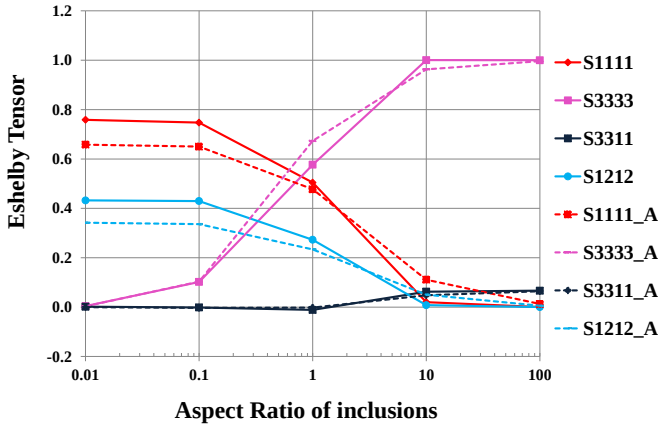

Figure 5.6: Comparison of the components of Eshelby tensor calculated for ellipsoidal inclusions embedded in transversely isotropic matrix (A denotes results obtained using analytical solutions)

After verifying the numerical integration scheme for different spherical and ellipsoidal inclusions embedded in isotropic and transversely isotropic matrices, this method is used to find the Eshelby tensor for spherical Ag_3Sn inclusions embedded in an anisotropic Sn matrix. The Elastic stiffness tensor for pure Sn has been taken from Kammer et al.[185] and the elastic stiffness tensor for Ag_3Sn inclusion is calculated based on the Young's modulus of Ag_3Sn inclusion (99 GPa) from nanoindentation measurements from Chromik et al. [152] and using a Poisson's ratio of 0.35 [59]. The effective composite stiffness tensor for eutectic Sn-Ag phase is now calculated using Equation 12 and the Eshelby tensor components derived for spherical Ag_3Sn inclusion embedded in a pure Sn phase.

$$\overleftrightarrow{L} = \overleftrightarrow{L}_0 + c_1(\overleftrightarrow{L}_1 - \overleftrightarrow{L}_0)[c_0 \overleftrightarrow{S} \overleftrightarrow{L}_0^{-1}(\overleftrightarrow{L}_1 - \overleftrightarrow{L}_0) + \overleftrightarrow{I}]^{-1} \quad (12)$$

Where, $\overleftrightarrow{L}$ = Effective stiffness tensor of the eutectic Sn-Ag phase; $\overleftrightarrow{L}_0$ = stiffness tensor of the Sn matrix; $\overleftrightarrow{L}_1$ = stiffness tensor of the spherical Ag_3Sn inclusion; $\overleftrightarrow{S}$ = Eshelby tensor of the spherical inclusion embedded in anisotropic Sn medium; $\overleftrightarrow{I}$ = identity tensor; c_1 & c_0 = volume fraction of Ag_3Sn inclusion and Sn matrix in composite RVE.

The effective stiffness tensor of the eutectic Sn-Ag matrix is next used to calculate the Eshelby tensor for ellipsoidal Sn inclusions embedded in anisotropic eutectic Sn-Ag matrix. Some of the components of the Eshelby tensor, for ellipsoidal inclusions embedded in anisotropic eutectic Sn-Ag matrix are plotted in Figure 5.7.

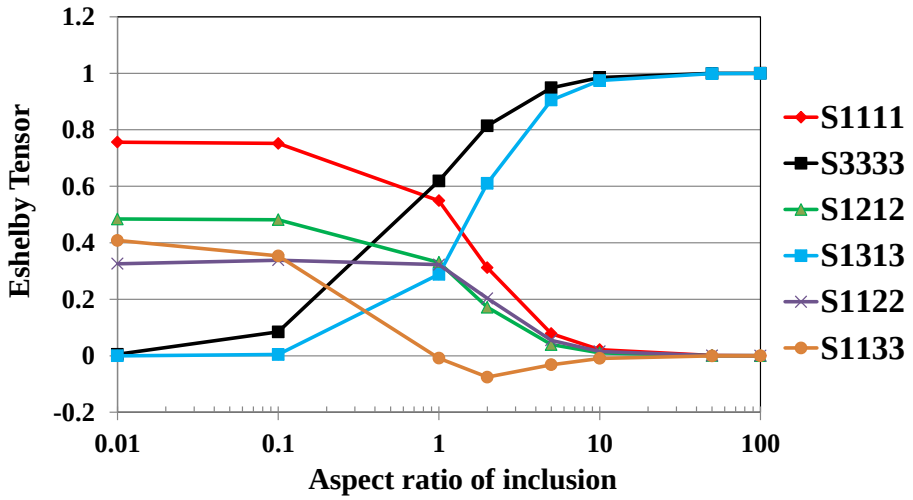

Figure 5.7: Eshelby tensor calculated for ellipsoidal inclusions embedded in fully anisotropic Eutectic Sn-Ag matrix

5.4. Results: Anisotropic transient creep rates of two SAC single crystals

In this Section, the anisotropic transient creep response of one of the two SAC305 single crystals will be utilized to calibrate the model and then the calibrated model will be used to predict the transient creep response of a second SAC305 single crystal specimen. In Subsection 5.4.1; the orientation image maps and corresponding Euler angles for both the SAC single crystals are presented. Co-ordinate transformation tensors to convert the creep strain rates from individual slip system axes to the crystal axes, and the crystal axes to the global specimen axes are also discussed. In Subsection 5.4.2, a recap of the anisotropic creep strain rates predicted along individual slip systems for one of the SAC305 single crystal #1 from Tier 1 calculations is presented for completeness. In Subsection 5.4.3, the anisotropic transient creep strain rate prediction for SAC305 single crystal #1 along principal crystallographic directions ise provided. In Subsection 5.4.4, the anisotropic transient creep rates along the global specimen axes for SAC305 single crystal Specimen #1 are calibrated to experimental data and the anisotropic transient creep rate for SAC305 single crystal Specimen #2 is predicted and compared against the experimental observation. The effect of varying the Euler angle on the transient creep rate of SAC305 single crystal #1 along the global specimen directions is presented next. In Subsection 5.4.5, the effect of volume fraction and aspect ratio of Sn inclusions on the anisotropic

transient creep rates along the global specimen direction in SAC305 single crystal Specimen #1 are discussed and finally the summary and conclusions from this study are provided in Section 5.5.

5.4.1. Orientation image map and Euler angle of two single crystal SAC305 specimens

Inverse pole figure map of SAC305 single crystal Specimen #1 and SAC305 single crystal Specimen #2 are presented in Figures 5.8 and 5.9. The misorientation angles between the sub grains in the single crystal are mostly less than 5°; therefore this SAC305 solder joint is assumed to be a single crystal. The Euler angles of the joint are used to convert the transient mobility (inverse of viscosity) from the slip system coordinate system to the crystal coordinate system, using the fourth order coordinate transformation (refer to Equation 13) and then further to the global specimen coordinate system. The anisotropic transient shear creep rates along the three most facile slip systems are converted to their respective time dependent in-plane shear viscosities by dividing the resolved shear stress along that slip system by the corresponding transient creep rates. Then, the viscosity matrix of the material along different slip systems are converted to in-plane shear mobilities along individual slip systems by taking their inverse. All other components other than in-plane shear mobility (M_{1212}) are zero.

$$\overset{\Leftrightarrow}{M}_{crystal} = \overset{\leftrightarrow}{a}^{T} \overset{\leftrightarrow}{a} \overset{\Leftrightarrow}{M}_{slipsystem} \overset{\leftrightarrow}{a}^{T} \overset{\leftrightarrow}{a} \quad (13)$$

Where, $\overset{\Leftrightarrow}{M}_{slipsystem}$ is fourth order mobility tensor (inverse of viscosity tensor). The fourth order viscosity tensors for both pure Sn phase and eutectic Sn-Ag phase are then combined using Mori-Tanaka homogenization theory (using Equation 1) to obtain the fourth order viscosity tensor for SAC single crystal in the crystal coordinate system using the fourth order Eshelby tensor (calculated in Section 5.3). Then, the fourth order viscosity tensor for SAC single crystal in the crystal coordinate system is further converted to the fourth order viscosity tensor in the global specimen coordinate system using the following coordinate transformation in Equation 14. The in-plane shear component (V_{1212}) of the effective viscosity of SAC single crystal in the global specimen coordinate system is then utilized to calculate the transient creep strain evolution in the specimen coordinate system; which is calibrated to the experimentally observed creep response.

$$\overset{\Leftrightarrow}{V}_{specimen} = \sum_{i=1}^{3} \overset{\leftrightarrow}{g}^{T} \overset{\leftrightarrow}{g} \overset{\leftrightarrow}{\Leftrightarrow} V_{crystal} \overset{\leftrightarrow}{g}^{T} \overset{\leftrightarrow}{g} \quad (14)$$

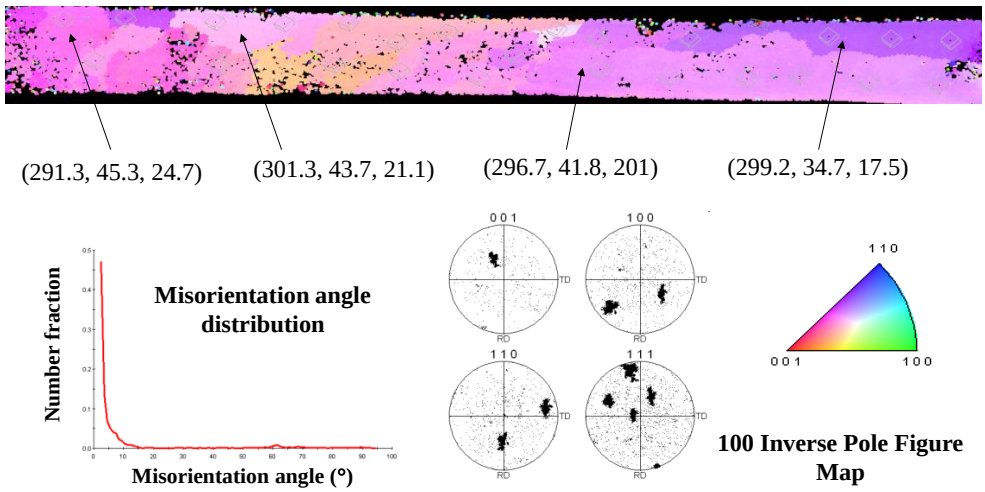

Figure 5.8: Inverse pole figure [100] map for SAC305 single crystal #1. Numbers inside parenthesis at four different locations of the joint refer to the Euler angles (φ_1, ϕ, φ_2), needed to convert the physical quantities from global co-ordinate system to crystal co-ordinate system

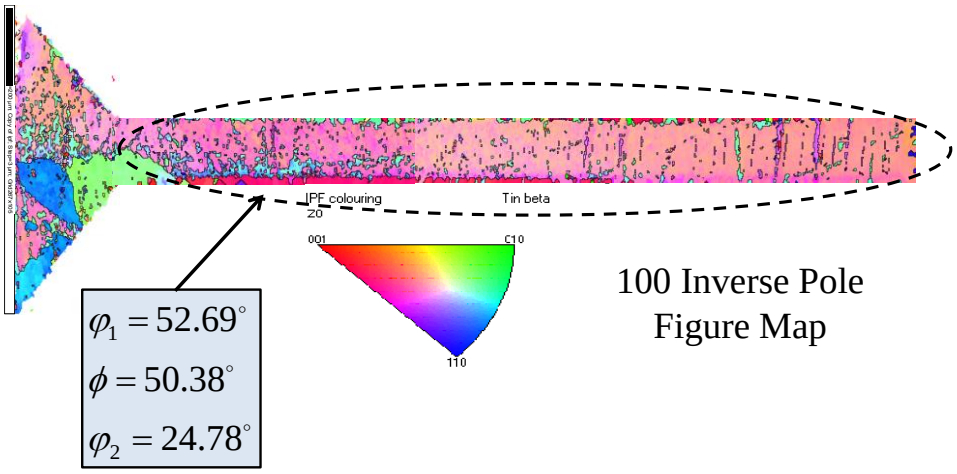

Figure 5.9: Inverse pole figure [100] map for SAC305 single crystal #2. Euler angles (φ_1 = 52.69°, ϕ = 50.38°, φ_2 = 24.78°) are calculated to be used to convert the physical quantities from global co-ordinate system to crystal co-ordinate system

The second order tensor used for converting quantities from sample coordinate system to crystal coordinate system is given by:

$$g_{ij}^{s \to c} = g_{\varphi_2} . g_{\phi} . g_{\varphi_1} \quad (15)$$

$$g_{ij}^{s\to c} = \begin{bmatrix} \cos\varphi_2 & \sin\varphi_2 & 0 \\ -\sin\varphi_2 & \cos\varphi_2 & 0 \\ 0 & 0 & 1 \end{bmatrix} \begin{bmatrix} 1 & 0 & 0 \\ 0 & \cos\phi & \sin\phi \\ 0 & -\sin\phi & \cos\phi \end{bmatrix} \begin{bmatrix} \cos\varphi_1 & \sin\varphi_1 & 0 \\ -\sin\varphi_1 & \cos\varphi_1 & 0 \\ 0 & 0 & 1 \end{bmatrix} \quad (16)$$

$$g_{ij}^{s\to c} = \begin{bmatrix} \cos\varphi_1\cos\varphi_2 - \sin\varphi_1\cos\phi\sin\varphi_2 & \sin\varphi_1\cos\varphi_2 + \cos\varphi_1\cos\phi\sin\varphi_2 & \sin\phi\sin\varphi_2 \\ -\cos\varphi_1\sin\varphi_2 - \sin\varphi_1\cos\phi\cos\varphi_2 & -\sin\varphi_1\sin\varphi_2 + \cos\varphi_1\cos\phi\cos\varphi_2 & \sin\phi\cos\varphi_2 \\ \sin\varphi_1\sin\phi & -\cos\varphi_1\sin\phi & \cos\phi \end{bmatrix} (17)$$

The second order tensor used for converting quantities from the crystal co-ordinate system to the slip system co-ordinate system is given by $\overleftrightarrow{a}$, where $\overleftrightarrow{a}$ is the second order co-ordinate transformation tensor comprising of direction cosines between the crystal axes ([h k l], [u v w] and [c_1 c_2 c_3] (=[h k l]×[u v w]) (cross product of loading plane normal and loading direction)) and individual slip system axes ([n_1 n_2 n_3], [b_1 b_2 b_3] and [t_1 t_2 t_3] (=[n_1 n_2 n_3]× [b_1 b_2 b_3]) (cross product of slip plane normal and slip direction)) (refer to Figure 5.10).

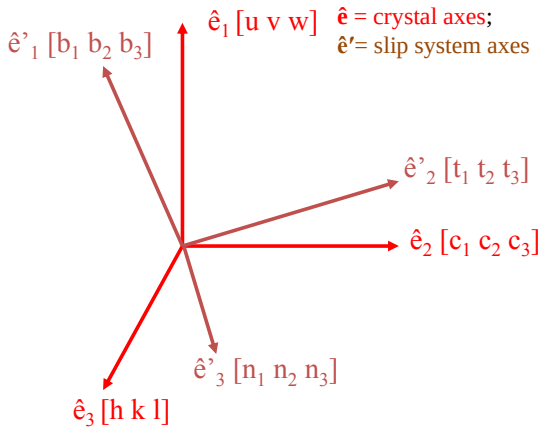

Figure 5.10: Co-ordinate transformation between crystal and slip system co-ordinate axes

The second order tensor $\overleftrightarrow{a}$ is given by:

$$a_{ij} = \begin{pmatrix} \cos\theta_{11} & \cos\theta_{12} & \cos\theta_{13} \\ \cos\theta_{21} & \cos\theta_{22} & \cos\theta_{23} \\ \cos\theta_{31} & \cos\theta_{32} & \cos\theta_{33} \end{pmatrix} \quad (18)$$

where,

$$\cos\theta_{11} = \frac{b_1 * u + b_2 * v + b_3 * w}{\sqrt{(b_1^2 + b_2^2 + b_3^2)}\sqrt{(u^2 + v^2 + w^2)}}$$

$$\cos\theta_{12} = \frac{b_1 * c_1 + b_2 * c_2 + b_3 * c_3}{\sqrt{(b_1^2 + b_2^2 + b_3^2)}\sqrt{(c_1^2 + c_2^2 + c_3^2)}}$$

$$\cos\theta_{13} = \frac{b_1 * h + b_2 * k + b_3 * l}{\sqrt{(b_1^2 + b_2^2 + b_3^2)}\sqrt{(h^2 + k^2 + l^2)}}$$

$$\cos\theta_{21} = \frac{t_1 * u + t_2 * v + t_3 * w}{\sqrt{(t_1^2 + t_2^2 + t_3^2)}\sqrt{(u^2 + v^2 + w^2)}}$$

$$\cos\theta_{22} = \frac{t_1 * c_1 + t_2 * c_2 + t_3 * c_3}{\sqrt{(t_1^2 + t_2^2 + t_3^2)}\sqrt{(c_1^2 + c_2^2 + c_3^2)}}$$

$$\cos\theta_{23} = \frac{t_1 * h + t_2 * k + t_3 * l}{\sqrt{(t_1^2 + t_2^2 + t_3^2)}\sqrt{(h^2 + k^2 + l^2)}}$$

$$\cos\theta_{31} = \frac{n_1 * u + n_2 * v + n_3 * w}{\sqrt{(n_1^2 + n_2^2 + n_3^2)}\sqrt{(u^2 + v^2 + w^2)}}$$

$$\cos\theta_{32} = \frac{n_1 * c_1 + n_2 * c_2 + n_3 * c_3}{\sqrt{(n_1^2 + n_2^2 + n_3^2)}\sqrt{(c_1^2 + c_2^2 + c_3^2)}}$$

$$\cos\theta_{33} = \frac{n_1 * h + n_2 * k + n_3 * l}{\sqrt{(n_1^2 + n_2^2 + n_3^2)}\sqrt{(h^2 + k^2 + l^2)}} \quad (19)$$

5.4.2. Anisotropic transient creep strain of Eutectic Sn-Ag phase and Sn phase along individual slip systems (Tier 1 results) for SAC single crystal Specimen #1

The anisotropic transient creep shear strain along the dominant slip systems for the eutectic Sn-Ag phase and the pure Sn phase is modeled in Part I of this two-part paper and the anisotropic creep strain of the eutectic Sn-Ag phase and Sn phase for individual slip systems are replotted in Figure 5.11 and 5.12 for completeness of this manuscript.

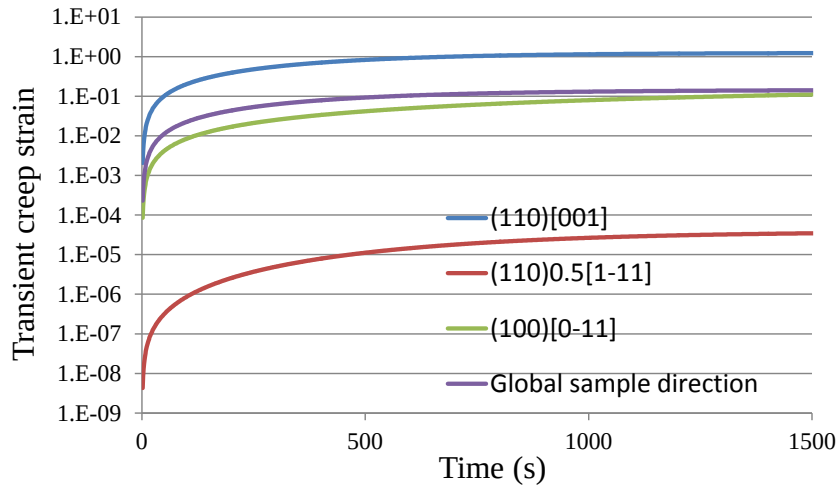

Figure 5.11: Anisotropic transient creep rates in Sn phase in SAC305 single crystal Specimen #1 at shear stress level of 10 MPa at RT

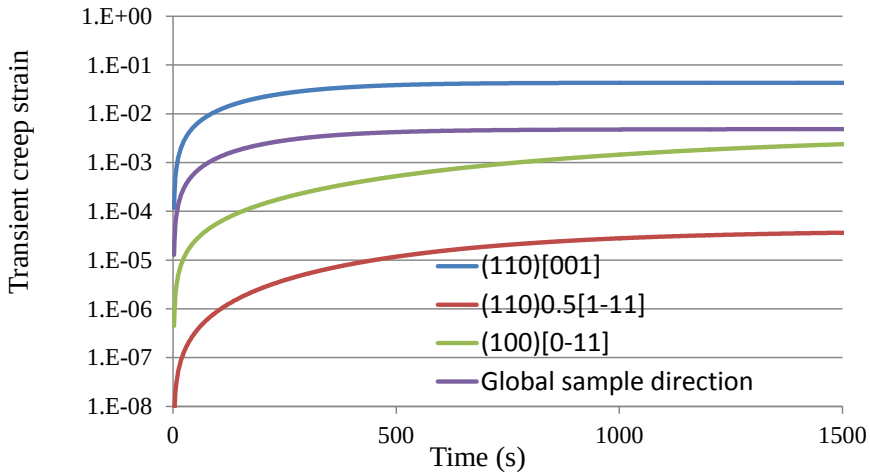

Figure 5.12: Anisotropic transient creep rates in a unit cell of eutectic Sn-Ag phase in SAC305 single crystal Specimen #1 at shear stress level of 10 MPa at RT

5.4.3. Anisotropic transient shear creep strain of SAC305 single crystal Specimen #1 in crystal co-ordinate system

The anisotropic transient shear creep rates along three most facile slip systems are converted to their respective time dependent in-plane shear viscosities by dividing the resolved shear stress along that slip system by the corresponding transient creep rates. Then, in-plane shear mobilities along individual slip system are obtained by inverting the viscosity tensors along those slip systems. All other

components other than in-plane shear mobility (M_{1212}) are zero. The mobilities of the eutectic Sn-Ag phase and the pure Sn phase are calculated along the crystal co-ordinate system for individual slip systems using Equation 13 and 18. Then the effective viscosity of SAC305 single crystal Specimen #1 is calculated using Equation 1 and the fourth order viscosity tensors of the eutectic Sn-Ag phase and the pure Sn phase in the crystal coordinate system. The transient creep strain along the [001] direction of SAC305 single crystal Specimen #1 is predicted to be (1-2) orders of magnitude higher than that along the [100]/[010] direction (refer to Figure 5.13).

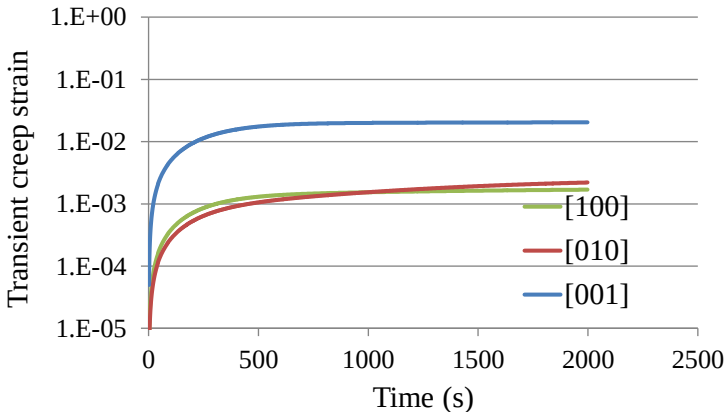

Figure 5.13: Anisotropic transient creep strain of SAC305 single crystal specimen #1 along principal crystallographic directions in crystal coordinate system at shear stress level of 10 MPa at RT

5.4.4. Anisotropic transient creep response of two SAC305 single crystal specimens along global sample loading direction

The anisotropic transient creep viscosity along the crystal co-ordinate system for SAC305 single crystal specimen #1 is further converted to the global sample axes by conducting the fourth order co-ordinate transformation using Equation 14 and then the sum of the in-plane shear viscosity along individual slip systems was calculated and calibrated with the experimentally observed transient creep strain of SAC305 single crystal Specimen #1 (refer to Figure 5.14).

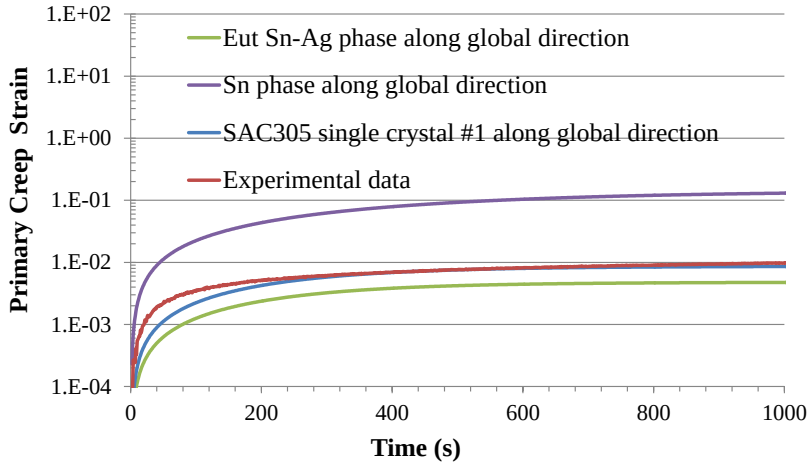

Figure 5.14: Predicted transient creep shear strain along global specimen coordinate system vs. experimentally observed creep shear strain of SAC305 single crystal #1

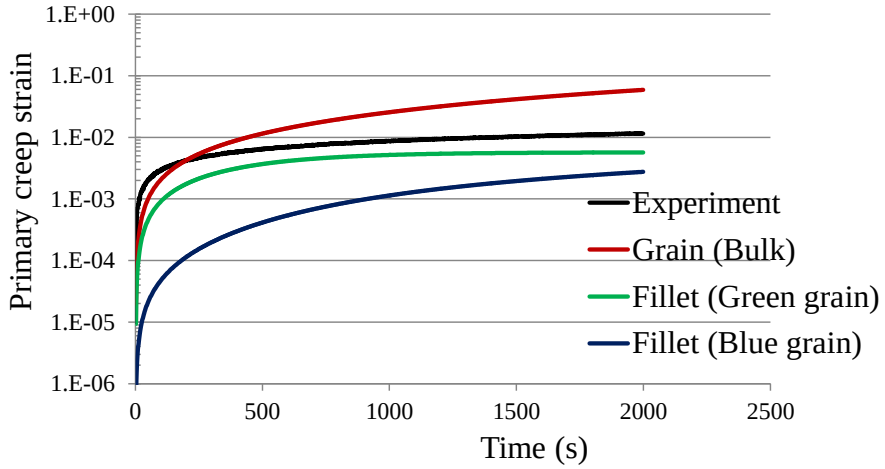

Figure 5.15: Predicted transient creep shear strain along global specimen coordinate system vs. experimentally observed creep shear strain of SAC305 single crystal #2 (predominantly single crystal in bulk)

The above calibrated multiscale model is then used to predict the transient creep response in another SAC305 single crystal #2 specimen (predominantly single crystal in the bulk – refer Figure 9 for OIM map). The transient creep strain in the bulk of the specimen is predicted to be higher than the experimentally observed creep strain. However, the transient creep strain predicted in the grain (Green and Blue) present in the fillet is smaller than that observed in the experiment (refer to Figure 5.15). Therefore, the two grains in the fillet are definitely reducing the effective creep strain along global specimen direction. Therefore, depending on the orientation of the grains in the fillet with respect to

the loading direction, the creep strain along the global direction can be increased or decreased. More importantly, the effect of grain boundary sliding between the adjacent grains also need to be considered before drawing any conclusion about the interactions between the grains. The above calibrated model is then used to study the effect of varying orientation (one of the Euler angles) on the predicted transient creep response along the global specimen direction in SAC305 single crystal Specimen #1. The predicted shear creep strain along the global specimen direction is found to vary by a factor of 1-3 orders of magnitude due to change in one of the Euler angles (φ_1) in SAC305 single crystal Specimen #1 (refer to Figure 5.16). The other two Euler angles (Φ and φ_2) are kept constant during the analysis. Variability of (1-3) orders of magnitude in the transient creep strain response has been previously reported in the literature [140] in solder specimens tested under similar loading condition at the same temperature. Therefore, the above model can be used to predict the transient creep response for any single crystal specimen with random orientation and the constitutive properties of the individual crystal can be further used to model the whole solder joint containing more than one grain, by modeling the grain boundary sliding.

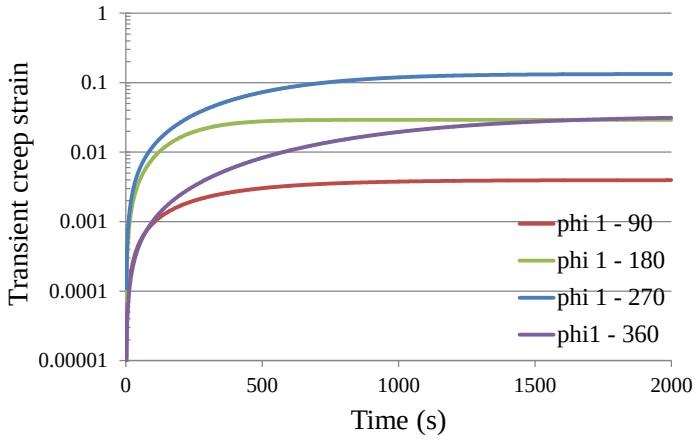

Figure 5.16: Effect of varying Euler angle (φ_1) on predicted transient creep strain along global specimen loading direction in SAC305 single crystal #1 at shear stress level of 10 MPa at RT

5.4.5. Effect of volume fraction and aspect ratio of Sn inclusions on transient creep rates of SAC305 single crystal #1 along global sample direction

Using the above calibrated model, the effect of volume fraction and aspect ratio of Sn inclusions on the transient creep response of SAC305 single crystal Specimen #1 is studied and the material is predicted to creep more (refer to Figure 5.17) with increase in volume fraction of Sn inclusion in the single crystal specimen from 35% to 75%. SAC single crystal is also predicted to creep more as the Sn inclusions shapes are changed from spherical to ellipsoidal. Out of the three aspect ratios studied here, disk shaped Sn inclusions contribute to higher creep strain compared to that of needle shaped and spherical shaped inclusions (refer to Figure 5.18).

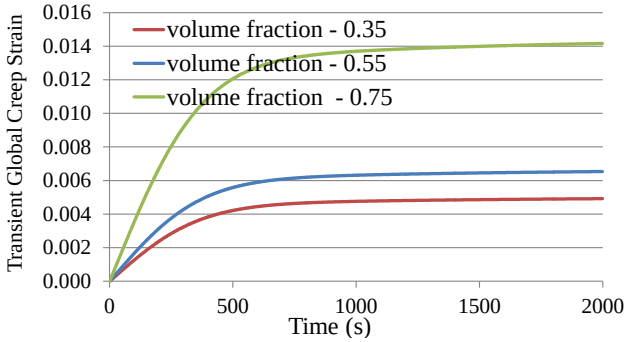

Figure 5.17: Effect of volume fraction of Sn inclusions on predicted transient creep response along global specimen loading direction in SAC305 single crystal Specimen #1 at shear stress level of 10 MPa at RT

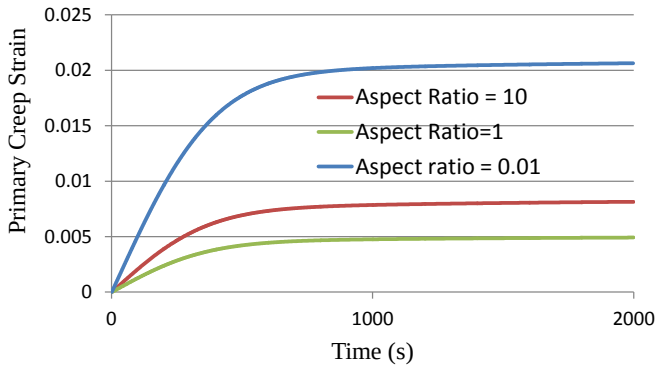

Figure 5.18: Effect of aspect ratio of Sn inclusions on predicted transient creep response along global specimen loading direction in SAC305 single crystal Specimen #1 at shear stress level of 10 MPa at RT

5.5. Summary and Conclusions

A multiscale mechanistic modeling approach was proposed in Part I of this two part paper, where the anisotropic transient creep rates of eutectic Sn-Ag phase (Tier 1) and pure Sn phase were modeled along dominant slip systems of single-crystal SAC solder. The anisotropic creep response of the eutectic phase (from Tier 1) is combined in this paper with the anisotropic creep response of Sn lobes at Tier 2 using the anisotropic Mori-Tanaka homogenization theory, to obtain the anisotropic transient creep response of SAC single crystal specimens along the principal crystallographic directions. The Eshelby strain concentration tensors required for this homogenization process are numerically evaluated for ellipsoidal Sn inclusions and cylindrical Cu_6Sn_5 inclusions embedded in an anisotropic eutectic Sn-Ag matrix. The above multiscale model is validated using experimentally observed transient creep response of one of the SAC305 single crystal specimens. The orientations of above two SAC single crystal specimens with respect to loading direction were identified with orientation image mapping and then utilized in the model to estimate resolved shear stress along dominant slip directions. Transient creep strain rates along the [001] direction of SAC305 single crystal Specimen #1 are predicted to be 1-2 orders of magnitude higher than those along the [100]/[010] direction. The proposed multiscale model is able to quantitatively capture the transient creep response of the second SAC305 single crystal Specimen #2 reasonably well. The predicted shear creep strain along the global specimen direction is found to vary by a factor of (1-3) orders of magnitude due to change in one of the Euler angles (φ_1) in SAC305 single crystal Specimen #1, which is in agreement with experimental observations. Parametric studies have also been conducted to predict the effect of changing volume fraction and aspect ratio of Sn inclusions on the anisotropic transient creep response of SAC single crystal #1. The model is able to capture the decrease in creep resistance of SAC305 single crystal, when the volume fraction of Sn inclusion in the SAC single crystal increases. Therefore, the above model can be used to predict transient creep response for any single crystal specimen with any random orientation. The constitutive properties of the individual crystal can be further used in future studies to model the whole solder joint containing more than one grain by modeling the grain boundary sliding.

Chapter 6 : Mechanistic Modeling of the Anisotropic Steady State Viscoplastic Response of SAC305 Single Crystal

Abstract

A multiscale modeling framework is proposed in this study to capture the influence of the inherent elastic anisotropy of single crystal Sn and the inherent heterogeneous microstructure of a single crystal SnAgCu (SAC) solder grain on the secondary creep response of the grain. The modeling framework treats the SAC microstructure as having several distinct length scales. The smallest length scale (Tier 0) consists of the Sn BCT lattice. The eutectic Sn-Ag micro-constituent, consisting of nanoscale Ag_3Sn IMC particles embedded in the single crystal BCT Sn matrix, is termed Tier 1. The single-crystal SAC microstructure, consisting of Sn dendrites and surrounding eutectic Sn-Ag phase, is termed Tier 2. Dislocation mechanics analysis is used to describe the dispersion strengthening in Tier 1 and homogenization theory is used at Tier 2 to describe the load sharing between the Sn dendrites and the surrounding eutectic Sn-Ag phase. At the Tier 1 level, the dispersion strengthening and creep resistance is a result of dislocation impediment by the nanoscale Ag_3Sn particles. At Tier 0, the line tension and mobility of dislocations in dominant slip systems of single crystal Sn is captured using elastic crystal anisotropy of body centered tetragonal (BCT) Sn and Stroh's matrix formalism. Dislocation recovery mechanisms, such as Orowan climb and detachment from nanoscale Ag_3Sn particles, are proposed to be the rate controlling mechanisms for creep deformation in the eutectic Sn-Ag phase (Tier 1) of a SAC single crystal. The anisotropic secondary creep rate of eutectic Sn-Ag phase (Tier 1), is then modeled using the above inputs and the saturated dislocation density calculated for dominant glide systems during secondary stage of creep. Saturated dislocation density is estimated as the equilibrium saturation between three competing processes: (1) dislocation generation; (2) dislocation impediment caused by back stress from pinning of dislocations at IMCs; and (3) dislocation recovery due to climb/detachment from IMCs. Secondary creep strain rate of eutectic Sn-Ag phase in three most facile slip systems is calculated and compared against the isotropic prediction. At low stress level secondary steady state creep rate along (110)[001] system is predicted to be ten times the creep

rate along (100)[0-11] system. However, at high stress level, secondary steady state creep rate along (110)[001] system is predicted to be ten thousand times the creep rate along (100)[0-11] system. The above predictions are in strong agreement with (1-4) orders of magnitude of anisotropy observed in steady state secondary creep response in SAC305 solder joints tested under identical loading conditions in experiments conducted by several authors. The above model is then combined with Eigen-strain methods and average matrix stress concepts to homogenize the load sharing between the Sn dendrites and the surrounding eutectic Ag-Sn matrix. The resulting steady state creep rates are predicted for a few discrete (single crystal and bi-crystal) SAC305 specimens. Very good agreement was observed between the predicted steady state creep rate and the measured creep rates for two SAC305 single crystal specimens. For the bi-crystal specimens, the predicted steady state creep rates for the individual crystals in the joint were found to bound the experimentally measured values. The predicted steady state creep rates for SAC3305 single crystal #1 specimen is found to vary by almost one order of magnitude due to systematic variation of the grain orientation of the Sn dendrites with respect to the loading direction. The original draft of this chapter is a journal paper and will be submitted to Material Science and Engineering: A and part of the paper has been accepted at USNCTAM, 2014 (United States National Congress on Theoretical and Applied Mechanics) at East Lansing, MI.

Keywords: Creep, anisotropy, dislocation density, BCT Sn, SAC solder, dislocation detachment, Orowan looping

6.1. Introduction

Lead-free solder interconnects have been prevalent in electrical and electronic equipment since 2006, with some exceptions. Many Sn based Pb-free solder alloys have been proposed as a replacement for the eutectic Sn37Pb, e.g. Sn2.5Ag, Sn-Bi, Sn-Zn, Sn-Zn-Bi, Sn-Ag-Bi, and Sn0.5Cu. Recently, industry has focused its interest on a hypoeutectic Sn-Ag-Cu alloy (SAC) because of its comparatively low melting temperature, competitive price, and good mechanical properties [186]–[189]. Research on the microstructure of SAC solder [190], [191], its evolution [192], [193], and mechanical properties [194]–[200] has been extensively conducted, but most of the studies don't provide any insights into a

detailed understanding of the heterogeneous behavior of this anisotropic material, since most of the studies consider the solder joint to be isotropic. Some modelling work has also been performed, usually considering the material as a single phase, isotropic homogeneous continuum [201], [202]. Erinc et al. [203] simulated fatigue damage in a SAC solder joint taking into account grain boundaries using cohesive zones. It has been reported in the literature that the anisotropic character of the β-Sn crystal structure (BCT) can lead to stress concentrations at Sn grain boundaries during thermal cycling [204], [205]. Furthermore, localized deformation has been shown to occur at the grain boundaries of Sn-rich solders upon thermal loading [206]. Thermal fatigue in Sn-rich alloys has also been reported to be influenced by the anisotropic crystallinity of the microstructure [207]. Recently, experimental evidence has been presented that these stress concentrations can actually lead to damage, purely due to the influence of thermal cycling without any external mechanical constraints [204]. Chen and Li [208] showed, using an anisotropic elastic finite element model of a multicrystal system, that stress concentrations arise at certain grain boundaries and triple junctions. Matin et al. [204] showed in a comparison between experimentally obtained data and a simulation for a thermally cycled SAC specimen, using an elastic analysis including anisotropic elastic and thermal expansion properties, that the locations of predicted stress concentrations correlated reasonably with damaged areas found in the experimental observations. In another recent study by Zamiri et al. [43], crystal plasticity analysis was used to evaluate stress and strain resulting from a 165°C temperature change in a single-crystal joint using two simplified geometries for solder joints. Phenomenological flow models for ten slip systems were estimated based upon semi quantitative information available in the literature, along with known anisotropic elastic property information. The results showed that the internal energy of the system is a strong function of the tin crystal orientation and geometry of the solder joint. The internal energy (and presumably the likelihood of damage) is highest when the crystal c-axis lies in the plane of the substrate, leading to significant plastic deformation. When the crystal a-axis lies in the plane of the substrate, deformation due to a 165°C temperature change is predominantly elastic.

Although few authors have taken the elastic anisotropy of Sn into their modeling, none of the finite element modeling efforts for reliability assessment of Pb-free interconnects have taken into account the viscoplastic anisotropy of grains and the coarse grained nature of the interconnects. The linear

coefficient of thermal expansion (CTE) of body-centered tetragonal β-tin is reported to be 30.5 ppm/°C along the [001] axis (c-axis) and 15.5 ppm/°C along the [100] and [010] (a- and b-axes) at room temperature [209]. Similarly, the Young's modulus is reported to be 69 GPa along the c-axis and 23 GPa along the a- and b-axes[209]. The large intrinsic anisotropy calls for a microstructure-based modeling of the viscoplastic response of SAC single crystal. Several studies have demonstrated that the failure of a SAC solder interconnect is governed not only by its location in terms of the distance from the neutral point (DNP) of an assembly but also by the orientation and number of grains [209] in the interconnect. In thermal cycling (TC) experiments, the fatigue cracks have been observed propagating along the Sn grain boundaries, near solder-pad interfaces, and also along the Sn/primary intermetallic interfaces. Numerous research studies are going on to understand the microstructure, fatigue, and creep and to develop proper constitutive models for these solder materials. However, most of those studies treat SAC solder as a homogeneous, isotropic material, and fail to predict the huge scatter observed in the constitutive response of these materials under identical fabrications protocols and loading conditions, due to the underlying anisotropy and heterogeneity of the grain structure [210]. Creep measurements conducted on microscale SAC305 solder specimens in a study conducted by Cuddalorepatta et al. [210] also show significant piece-to-piece variability in the creep behavior of specimens tested under identical loading conditions (refer to dotted circle in Figure 6.1 (b)). Microstructural analysis of these microscale SAC305 solder specimens reveals [210] that in spite of using consistent fabrication protocols, these specimens exhibit a non-repeatable coarse-grained Sn microstructure, similar to that seen in SAC joints in functional microelectronics.

In order to understand the effect of anisotropy of Sn and grain orientation on the variability of creep response of these SAC solder interconnects, a multiscale modeling approach is proposed where the microstructure can be classified into five distinct length scales, as shown in Figure 6.2. The electronic subsystem of the circuit board (Tier 5) is the highest level of scale relevant to interconnects. Tier 4 represents the structure that governs the complex evolving boundary conditions imposed on the actual physical geometry of the solder joint including the interfacial metallization that creates the intermetallic bond between the solder and the component. In our study, the Tier 4 structure is a

modified Iosipescu shear specimen. The next lower length scale (Tier 3) is the grain scale microstructure, typically consisting of an anisotropic single crystal or a few Sn grains and grain

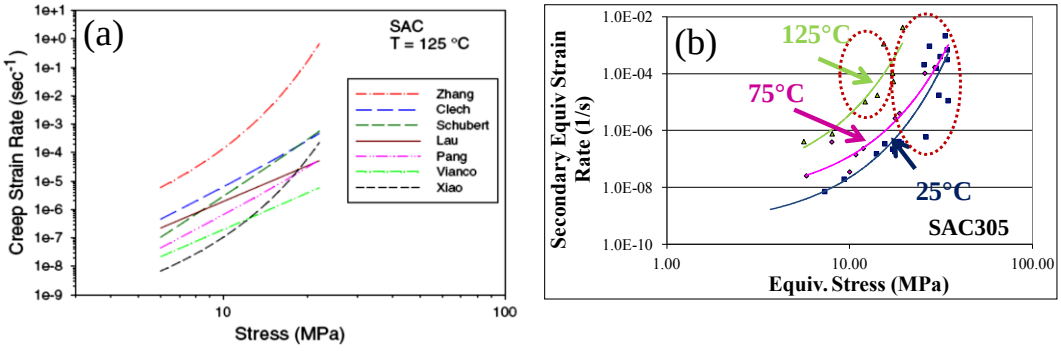

Figure 6.1: (a) (1-5) orders of magnitude variability in reported steady state creep rates [211] (b) (1-4) orders of magnitude of variability observed in steady state secondary creep response observed in SAC305 solder joints tested under identical loading conditions [210]

boundaries. At this length scale, crystal plasticity finite element models in conjunction with grain boundary models are effective. The next lower length scale (Tier 2) focuses on the structure within individual grains and is comprised of multiple tin dendrites arising from solidification. The dendrites are surrounded by an eutectic Sn-Ag micro-constituent that is the last to solidify. Embedded throughout this grain are additional micron scale intermetallic Cu_6Sn_5 precipitates. All of these features participate in load sharing, thus providing reinforcement strengthening. At this scale, effective modeling methods can be obtained from anisotropic homogenization theories popular in composite model. Tier 1 describes the structure of the eutectic Sn-Ag micro-constituent consisting of a locally homogeneous distribution of nanoscale Ag_3Sn intermetallic particles embedded in a mono-crystalline tin matrix. Here, anisotropic models of dislocation interactions with particles that depend on spacing/size are appropriate for describing the dispersion strengthening. Tier 0 refers to dislocation slip systems needed for modeling in Tier 1. Predicted creep rates along dominant slip systems of single crystal eutectic Sn-Ag phase in Tier 1 length scale will be used in conjunction with those for pure Sn dendrites to predict the anisotropic creep response of SAC single crystal using anisotropic micromechanics homogenization techniques.

A mechanistic multiscale modeling framework has been earlier proposed by Cuddalorepatta et al. [212], which can capture the physics of creep deformation at Tier 1 & 2 length scales. At the Tier 1

length scale, nanoscale Ag_3Sn particles in the eutectic region provide dispersion strengthening by interacting with nanoscale Ag_3Sn particles. The

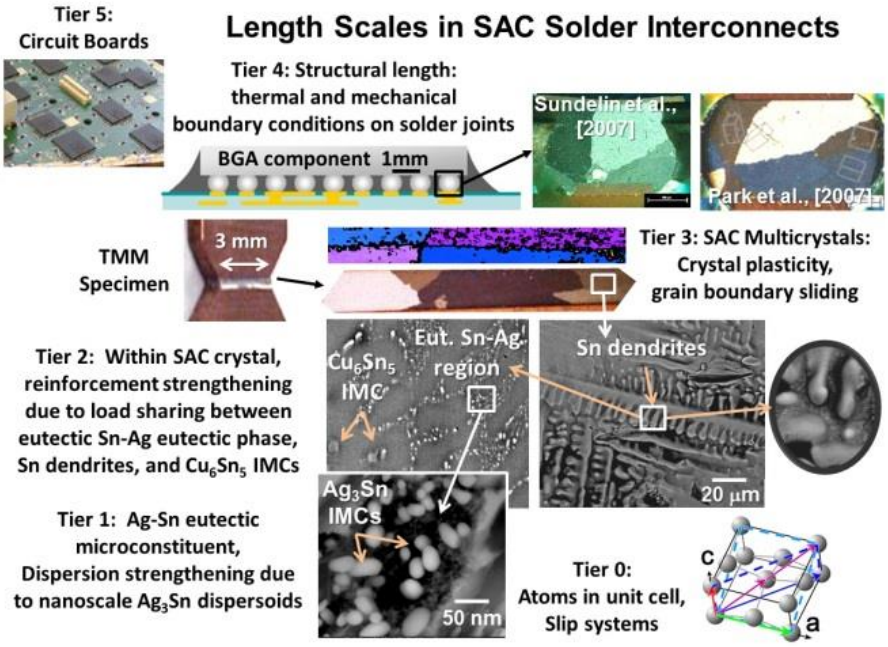

Figure 6.2: Multiple length scales (Tiers 0-5) in SnAgCu solder alloys

rate limiting process for dislocation motion is considered to be dislocation detachment mechanism based on the works of Rösler and Arzt [61], and implemented for a constant uniform dislocation density. However, the model in its current form is only valid for isotropic materials.

The current study improves on this model to capture the anisotropic steady state viscoplastic behavior observed in SAC solder alloys. To capture the effect of anisotropy present in BCT Sn structure, individual slip systems present in Sn are considered in this study. Line tension and viscous drag-coefficients (inverse of mobility) of dislocations in dominant slip systems of single crystal Sn is captured using fundamental elastic crystal anisotropy calculations. The anisotropic secondary creep response of the eutectic Sn-Ag phase, one of the primary phases in SAC systems, is then modeled using above inputs and saturated steady state dislocation density is calculated for dominant glide systems during secondary stage of creep. Dislocation density used in the isotropic model reported in [212] was based on a hypothetical assumption that all slip planes in BCT Sn are completely saturated with dislocations during the secondary stage of creep and a very high value of dislocation density (10^{21} m^{-2}) was assumed. However, this number has no physical basis and in the present study a new method

has been proposed where saturated dislocation density is estimated as the equilibrium saturation between three competing processes: (1) dislocation generation; (2) dislocation impediment caused by back stress from forest dislocations and from pinning of dislocations at IMCs; and (3) dislocation recovery due to climb/detachment from IMCs and forest dislocations.

One of the key parameters of the dislocation detachment model, relaxation parameter (k) [61], [62] used to capture the strong attractive interaction between dislocation and nanoscale particle during the post-climb phase, has been previously modeled as a function of stress and temperature. However, in this study, the relaxation parameter is treated as a fundamental property of the material, and has been mechanistically derived in this study by taking into account the detachment configuration of a dislocation over the particle, instead of using an empirically calibrated value. The magnitude of k governs how strongly the detachment mechanism contributes to the overall creep rate. Therefore, the primary objective of this paper is to predict the anisotropic secondary creep strain rates of eutectic Sn-Ag phase for the three most facile slip systems and compare against the isotropic prediction. The creep response of the eutectic phase (from Tier 1) is then combined with the creep of Sn lobes at Tier 2, using anisotropic Mori-Tanaka homogenization theory, to obtain the homogenized creep response of SAC305 single crystal. Furthermore, the multiscale model is validated using experimentally observed secondary creep response of two dissimilarly oriented SAC305 single crystal specimens. The orientations of above two SAC single crystal specimens with respect to loading direction are identified with orientation image mapping and then utilized in the model to estimate resolved shear stress along dominant slip directions. Multiple parametric studies are conducted to understand the effect of orientation and aspect ratio of Sn inclusions on the steady state creep response of one of the SAC305 single crystal specimen. Modeling approach for Tier 0 length scale is described in next Section 6.2; modeling approach for Tier 1 length scale is described in Section 6.3; modeling approach for Tier 2 length scale is described in Section 6.4; results and discussions will be provided in Section 6.5; and finally the chapter will conclude with summary and conclusions in Section 6.6.

6.2. Modeling Approach for Tier 0 length scale

The proposed modeling framework relies on the estimation of several fundamental parameters of BCT Sn lattice to capture the anisotropic creep behavior exhibited by SAC single crystal alloy. This section will discuss the approach and calculation of these parameters (line tension factor in Subsection 6.2.1; mobility in Subsection 6.2.2; and dislocation density in Subsection 6.2.3), which will be used as inputs to the above model to calculate the anisotropic creep strain rate of eutectic Sn-Ag phase and Sn phase at Tier 1 length scale in Section 6.3.

6.2.1. Calculation of line tension factor (K) for a dislocation in anisotropic single crystal BCT Sn

The matrix of stiffness constants of the 4/mmm class of the tetragonal system to which β tin belongs is:

$$C_{ij} = \begin{pmatrix} C_{11} & C_{12} & C_{13} & 0 & 0 & 0 \\ C_{12} & C_{11} & C_{13} & 0 & 0 & 0 \\ C_{13} & C_{13} & C_{33} & 0 & 0 & 0 \\ 0 & 0 & 0 & C_{44} & 0 & 0 \\ 0 & 0 & 0 & 0 & C_{44} & 0 \\ 0 & 0 & 0 & 0 & 0 & C_{66} \end{pmatrix}$$

Table 6.1: Dominant Sn slip systems observed in Sn **[156]**

SLIP SYSTEMS	SLIP SYSTEMS		RANK
	PLANE	DIR	
1	{100}	[001]	7
2	{110}	[001]	1
3	{100}	[010]	8
4	{110}	1/2[1-11]	2
5	{110}	[1-10]	4
6	{100}	[0-11]	3
7	{001}	[010]	6
8	{001}	[110]	10
9	{011}	[0-11]	5
10	{211}	[0-11]	9

To understand the slip behavior of Sn in SAC solder joints, the relative operation of different slip systems was analyzed in 196 joints with different orientations by Bieler et al. [141] and correlated with the c-axis orientation. Using the results from Bieler et al. [156], [157] the active slip systems in SAC solder considered here for this study are shown in Table 6.1. The elastic field of a straight edge

dislocation line in an anisotropic crystal was treated theoretically first by Eshelby et al. [158]. For anisotropic elasticity, the determination of the line tension factor (K) requires numerical approaches, and can be evaluated by using either sextic formalism proposed by Eshelby et al. [158] or integral formalism proposed by Barnett et al. [159]. Eshelby's sextic formalism method was modified by Stroh [160] and expressed with a matrix formalism, a form amenable to numerical computation.

6.2.2. Calculation of mobility of dislocation in pure BCT Sn (without any Ag_3Sn Particles)

In order to capture the evolution of dislocation density in dominant slip systems of single crystal Sn, which will be discussed next in Section 6.2.3, the velocity of a single edge dislocation in anisotropic Sn should be first calculated from fundamental principles. Velocity (v_0) of a single dislocation in an anisotropic medium (assuming there is no particle or forest dislocation or grain boundaries to exert any back stress on it or impede its motion) is given by [161]:

$$v_0{}^i = \frac{\tau^r{}_i b_i}{B_i} \qquad (1)$$

where, subscript "i" refers to the i^{th} slip system; τ^r_i is applied resolved shear stress along the i^{th} slip system; b_i is the Burger's vector along the i^{th} slip system; B_i is the viscous drag co-efficient along the i^{th} slip system. Viscous drag co-efficient (B_i) of an edge dislocation is given by [162]:

$$B_i = \frac{\eta b_i}{C_i^t} \qquad (2)$$

where, c_i^t is the transverse sound wave velocity in the i^{th} slip systems in Sn medium; and $c_i^t = (G_i/\tilde{\rho})^{0.5}$; where G_i is the shear modulus along the i^{th} slip direction of Sn and $\tilde{\rho}$ is the mass density of Sn, η is the thermal energy density of Sn. Thermal energy density of Sn can be calculated using Equation 3:

$$\eta = \tilde{\rho} * C_p * (T - T_D) \qquad (3)$$

Where, C_p is the specific heat capacity; T_D is the Debye temperature (200 K) of Sn; T is the test temperature in Kelvin.

6.2.3. Modeling saturated dislocation density in dominant slip systems of SAC solder

Steady state dislocation density (ρ_i^{sat}) is computed by modeling three competing processes: (1) dislocation generation; (2) dislocation impediment caused pinning of dislocations at IMCs; and (3) dislocation recovery due to detachment from IMCs in eutectic Ag_3Sn phase; and three competing processes: (1) dislocation generation; (2) dislocation impediment by forest dislocations in pure Sn matrix phase; and (3) dislocation recovery due to climb over forest dislocation and mass diffusion transport through Sn lattice. Cross slip mechanism has not been modeled due to lack of knowledge about cross-slip activation energy in BCT Sn. Molecular dynamics simulations need to be carried out in future to estimate the activation energy for cross-slip and incorporate that into the above dislocation models.

For the Ag_3Sn IMC phase, the steady state dislocation density (ρ_i) in the i^{th} slip system is modeled by:

$$\dot{\rho}_i(t) = v_0^i k_i \rho_i^{sat} (\tau_i^r - \frac{\zeta G_i b_i n_i}{\lambda} + \frac{\beta \zeta G_i b_i n_i}{\lambda}) = 0 \qquad (4)$$

where the number of dislocations pinned by Ag_3Sn IMC at steady state is given by:

$$n_i = (1 - f_{disp-IMC})(\pi / 6 f_{disp-IMC})^{(2/3)} \rho_i^{sat} \lambda^2 \qquad (5)$$

For the Sn phase, the steady state dislocation density is modeled by:

$$\dot{\rho}_i(t) = v_0^i k_i \rho_i^{sat} (\tau_i^r - \alpha G_i b_i \sum_j \sqrt{C_{ij} \rho_j^{sat}} + \xi \alpha G_i b_i \sum_j \sqrt{C_{ij} \rho_j^{sat}}) = 0 \qquad (6)$$

The first term of Equation 4 denotes dislocation generation, the second term denotes dislocation impediment by nanoscale Ag_3Sn IMCs, and the third term denotes recovery by dislocation climb/detachment from the particle; v_0^i is the initial resolved velocity of edge dislocation along the i^{th} slip system (this term is estimated as described earlier in Section 6.2.2); k_i ($=1/\alpha_1 K_i b_i$) is a model constant for the slip system; where K_i, b_i are the line tension factor and Burgers vector, respectively, for edge dislocation in the i^{th} slip system; α_1 (5E8) is a model constant to calibrate the model predictions to the experimental observation; τ_i^r is the resolved shear stress along the i^{th} slip system; G_i is shear modulus for the i^{th} slip system; ζ (=0.1) is the precipitate hardening calibration parameter; n_i is the number of dislocations getting trapped at Ag_3Sn IMCs for the it^h slip system; β (=0.5) is calibration

parameter for dislocation recovery from precipitates by climb/detachment; $f_{disp-IMC}$ is the volume fraction (=0.05; obtained using image processing) of Ag_3Sn dispersoids in eutectic Sn-Ag phase.

The first term of Equation 5 denotes dislocation generation, the second term denotes dislocation impediment by forest dislocations, and the third term denotes recovery by dislocation climb from forest dislocation; α (= 1) is a forest hardening calibration parameter lying between 0.1 and 2 [163]; ξ (=0.5) is forest hardening recovery parameter; C_{ij} (=0.01) is a constant capturing the interactions between the i^{th} and j^{th} slip systems. The interaction parameters (C_{ij}) are assumed to be 0.01 for all i and j, to capture the interactions between all slip systems in this study and need to be calibrated in future by simulating SAC single crystal experiments using discrete dislocation dynamics. Model constants used for calculations are summarized in Table 4.2 in Chapter 4 (Tier 1 anisotropic transient creep chapter).

6.3. Modeling Approach for Tier 1 length scale

In the Tier 1 length scale, nanoscale Ag_3Sn IMCs provide dispersion-strengthening to the Sn matrix by impeding the motion of dislocations in the eutectic Sn-Ag phase by pinning the dislocations (refer to Figure 6.3 [213]).

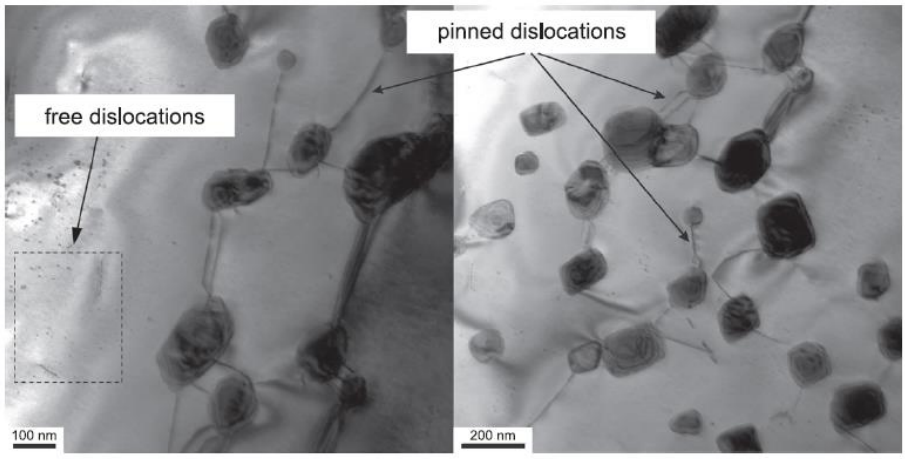

Figure 6.3: TEM micrographs of interaction of dislocations with nanoscale Ag_3Sn particles. Dislocations are pinned by Ag_3Sn particles and hinder their mobility [213]

The creep strengthening of the Sn matrix phase due to these particles and the effective properties of the eutectic Sn-Ag phase are modeled by capturing the impediment and competing recovery mechanisms

at the IMC particles. The competing recovery mechanisms include: dislocation climb and detachment (refer to Figure 6.4) from the nanoscale IMCs using Orowan climb model [214] and Rosler's detachment model [61], [62], respectively. The Orowan climb model is based on a dispersion strengthening creep model without threshold stress, originally proposed by Ansell and Weertman [214]. In this model, dislocations bypass the Ag_3Sn particles accumulated at Sn dendritic boundaries by bowing between them and forming classical Orowan loops. As more loops accumulate during continued creep deformation, their back stress prevents further dislocation bypass and eventually inhibits all deformation. However, these loops are able to reduce their energy by slowly climbing to the poles of the particles. During this climb they continue to shrink by self-annihilation, under their line tension. The overall creep rate is this controlled by the interfacial climb of these Orowan loops piled up against the particle at Sn dendrite boundaries.

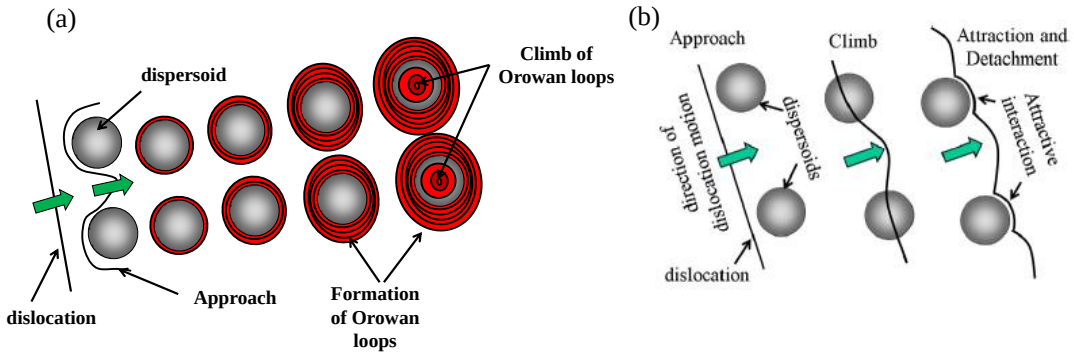

Figure 6.4: Recovery of dislocations from nanoscale Ag_3Sn dispersoids by (a) Orowan climb mechanism and (b) dislocation detachment mechanism

A strong attractive interaction between the climbing dislocation and particle is also observed in the post-climb phase of the dislocation [62], [215] and at certain stress levels, the detachment of the departing dislocation, rather than climb, is seen to be the rate limiting creep deformation mechanism. Therefore, contribution from both Orowan climb mechanism and dislocation detachment mechanism from the nanoscale Ag_3Sn particle has been calculated in this study and the creep rates are controlled by the mechanism which contributes to faster inelastic flow of dislocations in the material. The governing equations for both mechanisms are illustrated below. The net shear creep rate of the eutectic Sn-Ag region $(\dot{\gamma}^{i}_{\text{eut-Sn-Ag}})$ for each i^{th} slip system is derived from the assumption that the time taken

by the dislocation to traverse through a unit cell of the eutectic Sn-Ag phase is the sum of the time taken to travel over the Sn matrix phase and the Ag_3Sn IMC phase:

$$\frac{1}{\dot{\gamma}^{i}_{eut-SnAg}} = \frac{f_{mat}}{\dot{\gamma}^{i}_{mat}} + \frac{f_{disp-IMC}}{\dot{\gamma}^{i}_{disp-IMC}} \qquad (7)$$

where $\dot{\gamma}^{i}_{disp-IMC}$ using Orowan climb mechanism [147] is given by:

$$\dot{\gamma}^{i}_{disp-IMC} = \gamma_1 \frac{\pi \rho^{i}_{sat} \lambda^2 K_i b_i D}{k_B T} \frac{b_i}{d} \left(\frac{\tau^{i}_{sat}}{G_i}\right)^2 \qquad (8)$$

where $\dot{\gamma}^{i}_{disp-IMC}$ using Rosler detachment mechanism [146] is given by:

$$\frac{\dot{\gamma}^{i}_{disp-IMC}}{\dot{\gamma}^{i}_{0}} = \gamma_1 \exp\left(\frac{-K_i b_i^{\,2} r[(1-k_i)(1-\frac{\tau^{i}_{app}}{\tau^{i}_{d}})]^{\frac{3}{2}}}{k_B T}\right) \qquad (9)$$

where i refers to i^{th} slip system; $f_{disp-IMC}$ (=1-f_{mat}) refers to the volume fraction of Ag_3Sn in the eutectic Sn-Ag phase; b_i is Burgers vector for the i^{th} slip system in Sn; K_i is the line tension factor of pure edge dislocation for the i^{th} slip system in the Sn matrix (described in Subsection 2.1); r (approximately 25 nm) and λ (approximately 80 nm) are the average radius and interparticle spacing, respectively, of Ag_3Sn IMCs (obtained from image processing of ESEM images of SAC305 specimens with a specific aging protocol) [59]; d is the average pro-eutectic Sn dendrite size (approximately 10 μm) (also obtained from image processing), k_B is the Boltzmann constant (1.38E-23 $m^2kg/s^2/K$; T is the temperature in Kelvin (298 K); τ^{i}_{sat} is steady state effective shear stress along the i^{th} slip system; $\dot{\gamma}^{i}_{0}$ is the reference strain rate (refer to Equation 11, it is directly proportional to steady state dislocation density), τ^{i}_{d} is the athermal detachment stress along the i^{th} slip system (refer to Equation 10); G_i is the shear modulus along the i^{th} slip direction considered in BCT Sn [150]; ρ^{i}_{sat} is the steady state dislocation density in Ag_3Sn phase in i^{th} slip system during steady state creep (described in Subsection 6.2.3). k_i is the relaxation parameter (ratio of the line tension of the detaching dislocation at the particle matric interface versus that in the Sn matrix only). In Rosler's model (Equation 3), τ_{app} has been used instead of τ_{sat}; to model the situation where the backstress from the dislocations piling up near the particle are assumed to have similar effects on both the applied stress and the athermal

detachment stress. Therefore, it has been assumed that the ratio of saturated effective driving stress to saturated athermal detachment stress during secondary creep stage will remain equal to the ratio of applied shear stress to the initial athermal detachment stress. Details of the method to estimate the relaxation parameter are provided in Section 4.2 of Chapter 4 (Tier 1 anisotropic transient creep chapter).

Athermal detachment stress (τ^i_d) is given by:

$$\tau^i{}_d = \frac{K_i b_i}{2\lambda}\sqrt{1-k_i{}^2} \qquad (10)$$

and the reference strain rate ($\dot{\gamma}_0$) is:

$$\dot{\gamma}^i{}_0 = \frac{6\lambda\rho^i{}_{sat}}{b_i}[D_{0L}\exp(-\frac{Q_L}{RT}) + D_{0H}\exp(-\frac{Q_H}{RT})] \qquad (11)$$

where ρ^i_{sat} is the saturated dislocation density at a secondary stage of creep in the i^{th} slip system (described further in Section 6.2.3); subscripts "L" and "H" refer to low and high stress levels respectively; D_{0L} and D_{0H} are the diffusivity constants (1E-4 m^2/sec); Q is the activation energy (Q_L = 31 KJ/mol/K, Q_H = 69 KJ/mol/K); R is the universal gas constant (Further details are available in Reference 59).

The steady state creep rate ($\dot{\gamma}^i{}_{Sn}$) of the Sn matrix is modeled by modeling two competing recovery mechanisms (i) recovery of dislocations from forest dislocations by climbing over the impeding dislocation through formation of jogs/kinks and (ii) mass transport diffusion through the Sn lattice.

$$\dot{\gamma}^i{}_{Sn-C} = \frac{A_c D_c{}^i G_i b_i}{k_B T}(\frac{b_i}{\lambda_i})^2(\frac{\tau^i{}_{sat}}{G_i})^2 \qquad (12)$$

$$\dot{\gamma}^i{}_{Sn-MD} = \frac{A_{MD} D_{MD}{}^i G_i b_i}{k_B T}(\frac{b_i}{d})^2(\frac{\tau^i{}_{sat}}{G_i})^2 \qquad (13)$$

where A_C and A_{MD} are model constants for dislocation climb and mass diffusion mechanisms; τ^i_{sat} is steady state effective shear stress along the i^{th} slip system (modeled in Equation 6);

D_c^i ($[D_{0L}\exp(-\frac{Q_L}{RT}) + D_{0H}\exp(-\frac{Q_H}{RT})]$) is the diffusivity for climb process [212]; D_{MD}^i is the diffusivity for mass diffusion process (D_L + 200 D_P $(\tau/G_i)^2$); where D_L (= 6.3E-22 m^2/s) is lattice diffusivity co-efficient; D_P (=8.64E-13 m^2/s) is pipe diffusion co-efficient [111]; G_i is shear stiffness; λ_i is the spacing between the dislocations (inversely proportional to the square root of steady state dislocation density); λ_i= 1/sqrt(ρ^i_{sat}) where ρ^i_{sat} is the steady state dislocation density in Sn phase in the i^{th} slip system during secondary creep stage and is estimated by modeling three competing processes: (1) dislocation generation; (2) dislocation impediment caused by forest dislocations and (3) dislocation recovery processes listed before Equations 12 and 13. Further details of this Tier 1 model are provided in Section 4.2 in Chapter 4 (Tier 1 anisotropic transient creep chapter).

6.4. Modeling Approach for Tier 2 length scale

In Tier 2 length scale, anisotropic transient creep rates of eutectic Sn-Ag phase and Sn inclusion along three dominant slip systems are being utilized to predict the anisotropic creep rates of SAC single crystal. For an ellipsoidal inclusion embedded in a general anisotropic material Eshelby tensor $\overleftrightarrow{S}$ has to be determined numerically. For a composite with the inclusion phases characterized by the index i, and the matrix phase characterized by index 0, the effective viscosity of the single crystal composite is given by [183]:

$$\overleftrightarrow{V} = \overleftrightarrow{V}_0 + \sum_{i=1}^{2} c_i(\overleftrightarrow{V}_i - \overleftrightarrow{V}_0)[c_0\overleftrightarrow{S}\overleftrightarrow{V}_0^{-1}(\overleftrightarrow{V}_i - \overleftrightarrow{V}_0) + \overleftrightarrow{I}]^{-1} \quad (14)$$

Where, $\overleftrightarrow{V}$ = Effective viscosity of the composite RVE; $\overleftrightarrow{V}_0$ = viscosity of the matrix (eutectic Sn-Ag phase) obtained using Equation 7 (Tier 1) in the unit RVE; $\overleftrightarrow{V}_i$ = viscosity of the inclusion (Sn inclusion) obtained using Equations 12 and 13 (Tier 1) and Cu_6Sn_5 IMC in the unit RVE; $\overleftrightarrow{S}$ = Eshelby tensor of the ellipsoidal Sn inclusion and cylindrical Cu_6Sn_5 inclusion (cross-section is assumed to be elliptical) embedded in the anisotropic medium; $\overleftrightarrow{I}$ = 4^{th} order identity tensor; c_i&c_0 = volume

fractions of Sn (=0.55 in SAC305; obtained using image processing) and Cu_6Sn_5 (=0.03 in SAC305; obtained using image processing) inclusion and matrix, respectively, in the composite RVE.

However, there is no closed form analytical solution available for Eshelby's tensor for ellipsoidal inclusions (material principal axes of ellipsoidal Sn inclusions and that of eutectic Sn-Ag matrix are identical) embedded in an anisotropic eutectic Sn-Ag matrix. It has to be found out numerically. For a general anisotropic material, the Eshelby tensor (S) is computed by the following surface integral, parameterized on the surface of an unit sphere (Mura 1987) [216].

$$S_{ijkl} = \frac{1}{8\pi} L_{mnkl} \int_{-1}^{+1} d\zeta_3 \int_{0}^{2\pi} \{G_{imjn}(\xi') + G_{j\min}(\xi')\} d\omega \tag{15}$$

where

$$G_{ijkl}(\xi') = \xi_k' \xi_l' N_{ij}(\xi') / D(\xi') \tag{16}$$

$$\xi_i' = \zeta_i / a_i; \zeta_1 = (1-\zeta_3^2)^{1/2} \cos(\omega); \zeta_2 = (1-\zeta_3^2)^{1/2} \sin(\omega); \zeta_3 = \zeta_3 \tag{17}$$

$$D(\xi') = \varepsilon_{mnl} K_{m1} K_{n2} K_{l3}; N_{ij}(\xi') = \frac{1}{2} \varepsilon_{ikl} \varepsilon_{jmn} K_{km} K_{\ln}; K_{ik} = L_{ijkl} \xi_j' \xi_l' \tag{18}$$

where, ε_{ijk} is the permutation tensor and L_{ijkl} are the components of the stiffness tensor of the anisotropic material. In this work, a numerical scheme for the evaluation of S_{ijkl} is used [183] based on Equation 15. The double integration is performed using a Gaussian quadrature scheme:

$$S_{ijkl} = \frac{1}{8\pi} \sum_{p=1}^{M} \sum_{q=1}^{N} L_{mnkl} \{G_{imjn}(\omega_q, \zeta_{3p}) + G_{j\min}(\omega_q, \zeta_{3p})\} W_p W_q \tag{19}$$

where, M and N refer to the Gauss points used for integration over ζ_3 and ω, respectively, and W_p, W_q are the corresponding Gaussian weights.

6.5. Results and Discussions

Results and discussions are discussed in this section and subdivided into several subsections for clarity. Line tension (Tier 0) of dislocations is provided in Subsection 6.5.1; mobility of dislocations (Tier 0) are provided in Subsection 6.5.2; anisotropic steady state creep strain rates for pure Sn and eutectic Sn-

Ag phase (Tier 1) is provided in Subsection 6.5.3; calculation of S tensor (Tier 2) for ellipsoidal Sn inclusions embedded in anisotropic eutectic Sn-Ag matrix is provided in Subsection 6.5.4; anisotropic steady state creep strain rates for SAC single crystal (Tier 2) is provided in Subsection 6.5.5; quantitative model predictions vs. experimentally observed steady state creep rates for single crystal and bi-crystal specimens are provided in Subsection 6.5.6; and effect of varying orientation of Sn inclusions with respect to the loading direction on steady state creep rates of SAC single crystal is provided in Subsection 6.5.7.

6.5.1. Results: Line tension of dislocation in pure BCT Sn lattice (Tier 0)

Stroh's method has been adapted in this study to calculate the line tension of pure edge and screw dislocations in single crystal BCT Sn. The line tension factors for straight edge/screw dislocation lines in BCT Sn, using Stroh's matrix formalism formulated in MATLAB, are plotted in Figure 6.5 at 298 K and the underlying governing equations are provided in Appendix A1 of Chapter 4..

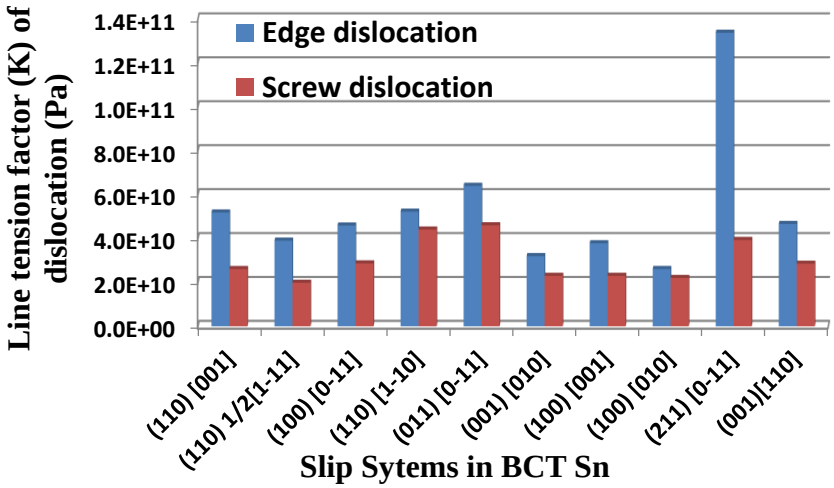

Figure 6.5: Line tension factor of dislocations in anisotropic BCT Sn at 298 K

In the interest of limiting the computational burden, all subsequent calculations in this study are limited to pure edge dislocations in the three most facile slip systems (slip systems # 2, 4 & 6 tabulated in Table 1) in eutectic Sn-Ag phase. Further details on the Tier 0 model are provided in Section 2 in Chapter 4 (Tier 1 anisotropic transient creep chapter).

6.5.2. Results: Mobility of dislocation in pure BCT Sn lattice (without any Ag_3Sn Particles)

The viscous drag coefficient and mobility calculated for the three selected slip systems using the above equations are shown in Figures 6.6 at 298 K.

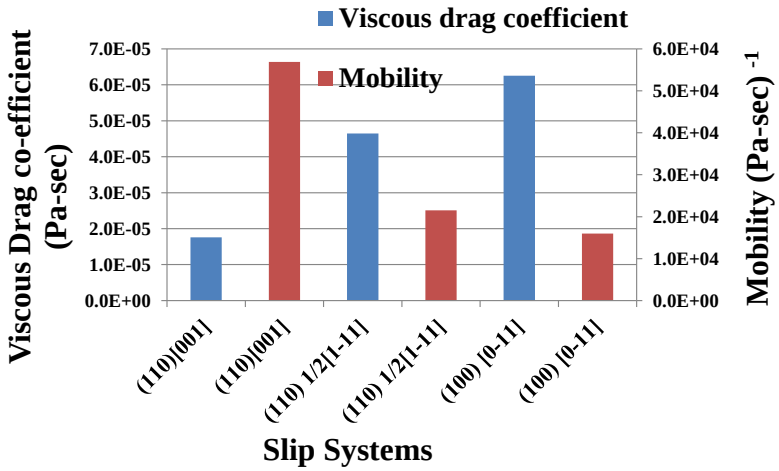

Figure 6.6: Mobility calculations for three facile slip systems in anisotropic BCT Sn at 298 K

(110)[001] & (100)[0-11] systems are found to be the most facile and most difficult slip systems, respectively, at room temperature, in single crystal Sn, out of the three selected slip systems. The initial velocity of individual dislocations in the above three slip systems in anisotropic Sn can now be calculated using the above results and Equation 8, and will be used as input to the analytical model developed for capturing the saturated steady state dislocation density during secondary creep stage in Section 6.2.3. Please refer to Section 4.2 in Chapter 4 (Tier 1 anisotropic transient creep chapter) for more details on the Tier 0 model.

6.5.3. Results: Anisotropic steady state creep rates of eutectic Sn-Ag phase and pure Sn phase (Tier 1)

Anisotropic secondary steady state creep rate for Ag_3Sn phase along three considered slip systems are predicted using Equation 8 by considering the Orowan climb mechanism as the rate controlling creep mechanism. Steady state creep rates for the three selected slip systems are plotted in Figure 6.7 and compared against the steady state creep rate for the SAC305 single crystal #1 along global specimen

direction. Steady state creep rate is predicted to be highest along the (110)0.5[1-11] slip system and lowest along the (100)[0-11] slip system; the difference being 3-4 orders of magnitude in the creep rates. This prediction clearly points towards the huge anisotropy one should expect in single crystal SAC solder joints, depending on the orientation of the crystal with respect to the loading direction.

However, as previously mentioned, dislocations piling up at the particle can also recover by dislocation detachment mechanism as proposed by Rosler [61]. Steady state creep rates for the Ag_3Sn phase is plotted in Figure 6.8 by considering the dislocation detachment mechanism as the rate controlling creep mechanism (Equation 9) and compared against the steady state creep rate for the SAC305 single crystal #1 along global specimen direction.

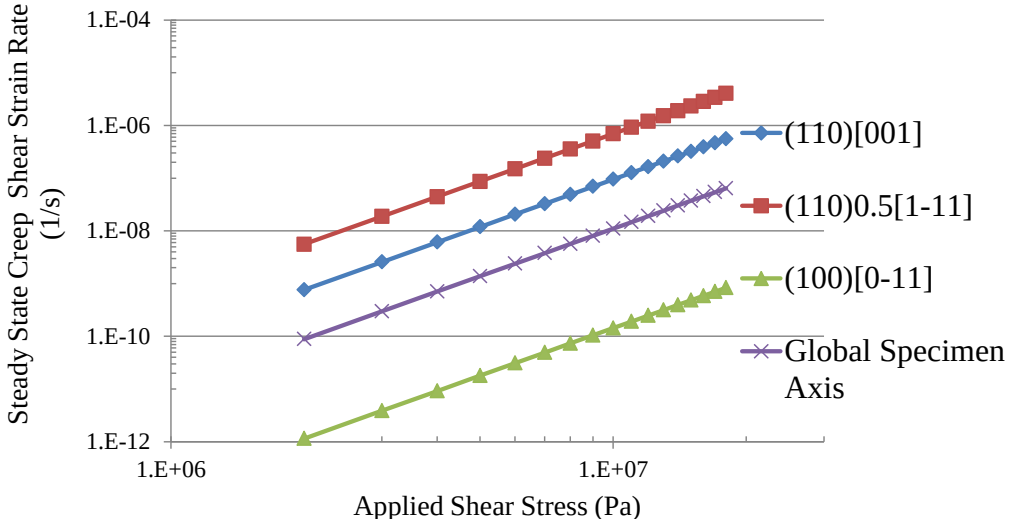

Figure 6.7: Anisotropic steady state creep rates predicted for three dominant slip systems in Ag_3Sn phase in SAC305 solder and SAC305#1 single crystal considering Orowan Climb as the rate controlling creep mechanism

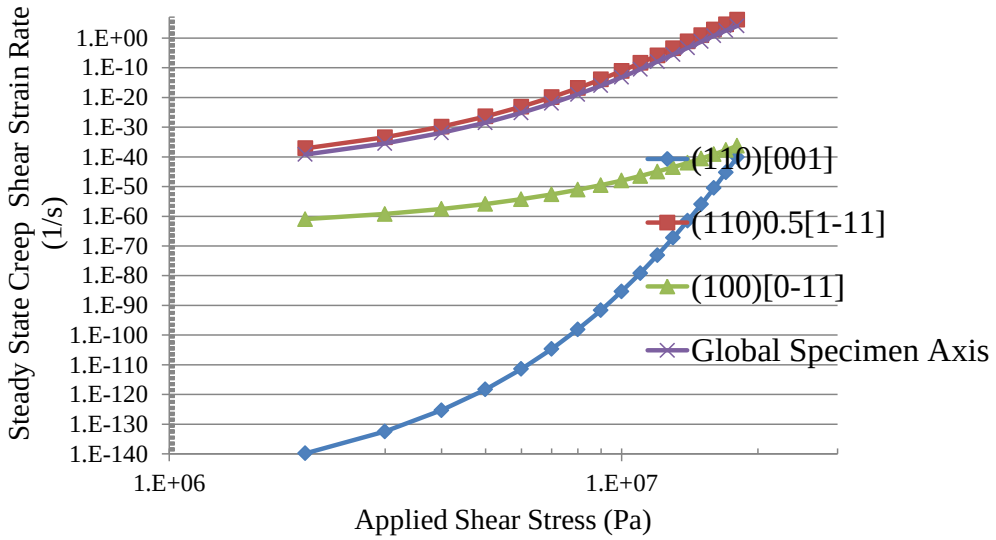

Figure 6.8: Anisotropic steady state creep rates predicted for three dominant slip systems in Ag_3Sn phase in SAC305 solder and SAC305#1 single crystal considering dislocation detachment as the rate controlling creep mechanism

At low stress levels, the creep rates predicted by Orowan climb model is much higher than the dislocation detachment model (refer to Figures 6.7 and 6.8), however at high stress levels, the rate of dislocation detachment becomes faster than dislocation climb and it can explain the high steady state creep rates observed experimentally in Figure 6.1. In other words, the Orowan climb model is able to capture the experimentally observed creep response well in low stress regimes, but it fails to capture the anisotropy observed at high stress levels. To overcome the above limitations of the two models, anisotropic secondary steady state creep rates for eutectic Sn-Ag phase along the three considered slip systems are captured by adding the predicted creep response from two models and thereby talking into consideration the contribution from both competing mechanisms because we think that both recovery mechanisms are acting in conjunction. Depending on the applied shear stress level, one mechanism starts dominating over the other and becomes the rate controlling creep mechanism in nanoscale Ag_3Sn phase.

Next, the steady state creep rates of pure Sn phase along three dominant slip systems are captured using Equations 12 and 13, where dislocation climb from impeding forest dislocations and mass transport diffusion are considered to be rate controlling mechanism. The predicted steady state creep rates of pure Sn dendrites is captured (refer to Figure 6.9) by adding the contribution of creep rates

from both recovery mechanisms discussed above and has been calibrated to experimentally reported anisotropic steady state creep data for Sn by Chu et al. [217].

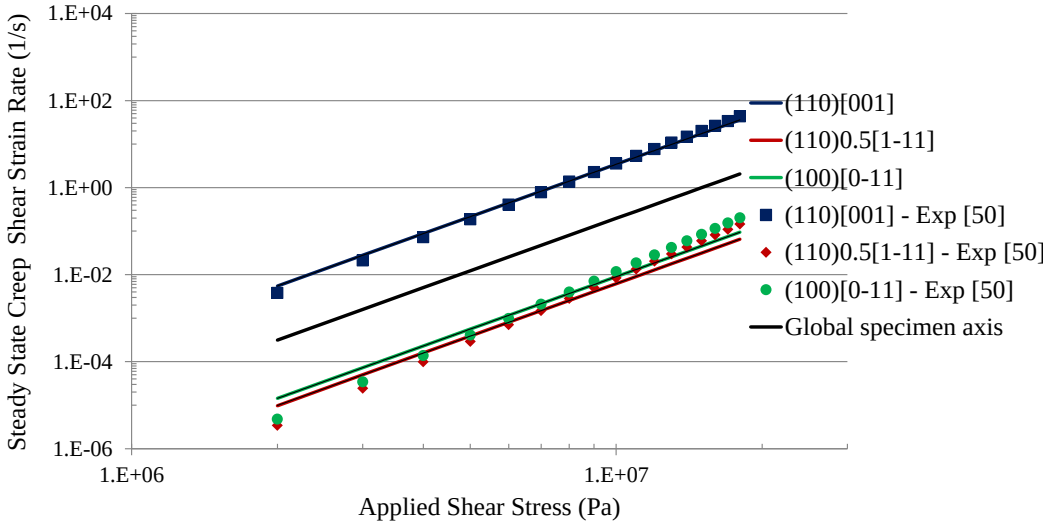

Figure 6.9: Anisotropic steady state creep rates predicted for three dominant slip systems in Sn phase in SAC305 solder and SAC305#1 single crystal considering dislocation climb and mass diffusion processes as the rate controlling creep mechanisms

Now, using the predicted anisotropic steady state creep rates for pure Ag_3Sn phase and pure Sn phase, the anisotropic steady state creep rates for eutectic Sn-Ag phase (using Equation 7) along the three dominant slip systems are plotted in Figures 6.10 against applied shear stress levels and compared against the isotropic steady state creep rate prediction from Cuddalorepatta et al [212]. The isotropic model prediction clearly fails to capture the orders of magnitude variability in creep rates, particularly at high stress regions. However, the proposed model can predict the anisotropic steady state creep rates observed in this highly heterogeneous single crystal or coarse grained SAC solder joints. Step discontinuities observed are because dislocation detachment mechanism becomes the rate controlling creep mechanism over Orowan climb mechanism at high stress level for (110) 0.5[1-11] slip system, whereas Orowan climb mechanism is still dominant creep mechanism for other two slip systems for the particular grain orientation.

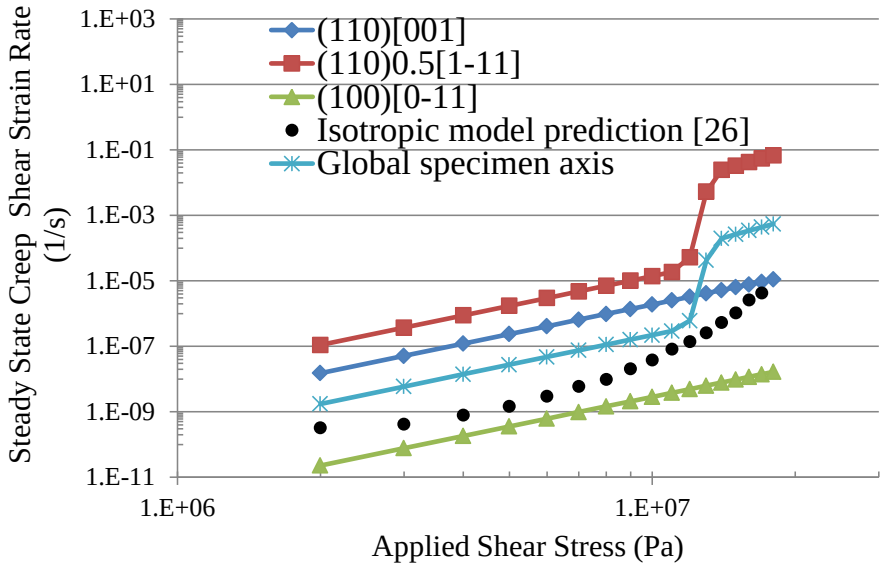

Figure 6.10: Anisotropic steady state creep rates predicted for three dominant slip systems in eutectic Sn-Ag phase in SAC305 solder and in SAC305#1 single crystal

6.5.4. Results: Modeling composite homogenization in Tier 2 length scale of SAC solder (Tier 2)

To calculate the S tensor for ellipsoidal Sn inclusions embedded in eutectic Sn-Ag matrix, the elastic stiffness tensor of eutectic Sn-Ag matrix first needs to be calculated. To calculate the elastic stiffness tensor of eutectic Sn-Ag matrix, the elastic stiffness tensor of Sn matrix and nanoscale spherical Ag_3Sn inclusions need to be calculated first. The elastic stiffness tensor for pure Sn has been taken from Kammer et al.[185] and the elastic stiffness tensor for Ag_3Sn inclusion is calculated based on the Young's modulus of Ag_3Sn inclusion (=99 GPa) from nanoindentation measurements from Chromik et al. [152] and using a Poisson's ratio of 0.35 [59]. The effective composite stiffness tensor for the eutectic Sn-Ag phase is now calculated using Equation 20 and the Eshelby tensor components derived for a spherical Ag_3Sn inclusion embedded in pure Sn phase.

$$\overleftrightarrow{L} = \overleftrightarrow{L}_0 + c_1(\overleftrightarrow{L}_1 - \overleftrightarrow{L}_0)[c_0 \overleftrightarrow{S} \overleftrightarrow{L}_0^{-1}(\overleftrightarrow{L}_1 - \overleftrightarrow{L}_0) + \overleftrightarrow{I}]^{-1} \quad (20)$$

Where, $\overleftrightarrow{L}$ = Effective stiffness tensor of the eutectic Sn-Ag phase; $\overleftrightarrow{L}_0$ = Stiffness tensor of the Sn matrix; $\overleftrightarrow{L}_1$ = stiffness tensor of the spherical Ag_3Sn inclusion; $\overleftrightarrow{S}$ = Eshelby tensor of the spherical

inclusion embedded in an anisotropic Sn medium; $\overset{\Leftrightarrow}{I}$ = 4th order identity tensor; c_1 & c_0 = volume fractions of Ag_3Sn inclusion and Sn matrix, respectively, in the composite RVE.

Now, the effective stiffness tensor of the eutectic Sn-Ag matrix is used to calculate the Eshelby tensor for ellipsoidal Sn inclusions embedded in the anisotropic eutectic Sn-Ag matrix. Selected components of the Eshelby tensor, for ellipsoidal inclusions embedded in anisotropic eutectic Sn-Ag matrix, are plotted in Figure 6.11. Please refer to Section 5.3 in Chapter 5 (Tier 2 anisotropic transient creep chapter) for more details on the Tier 2 modeling work.

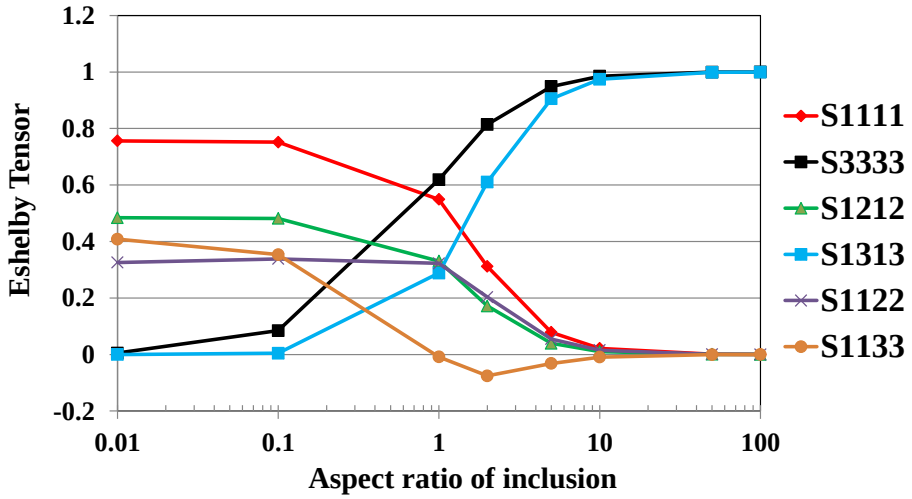

Figure 6.11: Eshelby tensor calculated for ellipsoidal inclusions embedded in fully anisotropic Eutectic Sn-Ag matrix

6.5.5. Anisotropic steady state creep rates of SAC single crystal (Tier 2)

Anisotropic steady state creep rates calculated along the dominant slip systems for eutectic Sn-Ag phase and pure Sn phase are then combined together using the calculated Eshelby tensor using anisotropic micromechanics homogenization theory (refer to Equation 14) to predict the anisotropic steady state creep rates of SAC305 single crystal and are plotted in Figure 6.12. In Figure 6.13, the isotropic model prediction and anisotropic model prediction for SAC305 single crystal #1 (grain orientation provided in Figure 6.14) are plotted on top of the experimental creep data observed.

Clearly, the anisotropic creep rate predictions from Figure 6.13 along three dominant slip systems are able to capture the variability observed in experiments (Figure 6.14).

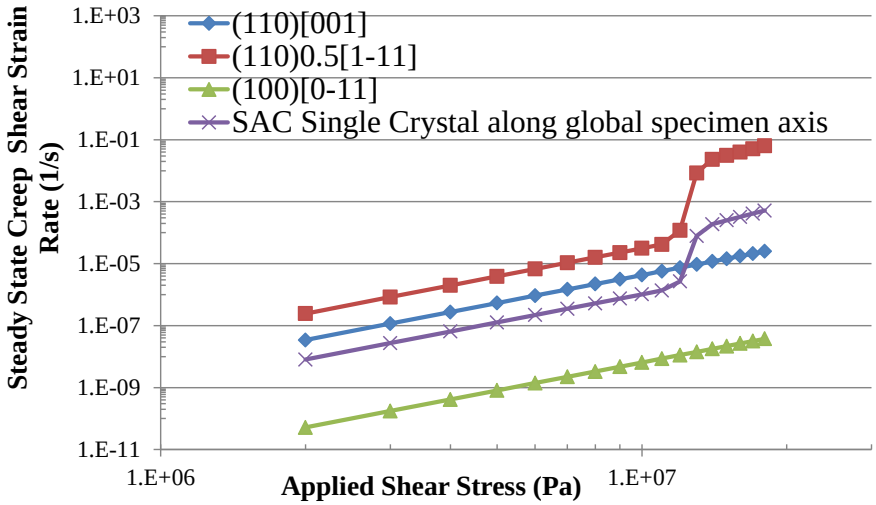

Figure 6.12: Anisotropic steady state creep rates predicted for three dominant slip systems in SAC305 single crystal

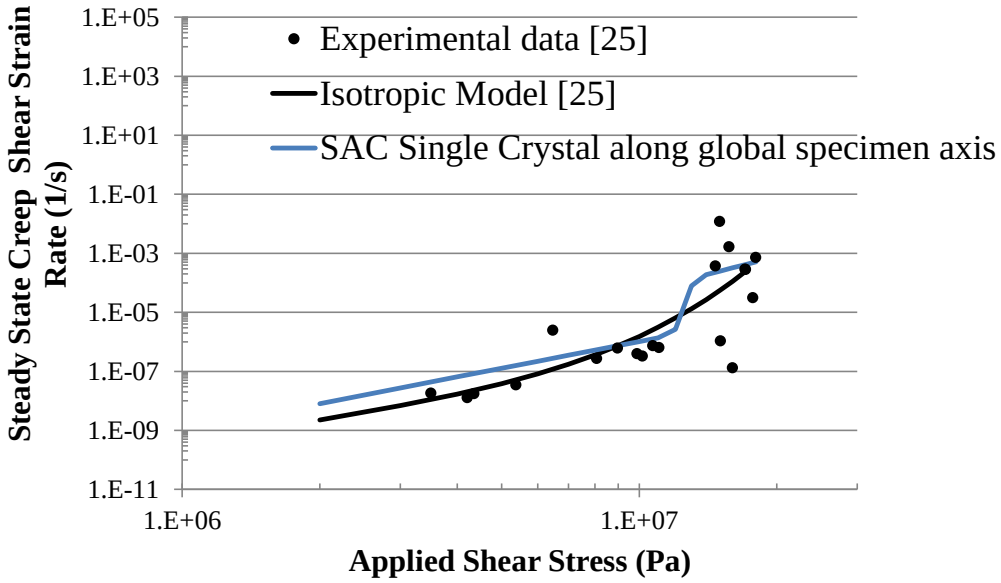

Figure 6.13: Anisotropic steady state creep rates predicted for three dominant slip systems in SAC305 single crystals compared against the experimental creep data from coarse grained SAC305 specimens

The above predictions are in agreement with (1-4) orders of magnitude of variability observed in steady state secondary creep response observed in SAC305 solder joints tested under identical loading conditions. The above model is then further used to predict the steady state creep rates of few discrete (single crystal and bi-crystal) SAC305 specimens in the next Subsection 4.6.

6.5.6. Predicted steady state creep rates of two SAC305 single crystal and two SAC305 bi-crystal specimens

Here, in this Section, orientation image maps (OIM) of four discrete SAC305 specimens will be presented along with the Euler angles of the individual grains present in the joint. The three Euler angles of each crystal are used to calculate the resolved shear stress along the three dominant slip systems (considered in this study) by conducting co-ordinate transformation on second order applied stress tensor. Furthermore, the Euler angles are used to convert the fourth order viscosity tensors of eutectic Sn-Ag phase and pure Sn phase obtained along individual slip system axes to crystal axes and then back to global specimen axes. In-plane shear viscosity term in the global specimen axes is finally used to calculate the steady state creep rate from the model and has been compared against the experimental observation using histograms for each crystal present in the joint. A crystal is considered to be different from another crystal only if the misorientation angle between the crystals is more than 5°; otherwise they are considered to be sub grains and part of the same crystal orientation.

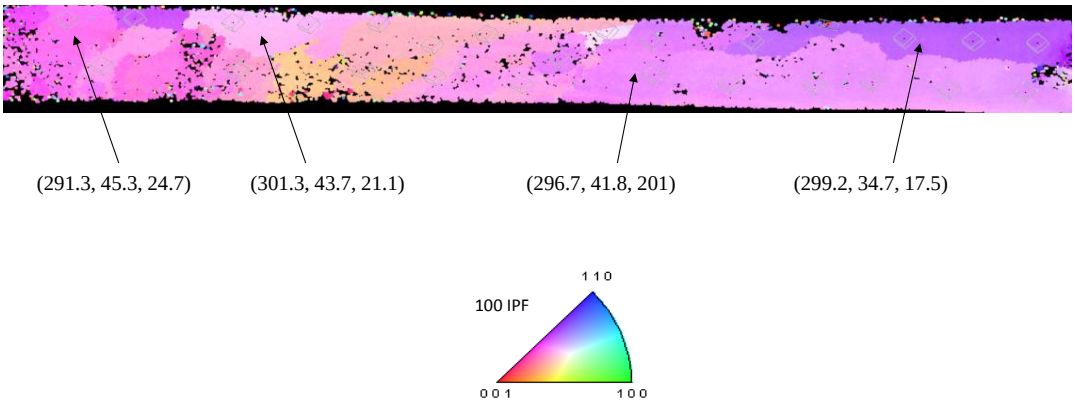

Figure 6.14: Inverse pole figure [100] map of SAC305 #1 single crystal. Numbers inside parenthesis at four different locations of the joint refer to the Euler angles (φ_1, ϕ, φ_2), needed to convert the physical quantities from global co-ordinate system to crystal co-ordinate system

In SAC305 single crystal #1, the Euler angles measured at four different locations in the joint point towards a predominantly single crystal structure with minimal orientation gradient across the length of the joint. Therefore, the average of these four orientations is taken to calculate the three average Euler angles, which is further used to resolve the shear stress along the slip systems. The second order

coordinate transformation tensor used for converting physical quantities from the sample coordinate system (loading directions) to the crystal coordinate system is given by:

$$g_{ij}^{s\to c} = g_{\varphi_2}.g_{\phi}.g_{\varphi_1} \quad (21)$$

$$g_{ij}^{s\to c} = \begin{bmatrix} \cos\varphi_1\cos\varphi_2 - \sin\varphi_1\cos\phi\sin\varphi_2 & \sin\varphi_1\cos\varphi_2 + \cos\varphi_1\cos\phi\sin\varphi_2 & \sin\phi\sin\varphi_2 \\ -\cos\varphi_1\sin\varphi_2 - \sin\varphi_1\cos\phi\cos\varphi_2 & -\sin\varphi_1\sin\varphi_2 + \cos\varphi_1\cos\phi\cos\varphi_2 & \sin\phi\cos\varphi_2 \\ \sin\varphi_1\sin\phi & -\cos\varphi_1\sin\phi & \cos\phi \end{bmatrix} \quad (22)$$

Thus, the applied shear stress τ_{sample} is converted to the principal axes of the crystal properties, $\tau_{crystal}$ as follows:

$$\overleftrightarrow{\tau}_{crystal} = \overleftrightarrow{g}\begin{bmatrix} 0 & \tau_{sample} & 0 \\ \tau_{sample} & 0 & 0 \\ 0 & 0 & 0 \end{bmatrix}\overleftrightarrow{g}^{T} \quad (23)$$

Next the resolved shear stress $\tau_{slipsystem}$ along the dominant slip directions is obtained as follows:

$$\overleftrightarrow{\tau}_{slipsystem} = \overleftrightarrow{a}\,\overleftrightarrow{\tau}_{crystal}\,\overleftrightarrow{a}^{T} \quad (24)$$

where $\overleftrightarrow{a}$ is the second order coordinate transformation tensor comprising of direction cosines between the crystal axes ([h k l], [u v w] and [h k l]×[u v w] (cross product of the loading plane normal and the loading direction)) and the individual slip system axes ([n_1 n_2 n_3], [b_1 b_2 b_3] and [n_1 n_2 n_3]× [b_1 b_2 b_3] (cross product of the slip plane normal and the slip direction)), respectively.

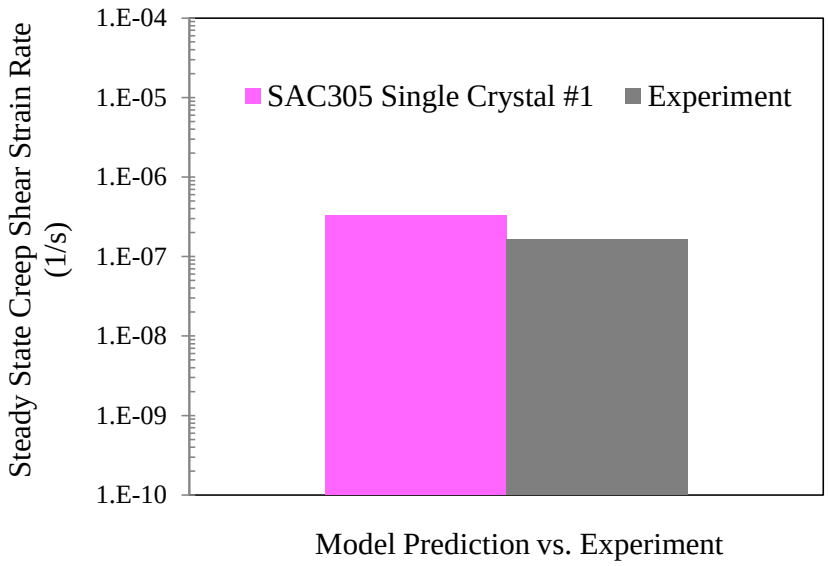

Figure 6.15: Steady state creep rate prediction for the single crystal SAC305 #1 specimen vs. experimentally observed steady state creep rate

Steady state shear creep rates along three different slip systems are converted to their respective in-plane shear viscosities by dividing the resolved shear stress along that slip system by the corresponding steady state creep rates. Then, the viscosities of the material along different slip systems are converted to in-plane shear mobilities along individual slip system by taking the inverse values. All other components other than in-plane shear mobility (M_{1212}) are zero.

$$\overleftrightarrow{M}_{crystal} = \overleftrightarrow{a}^{T} \leftrightarrow \overleftrightarrow{a} \overleftrightarrow{M}_{slipsystem} \overleftrightarrow{a}^{T} \leftrightarrow \overleftrightarrow{a} \quad (25)$$

Where, $\overleftrightarrow{M}_{slipsystem}$ is the fourth order mobility tensor (inverse of the viscosity tensor). The fourth order mobility tensor in the slip system axes are converted to the crystal axes using the above coordinate transformation. The fourth order viscosity tensors for both pure Sn phase and eutectic Sn-Ag phase along the crystal axes are then combined using Mori-Tanaka homogenization theory (using Equation 14) to obtain the fourth order viscosity tensor for SAC single crystal in crystal coordinate system using the fourth order Eshelby tensor (calculated in Subsection 6.5.4). Then, the fourth order viscosity tensor for SAC single crystal in crystal coordinate system is further rotated to obtain the fourth order viscosity tensor in the global specimen coordinate system using the following coordinate transformation in Equation 26. The in-plane shear component (V_{1212}) of the effective viscosity of SAC single crystal in

global specimen coordinate system is then utilized to calculate the steady state creep rate in the specimen coordinate system; which is then compared against the experimentally observed steady state creep response.

$$\overset{\Leftrightarrow}{V}_{specimen} = \sum_{i=1}^{3} \overset{\leftrightarrow}{g}^{T} \overset{\leftrightarrow}{g} \overset{\Leftrightarrow}{V}_{crystal} \overset{\leftrightarrow}{g}^{T} \overset{\leftrightarrow}{g} \quad (26)$$

Good agreement (refer to Figure 6.15) is observed between the predicted steady state creep rate of SAC305 single crystal #1 specimen and the measured creep rate experimentally using a Thermo-Mechanical Microscale (TMM) test machine [210]. Details of the test setup are provided in Reference 28. Then the model is further used to predict the steady state creep response of SAC305 #2

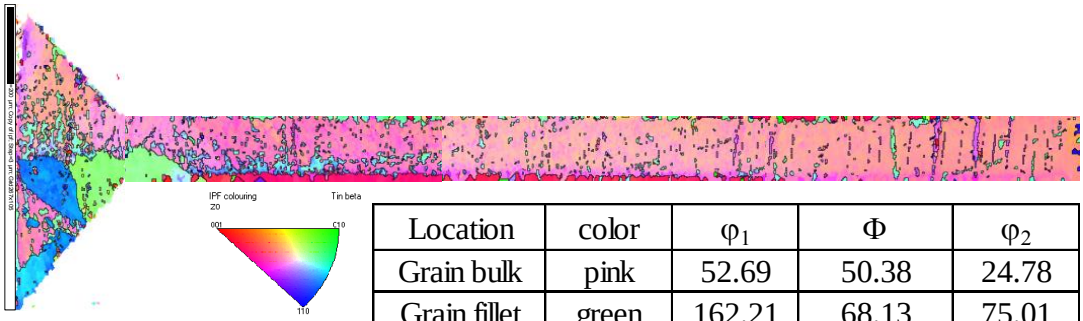

Location	color	φ_1	Φ	φ_2
Grain bulk	pink	52.69	50.38	24.78
Grain fillet	green	162.21	68.13	75.01
Grain fillet	blue	106.61	114.54	26.10

Figure 6.16: Inverse pole figure [100] map of SAC305 #2 single crystal. Numbers in the table corresponds to the Euler angles (φ_1, ϕ, φ_2) of three grains, needed to calculate the resolved shear stress along individual slip systems in each crystal

(another predominantly single crystal specimen in the bulk; refer to Figure 6.16). Two dissimilarly oriented grains (blue and green colored) in the fillet region are also considered for calculation to see their effect on the steady state creep rate of the specimen. The predicted steady state creep rate for the crystal in the bulk comes out to be very close to the experimentally observed creep rate. The blue grain contributes to creep rate; one order of magnitude more than the experimentally measured value and green grain contributes to creep rate; one order of magnitude less than the experimentally measured value (refer to Figure 6.17).

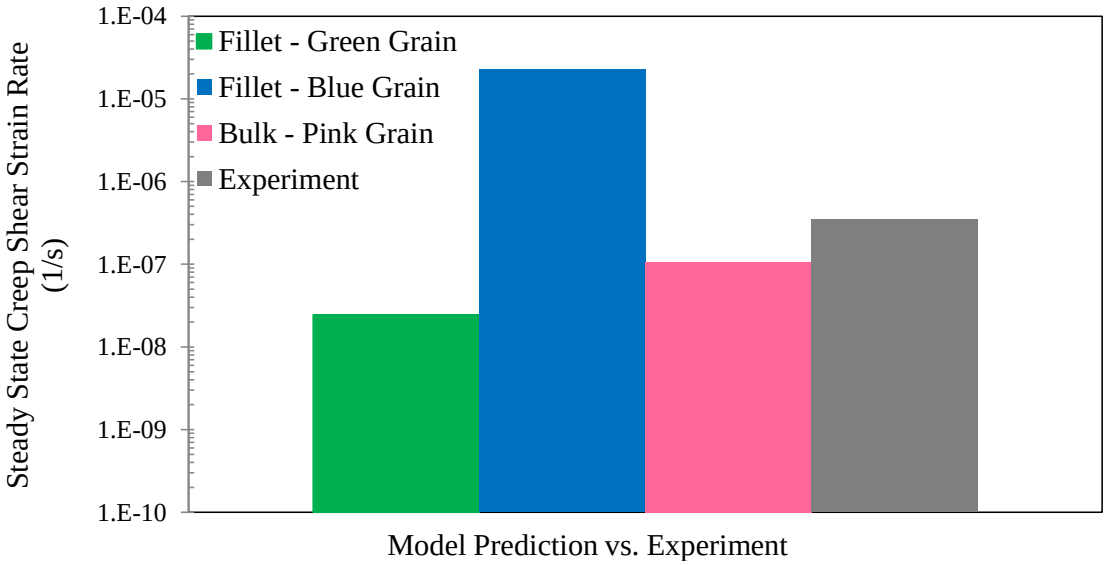

Figure 6.17: Steady state creep rate prediction for the single crystal SAC305 #2 specimen vs. experimentally observed steady state creep rate

Then the model is further utilized to predict the steady state creep response of two bi-crystal specimens (OIM maps of the specimens are given in Figures 6.18 and 6.20) tested using the TMM test setup. The predicted steady state creep strain rate in the light green grain in the SAC305 #3 bi-crystal specimen is two orders of magnitude higher than the rate predicted for the dark green grain in the bulk (refer to Figure 6.19). It is very interesting to note that the experimentally measured steady state creep rate falls between the two predicted values; which points towards partial contribution from active slip systems in both grains during the creep deformation process and possible grain boundary sliding. However, the predicted steady state creep strain rate in the yellow grain (in the left) in the SAC305 #4 bi-crystal specimen is closer to the experimentally measured steady state creep rate and one order of magnitude higher than the rate predicted for the red grain (in the right) in the bulk (refer to Figure 6.21). Future work will focus on modeling these two whole joints using FEA and including the creep strain contribution due to grain boundary sliding.

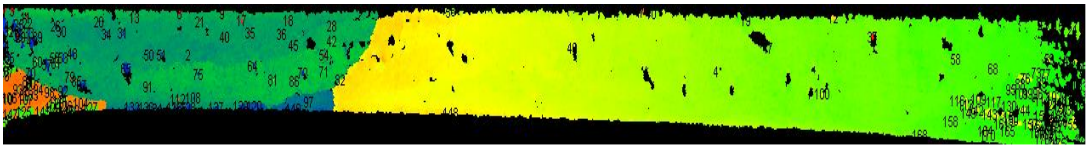

Location	color	φ_1	Φ	φ_2
Grain bulk - left	dark green	279.85	35.86	55.91
Grain bulk - right	light green	33.95	69.55	358.62

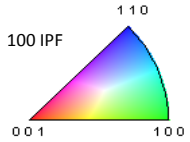

Figure 6.18: Inverse pole figure [100] map of SAC305 #3 bi-crystal. Numbers in the table corresponds to the Euler angles (φ_1, ϕ, φ_2) of two grains, needed to calculate the resolved shear stress along individual slip systems in each crystal

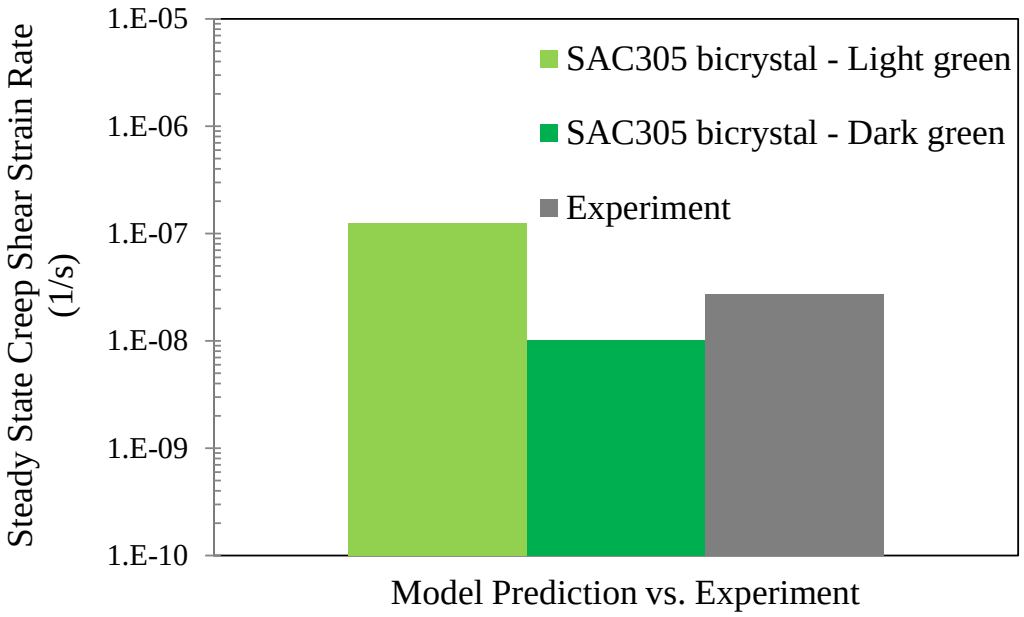

Figure 6.19: Steady state creep rate prediction for the bi-crystal crystal SAC305 #3 specimen vs. experimentally observed steady state creep rate

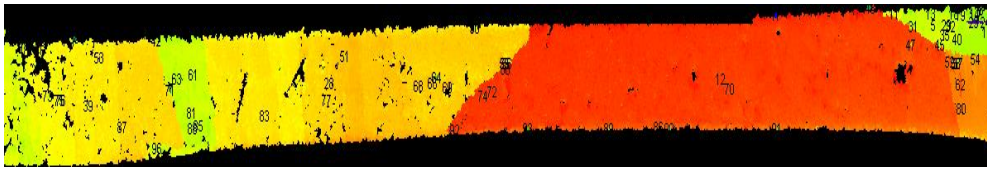

Location	color	φ_1	Φ	φ_2
Grain bulk - left	yellow	225.89	28.91	96.00
Grain bulk - right	red	17.52	18.84	304.94

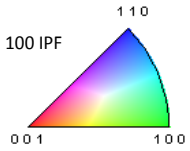

Figure 6.20: Inverse pole figure [100] map of SAC305 #4 bi-crystal. Numbers in the table corresponds to the Euler angles (φ_1, ϕ, φ_2) of two grains, needed to calculate the resolved shear stress along individual slip systems in each crystal

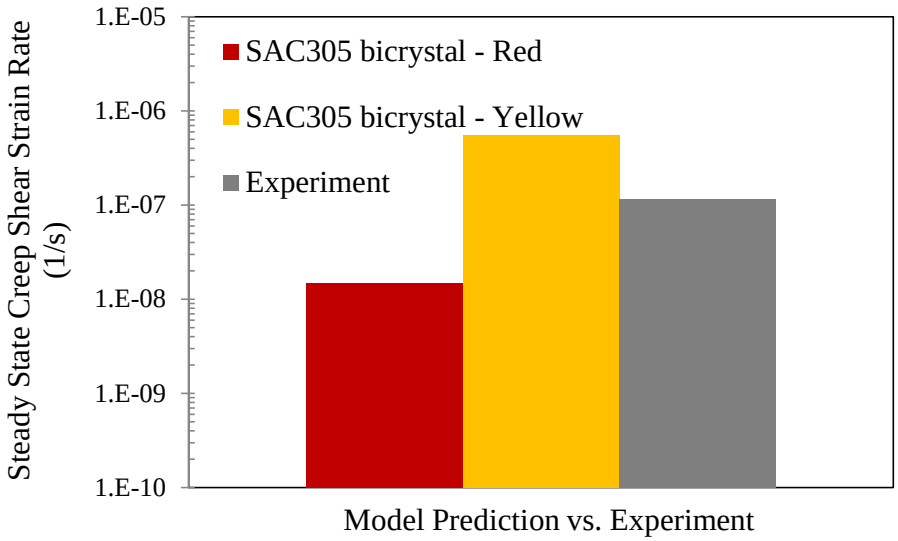

Figure 6.21: Steady state creep rate prediction for the bi-crystal crystal SAC305 #4 specimen vs. experimentally observed steady state creep rate

6.5.7. Effect of orientation of Sn inclusions on steady state creep rates of SAC305 single crystal

In this section, effect of orientation of Sn inclusions on the steady state creep rates is parametrically studied. The effect of orientation of Sn inclusions on the steady state creep rates is also studied. The

predicted steady state creep rate for SAC3305 single crystal #1 specimen is found to vary by almost one order of magnitude (refer to Figure 6.22) due to systematic variation of one of the Euler angles (φ_1) from 90° to 360°.

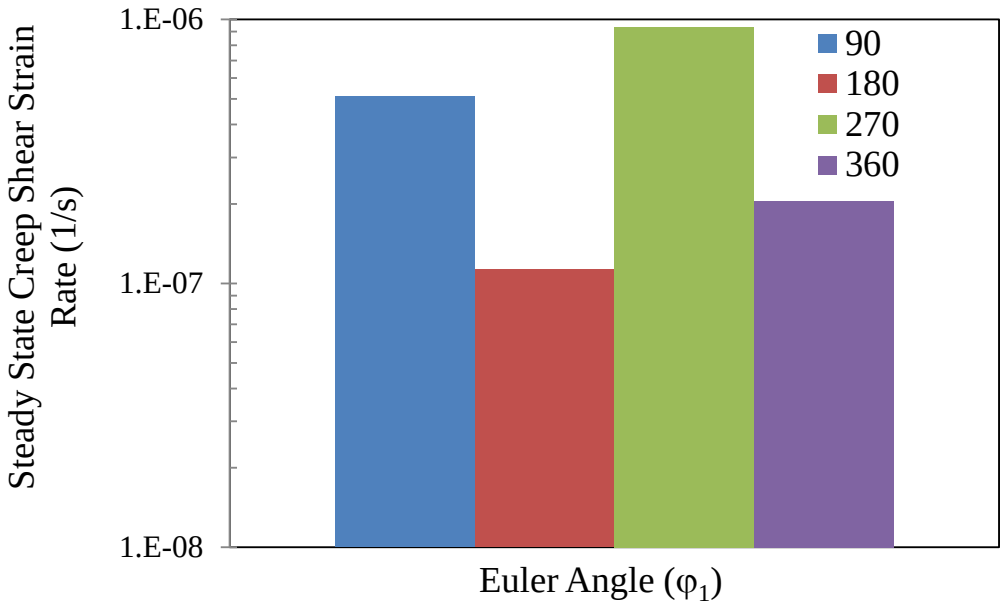

Figure 6.22: Effect of orientation (by varying φ_1; one of the Euler angles) of Sn inclusions on predicted steady state creep rates of SAC305 single crystal #1 along global specimen direction

6.6. Summary and Conclusions

A multiscale modeling framework is proposed in this study to capture the influence of the inherent elastic anisotropy in single crystal Sn on the measured secondary creep response of a single crystal SnAgCu (SAC) solder. Orowan climb mechanism and dislocation detachment mechanism from nanoscale Ag_3Sn particles are proposed to be the rate controlling creep mechanisms in the eutectic Sn-Ag phase of SAC single crystal. Line tension and mobility of dislocations in dominant slip systems of single crystal Sn is captured using elastic crystal anisotropy of body centered tetragonal (BCT) Sn and Stroh's matrix formalism. The anisotropic secondary creep rates of eutectic Sn-Ag phase, one of the primary phases in SAC systems, are then modeled using above inputs and saturated dislocation density calculated for dominant glide systems during secondary stage of creep. Saturated dislocation density is estimated as the equilibrium saturation between three competing processes: (1) dislocation generation;

(2) dislocation impediment caused by back stress from pinning of dislocations at IMCs; and (3) dislocation recovery due to detachment from IMCs. Secondary creep strain rate of eutectic Sn-Ag phase in three most facile slip systems is calculated and compared against the isotropic prediction. At low stress level secondary steady state creep rate along (110)[001] system is predicted to be ten times the creep rate along (100)[0-11] system. However, at high stress level, secondary steady state creep rate along (110)[001] system is predicted to be ten thousand times the creep rate along (100)[0-11] system. The above predictions are in strong agreement with (1-4) orders of magnitude of anisotropy observed in steady state secondary creep response in SAC305 solder joints tested under identical loading conditions in experiments conducted by several authors. The above model is then further used to predict the steady state creep rates of few discrete (single crystal and bi-crystal) SAC305 specimens. A very good agreement was observed between the predicted steady state creep rate of two SAC305 single crystal specimens and measured creep rates. For the bi-crystal specimens, experimentally measured steady state creep rates were found to fall between the predicted creep rates for individual crystals in the joint; pointing towards possible grain boundary sliding during the creep deformation process. Predicted steady state creep rates for SAC3305 single crystal #1 specimen is found to vary by almost one order of magnitude due to systematic variation of the orientation of Sn dendrites with respect to the loading direction.

Chapter 7： Mechanistic Prediction of the Effect of Microstructural Coarsening on Creep Response of Sn3.0Ag0.5Cu Solder Joints

Abstract

Mechanistic microstructural models have been developed to capture the effect of isothermal aging on time dependent viscoplastic response of Sn3.0Ag0.5Cu (SAC305) solders. SAC solders undergo continuous microstructural coarsening during both storage and service because of its high homologous temperature. The microstructures of these low melting point alloys continuously evolve during service. This results in evolution of creep properties of the joint over time, thereby influencing the long term reliability of microelectronic packages. It is well documented that isothermal aging degrades the creep resistance of SAC solder. SAC305 alloy is aged for (24-1000) hours at (25-100)°C (~ 0.6-0.8×T_{melt}). Then, we use cross-sectioning and image processing techniques to periodically quantify the effect of isothermal aging quantitatively on phase coarsening and evolution in SAC305 solder. The characteristic parameters monitored during isothermal aging include size, area fraction, and inter-particle spacing of nanoscale Ag_3Sn intermetallic compounds (IMCs) and volume fraction of micronscale Cu_6Sn_5 IMCs, as well as the area fraction of pure tin dendrites.

Effects of above microstructural evolution on secondary creep constitutive response of SAC305 solder joints were then modeled using a mechanistic multiscale creep model. The mechanistic phenomena modeled include: (1) dispersion strengthening by coarsened nanoscale Ag_3Sn IMCs in the eutectic phase; and (2) load sharing between pro-eutectic Sn dendrites and the surrounding coarsened eutectic Sn-Ag phase and microscale Cu_6Sn_5 IMCs.

The coarse-grained polycrystalline Sn microstructure in SAC305 solder was not captured in the above model because isothermal aging do not cause any significant change in the initial grain size and orientation of SAC305 solder joints. The above mechanistic model can successfully capture the drop in creep resistance due to the influence of isothermal aging on SAC305 single crystals. Contribution of grain boundary sliding to the creep strain of coarse grained joints has not been modeled in this study.

The original draft of this chapter is a journal paper and will be submitted to Journal of Materials Science and part of the paper has been accepted at InterPACK, 2013 (International Technical Conference and Exhibition on Packaging and Integration of Electronic and Photonic Microsystems) at Burlingame, CA.

7.1. Introduction

The creep behavior of lead free SAC solders at a given temperature and loading condition is controlled by the morphology of the solder. However, the microstructure of these low melting point SAC solders continuously evolve during service and storage. The microstructure of SAC solder consists of Ag_3Sn IMCs, Cu_6Sn_5 IMC phases, and pro-eutectic tin rich phase. Both Ag_3Sn and Cu_6Sn_5 IMCs undergo coarsening via Ostwald ripening, where the larger particles grow at the expense of smaller particles [218]–[220]. The size and distribution of the IMC phases change with isothermal aging. Size and volume fraction of pro-eutectic Sn dendritic lobes also changes as a function of aging time and temperature. This microstructural coarsening in SAC solder governs their mechanical properties. However, there is a lack of general agreement on the effect of aging on the evolution of the grain size. Lee et al. [221] reported a negligible change in the grain size of β-Sn in Sn-3.5Ag, Sn-3.8Ag-0.7Cu and Sn-0.7Cu solders while, Dutta et al. [77] reported a decrease in the β-Sn grain size in Sn-Ag and Sn-Cu solders following isothermal aging at 170°C for 2 hours. Additionally, some recrystallization is also reported near the precipitate clusters in the eutectic regions [77], [218], [222], [223], showing that the growth of preexisting particles during aging plays an important role in recrystallization.

Effect of isothermal aging on the secondary creep response of two lead-free solders (Sn3.0Ag0.5Cu and Sn4.0Ag0.5Cu) was studied by Ma et al. [166], where isothermal aging was conducted for varying durations (3 days, 6 days, 9 days, 21 days, 42 days, and 63 days) at room temperature (RT). For both alloys, RT aging affects both the minimum creep strain rate in the secondary creep regime and the elapsed time before tertiary creep and rupture. For the highest stress level considered, the secondary creep strain rate increased by factors of 16X for Sn4.0Ag0.5Cu and 73X for Sn3.0Ag0.5Cu during the 63 days of RT aging. In another study by the same group [224], they also studied the effect of elevated temperature aging (80, 100, 125, 150°C) on the creep resistance of Sn3.0Ag0.5Cu and Sn4.0Ag0.5Cu

solders. The samples were aged for various durations (0-6 months). Elevated temperature aging for longer durations drastically reduced the secondary creep resistance of the above alloys by orders of magnitude. The decrease in creep resistance was hypothesized to be due to coarsening of size of second phase particles (Ag_3Sn) at high temperature. It has also been reported that large-sized Ag_3Sn IMCs are undesirable since they greatly degrade the reliability of solders [225]. Similar observations have also been reported by Xiao et al. [226] for Sn3.9Ag0.6Cu and Sn37Pb alloys that were aged at 180°C. It has also been reported that aging decreases the hardness of solder joints and makes them more susceptible to creep deformation and rupture of the joint [227], [228]. Chen et al. compared pure Sn and three Sn-Ag-Cu alloys to show the changes in activation energy and stress exponent for different concentrations of Ag and Cu [222]. Dutta et al. [77] studied the effect of short time aging on ball grid array Sn-4Ag-0.5Cu. Moreover, all the above studies have been purely experimental and do not provide much insight into the physics of microstructural evolution occurring during isothermal aging at either room temperature or high temperature and its effect on the creep response of these alloys. An adaptive microstructural coarsening model is required to explain the above results based on the underlying physical mechanisms. Previously, Dutta et al. [223] used a semi-empirical Ansell-Weertman model to explain the effect of coarsening of Ag_3Sn particles on the steady state creep behavior of SAC alloys. While this approach is convenient and easy to implement, it does not address any other microstructural features except for Ag_3Sn particles.

The current study adopts a detailed mechanistic model to capture more detailed microstructural aspects of solders including size and spacing of Ag_3Sn IMC particles, size and area fraction of Cu_6Sn_5 IMC particles, and area fraction of pro-eutectic Sn dendritic lobes. The model takes into account the interactions of dislocations with nanoscale Ag_3Sn particles in the eutectic phase and considers the Orowan looping and dislocation detachment to be rate controlling mechanisms operating in parallel. Saturated dislocation density, a critical parameter in the model, is not assumed constant; rather it evolves with applied stress and temperature. Saturated dislocation density during secondary stage of creep is estimated as the equilibrium saturation between three competing processes: (1) dislocation generation; (2) dislocation impediment caused by back stress from pinning of dislocations at IMCs; and (3) dislocation recovery due to detachment from IMCs. The above model has been utilized to understand the effect of isothermal aging on secondary creep response of SAC solder alloys.

In next Section 7.2, optical image processing techniques have been utilized to quantify the microstructural evolution in SAC solder as a function of isothermal aging. In Section 7.3, effect of isothermal aging at varying temperatures and durations on steady state creep resistance of SAC305 solder has been demonstrated. In Section 7.4, multiscale mechanistic creep model developed to capture the effect of interactions of dislocation with evolving microstructure is discussed. Finally, in Section 7.5, mechanistic predictions using the above model are compared against the experimental observations to validate the model. And lastly, the article concludes with major conclusions, and limitations of the model in Section 7.6 and 7.7 respectively.

7.2. Microstructural Evolution Characterization

The material characterization vehicle consisted of 2512 resistors mounted on a flame retardant (FR4) board (Figure 7.1). The underlying substrate was copper (Cu) on organic solderability preservative (OSP). Sn96.5Ag3.0Cu0.5 (SAC305) solder was analyzed. The reflow profile consisted of a reflow temperature of 244ºC, time above liquidus of 50-74 seconds, a ramp-up rate of 0.4825ºC/sec, and a ramp-down rate of 3.41ºC/sec. Aging was conducted at 100ºC for 24, 600, and 1000 hours, and comparisons were made with specimens aged at room temperature (RT) for 24 hours. The test specimens (resistors on FR4 board) were cut out from the test board (shown in Figure 7.1) and were aged as per the aging conditions mentioned above.

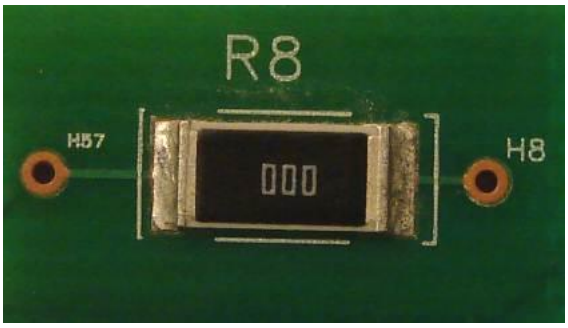

Figure 7.1: Test specimen

Three specimens per aging condition were analyzed for the microstructural study. After isothermal aging, the components were mounted in the epoxy, cross-sectioned, and polished. Chemical etching was carried out with a solution of 2% HCL, 4% HNO_3 and 94% C_2H_5OH at room temperature. The

solution etches the Sn and IMCs in the solder at different rates, with Sn etching faster than the IMCs. This helps to reveal distinct IMCs for optical measurements. The etching time was kept at 5 seconds for optimum etching. The test specimens were then analyzed under environmental scanning microscopy (ESEM).

7.2.1. Optical Image Processing Work

The microstructural images of aged SAC solders taken using ESEM were further analyzed using optical image processing software to capture the evolution of microstructure as a function of aging duration as shown in Figure 7.2. Since the accuracy of the data obtained from the images highly depends on the quality of the images, extreme care should be taken in preparing scratch-free and inclusion-free samples. The first step in the image processing is to calibrate the images with the scale given at the bottom of the images. Then, the contrast and brightness values of the image were adjusted to clearly identify the IMCs. Thereafter, the individual IMCs were selected by adjusting the gray scale in the histogram distribution of the images.

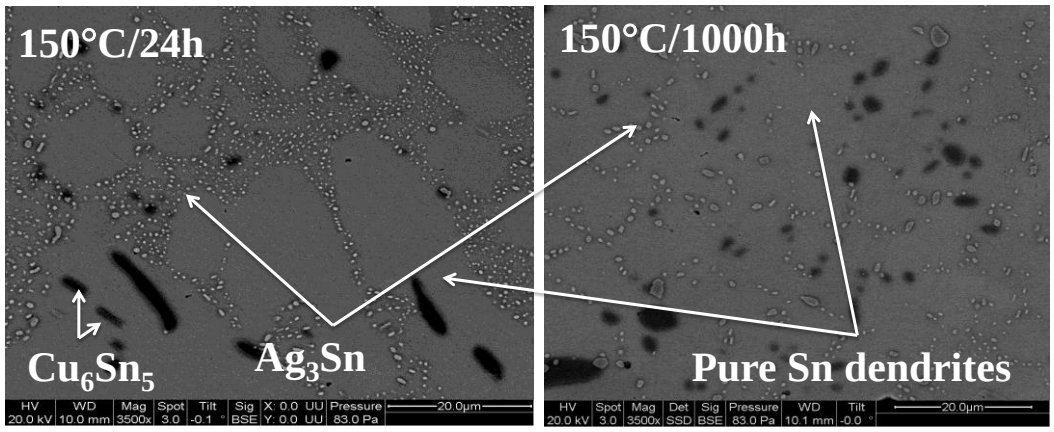

Figure 7.2: Evolution of size of Ag_3Sn particles with isothermal aging at 150°C from 24 hours to 1000 hours

7.2.2. Ag_3Sn and Cu_6Sn_5 Phase Size Measurements

For the measurement of area of the Ag_3Sn and Cu_6Sn_5 particles, the outline of the IMCs was selected by adjusting the gray scale of the histogram. It should be noted that the IMCs falling on the boundary

of area of interest (AOI) were excluded from the measurements since it was not known what fraction of their area was outside the AOI. As seen in Figure 7.3, Ag_3Sn IMCs were brighter than the Cu_6Sn_5 IMCs owing to the difference in atomic numbers wherein heavier compounds appear brighter under back scattered electron microscopy imaging. Hence, the gray scale of the image was adjusted once for Ag_3Sn IMC and then for Cu_6Sn_5 IMC.

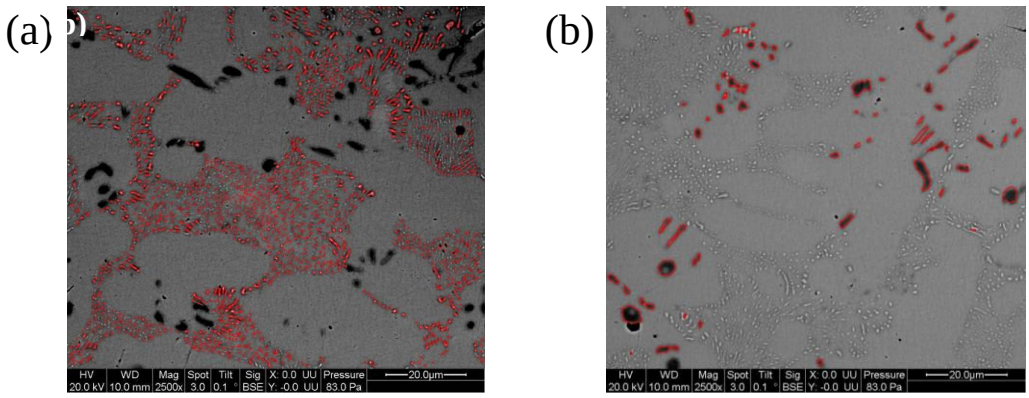

Figure 7.3: (a) Ag_3Sn, and (b) Cu_6Sn_5 particle size measurement

The average size of nanoscale Ag_3Sn particles in SAC305 specimens after 1000 hours of isothermal aging at 100°C was found to increase by 34% compared to that in specimens aged at RT for 24 hours (as shown in Figure 7.4). Size of Ag_3Sn IMCs showed a monotonic increasing trend with increasing aging duration at the same temperature (100°C). During isothermal aging, nanoscale Ag_3Sn IMCs in the solder bulk coarsened and grew larger by consuming the smaller IMCs through a process known as Ostwald's ripening, resulting in continuous evolution of both size and spacing. However, the size and area fraction of micronscale Cu_6Sn_5 phases did not exhibit a monotonic trend. Size of Cu_6Sn_5 IMCs (as shown in Figure 7.5) present in a unit representative volume element (RVE) in the bulk of solder increased by almost 35% with increasing aging duration until 600 hours at 100°C. But after 1000 hours of isothermal aging at 100°C, the size of Cu_6Sn_5 decreased by 11% in the unit RVE. Number of Cu_6Sn_5 IMCs increased leading to more homogeneous distribution of Cu_6Sn_5 particles in a unit RVE Sn matrix.

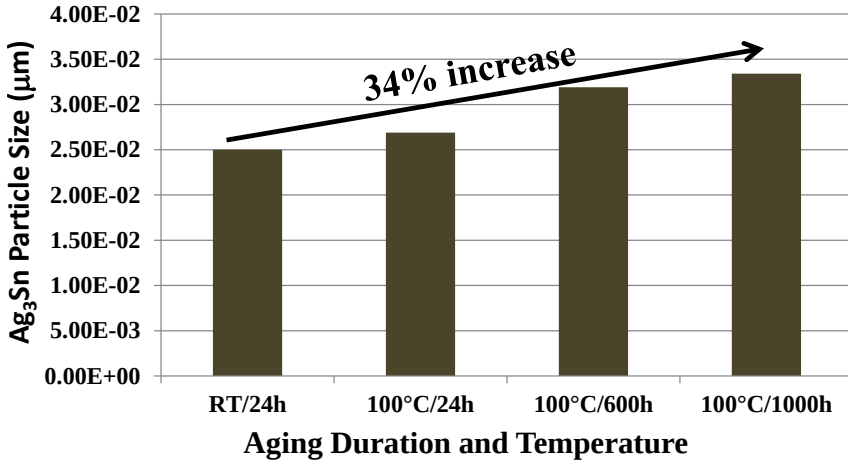

Figure 7.4: Evolution of Ag_3Sn particle size as a function of aging duration and temperature

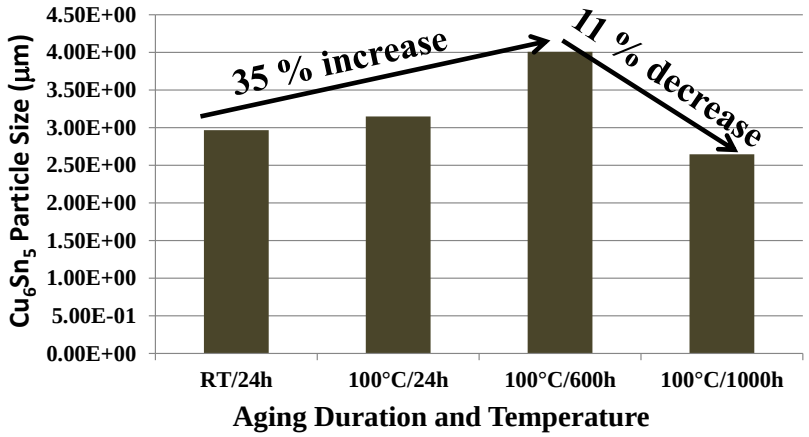

Figure 7.5: Evolution of Cu_6Sn_5 particle size as a function of aging duration and temperature

7.2.3. Ag_3Sn and Cu_6Sn_5 Particle Spacing

The changes in the distribution of Ag_3Sn and Cu_6Sn_5 IMCs during aging were assessed by using the segmentation and pruning features of the image processing software. The image consisting of the selected areas from the previous step was subjected to "segmentation" by thresholding the image, in which the Ag_3Sn IMCs and the background were separated as two distinct zones (black and white). Thus, the original gray scale image was converted to a binary image in which the Ag_3Sn IMCs (in SAC305) were set to black, while the background was set to white. Next, the pruning operation was carried out on the image by constructing a Voronoi diagram.

A Voronoi diagram of a point set is a subdivision of the plane into polygonal regions (some of which may be infinite), where each region is the set of points in the plane that are closer to some input point

than to any other input point. The centers of the circumcircles in a Delaunay triangulation can be connected to obtain the Voronoi diagram (see Figure 7.6), where Delaunay triangulation is a surface triangulation technique used to analyze the spatial distribution. The area of each Voronoi cell surrounding an IMC is calculated and the spatial distribution of these areas is found to be bimodal. Clearly, the spacing between Ag_3Sn IMCs can be determined by calculating twice the radius of the Voronoi cells (refer to Figure 7.7) of smaller size out of one of the two dominant size distributions.

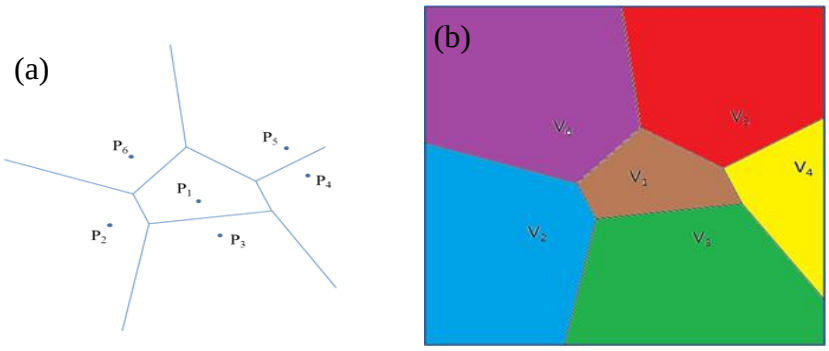

Figure 7.6: (a) Particles 1–5 and (b) Voronoi cells V1–V6

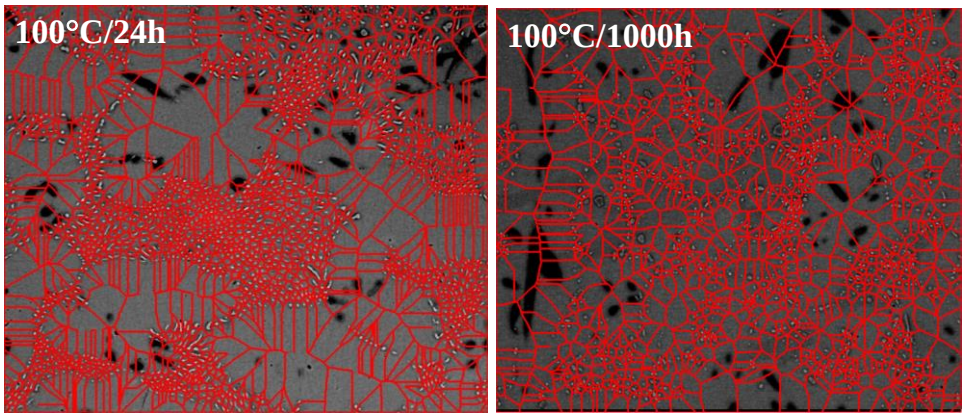

Figure 7.7: Voronoi diagrams for selected Ag_3Sn IMCs

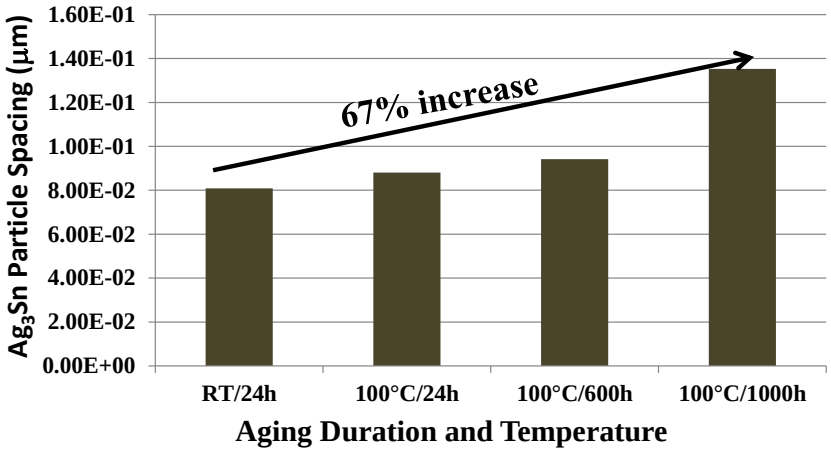

Figure 7.8: Evolution of Ag_3Sn particle spacing as a function of aging duration and temperature

Average size of the Voronoi cells surrounding the particles gradually increases as the specimens are aged for longer duration say 24 hours to 1000 hours (please refer to Figure 7.7), thereby indicating increase in particle spacing. The average spacing between the Ag_3Sn particles increased by almost 67% in SAC305 after 1000 hours of aging compared to that of RT aged specimens (refer to Figure 7.8). Spacing of Ag_3Sn IMCs shows a monotonic increasing trend with increasing aging duration at the same temperature.

The area fraction of the eutectic component of the microstructure (Sn and Ag_3Sn IMCs) is captured by selecting the eutectic component in multiple locations separately. The area fraction of pro-eutectic Sn dendrites is calculated by subtracting the volume fraction of the eutectic component (shaded in white) from the total volume of the solder joint in unit RVE captured in Figure 7.9. It was also observed that with aging time the area fraction of eutectic Sn-Ag phase decreased and that of pro-eutectic Sn dendrites in unit RVE increased. This was due to coarsening of Ag_3Sn IMCs present in eutectic Sn-Ag phase.

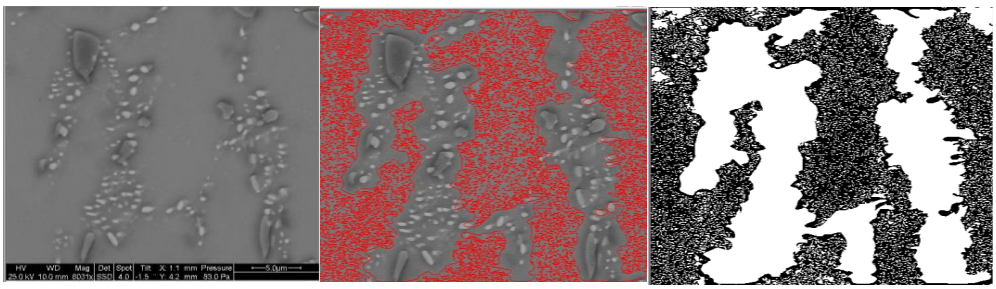

Figure 7.9: Calculation of area fraction of pro-eutectic Sn dendrites in an unit RVE

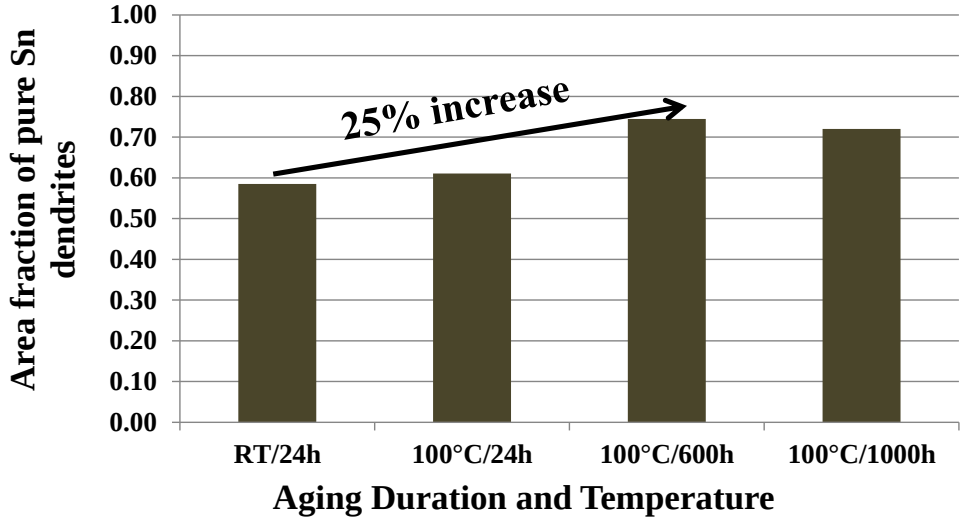

Figure 7.10: Evolution of area fraction of pure Sn dendrites as a function of aging duration and temperature

Area fraction of Sn dendrites was found to increase by 25% in SAC305 after 1000 hours of isothermal aging. Since the sum of the volume fractions of the pure Sn dendritic phases, eutectic Sn-Ag phase, and micronscale Cu_6Sn_5 phase is constant and is equal to unity, the volume fraction of eutectic Sn-Ag phase can be deduced from the data given in Table 1.

Table 7.1: Microstructural parameters in SAC305 solder during isothermal aging at room temperature and 100°C.

Aging Conditions	SAC305				
	Size of Ag_3Sn r (m)	Spacing of Ag_3Sn λ (m)	Size of Cu_6Sn_5 R_{rein} (m)	Volume fraction of Cu_6Sn_5 (f_{rein})	Volume fraction of pure Sn dendrites (f_{incl})
RT	2.50E-08	8.09E-08	2.97E-06	0.0195	0.59
100°C/24h	2.69E-08	9.21E-08	3.15E-06	0.0225	0.61
100°C/600h	3.19E-08	1.15E-07	4.01E-06	0.0205	0.74
100°C/1000h	3.34E-08	1.35E-07	2.65E-06	0.0147	0.72

7.3. Experimental Observations

The constitutive creep response of SAC305 alloys aged for varying durations has been measured using a custom built thermo-mechanical micro scale (TMM) test system. The test setup used in this work has been described in more detail elsewhere [229]. The specimen configuration used in the current work is

shown schematically in Figure 7.11. The specimen is a modified version of the notched shear specimen developed by Iosipescu [80]. The advantage of this specimen configuration is that the stress distribution in joint volume is quite uniform because of the notches [81]. The fabricated specimens in this study have a nominal solder joint height of about 180 μm. This dimension is of the same length scale as typical functional solder interconnects found in electronic assemblies. The specimens were deformed in mechanical shear. The TMM test system is schematically depicted in Figure 7.12.

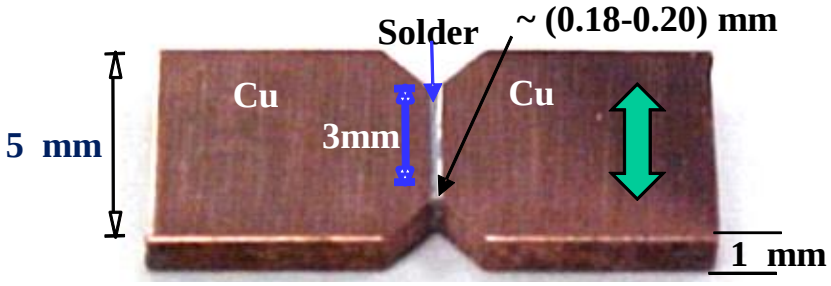

Figure 7.11: TMM specimen

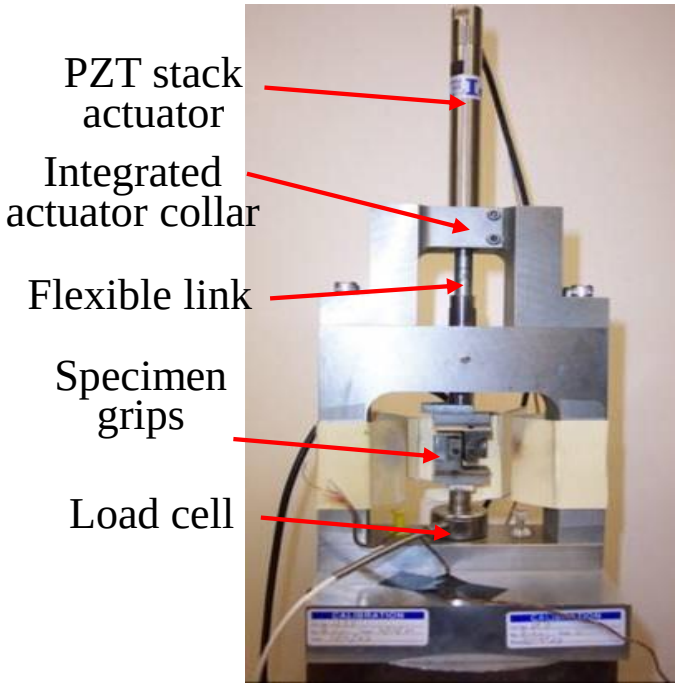

Figure 7.12: TMM test system

SAC305 TMM specimens aged at two different durations (RT for 24 hours and 100°C for 24 hours) are tested under force control using TMM setup. Steady state creep strain rates for the above two sets of specimens are plotted against varying applied shear stress levels tested at room temperature. Steady

state creep resistance of the material is found to degrade by almost (1-2) orders of magnitude due to increase in pre-conditioning temperature from RT to 100°C (refer to Figure 7.13).

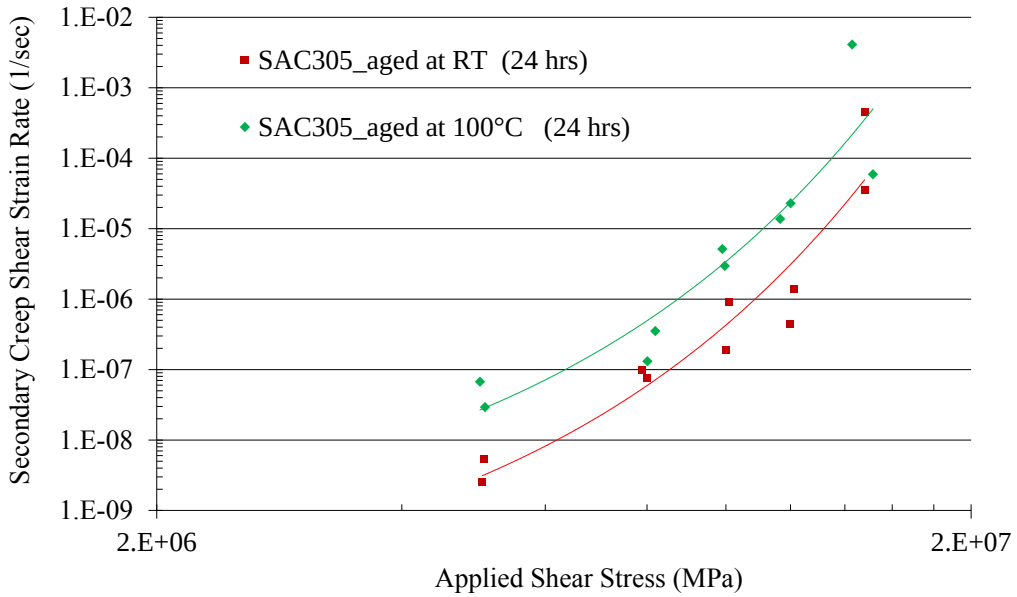

Figure 7.13: Steady state creep resistance of SAC305 TMM specimens aged at two different temperatures for same duration

7.4. Multiscale Micromechanics Creep Model

The microstructure of typical SAC solder interconnects can be broadly classified into four distinct length scales, as shown in Figure 7.14. The structural length scale (characteristic geometric dimensions of interconnect) forms the highest length scale (Tier 4), and features of interest at this length scale are the actual physical dimensions and geometry of the joint. Tier 4 features also include the neighboring metallization layers (Cu in this case) being soldered to SAC solder, and intermetallic layers separating the metallization from the solder materials. The next lower length scale (Tier 3) in a coarse-grained joint typically consists of a few highly anisotropic Sn grains and grain boundaries. The next lower length scale (Tier 2) looks at the structure of individual grains comprising multiple tin dendrites within each Sn grain that are surrounded by a eutectic Sn-Ag matrix. Embedded throughout this grain are micron scale Cu_6Sn_5 intermetallic particles. Finally, the lowest length scale (Tier 1) describes the structure of the eutectic Sn-Ag matrix, which consists of a statistically homogeneous distribution of nanoscale Ag_3Sn intermetallic particles embedded in pure mono-crystalline tin matrix.

Tier 3 & 4 features have not been considered in this model because isothermal aging does not significantly change the grain size and orientation. Only Tier 1 and Tier 2 microstructures are captured in this study, because the microstructural features in these two length scales are most sensitive to the effects of isothermal aging and therefore, predictions from this model will be valid for SAC305 single crystal; not coarse grained specimens.

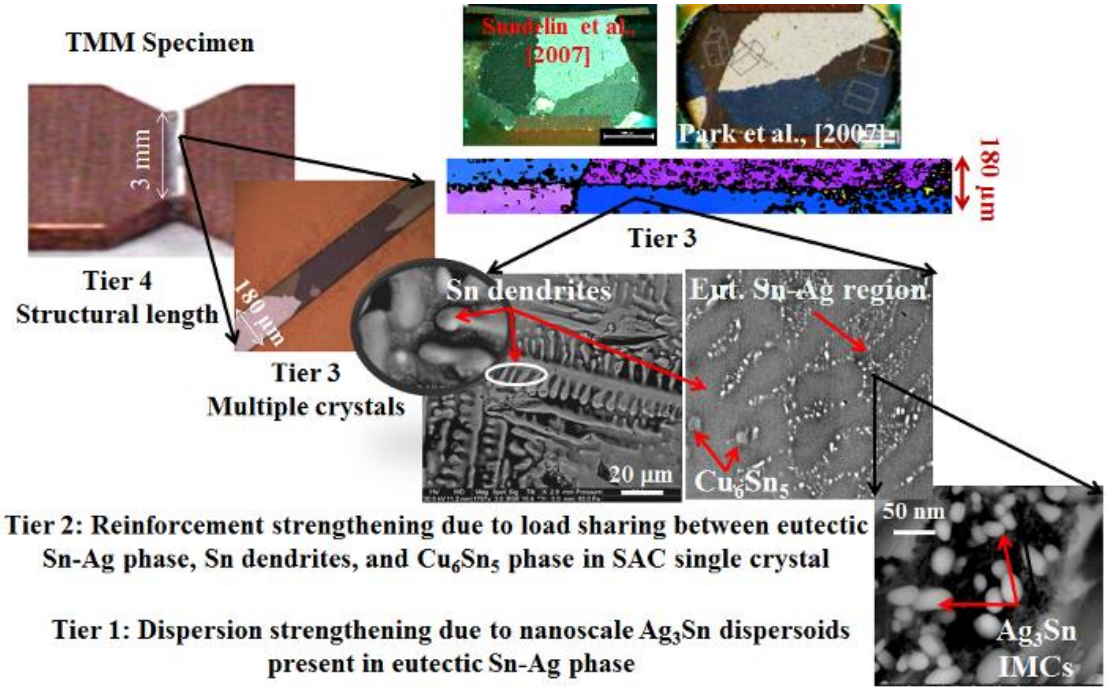

Figure 7.14: Multiple length scales and strengthening mechanisms in SAC solder alloys

In the Tier 1 length scale, nanoscale Ag_3Sn IMCs provide dispersion-strengthening to the Sn matrix by impeding the motion of dislocations in the eutectic Sn-Ag phase by pinning the dislocations (refer to Figure 7.15 [213]).

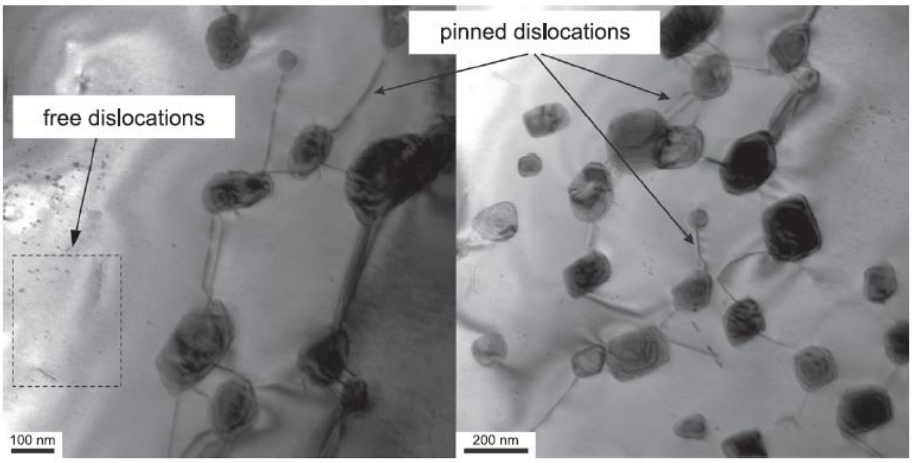

Figure 7.15: TEM micrographs of interaction of dislocations with nanoscale Ag_3Sn particles. Dislocations are pinned by Ag_3Sn particles and hinder their mobility **[213]**

The creep strengthening of the Sn matrix phase due to these particles and the effective properties of the eutectic Sn-Ag phase are modeled by capturing the competing recovery mechanisms: dislocation climb and detachment (refer to Figure 7.16) from the nanoscale IMCs using Orowan climb model [214] and Rosler's dislocation detachment model [61], [62] respectively. Two competing recovery mechanisms (Orowan climb and dislocation detachment) are proposed which run in parallel. A dispersion strengthening creep model without threshold stress, originally proposed by Ansell and Weertman [214] is considered to model the Orowan climb mechanism where dislocations bypass the Ag_3Sn particles accumulated at Sn dendritic boundaries by bowing between them. Orowan loops form around these Ag_3Sn particles during creep deformation, their back stress prevents further dislocation bypass and eventually inhibit all deformation. However, these loops can be eliminated by shrinking under their line tension during climb at the particle interface, thereby, assuming that the overall creep rate is controlled by the interfacial climb of these Orowan loops piled up against the particle at Sn dendrite boundaries. A strong attractive interaction between the climbing dislocation and particle is also observed in the post-climb phase of the dislocation [62], [215] and the detachment of the departing dislocation rather than climb is seen to be the rate limiting creep deformation mechanism. Therefore, contribution from both Orowan climb mechanism and dislocation detachment mechanism from the nanoscale Ag_3Sn particle has been calculated in this study and the creep rates are controlled by the

mechanism which contributes to faster plastic flow of dislocations in the material. The governing equations for both mechanisms are illustrated below.

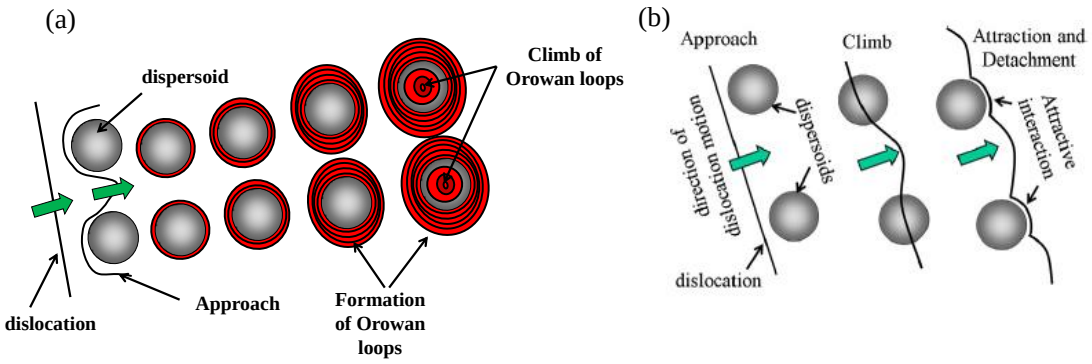

Figure 7.16: Recovery of dislocations from nanoscale Ag_3Sn dispersoids by (a) Orowan climb mechanism and (b) dislocation detachment mechanism

The net shear creep rate of the eutectic Sn-Ag region ($\dot{\gamma}_{eut\text{-}Sn\text{-}Ag}$) is derived from the assumption that the time taken by the dislocation to traverse through a unit cell of the eutectic Sn-Ag phase is the sum of the time taken to taken to travel over Sn matrix phase and Ag_3Sn IMC phase:

$$\frac{1}{\dot{\gamma}_{eut-SnAg}} = \frac{f_{mat}}{\dot{\gamma}_{mat}} + \frac{f_{disp-IMC}}{\dot{\gamma}_{disp-IMC}} \qquad (1)$$

where $\dot{\gamma}_{disp-IMC}$ using Orowan climb mechanism is given by:

$$\dot{\gamma}_{disp-IMC} = \frac{\pi \rho_{sat} \lambda^2 KbD}{k_B T} \frac{b}{d} \left(\frac{\tau_{sat}}{G}\right)^2 \qquad (2)$$

where $\dot{\gamma}_{disp-IMC}$ using Rosler detachment mechanism is given by:

$$\frac{\dot{\gamma}_{disp-IMC}}{\dot{\gamma}_0} = \exp\left(\frac{-Kb^2 r[(1-k)(1-\frac{\tau_{app}}{\tau_d})]^{\frac{3}{2}}}{k_B T}\right) \qquad (3)$$

Where, $f_{disp\text{-}IMC}$ (=1-f_{mat}) refers to the volume fraction of Ag_3Sn in the eutectic Sn-Ag phase; b is Burgers vector (3.18E-10 m) in Sn; K (5.18E10 Pa) is the line tension factor of pure edge dislocation in Sn matrix; r (25 nm; obtained using image processing on ESEM images of SAC305 specimens) and λ (80 nm; obtained using image processing on ESEM images of SAC305 specimens) are the average

radius and interparticle spacing of Ag_3Sn IMCs (obtained from image processing) [59]; d is the average pro-eutectic Sn dendrite size (10 μm) (obtained from image processing), k_B is the Boltzmann constant (1.38E-23 $m^2kg/s^2/K$; T is the temperature in Kelvin (298 K); τ_{sat} is steady state effective stress; $\dot{\gamma}_0$ is the reference strain rate (refer to Equation 5, it is directly proportional to steady state dislocation density), τ_d is the athermal detachment stress (refer to Equation 4); G (21.9E9 Pa) is the shear modulus in BCT Sn [150]; ρ_{sat} is the steady state dislocation density in Ag_3Sn phase and is estimated by modeling three competing processes: (1) dislocation generation; (2) dislocation impediment from pinning of dislocations at IMCs; and (3) dislocation recovery due to climb/detachment from IMCs; k (0.94-0.98) is the relaxation parameter (ratio of the line tension of the detaching dislocation at the particle matric interface versus that in the Sn matrix only). In Rosler's model (Equation 3), τ_{app} has been used instead of τ_{sat}; because authors believe that during the steady state creep the dislocations piling up near the particle are going to exert certain amount of pileup stress on the detaching dislocation, which is going to alter both the applied stress and the athermal detachment stress. Therefore, it has been assumed that the ratio of saturated effective driving stress to saturated athermal detachment stress during secondary creep stage will be very close to the ratio of initial applied stress to initial athermal detachment stress.

Please refer to Section 4.2 in Chapter 4 (Tier 1 anisotropic transient creep chapter) for more details on estimation of relaxation parameter.

Athermal detachment stress (τ_d) is given by:

$$\tau_d = \frac{Kb}{2\lambda}\sqrt{1-k^2} \qquad (4)$$

and the reference strain rate ($\dot{\gamma}_0$) is:

$$\dot{\gamma}_0 = \frac{6\lambda\rho_{sat}}{b}[D_{0L}\exp(-\frac{Q_L}{RT}) + D_{0H}\exp(-\frac{Q_H}{RT})] \qquad (5)$$

where ρ_{sat} is the saturated dislocation density at a secondary stage of creep; subscripts "L" and "H" refer to low and high stress levels respectively; D_{0L} and D_{0H} are the diffusivity constants (1E-4 m^2/sec); Q is the activation energy (Q_L = 31 KJ/mol/K, Q_H = 69 KJ/mol/K); R is the universal gas constant

(please refer to Chapter 6 for more details). The steady state creep rate ($\dot{\gamma}_{Sn}$) of the Sn matrix is modeled by modeling two competing recovery mechanisms (i) recovery of dislocations from forest dislocations by climbing over the impeding dislocation through formation of jogs/kinks and (ii) mass transport diffusion through the Sn lattice.

$$\dot{\gamma}_{Sn-C} = \frac{A_c D_c G b}{k_B T}\left(\frac{b}{\lambda}\right)^2\left(\frac{\tau_{sat}}{G}\right)^2 \quad (6)$$

$$\dot{\gamma}_{Sn-MD} = \frac{A_{MD} D_{MD} G b}{k_B T}\left(\frac{b}{d}\right)^2\left(\frac{\tau_{sat}}{G}\right)^2 \quad (7)$$

where A_C and A_{MD} are model constants for dislocation climb and mass diffusion mechanisms; D_c ($[D_{0L}\exp(-\frac{Q_L}{RT}) + D_{0H}\exp(-\frac{Q_H}{RT})]$) is the diffusivity for climb process; D_{MD} is the diffusivity for mass diffusion process (D_L + 200 D_P $(\tau/G)^2$); where D_L= 6.3E-22 m^2/s is lattice diffusivity co-efficient; D_P (=8.64E-13 m^2/s) is pipe diffusion co-efficient ; G is shear stiffness; λ is the spacing between the dislocations (inversely proportional to the square root of steady state dislocation density); ρ_{sat} the steady state dislocation density in Sn phase during secondary creep stage and is estimated by modeling three competing processes: (1) dislocation generation; (2) dislocation impediment caused by forest dislocations and (3) dislocation recovery either by climb from forest dislocation through formation of jogs/kinks. Please refer to Section 6.3 in Chapter 6 (Secondary creep chapter) for more details on the dislocation density model.

Table 7.2: Dominant slip systems in BCT Sn

SLIP SYSTEMS	SLIP SYSTEMS		RANK
	PLANE	DIR	
1	{100}	[001]	7
2	{110}	[001]	1
3	{100}	[010]	8
4	{110}	1/2[1-11]	2
5	{110}	[1-10]	4
6	{100}	[0-11]	3
7	{001}	[010]	6
8	{001}	[110]	10
9	{011}	[0-11]	5
10	{211}	[0-11]	9

β-tin shows considerable elastic/plastic anisotropy. To understand the slip behavior of Sn in SAC solder joints, relative operation of different slip systems was analyzed in 196 joints with different orientations by Bieler et al. [141] and correlated with the c-axis orientation. Using the result from Bieler et al. [156], [157] active slip systems in SAC solder considered here for this study are ranked in Table 7.2. In order to calculated saturated dislocation density during secondary stage of creep, three dominant slips systems (ranked 1, 2 and 3 in Table 2, since body centered tetragonal Sn is a highly anisotropic material) are considered and saturated dislocation densities for all three systems are estimated as the equilibrium saturation between three competing processes: (1) dislocation generation; (2) dislocation impediment caused by back stress from pinning of dislocations at IMCs; and (3) dislocation recovery due to detachment from IMCs. Steady state dislocation density in Sn phase is estimated by modeling three competing processes: (1) dislocation generation; (2) dislocation impediment caused by forest dislocations and (3) dislocation recovery either by climb from forest dislocation through formation of jogs/kinks. Steady state dislocation density is calculated for three dominant slip systems and the average of the three was taken as isotropic dislocation density for further calculations. Steady state dislocation density is plotted for three dominant slip systems in Ag_3Sn phase in eutectic Sn-Ag phase in Figure 7.17 for specimens aged at RT for 24 hours for illustration purpose.

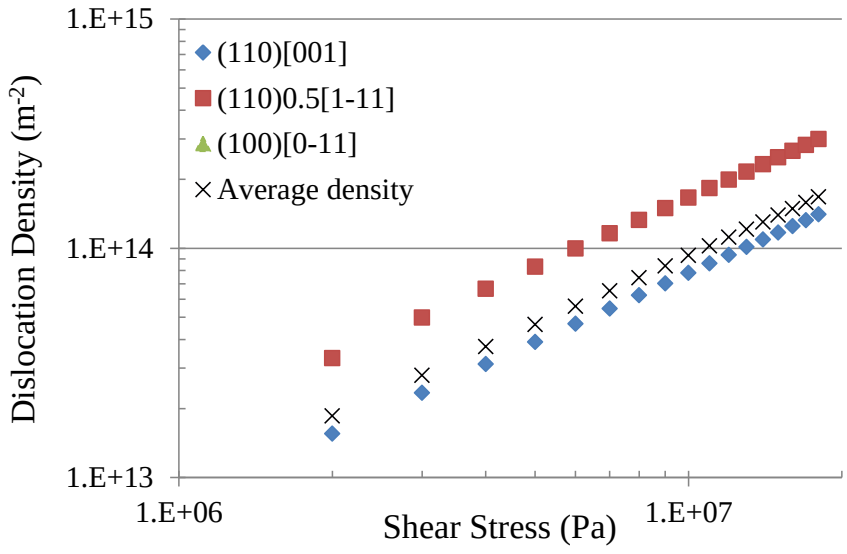

Figure 7.17: Saturated dislocation density during secondary stage of creep for three dominant slip systems in SAC305 solder and average dislocation density used for calculations for specimen aged at RT for 24 hours

In Tier 2 length scale, steady state creep rates of eutectic Sn-Ag phase (calculated using Equations 1, 2 and 3) and Sn inclusion (calculated using Equations 6 and 7) along three dominant slip systems are being utilized to predict the steady state creep rates of SAC single crystal. For a spherical Sn inclusion and cylindrical Cu_6Sn_5 inclusion embedded in a isotropic eutectic Sn-Ag phase, S_{1212} (shear component of the Eshelby tensor) is taken from Mura [216]. For a composite with the inclusion phases characterized by the index i, and the matrix phase characterized by index 0, the effective viscosity of the single crystal SAC305 composite is given by:

$$V = V_0 + \sum_{i=1}^{2} c_i (V_i - V_0)[c_0 S_i V_0^{-1}(V_i - V_0) + 1]^{-1} \quad (8)$$

$$S_{1212} = \frac{4 - 5\nu}{15(1-\nu)} \quad (9)$$

$$S_{1212} = \frac{1}{2(1-\nu)}\left(\frac{1}{4} + \frac{1-2\nu}{2}\right) \quad (10)$$

where, V = Effective viscosity of the composite RVE; V_0 = viscosity of the matrix (eutectic Sn-Ag phase) in unit RVE; V_i = viscosity of the inclusion (Sn inclusion) and Cu_6Sn_5 IMC in unit RVE; S = In-plane shear component (S_{1212}) of the Eshelby tensor of the spherical Sn inclusion (Equation 9) and cylindrical Cu_6Sn_5 inclusion (Equation 10) (cross-section is assumed to be elliptical) embedded in isotropic eutectic Sn-Ag matrix; c_i&c_0 = volume fraction of Sn (0.55 in SAC305; obtained using image processing) and Cu_6Sn_5 (0.03 in SAC305; obtained using image processing) inclusion and volume fraction of matrix in composite RVE; ν (=0.35) is the Poisson's ratio of matrix.

7.5. Mechanistic Model Predictions

Steady state creep strain rates of Ag_3Sn phase predicted for the specimens aged at 100°C for 24 hours are plotted in Figure 7.18; considering Orowan climb as the rate controlling mechanism using Equation 2. Steady state creep strain rates of Ag_3Sn phase predicted for the specimens aged at 100°C for 24 hours are plotted in Figure 7.19; considering dislocation detachment as the rate controlling mechanism using Equation 3. Since both mechanisms act in parallel as recovery mechanism, creep strain rates from both mechanisms are summed up to find out the rate controlling mechanism at different stress levels.

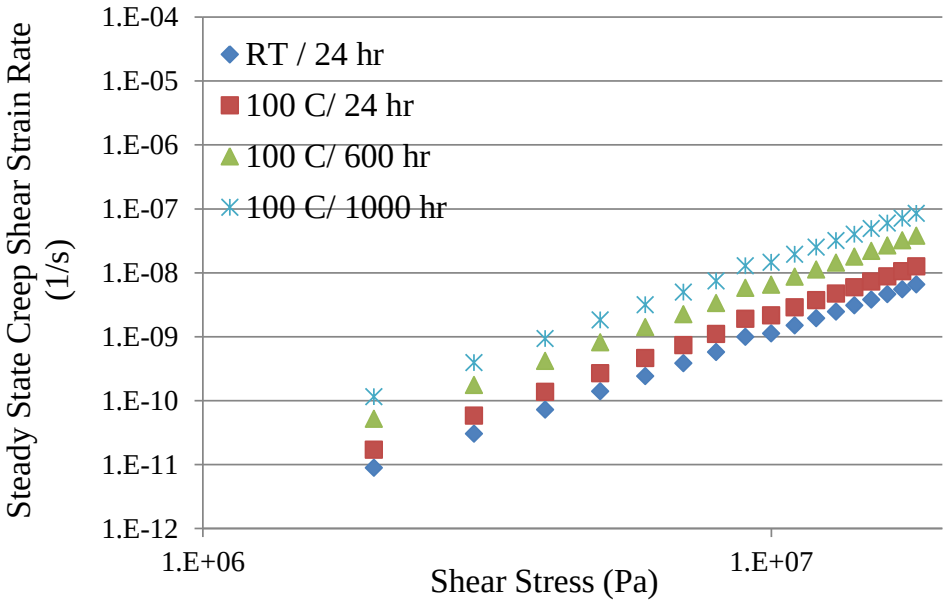

Figure 7.18: Predicted steady state creep strain rates for Ag_3Sn phase, considering Orowan climb as rate controlling mechanism

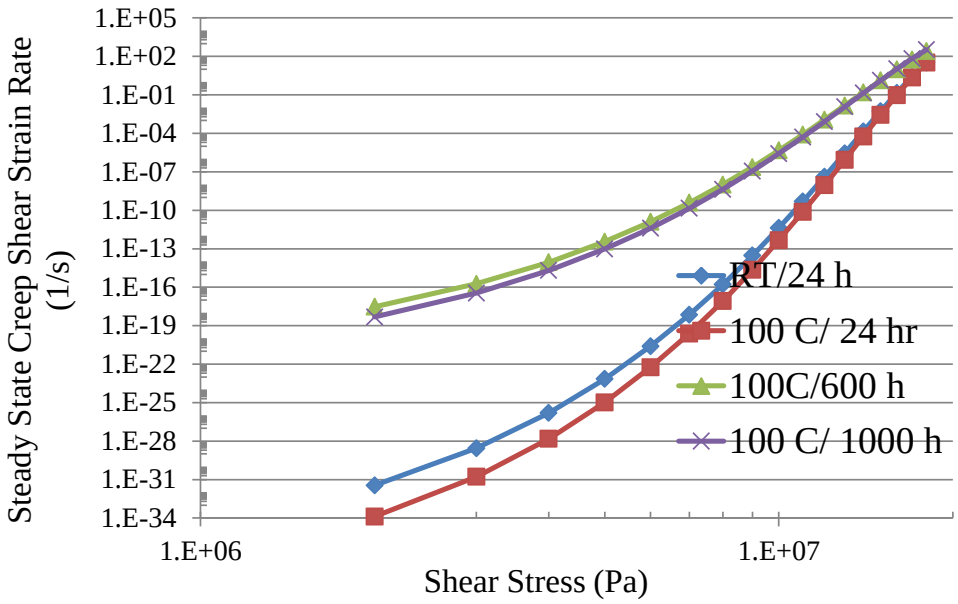

Figure 7.19: Predicted steady state creep strain rates for Ag_3Sn phase, considering dislocation detachment as rate controlling mechanism

Steady state creep strain rates of pure Sn dendritic phase is plotted in Figure 7.20 by combining the creep strain rates predicted using dislocation climb (Equation 6) and mass diffusion as rate controlling mechanism (Equation 7). Steady state creep strain rates of eutectic Sn-Ag phase predicted for the specimens for all aging conditions are plotted in Figure 7.20 by combining the creep strain rates predicted for Ag_3Sn phase and pure Sn phase using Equation 1. As evident from Figure 7.20, steady state creep rates predicted for eutectic Sn-Ag phase is governed by Orowan climb of dislocation at low stress level and dislocation detachment at high stress level and finally it catches up with the creep rates for pure Sn phase for specimens which have been aged for longer duration.

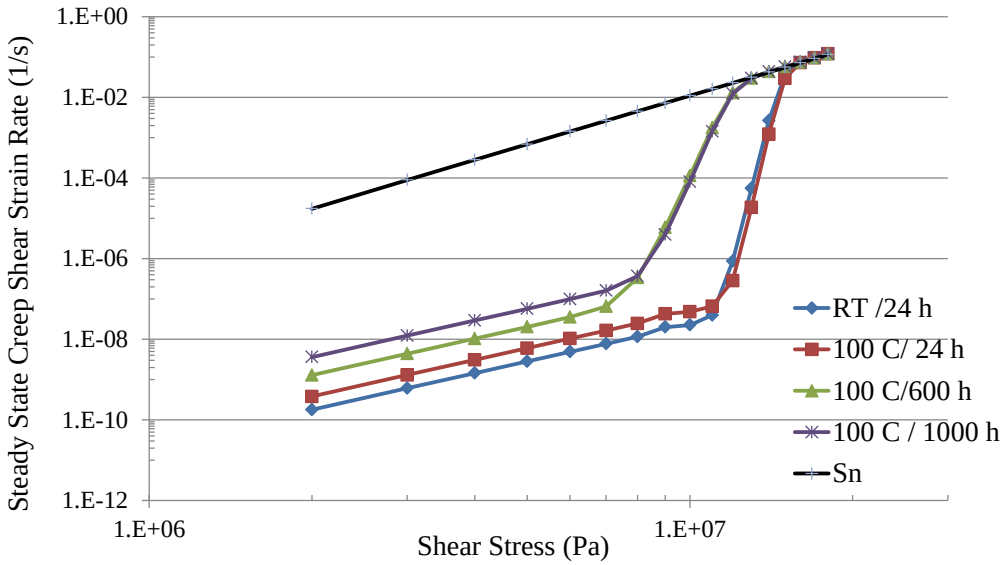

Figure 7.20: Predicted steady state creep strain rates for eutectic Sn-Ag phase and pure Sn dendritic phase in SAC305 single crystal specimens aged for different durations

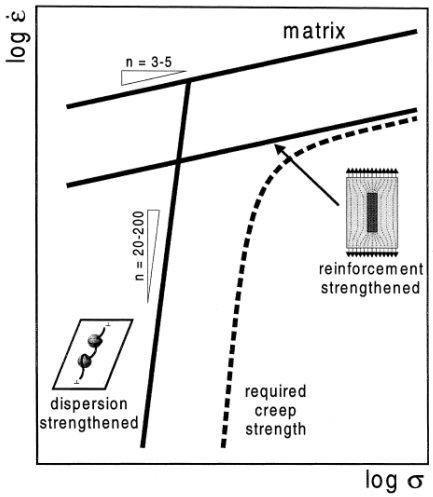

Figure 7.21: Schematic representation of steady state creep strain rate vs. applied stress for particle free matrix, dispersion strengthened material and reinforcement strengthened material [230]

With the increase in isothermal aging duration to 600/1000 hours, the predicted secondary creep resistance of eutectic Sn-Ag phase in SAC305 solder decreased by (4-6) orders of magnitude (refer to Figures 7.20). Creep performance dropped by orders of magnitude in specimens aged for a longer duration because of the increase in size and spacing of nanoscale Ag_3Sn IMCs. Consequently, they are unable to pin the dislocations gliding and climbing over them, thereby reducing the creep resistance. These mechanistic model prediction trends are in agreement with experimental observations reported

in literature [166], [224]. Mechanistic model also predicts a gradual change in slope of the steady state creep curve after certain shear stress level (10 MPa for SAC305 in this study) (refer to Figures 7.20). This sudden change in slope is due to change in rate controlling creep mechanism from Orowan climb to dislocation detachment mechanism. Consequently, secondary creep strain rates predicted for eutectic Sn-Ag phase becomes gradually equal to the strain rate predicted for the reinforced Sn matrix as previously reported in literature [230] as shown in Figure 7.21. Stress exponent predicted for dispersion and precipitation strengthened SAC305 is low (3-4) in low stress regime for first three aging durations and gradually gets higher (~10-12) at high stress regime with increase in aging durations. Steady state creep shear strain rates for SAC305 single crystals are the calculated using viscosities for individual phases (eutectic Sn-Ag phase and pure Sn phase) using Equation 13. Steady state creep strain rates predicted for SAC305 single crystal specimens aged at multiple durations are plotted in Figure 7.22 and compared against the experimentally measured creep rates presented earlier in Figure 7.13. Although the model is able to capture the right trend, detailed anisotropic multiscale models (e.g. in Secondary creep chapter) is needed to model the creep response of discrete specimens. Since, we have only modeled the creep response of single crystal specimens and not captured the contribution of grain boundary sliding; as we would expect in coarse grained specimens the model predictions will be little off from the experimentally measured creep rates.

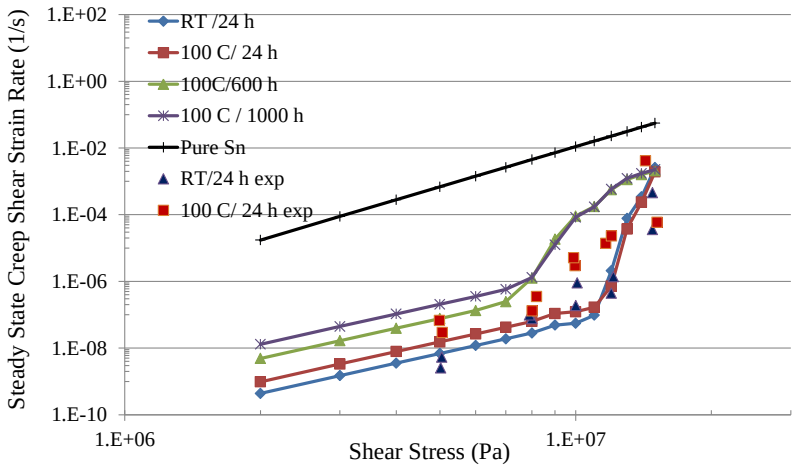

Figure 7.22: Predicted steady state creep strain rates for SAC305 single crystal specimens aged for different durations; compared against the experimentally observed creep rates (coarse grained specimens) for two different aging conditions

As evident from the Figure 7.22, nanoscale Ag_3Sn IMCs are effective in pinning dislocations only up to a certain critical spacing between them for a certain volume fraction in eutectic Sn-Ag phase above which it becomes ineffective in providing dispersion strengthening to the Sn matrix. Figure 7.22 illustrates the above argument; it shows that the secondary creep strain rate of SAC305 single crystal predicted by the multiscale model is (2-5) orders of magnitude lower than that of pure Sn dendritic phase after it is subjected to room temperature aging for 24 hours. But when the same solder alloy is subjected to 1000 hours of isothermal aging at 100°C, the secondary creep response of the SAC305 single crystal comes very close [(1-2) orders of magnitude] to that of secondary creep response of Sn matrix phase. This is because eutectic Sn-Ag phase becomes more uniformly distributed instead of being clustered after extended hours of isothermal aging, and the dispersion strengthening provided by nanoscale Ag_3Sn IMCs almost reduces due to the increase in spacing between Ag_3Sn IMCs above a certain critical limit. Although the current model is based on certain simplifying assumptions, it is able to capture all the right trends as observed in experiments. The current model assumes that interaction effects between neighboring Sn dendrites are negligible, which is not true and needs to be investigated in the future. Further experimental validation is also needed to calibrate the model to experimental creep rates for more specimens aged at multiple durations and temperature in future. Contribution of grain boundary sliding to the creep strain also needs to be modeled in future to make the model more robust and applicable to coarse grained SAC specimens.

7.6. Summary & Conclusions

This paper discusses the effect of isothermal aging on the microstructural evolution and creep properties of SAC305 solder. Both the size and spacing of Ag_3Sn IMCs in the solder bulk show a monotonic increasing trend with increasing aging duration at 100ºC. However, the size and volume fraction of micronscale Cu_6Sn_5 phases exhibit a non-monotonic trend with aging. The size of the Cu_6Sn_5 IMCs present in the bulk of both solders increases by almost 35–45% with increasing aging duration until 600 hours at 100°C; but after 1000 hours the IMC size decreases due to an increase in the Cu_6Sn_5 count and more homogeneous distribution in the Sn matrix.

The secondary creep constitutive response of SAC305 solder interconnects was modeled using a mechanistic multiscale creep model. The results showed that the secondary creep resistance of SAC305 alloy decreased after isothermal aging at 100°C for 24 hours compared to that of room temperature aged specimens by one order of magnitude. The decrease became more drastic after long-term aging (≥600 hours). Steady state creep rates predicted for eutectic Sn-Ag phase is governed by Orowan climb of dislocation at low stress level and dislocation detachment at high stress level and finally it catches up with the creep rates for pure Sn for specimens which have been aged for longer duration. Secondary creep strain rate of SAC305 single crystal predicted by the multiscale model is (7-8) orders of magnitude lower than that of pure Sn dendritic phase after it is subjected to room temperature aging for 24 hours. But when the same solder alloy is subjected to 1000 hours of isothermal aging at 100°C, the secondary creep response of the SAC305 single crystal comes very close [(1-2) orders of magnitude] to that of secondary creep response of Sn matrix phase. This is because eutectic Sn-Ag phase becomes more uniformly distributed instead of being clustered after extended hours of isothermal aging, and the dispersion strengthening provided by nanoscale Ag_3Sn IMCs almost reduces due to the increase in spacing between Ag_3Sn IMCs above a certain critical limit. Although the current model is based on certain simplifying assumptions, it is able to capture all the right trends as observed in experiments. The current model assumes that interaction effects between neighboring Sn dendrites are negligible, which is not true and needs to be investigated in the future. Further experimental validation is also needed to calibrate the model to experimental creep rates for more specimens aged at multiple durations and temperature in future. Contribution of grain boundary sliding to the creep strain also needs to be modeled in future to make the model more robust and applicable to coarse grained SAC specimens.

Chapter 8 : Anisotropic Single Crystal Creep Rate Model Prediction for SAC105 and SAC105X (X = Mn and Sb) Single Crystal Using Modified Dislocation Density Based Secondary Creep Model

Introduction and motivation for this study is already discussed in Chapter 3 of the dissertation (Multiscale modeling of the Effect of Micro-alloying Mn and Sb on Viscoplastic Response of SAC105 Solder). Mechanistic models of dislocation climb and detachment were used to capture the effect of additions of trace amounts of Mn or Sb on the viscoplastic properties of SAC105. The creep properties are affected via dispersion-strengthening due to nanoscale Ag_3Sn IMCs in the eutectic Sn-Ag phase of low silver content SAC solders. These nanoscale dislocation density models were combined at the next larger length scale (that of Sn dendrites and eutectic Sn-Ag colonies), with traditional micromechanics-based homogenization schemes, to capture the load-sharing between the eutectic component and Sn dendrites, to predict the creep strain rates of SAC solder single crystal composites. Major conclusions from that chapter were that the addition of trace amounts of Mn does not refine the grain structure in SAC105 solder joints, confirmed using orientation image mapping and does not form any new phase in SAC105-05Mn joint, confirmed using synchrotron diffraction analysis. The volume fraction of the Ag_3Sn IMCs in the eutectic component is higher in SAC105-05Mn alloys compared to that in SAC105. Addition of trace amount of Mn also resulted in reduced spacing between micronscale Cu_6Sn_5 IMCs because the addition of Mn promoted homogeneous distribution of micronscale Cu_6Sn_5 IMCs. This leads to a smaller Cu_6Sn_5 size and reduced interparticle spacing in SAC105-05Mn compared to that in SAC105. The volume fraction of primary Sn dendrites in an unit RVE is also found to be higher in SAC105 solder compared to that in SAC105-05Mn alloy. The secondary creep resistance of SAC105 solder is predicted to be (1-2) orders of magnitude lower than that of SAC105-05Mn solder, which was able to explain qualitatively the experimental data. This is because the strengthening co-efficient is higher in case of SAC105-05Mn compared to that of SAC105, since it is

inversely proportional to the size and directly proportional to the volume fraction of Cu_6Sn_5 IMCs in SAC solder. The reinforced Sn matrix in SAC105-55Sb is (5-6) orders of magnitude more creep resistant compared to that of SAC105 due to solid solution strengthening of Sn matrix by Sb. The solid solution strengthening of the Sn matrix due to the addition of Sb coupled with the higher volume fraction of Ag_3Sn IMCs in the eutectic component explain the observed higher creep resistance of SAC105-55Sb compared to that of SAC105. The proposed multiscale model captures the secondary creep response of SAC105 and SAC105X solder composites reasonably well.

However, as pointed out in the Chapter 6 of the dissertation (Mechanistic Modeling of the Anisotropic Steady State Viscoplastic Response of SAC305 Single Crystal), the above model used in Chapter 3 was isotropic and had several limitations and cannot really capture the piece to piece variability in creep response of solder joints due to change in grain orientation with respect to loading direction. Therefore, the modeling techniques described in Section 6.2 of Chapter 6 have been utilized here to model the creep response for SAC105 and SAC105X solder joints. Dislocation line tension, mobility of dislocations, dislocation density calculations and composite homogenization techniques in anisotropic medium (described in Section 6.3 of Chapter 6) have been utilized here to predict the creep response of SAC and SAC105X single crystal solder joints. Results are being discussed in next section to understand the capability of the proposed anisotropic model (Chapter 6) to explain the piece to piece variability in the creep response of these coarse grained SAC105X solder joints.

8.1. Mechanistic Model Predictions

Saturated dislocation density during secondary stage of creep, for three dominant slips systems (Table 6.1 in Chapter 6), are calculated using the Equations in Section 6.3 of Chapter 6. Average of the three steady state dislocation densities calculated for three dominant slip systems is taken as isotropic dislocation density for further calculations for all three solder materials (SAC105 and SAC105X). Average steady state dislocation density in Ag_3Sn phase in eutectic Sn-Ag phase is plotted in Figure 8.1 for all three solder materials at RT. Average steady state dislocation density in SAC105X solder is predicted to be one order of magnitude lower than that of SAC105 because of reduced interparticle spacing between nanoscale Ag_3Sn IMCs in SAC105X.

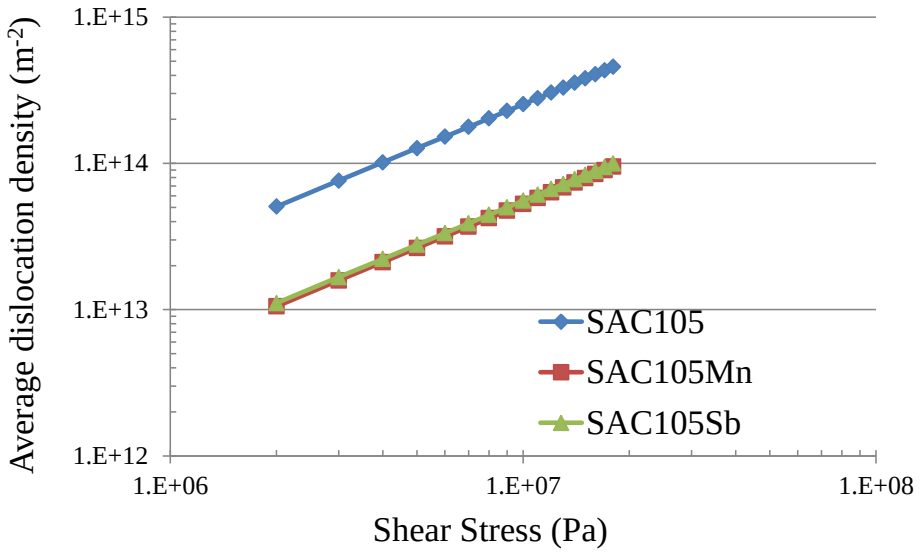

Figure 8.1: Average steady state dislocation density in eutectic Sn-Ag phase for SAC105 and SAC105X solder materials at RT

Steady state creep strain rates of Ag_3Sn phase predicted for all three solder materials are plotted in Figure 8.2; considering Orowan climb as the rate controlling mechanism using Equation 2 in Chapter 6. Steady state creep strain rates of Ag_3Sn phase predicted for all three solder materials are plotted in Figure 8.3; considering dislocation detachment as the rate controlling mechanism using Equation 3 in Chapter 6. Since both mechanisms act in parallel as recovery mechanism, creep strain rates from both mechanisms are summed up to find out the rate controlling mechanism at different stress levels and plotted in Figure 8.4.

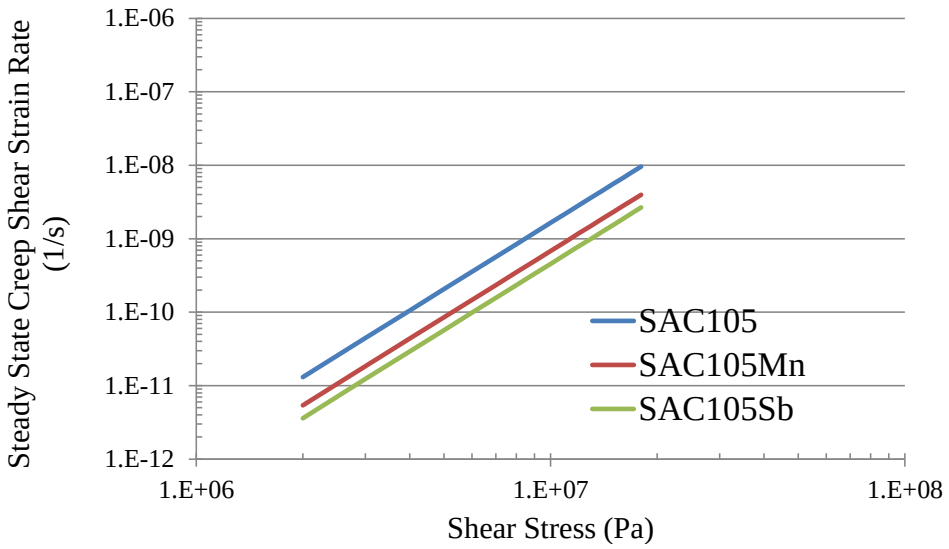

Figure 8.2: Steady state creep strain rates in Ag_3Sn phase in eutectic Sn-Ag phase (Tier 1) for SAC105 and SAC105X solder materials at RT considering Orowan Climb as the rate controlling creep mechanism

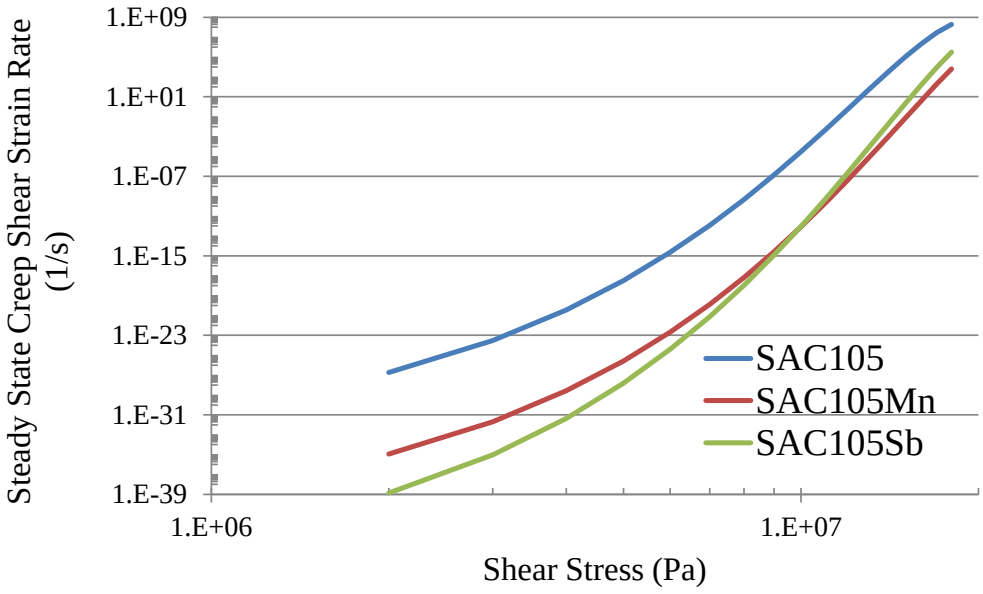

Figure 8.3: Steady state creep strain rates in Ag_3Sn phase in eutectic Sn-Ag phase (Tier 1) for SAC105 and SAC105X solder materials at RT considering Rosler's detachment model as the rate controlling creep mechanism

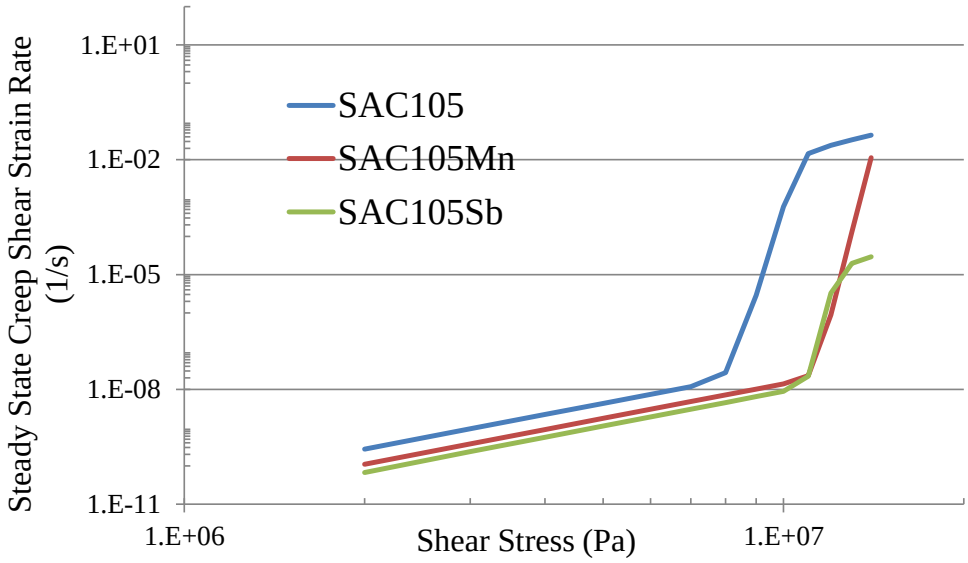

Figure 8.4: Steady state creep strain rates (Tier 1) in eutectic Sn-Ag phase for SAC105 and SAC105X solder materials at RT considering both Orowan and Rosler's model

As evident from Figure 8.4, steady state creep rates predicted for eutectic Sn-Ag phase is governed by Orowan climb of dislocation at low stress level and dislocation detachment at high stress level and finally it catches up with the creep rates for pure Sn phase at very high stress levels.

Anisotropic steady state creep rates calculated along dominant slip systems for eutectic Sn-Ag phase and pure Sn phase is then combined together using calculated Eshelby tensor using anisotropic micromechanics homogenization theory (refer to Equation 13 in Chapter 6) to predict the anisotropic steady state creep rates of SAC105/SAC105X single crystals and is plotted in Figure 8.5. Although the model is able to capture the right trend, the model predictions for creep rates for SAC105/SAC105X single crystals are off from the measured steady state creep rates of coarse grained specimens. Since, we have only modeled the creep response of single crystal specimens and not captured the contribution of grain boundary sliding; as we would expect in coarse grained specimens the model predictions will be different from the experimentally measured creep rates.

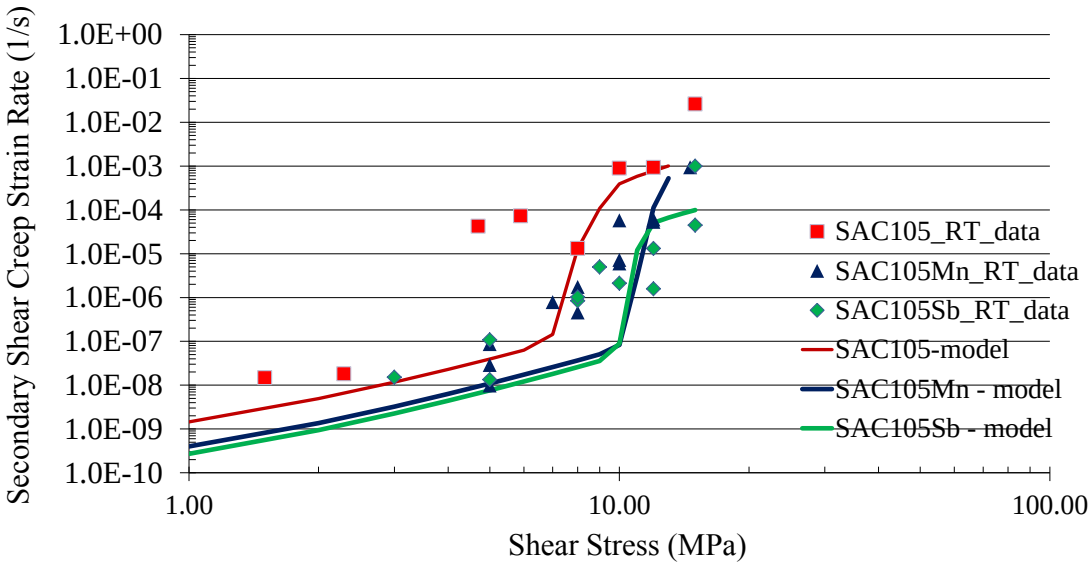

Figure 8.5: Steady state creep strain rates predicted for SAC105 and SAC105X single crystal solders (Tier 1 and Tier 2 combined) compared against the measured steady state creep rates of coarse grained SAC105/SAC105X solder joints

Here, in this section, the proposed anisotropic secondary creep model (in Chapter 6) is now used to predict the steady state creep rate of two coarse grained SAC105Mn specimens using their orientation image maps (OIM) of two discrete SAC105Mn specimens. The Euler angles of the individual grains present in the joints are first obtained using the OIM maps of the two coarse grained specimens obtained using electron back scatter detector (see Figure 8.6). The three Euler angles (see Figure 8.7) of each crystal have been used to calculate the resolved shear stress along the three dominant slip systems (considered in this study) by conducting co-ordinate transformation on second order applied stress tensor. Furthermore, the Euler angles have been used to convert the fourth order viscosity tensors of eutectic Sn-Ag phase and pure Sn phase obtained along individual slip system axes to crystal axes and then back to global specimen axes.

(a) SAC105Mn-2 specimen

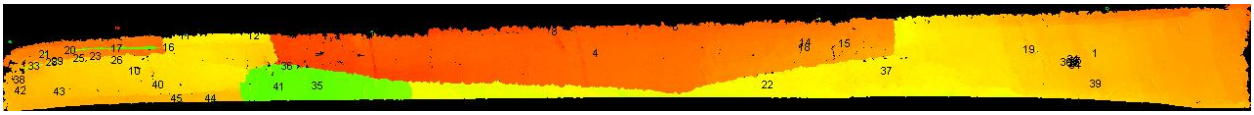

(b) SAC105Mn-4 specimen

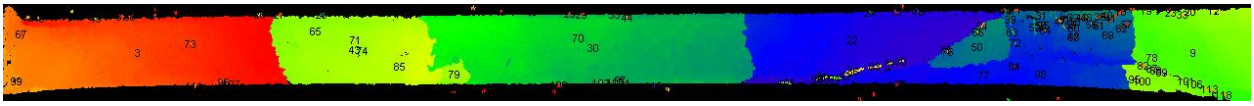

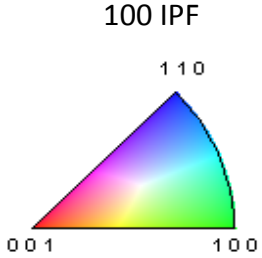

Figure 8.6: Inverse pole figure [100] map of (a) SAC105Mn-2 and (b) SAC105Mn-4 coarse grained specimen

Grain no.	phi 1	PHI	phi2
4	344.708	38.411	58.45
1	196.838	82.689	127.06
10	201.897	54.196	125.42
22	308.639	30.096	41.79
35	321.001	69.4	82.63

Grain no.	phi 1	PHI	phi2
30	111.525	55.699	212.9
3	186.282	75.507	154.77
22	287.988	93.756	92.02
43	220.468	50.731	142.84
9	39.613	68.962	295.04

Figure 8.7: Euler Angles for five largest grains in (a) SAC105Mn-2 and (b) SAC105Mn-4 coarse grained specimens

Using the Euler angles and anisotropic steady state viscosities of eutectic Sn-Ag phase and pure Sn phase in SAC105Mn, anisotropic steady state creep rates for individual grains in SAC105Mn-2 and SAC105Mn-4 specimens are plotted in Figures 8.8 and 8.9.

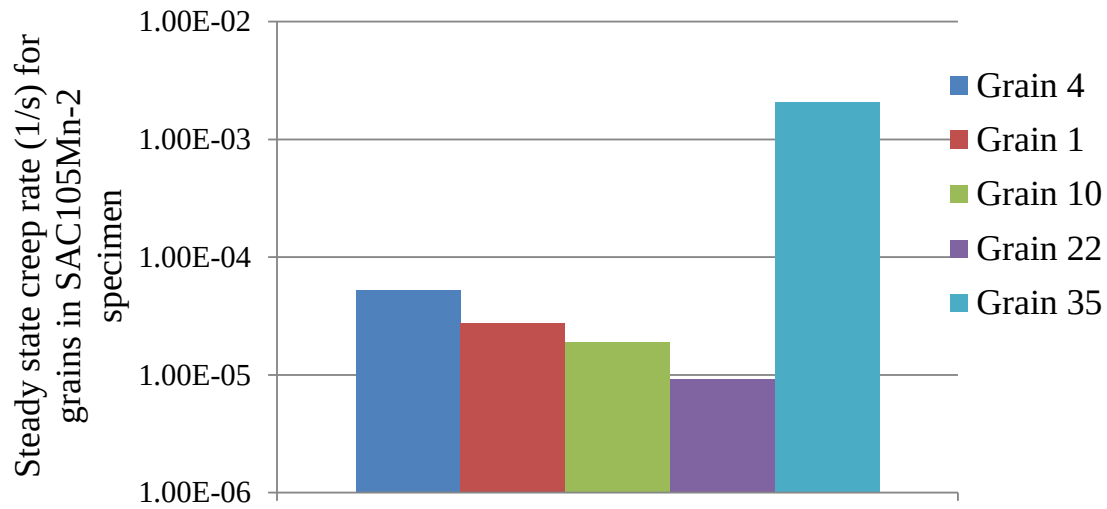

Figure 8.8: Predicted steady state creep rates for five largest crystals in SAC105Mn-2 specimen

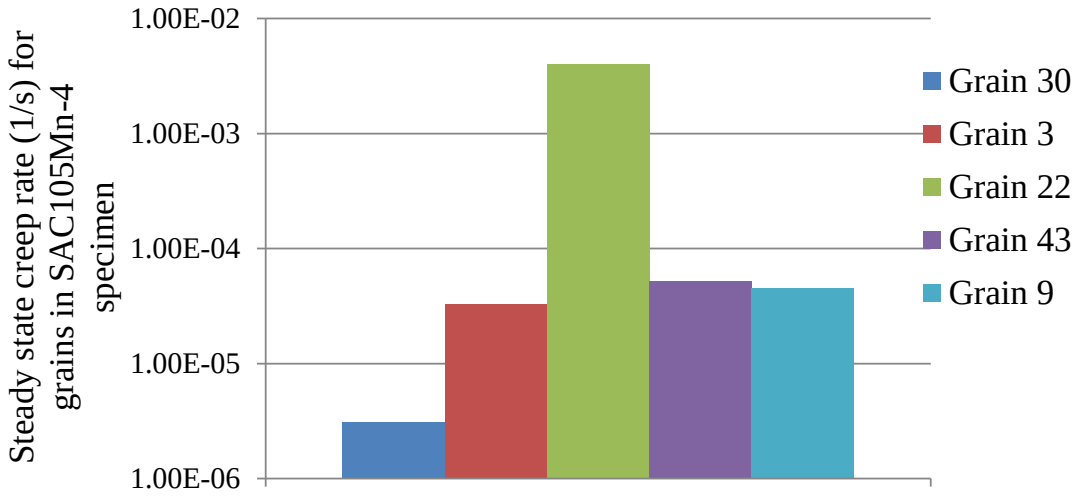

Figure 8.9: Predicted steady state creep rates for five largest crystals in SAC105Mn-4 specimen

Assuming that the viscoplastic creep mechanism is acting in parallel in individual grains in the two coarse grained specimens, steady state creep rate for the whole solder joint is predicted by using a weighted average (using area fraction of each grain) of the creep rates for individual crystals. Contribution from grain boundary sliding is not taken into account in this model and is a limitation of this study. Predicted steady state creep rates for SAC105Mn-2 and SAC105Mn-4 are then compared against the experimentally measured creep rates and plotted in Figure 8.10.

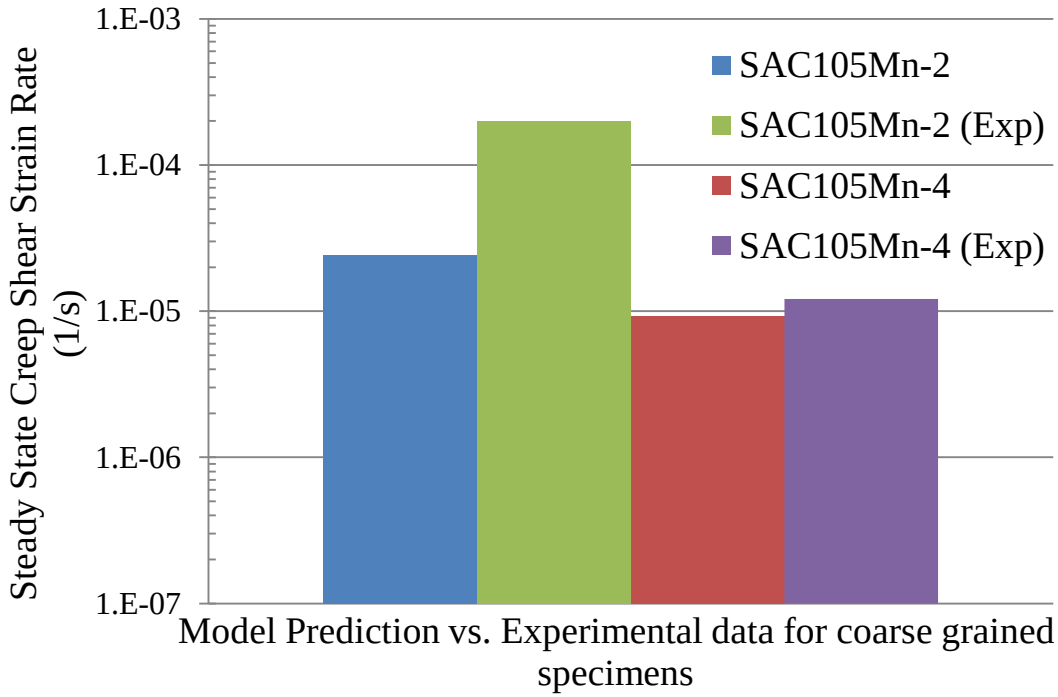

Figure 8.10: Predicted steady state creep rates vs. experimentally observed steady state creep rates for SAC105Mn-2 and SAC105Mn-4 without modeling the effect of grain boundary sliding

8.2. Summary and Conclusions

The anisotropic steady state creep model is able to capture the experimentally observed creep rates of the coarse grained specimens reasonably well. Predicted steady state creep rate is less than that of the experimentally observed rates probably because of the effect of grain boundary sliding is not considered in this study. Contribution of grain boundary sliding to creep strain should be modeled in future to accurately predict the anisotropic steady state creep rates of coarse grained specimens.

Chapter 9 : Summary & Conclusions, Contributions and Limitations & Future Work

Based on the current state-of-the-art of constitutive modeling of the viscoplastic response of microscale heterogeneous SAC solder alloys, this dissertation focused on ten critical unresolved research issues, identified in Chapter 1, that would enhance our understanding of these solder alloys. The ten critical issues are:

1. Microscale SAC solder mechanical properties exhibit significant anisotropy in the as-fabricated state, due to the coarse-grained microstructure and the anisotropy of single crystal Sn. There are no studies that have provided mechanics-based predictive capability to estimate the primary or secondary creep constitutive behavior of such joints based on microstructural morphology, although several studies have pointed towards significant anisotropy in elastic and plastic properties of BCT Sn.
2. The coarse-grained morphology and the single-grain anisotropy together result in every joint having a unique creep response in the global loading axes. This result in significant scatter observed in primary and secondary creep response and this needs to be understood from the microstructural standpoint. The huge variability in primary creep measurements is significantly larger than that observed for secondary creep and also needs to be explored by considering the evolution of dislocation density in primary slip systems of Sn by modeling simultaneously dislocation generation, impediment by forest dislocations and Ag_3Sn particles and dislocation recovery from particles and forest dislocations in dominant slip systems during the creep process. Dislocation density used in a past study by Cuddalorepatta et al. [8] is based on a hypothetical assumption that all the slip planes in BCT Sn are completely saturated with very high dislocation density (~1E21 m^{-2}) when the creep deformation advances to the secondary creep regime. This assumption makes the secondary creep response isotropic and needs to be re-examined in light of the joint-to-joint variability observed in creep response of solder joints.
3. There has been no study which focuses on anisotropic evolution of dislocation density during primary and secondary creep regime along dominant slip systems. This needs to be modeled by

explicitly modeling multiple creep recovery mechanisms (particularly dislocation climb and detachment mechanisms) observed in dispersion strengthened materials e.g. SAC alloys.

4. The detachment of dislocations climb during secondary creep is captured in the literature [59], [60] using dilute concentration approximation (i.e. the model considers only the interaction of a single dislocation with the Ag_3Sn IMC). Interactions between neighboring dislocation fronts need to be accounted for, to handle non-dilute dislocation densities.

5. One of the key parameters of the dislocation detachment model, relaxation parameter (k) [61], [62] (ratio of line tension of dislocation at particle-matrix interface to that in matrix only) used to capture the strong attractive interaction between dislocation and nanoscale particle during the post-climb phase, has been previously modeled as a function of stress and temperature and calibrated against experimental observations of secondary creep rates. However, authors think it is a fundamental property of the material and should have a constant value. The magnitude of k governs how strongly the detachment mechanism contributes to the overall creep rate.

6. SAC alloy is treated as a composite consisting of soft pure Sn dendrite inclusions embedded in a dispersion-strengthened and reinforcement-strengthened Sn-Ag eutectic "matrix". The effective properties of this composite have been obtained in the literature using simple isotropic self-consistent homogenization micromechanics theories [63]. There are no studies that have provided ways to predict the anisotropic viscoplastic properties of SAC single crystals along principal crystallographic directions, based on the time-dependent anisotropic creep response of the individual micro-constituents such as ellipsoidal Sn dendrites and the anisotropic creep properties of the eutectic Sn-Ag phase.

7. The Sn dendritic geometry needs to be extended to handle dendrite lobes of different types of non-spherical geometries because this contributes to the anisotropy of the creep response. Past studies [59] were restricted to spherical lobes of the Sn dendrites.
8. The microstructure of Sn dendrites, nanoscale Ag_3Sn IMCs, and Cu_6Sn_5 IMCs are known to evolve as a function of aging time and temperature, with significant effect on the constitutive response. However, there is no mechanistic predictive capability in the literature to predict the

effect of this microstructural evolution on the primary and secondary creep response of solder interconnects. Hence the practice of utilizing the as-fabricated mechanical properties for modeling the behavior of solder throughout the entire service life is questionable and needs to be investigated.

9. There has been no microstructural bottom-up study in the literature which provides a pro-active way to predict the solder response for any morphology, rather than having to empirically (and parametrically) determine it for every microstructural combination encountered in different solder alloys. Such an empirical approach available in the literature is prohibitively slow and expensive for today's product development cycle time.
10. Effect of the addition of trace elements e.g. Mn and Sb on the creep response of low silver SAC solder has not been explored. There has been no mechanistic modeling study to predict the effect of micro-alloying on creep response of SAC alloys.

The conclusions from the dissertation are discussed in Subsection 9.1, contributions from the dissertation are discussed in Subsection 9.2 and future work from this study is discussed in Subsection 9.3. All three subsections have been summarized next in the same sequence as the chapters are laid out in the dissertation to answer the above issues.

9.1. Summary & Conclusions

Chapter 4: Multiscale modeling of the transient creep response of SAC single crystals – Part I

i] In Tier I, creep deformation is governed by dislocation impediment and recovery at nanoscale Ag_3Sn particles, with recovery being the rate controlling mechanism. Dislocation climb and dislocation detachment at the Ag_3Sn particles are proposed to be the competing rate controlling recovery mechanisms at low (< 12 MPa) and high stress levels (> 12 MPa) respectively and match with the experimental data.

ii] Line tension factor and mobility of dislocations in dominant slip systems of single crystal Sn are estimated based on the elastic crystal anisotropy of body centered tetragonal (BCT) Sn. Line tension factor is found to vary by one order of magnitude between the studied ten slip systems in BCT Sn lattice at RT. Mobility of edge dislocations in most facile slip system is found to be (2-4) times that of

the other two studied slip systems, which is believed to contribute to the anisotropic flow in the SAC single crystal material.

iii] The anisotropic transient creep rate of the eutectic Sn-Ag phase of Tier I is then modeled using above inputs and the evolving dislocation density calculated for dominant glide systems during the transient stage of creep. The evolving dislocation density history is estimated by modeling the equilibrium between five competing processes: (1) dislocation generation; (2) dislocation impediment due to forest dislocations; (3) recovery (by climb and diffusion) from forest dislocations; (4) dislocation impediment caused by back stress from pinning of dislocations at IMC particles; and (5) dislocation recovery due to climb/detachment from Ag_3Sn IMC particles. Of these mechanisms, the third and fifth mechanisms are found to be the rate governing mechanisms for anisotropic transient creep deformation processes for the Sn matrix and for the Ag_3Sn IMC particles, respectively, for the eutectic Sn-Ag alloy. Rate of increase in dislocation density under the applied shear (10 MPa) stress at RT is along (110)0.5[1-11] is found to be one order of magnitude higher than that of in (100)[0-11] slip system because of difference in resolved shear stress for the particular grain orientation found in SAC305 single crystal #1.

iv] The dominant slip systems are determined based on the dislocation mobility and on the orientation angle between the crystal principal axes and the loading direction. Transient creep rate is predicted to be highest along (110)0.5[1-11] slip system and lowest along (100)[0-11] system because of the difference in resolved shear stress and average initial resolved velocity along the slip systems for a particular loading direction in the modeled single crystal SAC305 specimen.

v] Transient creep strain along the most facile slip system (110)[001] is predicted to increase by (1-2) orders of magnitude as the interparticle spacing between nanoscale IMCs increases by a factor of three. Similarly, increase in the volume fraction of nanoscale Ag_3Sn IMCs is predicted to decrease the transient creep rates along (110)[001], which is in agreement with experimental observations.

Chapter 5: Multiscale modeling of the transient creep response of SAC single crystals – Part II

i] The anisotropic creep response of the eutectic phase (from Tier 1) is combined with anisotropic creep response of Sn lobes at Tier 2 using the anisotropic Mori-Tanaka homogenization theory in this paper, to obtain the anisotropic transient creep response in of SAC single crystal along principal crystallographic directions. The Eshelby strain concentration tensors required for this homogenization

process are calculated numerically for ellipsoidal Sn inclusions and cylindrical Cu_6Sn_5 embedded in anisotropic eutectic Sn-Ag matrix. The above model can be used to predict transient creep response for any single crystal specimen with any random orientation with respect to the loading direction.

ii] The multiscale model is validated using experimentally observed transient creep response of one of the SAC305 single crystal specimens. The orientations of SAC single crystal specimens with respect to loading direction were identified with orientation image mapping and then utilized in the model to estimate resolved shear stress along dominant slip directions. The proposed calibrated multiscale model is able to quantitatively predict the transient creep response of second SAC305 single crystal and is in good agreement with the experimentally observed transient creep response.

iii] Transient creep strain rates along [001] direction of SAC305 single crystal #1 is predicted to be 1-2 orders of magnitude higher than that of along [100]/[010] direction.

iv] Predicted shear creep strain along global specimen direction is found to vary by a factor of (1-3) orders of magnitude due to change in one of the Euler angles (φ_1) in SAC305 single crystal #1, which is in agreement with experimental observations.

v] Parametric studies have also been conducted to predict the effect of changing volume fraction and aspect ratio of Sn inclusions on the anisotropic transient creep response of SAC single crystal #1. The model is able to capture the decrease in creep resistance of SAC305 single crystal, when the volume fraction of Sn inclusion in the SAC single crystal increases, which is in agreement with experimental observations.

Chapter 6: Multiscale modeling of the secondary creep response of SAC single crystals

i] At low stress level (<12 MPa), the secondary steady state creep rate along the (110)[001] slip system is predicted to be ten times the creep rate along the (100)[0-11] system. However, at high stress level (>12 MPa), the secondary steady state creep rate along the (110)[001] slip system is predicted to be ten thousand times the creep rate along the (100)[0-11] system. The above predictions are in strong agreement with (1-4) orders of magnitude of anisotropy observed in steady state secondary creep response in SAC305 solder joints tested under identical loading conditions in experiments conducted by several authors [139], [140].

ii] The proposed model is then further used to predict the steady state creep rates of few selected (single crystal and bi-crystal) SAC305 specimens. Very good agreement was observed between the predicted steady state creep rate of two SAC305 single crystal specimens and measured creep rates of the same specimens.

iii] For the bi-crystal specimens, experimentally measured steady state creep rates were found to fall between the predicted creep rates for individual crystals in the joint; pointing towards possible grain boundary sliding during the creep deformation process of multi-crystal specimens.

iv] The predicted steady state creep rate for SAC305 single crystal #1 specimen is found to vary by almost one order of magnitude due to systematic variation of the orientation of Sn dendrites with respect to the loading direction.

Chapter 7: Multiscale modeling of the effect of aging on secondary creep response of SAC305 solder joints

i] The secondary creep constitutive response of SAC305 solder interconnects was modeled using the proposed mechanistic multiscale creep model. Model predicts that the secondary creep resistance of SAC305 alloy decreased after isothermal aging at 100°C for 24 hours compared to that of room temperature aged specimens by one order of magnitude. The decrease becomes more drastic (2-3 orders of magnitude) after long-term aging (≥600 hours); which is agreement with the experimental data.

ii] The steady state creep rates predicted for eutectic Sn-Ag phase are governed by Orowan climb of dislocation at low stress level (<12 MPa) and dislocation detachment at high stress level (>12 MPa) and finally it catches up with the creep rates for pure Sn for specimens which have been aged for longer duration (≥600 hours).

ii] The secondary creep strain rate of SAC305 single crystal predicted by the multiscale model is (7-8) orders of magnitude lower than that of pure Sn dendritic phase after it is subjected to room temperature aging for 24 hours. But when the same solder alloy is subjected to 1000 hours of isothermal aging at 100°C, the secondary creep response of the SAC305 single crystal comes very close [(1-2) orders of magnitude] to that of of the Sn matrix phase. This is because the eutectic Sn-Ag phase becomes more uniformly distributed instead of being clustered after extended hours of isothermal aging, and the

dispersion strengthening provided by nanoscale Ag_3Sn IMCs reduces due to the increase in spacing between Ag_3Sn IMCs. Although the current model is based on certain simplifying assumptions, it is able to capture all these trends observed in experiments.

Chapter 3 & 8: Multiscale modeling of the effect of addition of trace elements (Mn & Sb) on secondary creep response of SAC105 solder joints

i] This study investigates time-dependent viscoplastic response of two relatively new SAC105-X solders —SAC105-05Mn (Sn1.0Ag0.5Cu (SAC105) doped with 0.05 wt-percent Mn); and SAC105-55Sb (SAC105 doped with 0.55 wt-percent Sb). The results showed that the addition of Mn or Sb increases the creep resistance of SAC105 solder by one to two orders of magnitude at the tested stress levels of 2–20 MPa.

ii] The addition of trace amounts of Mn does not refine the grain structure in SAC105 solder joints, confirmed using orientation image mapping and does not form any new phase in SAC105-05Mn joint, confirmed using synchrotron diffraction analysis.

iii] The addition of Mn as a fourth alloying element promotes homogeneous distribution of micron-scale Cu_6Sn_5 intermetallic compounds (IMCs), thereby reducing their interparticle spacing as compared to their spacing in SAC105. On the other hand, addition of Sb does not change the spacing of the Cu_6Sn_5 particle, but reduces the average size of the Sn dendritic lobes. Moreover, Sb also forms solid solution with Sn and strengthens the Sn matrix in SAC105-55Sb itself.

iv] The effects of these microstructural changes (obtained using quantitative image processing) on secondary creep constitutive response of SAC105 solder interconnects were then modeled using a mechanistic multiscale creep model. The mechanistic model was able to capture the trends in the secondary creep constitutive response of the alloys accurately and explain the improvement in the creep resistance of SAC105 due to the addition of Mn and Sb.

9.2. Contributions

Chapter 4: Multiscale modeling of the transient creep response of SAC single crystals – Part I

i] Anisotropic modeling of the transient creep response of the eutectic Sn-Ag phase and pure Sn phase in single crystal SAC solder has been conducted for the very first time and calibrated with the help of limited experimental data.

ii] Line tension and mobility of dislocations along dominant slip systems of anisotropic single crystal BCT Sn have been calculated for the very first time, which has been used to model the evolution of dislocation density in this highly heterogeneous BCT Sn medium. These parameters can also be used as inputs for discrete dislocation dynamics simulations of pure single crystal Sn in future.

iii] The evolution of dislocation density history in eutectic Sn-Ag phase in single crystal SAC solder has been estimated for the first time, by modeling the equilibrium between five competing processes: (1) dislocation generation; (2) dislocation impediment due to forest dislocations; (3) recovery (by climb and diffusion) from forest dislocations; (4) dislocation impediment caused by back stress from pinning of dislocations at IMC particles; and (5) dislocation recovery due to climb/detachment from Ag_3Sn IMC particles. The proposed model is able to explain the piece to piece to variability in transient creep response of eutectic Sn-Ag phase in SAC single crystal.

Chapter 5: Multiscale modeling of the transient creep response of SAC single crystals – Part II

i] This is the first mechanistic model for anisotropic transient creep modeling of SAC single crystals, and has been developed by combining the mechanistic prediction of creep response of the eutectic phase (from Tier 1) with mechanistic prediction of creep response of Sn lobes at Tier 2, using the anisotropic Mori-Tanaka homogenization theory. The proposed multiscale model was calibrated with the help of one single crystal specimen and was able to quantitatively capture the transient creep response of a second SAC305 single crystal reasonably well.

ii] The Eshelby strain concentration tensors required for this homogenization process are calculated numerically for ellipsoidal Sn inclusions embedded in anisotropic eutectic Sn-Ag matrix. Anisotropic creep rates of SAC single crystal can now be calculated for any non-spherical Sn dendritic geometry induced by variations in cooling rates during the reflow process using the calculated Eshelby tensor.

iii] This is the first study to provide parametric insights based on mechanistic microstructural predictions of the effect of grain orientation on the anisotropic transient creep response of SAC single crystals. Predicted shear creep strain along global specimen direction is found to vary by a factor of (1-3) orders of magnitude due to change in one of the Euler angles (φ_1) in SAC305 single crystal #1, which is in agreement with experimental observations.

Chapter 6: Multiscale modeling of the secondary creep response of SAC single crystals

All the contributions of Chapters 4 and 5 apply to this study.

Chapter 7: Multiscale modeling of the effect of aging on secondary creep response of SAC305 solder joints

The proposed multiscale model is capable of predicting both transient and secondary creep response of SAC specimens which have been isothermally aged at multiple durations and temperatures. The mechanistic model is capable of saving significant amount of test time and resources, which goes into testing these microscale specimens at multiple test and aging conditions in laboratories.

Chapter 3 & 8: Multiscale modeling of the effect of addition of trace elements (Mn & Sb) on secondary creep response of SAC105 solder joints

i] Investigated the effects of addition of trace elements (Mn and Sb) on grain morphology, as-cast microstructure and creep response of low silver content SAC105 solder.

ii] Mechanistically modeled the effect of SAC105 micro-alloying using the newly proposed multiscale visco-plastic model. The proposed model is able to capture the piece to piece variability in secondary creep response of two SAC105Mn coarse-grained specimens. This is the first mechanistic modeling study to be able to predict the effect of micro-alloying on creep response.

9.3. Limitations & Future Work

Chapter 4: Multiscale modeling of the transient creep response of SAC single crystals – Part I

i] Contribution of cross-slip phenomena in screw dislocations to transient creep response has been ignored in this study. Molecular dynamics simulations need to be carried out in future to estimate the activation energy for cross-slip so that it can be incorporated into the dislocation density evolution and dislocation recovery models.

ii] Relaxation parameter “k” has been mechanistically derived in this study by taking into account the detachment configuration of a dislocation over the particle instead of using empirically obtained values. The magnitude of “k” governs how strongly the detachment mechanism contributes to the overall creep rate. However, molecular dynamics simulations need to be carried out in future to accurately estimate the relaxation parameter for different 3D configurations of edge/screw dislocations impeded by 3D particles in anisotropic single crystal SAC solder.

iii] The analytical dislocation density evolution model proposed in this study should be calibrated with experimental creep data of eutectic Sn-Ag phase in single crystal SAC solder for better resolution of calibration parameters. Since, fabricating single crystal solder joints is difficult, the analytical model can also be calibrated to creep response from discrete dislocation dynamics simulation of eutectic Sn-Ag phase in single crystal Sn. Line tension and mobility of dislocations in anisotropic Sn medium, calculated in this study, can be used as input parameters for discrete dislocation dynamics simulation. Particle stress fields and stress fields of edge/screw dislocations in anisotropic Sn medium need to be modeled first to model the creep response of SAC single crystals using discrete dislocation dynamics.

iv] In dislocation climb and detachment model, the dislocations are assumed to be randomly distributed in the crystal, so that their stress fields upon the dislocation overcoming the dispersoids are neglected. However, in most practical applications, resulting spatial distribution of lattice dislocations is not random and the stress fields from these pile-ups cannot anymore be assumed to cancel at all points within the material. These stress fields will affect the lead pile-up dislocation pinned by the dispersoid, and either aid or hinder the bypassing processes (Orowan climb or detachment process) by which the controlling dislocation overcomes its obstacle, and thus will increase or decrease the value of the threshold stress. The effect of pileup stress on the effective stress for Orowan Climb and detachment stress for Rosler’s model needs to be modeled in future. As a part of this study, preliminary work on the effect of pileup on the dislocation detachment stress have been modeled and described in the appendix for future work.

Chapter 5: Multiscale modeling of the transient creep response of SAC single crystals – Part II

i] Interactions between neighboring Sn dendrites have not been explicitly modeled in this study, which is a part of the future work. As a result, this study is appropriate for dilute concentration of dendrites and loses accuracy as the dendrite concentration increases.

ii] Contribution of grain boundary sliding to total creep strain has not been modeled in this study. The scope of this dissertation is limited to the anisotropic primary and secondary creep modeling of SAC single crystals. To extend this study in future to predict the anisotropic creep response of coarse grained SAC solder joint, the model will need to include the mechanics of grain boundary sliding.

iii] The outputs of this study can be used as inputs for crystal plasticity finite element (CPFE) modeling in future to capture the thermomechanical cyclic fatigue response of SAC solder joints using anisotropic elastic, plastic and creep properties of single crystal SAC solder.

iv] The proposed model can be used to predict transient creep response for any single crystal specimen with any random orientation and the constitutive properties of individual crystal can be further used to model the whole solder joint containing more than one grain by modeling the grain boundary sliding in future.

Chapter 6: Multiscale modeling of the secondary creep response of SAC single crystals

All the limitations and future work of Chapters 4 and 5 apply to this study.

Chapter 7: Multiscale modeling of the effect of aging on secondary creep response of SAC305 solder joints

i] Further experimental validation is also needed to calibrate the model with experimentally measured creep rates of single crystal SAC specimens aged at multiple durations and temperature in future.

ii] This model appears to provide reasonable predictions (at least for explaining qualitative trends) for coarse-grained joints in as-fabricated stage, but the accuracy systematically drops as the joints are aged for longer duration, resulting in increased spacing between coarse Ag_3Sn IMCs.

Chapter 3 & 8: Multiscale modeling of the effect of addition of trace elements (Mn & Sb) on secondary creep response of SAC105 solder joints

i] This model appears to provide reasonable predictions (at least for explaining qualitative trends) for coarse-grained joints, but the accuracy systematically drops as the contribution of grain boundary

effects begins to increase during loading-induced dynamic recrystallization in thermal cycling conditions.

ii] The anisotropic steady state creep model is able to qualitatively capture the experimentally observed trends in the creep rates of the coarse grained specimens reasonably well, but under-predicts the absolute values of the steady state creep rate , probably because the contribution to creep strain due to grain boundary sliding is not considered in this study. Contribution of grain boundary sliding to creep strain should be modeled in future using FEA to accurately predict the anisotropic steady state creep rates of coarse grained specimens.

Appendices

A1. MATLAB code for calculating dislocation line tension in anisotropic medium

```
clc
clear all
close all
% Elastic stiffness matrix of BCT Sn (from Rayne & Chandrasekhar) and from (Kammer, Cardinal, Vold & Glicksman)
 c11=72.3E9; c12=59.4E9; c13=35.78E9; c33=88.4E9; c44=22.03E9; c66=24.0E9;%values in Pa at 300K
% Elastic stiffness matrix of BCT Sn (from Kammer, Cardinal, Vold & Glicksman)
% c11=65.8E9; c12=58.6E9; c13=37.7E9; c33=80.8E9; c44=19.1E9; c66=21.4E9;%values in Pa at 418 K
c(1,1,1,1) = c11; c(2,2,2,2) = c11; c(3,3,3,3) = c33;
c(1,1,2,2) = c12; c(1,1,3,3) = c13; c(2,2,1,1) = c12;
c(2,2,3,3) = c13; c(3,3,1,1) = c13; c(3,3,2,2) = c13;
c(3,1,3,1) = c44; c(2,3,2,3) = c44; c(3,2,3,2) = c44;
c(1,2,2,1) = c66; c(2,1,1,2) = c66; c(1,3,3,1) = c44;
c(3,1,1,3) = c44; c(2,3,3,2) = c44; c(3,2,2,3) = c44;

% Define slip system m0(slip direction)and n0(slip plane)
n0=[0 0 1]; % slip plane
m0=[1 1 0]; % slip direction
%Define mn, nn, mm matrices for setting up the eigen value problem
a=zeros(3);
nn=a;
nm=a;
mn=a;
mm=a;
for j=1:3
   for k=1:3
      for i=1:3
         for l=1:3
            nn(j,k)=nn(j,k)+n0(i)*c(i,j,k,l)*n0(l);
            nm(j,k)=nm(j,k)+n0(i)*c(i,j,k,l)*m0(l);
            mm(j,k)=mm(j,k)+m0(i)*c(i,j,k,l)*m0(l);
         end
      end
   end
end
mn=nm';
%Create 6x6 matrix N0
N0=zeros(6);
invnn = inv(nn);
N0=-[invnn*nm,invnn;mn*invnn*nm-mm,mn*invnn];
%Solve Eigen equation
[V,D]=eig(N0);
%initializing A, L and P
A = a;
L = a;
P=zeros(1,3);
```

```
for alpha=1:3
   if imag(D(2*alpha,2*alpha))>0
      P(alpha)=D(2*alpha,2*alpha);
      A(:,alpha)=V(1:3,2*alpha);
      L(:,alpha)=V(4:6,2*alpha);
   else
      P(alpha)=D(2*alpha-1,2*alpha-1);
      A(:,alpha)=V(1:3,2*alpha-1);
      L(:,alpha)=V(4:6,2*alpha-1);
   end
end

%normalize A and L
for alpha=1:3
   %AialphaLibeta+AibetaLialpha=delta(alpha,beta)
   ralpha = sqrt(2*sum(A(:,alpha).*L(:,alpha)));
   A(:,alpha) = A(:,alpha)/ralpha;
   L(:,alpha) = L(:,alpha)/ralpha;
end
%Construct Q, B, S matrices using A and L
I=sqrt(-1);
Q = real(2*I*A*A.');
B = real(2*I*L*L.');
S = real(2*I*A*L.'-I*eye(3));
[V D]=eig(B);
```

A2. MATLAB code for Eshelby tensor calculations in anisotropic medium

```
clc
clear all
close all
format short
syms x x1 x2 x3 w real

A1=1;
A2=1;
A3=1;


% Stiffness constants for BCT Sn material (not transversely isotropic)

% c11=72.3E9; c12=59.4E9; c13=35.7E9; c33=88.4E9; c44=22.03E9; c66=6.45E9;
% c14=0; c15=0; c16=0;
% c21=c12; c22=c11; c23=c13; c24=0; c25=0; c26=0;
% c31=c13; c32=c13; c34=0; c35=0; c36=0;
% c41=0; c42=0; c43=0; c45=0; c46=0;
% c51=0; c52=0; c53=0; c54=0; c55= c44; c56=0;
% c61=0; c62=0; c63=0; c64=0; c65=0;

% Model constants for Al matrix (SiC whiskers) from PJ Withers paper; pp 770

c11=2.179E10; c12=0.579E10; c13=0.689E10; c33=10.345E10; c44=1E10; c66=0.8E10;%values in
Pa
c14=0; c15=0; c16=0;
```

```
c21=c12; c22=c11; c23=c13; c24=0; c25=0; c26=0;
c31=c13; c32=c13; c34=0; c35=0; c36=0;
c41=0; c42=0; c43=0; c45=0; c46=0;
c51=0; c52=0; c53=0; c54=0; c55= c44; c56=0;
c61=0; c62=0; c63=0; c64=0; c65=0;


C(1,1,1,1) = c11; C(1,1,2,2) = c12; C(1,1,3,3) = c13; C(1,1,2,3)=c14; C(1,1,1,3)=c15; C(1,1,1,2)=c16;
C(1,1,3,2)=c14; C(1,1,3,1)=c15; C(1,1,2,1)=c16;
C(2,2,1,1) = c21; C(2,2,2,2) = c22; C(2,2,3,3) = c23; C(2,2,2,3)=c24; C(2,2,1,3)=c25; C(2,2,1,2)=c26;
C(2,2,3,2)=c24; C(2,2,3,1)=c25; C(2,2,2,1)=c26;
C(3,3,1,1) = c31; C(3,3,2,2) = c32; C(3,3,3,3) = c33; C(3,3,2,3)=c34; C(3,3,1,3)=c35; C(3,3,1,2)=c36;
C(3,3,3,2)=c34; C(3,3,3,1)=c35; C(3,3,2,1)=c36;
C(2,3,1,1) = c41; C(2,3,2,2) = c42; C(2,3,3,3) = c43; C(2,3,2,3)=c44; C(2,3,1,3)=c45; C(2,3,1,2)=c46;
C(2,3,3,2)=c44; C(2,3,3,1)=c45; C(2,3,2,1)=c46; C(3,2,1,1)=c41; C(3,2,2,2)=c42; C(3,2,3,3)=c43;
C(1,3,1,1) = c51; C(1,3,2,2) = c52; C(1,3,3,3) = c53; C(1,3,2,3)=c54; C(1,3,1,3)=c55; C(1,3,1,2)=c56;
C(3,1,1,1)=c51; C(3,1,2,2)=c52; C(3,1,3,3)=c53; C(1,3,3,2)=c54; C(1,3,3,1)=c55; C(1,3,2,1)=c56;
C(1,2,1,1) = c61; C(1,2,2,2) = c62; C(1,2,3,3) = c63; C(1,2,2,3)=c64; C(1,2,1,3)=c65; C(1,2,1,2)=c66;
C(2,1,1,1)=c61; C(2,1,2,2)=c62; C(2,1,3,3)=c63; C(1,2,3,2)=c64; C(1,2,3,1)=c65; C(1,2,2,1)=c66;
A3=1/A3;

x1=(sqrt(1-x^2)*sin(w))/A1;
x2=(sqrt(1-x^2)*cos(w))/A2;
x3=x/A3;

% CALCULATE Kik(xeta)

K_11=C(1,1,1,1)*x1^2+C(1,1,1,2)*x1*x2+C(1,1,1,3)*x1*x3+C(1,2,1,1)*x2*x1+C(1,2,1,2)*x2^2+C(
1,2,1,3)*x2*x3+C(1,3,1,1)*x3*x1+C(1,3,1,2)*x3*x2+C(1,3,1,3)*x3^2;
K_22=C(2,1,2,1)*x1^2+C(2,1,2,2)*x1*x2+C(2,1,2,3)*x1*x3+C(2,2,2,1)*x2*x1+C(2,2,2,2)*x2^2+C(
2,2,2,3)*x2*x3+C(2,3,2,1)*x3*x1+C(2,3,2,2)*x3*x2+C(2,3,2,3)*x3^2;
K_33=C(3,1,3,1)*x1^2+C(3,1,3,2)*x1*x2+C(3,1,3,3)*x1*x3+C(3,2,3,1)*x2*x1+C(3,2,3,2)*x2^2+C(
3,2,3,3)*x2*x3+C(3,3,3,1)*x3*x1+C(3,3,3,2)*x3*x2+C(3,3,3,3)*x3^2;
K_12=C(1,1,2,1)*x1^2+C(1,1,2,2)*x1*x2+C(1,1,2,3)*x1*x3+C(1,2,2,1)*x2*x1+C(1,2,2,2)*x2^2+C(
1,2,2,3)*x2*x3+C(1,3,2,1)*x3*x1+C(1,3,2,2)*x3*x2+C(1,3,2,3)*x3^2;
K_13=C(1,1,3,1)*x1^2+C(1,1,3,2)*x1*x2+C(1,1,3,3)*x1*x3+C(1,2,3,1)*x2*x1+C(1,2,3,2)*x2^2+C(
1,2,3,3)*x2*x3+C(1,3,3,1)*x3*x1+C(1,3,3,2)*x3*x2+C(1,3,3,3)*x3^2;
K_21=C(2,1,1,1)*x1^2+C(2,1,1,2)*x1*x2+C(2,1,1,3)*x1*x3+C(2,2,1,1)*x2*x1+C(2,2,1,2)*x2^2+C(
2,2,1,3)*x2*x3+C(2,3,1,1)*x1*x3+C(2,3,1,2)*x2*x3+C(2,3,1,3)*x3^2;
K_23=C(2,1,3,1)*x1^2+C(2,1,3,2)*x1*x2+C(2,1,3,3)*x1*x3+C(2,2,3,1)*x2*x1+C(2,2,3,2)*x2^2+C(
2,2,3,3)*x2*x3+C(2,3,3,1)*x3*x1+C(2,3,3,2)*x3*x2+C(2,3,3,3)*x3^2;
K_31=C(3,1,1,1)*x1^2+C(3,1,1,2)*x1*x2+C(3,1,1,3)*x1*x3+C(3,2,1,1)*x2*x1+C(3,2,1,2)*x2^2+C(
3,2,1,3)*x2*x3+C(3,3,1,1)*x1*x3+C(3,3,1,2)*x2*x3+C(3,3,1,3)*x3^2;
K_32=C(3,1,2,1)*x1^2+C(3,1,2,2)*x1*x2+C(3,1,2,3)*x1*x3+C(3,2,2,1)*x2*x1+C(3,2,2,2)*x2^2+C(
3,2,2,3)*x2*x3+C(3,3,2,1)*x1*x3+C(3,3,2,2)*x2*x3+C(3,3,2,3)*x3^2;


% CALCULATE Nij(xeta)

RN_11=(K_22*K_33-2*K_23);
RN_22=(K_11*K_33-2*K_13);
RN_33=(K_11*K_22-2*K_12);
RN_23=-(K_11*K_23-K_13*K_12);
RN_13=(K_12*K_23-K_13*K_22);
RN_12=-(K_12*K_33-K_23*K_13);
RN_21=(K_32*K_13-K_33*K_12);
RN_31=(K_12*K_23-K_13*K_22);
```

```
RN_32=(K_13*K_21-K_11*K_23);


% CALCULATE D(xeta)

D=(K_11*K_22*K_33)+(K_21*K_32*K_13)+(K_31*K_12*K_23)-(K_11*K_32*K_23)-
(K_21*K_12*K_33)-(K_31*K_22*K_13);

% Calculate Green's function
G_1111=x1*x1*RN_11/D;
G_1112=x1*x2*RN_11/D;
G_1113=x1*x3*RN_11/D;
G_1121=G_1112;
G_1122=x2*x2*RN_11/D;
G_1123=x2*x3*RN_11/D;
G_1131=G_1113;
G_1132=G_1123;
G_1133=x3*x3*RN_11/D;

G_2211=x1*x1*RN_22/D;
G_2212=x1*x2*RN_22/D;
G_2213=x1*x3*RN_22/D;
G_2221=G_2212;
G_2222=x2*x2*RN_22/D;
G_2223=x2*x3*RN_22/D;
G_2231=G_2213;
G_2232=G_2223;
G_2233=x3*x3*RN_22/D;

G_3311=x1*x1*RN_33/D;
G_3312=x1*x2*RN_33/D;
G_3313=x1*x3*RN_33/D;
G_3321=G_3312;
G_3322=x2*x2*RN_33/D;
G_3323=x2*x3*RN_33/D;
G_3331=G_3313;
G_3332=G_3323;
G_3333=x3*x3*RN_33/D;

G_2311=x1*x1*RN_23/D;
G_3211=x1*x1*RN_32/D;
G_2312=x1*x2*RN_23/D;
G_3212=x1*x2*RN_32/D;
G_2313=x1*x3*RN_23/D;
G_3213=x1*x3*RN_32/D;
G_2321=G_2312;
G_3221=G_3212;
G_2322=x2*x2*RN_23/D;
G_3222=x2*x2*RN_32/D;
G_2323=x2*x3*RN_23/D;
G_3223=x2*x3*RN_32/D;
G_2331=G_2313;
G_3231=G_3213;
G_2332=G_2323;
G_3232=G_3223;
G_2333=x3*x3*RN_23/D;
G_3233=x3*x3*RN_32/D;
```

```
G_1311=x1*x1*RN_13/D;
G_3111=x1*x1*RN_31/D;
G_1312=x1*x2*RN_13/D;
G_3112=x1*x2*RN_31/D;
G_1313=x1*x3*RN_13/D;
G_3113=x1*x3*RN_31/D;
G_1321=G_1312;
G_3121=G_3112;
G_1322=x2*x2*RN_13/D;
G_3122=x2*x2*RN_31/D;
G_1323=x2*x3*RN_13/D;
G_3123=x2*x3*RN_31/D;
G_1331=G_1313;
G_3131=G_3113;
G_1332=G_1323;
G_3132=G_3123;
G_1333=x3*x3*RN_13/D;
G_3133=x3*x3*RN_31/D;

G_1211=x1*x1*RN_12/D;
G_2111=x1*x1*RN_21/D;
G_1212=x1*x2*RN_12/D;
G_2112=x1*x2*RN_21/D;
G_1213=x1*x3*RN_12/D;
G_2113=x1*x3*RN_21/D;
G_1221=G_1212;
G_2121=G_2112;
G_1222=x2*x2*RN_12/D;
G_2122=x2*x2*RN_21/D;
G_1223=x2*x3*RN_12/D;
G_2123=x2*x3*RN_21/D;
G_1231=G_1213;
G_2131=G_2113;
G_1232=G_1223;
G_2132=G_2123;
G_1233=x3*x3*RN_12/D;
G_2133=x3*x3*RN_21/D;

% Create functions for double numerical integration using n-point Gauss Quadrature

F_1111=2*(C(1,1,1,1)*G_1111+C(1,2,1,1)*G_1112+C(1,3,1,1)*G_1113+C(2,1,1,1)*G_1211+C(2,2,
1,1)*G_1212+C(2,3,1,1)*G_1213+C(3,1,1,1)*G_1311+C(3,2,1,1)*G_1312+C(3,3,1,1)*G_1313);
F_1122=2*(C(1,1,2,2)*G_1111+C(1,2,2,2)*G_1112+C(1,3,2,2)*G_1113+C(2,1,2,2)*G_1211+C(2,2,
2,2)*G_1212+C(2,3,2,2)*G_1213+C(3,1,2,2)*G_1311+C(3,2,2,2)*G_1312+C(3,3,2,2)*G_1313);
F_1133=2*(C(1,1,3,3)*G_1111+C(1,2,3,3)*G_1112+C(1,3,3,3)*G_1113+C(2,1,3,3)*G_1211+C(2,2,
3,3)*G_1212+C(2,3,3,3)*G_1213+C(3,1,3,3)*G_1311+C(3,2,3,3)*G_1312+C(3,3,3,3)*G_1313);

F_2211=2*(C(1,1,1,1)*G_2121+C(1,2,1,1)*G_2122+C(1,3,1,1)*G_2123+C(2,1,1,1)*G_2221+C(2,2,
1,1)*G_2222+C(2,3,1,1)*G_2223+C(3,1,1,1)*G_2321+C(3,2,1,1)*G_2322+C(3,3,1,1)*G_2323);
F_2222=2*(C(1,1,2,2)*G_2121+C(1,2,2,2)*G_2122+C(1,3,2,2)*G_2123+C(2,1,2,2)*G_2221+C(2,2,
2,2)*G_2222+C(2,3,2,2)*G_2223+C(3,1,2,2)*G_2321+C(3,2,2,2)*G_2322+C(3,3,2,2)*G_2323);
F_2233=2*(C(1,1,3,3)*G_2121+C(1,2,3,3)*G_2122+C(1,3,3,3)*G_2123+C(2,1,3,3)*G_2221+C(2,2,
3,3)*G_2222+C(2,3,3,3)*G_2223+C(3,1,3,3)*G_2321+C(3,2,3,3)*G_2322+C(3,3,3,3)*G_2323);

F_3311=2*(C(1,1,1,1)*G_3131+C(1,2,1,1)*G_3132+C(1,3,1,1)*G_3133+C(2,1,1,1)*G_3231+C(2,2,
1,1)*G_3232+C(2,3,1,1)*G_3233+C(3,1,1,1)*G_3331+C(3,2,1,1)*G_3332+C(3,3,1,1)*G_3333);
```

```
F_3322=2*(C(1,1,2,2)*G_3131+C(1,2,2,2)*G_3132+C(1,3,2,2)*G_3133+C(2,1,2,2)*G_3231+C(2,2,
2,2)*G_3232+C(2,3,2,2)*G_3233+C(3,1,2,2)*G_3331+C(3,2,2,2)*G_3332+C(3,3,2,2)*G_3333);
F_3333=2*(C(1,1,3,3)*G_3131+C(1,2,3,3)*G_3132+C(1,3,3,3)*G_3133+C(2,1,3,3)*G_3231+C(2,2,
3,3)*G_3232+C(2,3,3,3)*G_3233+C(3,1,3,3)*G_3331+C(3,2,3,3)*G_3332+C(3,3,3,3)*G_3333);

F_2323=2*(C(1,1,2,3)*G_2131+C(1,2,2,3)*G_2132+C(1,3,2,3)*G_2133+C(2,1,2,3)*G_2231+C(2,2,
2,3)*G_2232+C(2,3,2,3)*G_2233+C(3,1,2,3)*G_2331+C(3,2,2,3)*G_2332+C(3,3,2,3)*G_2333);
F_1313=2*(C(1,1,1,3)*G_1131+C(1,2,1,3)*G_1132+C(1,3,1,3)*G_1133+C(2,1,1,3)*G_1231+C(2,2,
1,3)*G_1232+C(2,3,1,3)*G_1233+C(3,1,1,3)*G_1331+C(3,2,1,3)*G_1332+C(3,3,1,3)*G_1333);
F_1212=2*(C(1,1,1,2)*G_1121+C(1,2,1,2)*G_1122+C(1,3,1,2)*G_1123+C(2,1,1,2)*G_1221+C(2,2,
1,2)*G_1222+C(2,3,1,2)*G_1223+C(3,1,1,2)*G_1321+C(3,2,1,2)*G_1322+C(3,3,1,2)*G_1323);

%  Use 2-point Gauss Quadrature and n-point Gauss Quadrature to do the first integration over xeta
and second integration over omega

% % 2 point Gauss-Legendre Abscissas and Weights

% nx=[4.9554
%     1.3278];
% nw=[3.1416
%     3.1416];

% % 3 point Gauss-Legendre Abscissas and Weights

% nx=[5.5751
%     3.1416
%     0.7081];
% nw=[1.7453
%     2.7925
%     1.7453];

% 5 point Gauss-Legendre Abscissas and Weights

% nx=[5.9884
%     4.8332
%     3.1416
%     1.4499
%     0.2947];
% nw=[0.7443
%     1.5037
%     1.7872
%     1.5037
%     0.7443];

% % 10 point Gauss-Legendre Abscissas and Weights

% nx=[6.2012
%     5.8593
%     5.2760
%     4.5031
%     3.6093
%     2.6739
%     1.7800
%     1.0072
%     0.4239
%     0.0820];
%
```

```
% nw=[0.2095
%     0.4695
%     0.6883
%     0.8459
%     0.9284
%     0.9284
%     0.8459
%     0.6883
%     0.4695
%     0.2095];

% % 20 point Gauss-Legendre Abscissas and Weights
%
% nx=[6.2616
% 6.17
% 6.0075
% 5.7778
% 5.4863
% 5.1398
% 4.7465
% 4.3156
% 3.8572
% 3.382
% 2.9012
% 2.426
% 1.9676
% 1.5367
% 1.1434
% 0.7969
% 0.5054
% 0.2757
% 0.1132
% 0.0216];
%
% nw=[0.0553
% 0.1276
% 0.1969
% 0.2616
% 0.3202
% 0.3713
% 0.4137
% 0.4464
% 0.4686
% 0.4799
% 0.4799
% 0.4686
% 0.4464
% 0.4137
% 0.3713
% 0.3202
% 0.2616
% 0.1969
% 0.1276
% 0.0553];

% % 50 point Gauss-Legendre Abscissas and Weights
```

```
% nx=[6.2796
% 6.2644
% 6.2372
% 6.1979
% 6.1469
% 6.0842
% 6.0101
% 5.9249
% 5.829
% 5.7227
% 5.6063
% 5.4805
% 5.3456
% 5.2022
% 5.0507
% 4.892
% 4.7264
% 4.5547
% 4.3775
% 4.1956
% 4.0096
% 3.8202
% 3.6282
% 3.4343
% 3.2393
% 3.0439
% 2.8489
% 2.655
% 2.463
% 2.2736
% 2.0876
% 1.9056
% 1.7285
% 1.5568
% 1.3912
% 1.2324
% 1.081
% 0.9376
% 0.8027
% 0.6768
% 0.5605
% 0.4542
% 0.3582
% 0.2731
% 0.199
% 0.1363
% 0.0852
% 0.046
% 0.0187
% 0.0036];
%
% nw=[0.0091
% 0.0212
% 0.0333
% 0.0452
% 0.0569
% 0.0684
```

```
% 0.0797
% 0.0906
% 0.1012
% 0.1114
% 0.1212
% 0.1305
% 0.1393
% 0.1475
% 0.1552
% 0.1623
% 0.1687
% 0.1745
% 0.1797
% 0.1841
% 0.1878
% 0.1908
% 0.1931
% 0.1946
% 0.1953
% 0.1953
% 0.1946
% 0.1931
% 0.1908
% 0.1878
% 0.1841
% 0.1797
% 0.1745
% 0.1687
% 0.1623
% 0.1552
% 0.1475
% 0.1393
% 0.1305
% 0.1212
% 0.1114
% 0.1012
% 0.0906
% 0.0797
% 0.0684
% 0.0569
% 0.0452
% 0.0333
% 0.0212
% 0.0091];



F_1111_x1=1*subs(F_1111,x,0.5774);
F_1111_w1=sum(nw.*subs(F_1111_x1,w,nx));
F_1111_x2=1*subs(F_1111,x,-0.5774);
F_1111_w2=sum(nw.*subs(F_1111_x2,w,nx));
I_1111=F_1111_w1+F_1111_w2;

F_1122_x1=1*subs(F_1122,x,0.5774);
F_1122_w1=sum(nw.*subs(F_1122_x1,w,nx));
F_1122_x2=1*subs(F_1122,x,-0.5774);
F_1122_w2=sum(nw.*subs(F_1122_x2,w,nx));
```

```
I_1122=F_1122_w1+F_1122_w2;

F_1133_x1=1*subs(F_1133,x,0.5774);
F_1133_w1=sum(nw.*subs(F_1133_x1,w,nx));
F_1133_x2=1*subs(F_1133,x,-0.5774);
F_1133_w2=sum(nw.*subs(F_1133_x2,w,nx));
I_1133=F_1133_w1+F_1133_w2;

F_2211_x1=1*subs(F_2211,x,0.5774);
F_2211_w1=sum(nw.*subs(F_2211_x1,w,nx));
F_2211_x2=1*subs(F_2211,x,-0.5774);
F_2211_w2=sum(nw.*subs(F_2211_x2,w,nx));
I_2211=F_2211_w1+F_2211_w2;

F_2222_x1=1*subs(F_2222,x,0.5774);
F_2222_w1=sum(nw.*subs(F_2222_x1,w,nx));
F_2222_x2=1*subs(F_2222,x,-0.5774);
F_2222_w2=sum(nw.*subs(F_2222_x2,w,nx));
I_2222=F_2222_w1+F_2222_w2;

F_2233_x1=1*subs(F_2233,x,0.5774);
F_2233_w1=sum(nw.*subs(F_2233_x1,w,nx));
F_2233_x2=1*subs(F_2233,x,-0.5774);
F_2233_w2=sum(nw.*subs(F_2233_x2,w,nx));
I_2233=F_2233_w1+F_2233_w2;

F_3311_x1=1*subs(F_3311,x,0.5774);
F_3311_w1=sum(nw.*subs(F_3311_x1,w,nx));
F_3311_x2=1*subs(F_3311,x,-0.5774);
F_3311_w2=sum(nw.*subs(F_3311_x2,w,nx));
I_3311=F_3311_w1+F_3311_w2;

F_3322_x1=1*subs(F_3322,x,0.5774);
F_3322_w1=sum(nw.*subs(F_3322_x1,w,nx));
F_3322_x2=1*subs(F_3322,x,-0.5774);
F_3322_w2=sum(nw.*subs(F_3322_x2,w,nx));
I_3322=F_3322_w1+F_3322_w2;

F_3333_x1=1*subs(F_3333,x,0.5774);
F_3333_w1=sum(nw.*subs(F_3333_x1,w,nx));
F_3333_x2=1*subs(F_3333,x,-0.5774);
F_3333_w2=sum(nw.*subs(F_3333_x2,w,nx));
I_3333=F_3333_w1+F_3333_w2;

F_2323_x1=1*subs(F_2323,x,0.5774);
F_2323_w1=sum(nw.*subs(F_2323_x1,w,nx));
F_2323_x2=1*subs(F_2323,x,-0.5774);
F_2323_w2=sum(nw.*subs(F_2323_x2,w,nx));
I_2323=F_2323_w1+F_2323_w2;

F_1313_x1=1*subs(F_1313,x,0.5774);
F_1313_w1=sum(nw.*subs(F_1313_x1,w,nx));
F_1313_x2=1*subs(F_1313,x,-0.5774);
F_1313_w2=sum(nw.*subs(F_1313_x2,w,nx));
I_1313=F_1313_w1+F_1313_w2;

F_1212_x1=1*subs(F_1212,x,0.5774);
```

```
F_1212_w1=sum(nw.*subs(F_1212_x1,w,nx));
F_1212_x2=1*subs(F_1212,x,-0.5774);
F_1212_w2=sum(nw.*subs(F_1212_x2,w,nx));
I_1212=F_1212_w1+F_1212_w2;


% Calculate Eshelby (S) tensor for general anisotropic material

S_1111=I_1111/8/pi()
S_1122=I_1122/8/pi()
S_1133=I_1133/8/pi()
S_2211=I_2211/8/pi()
S_2222=I_1111/8/pi()
S_2233=I_2233/8/pi()
S_3311=I_3311/8/pi()
S_3322=I_3322/8/pi()
S_3333=1-(I_2222/8/pi())
S_1212=I_1212/8/pi()
S_1313=I_1313/8/pi()
S_2323=I_2323/8/pi()


% The determination of the elastic field of an ellipsoidal inclusion in a transversely isotropic medium - P.J. Withers (Philosophical Magazine A, 1989, vol. 59, No. 4, pp. 759-781)
% Stiffness tensor of Eut. Sn-Ag matrix
% L0 = stiffness matrix for eutectic Sn-Ag phase
clc
clear all
close all


% Model constants for Al matrix (SiC whiskers) from PJ Withers paper; pp 770
% L0=[2.179E10 0.579E10 0.689E10 0 0 0;0.579E10 2.179E10 0.689E10 0 0 0;0.689E10 0.689E10 10.345E10 0 0 0;0 0 0 1E10 0 0;0 0 0 0 1E10 0;0 0 0 0 0 0.8E10];

% Model constants isotropic material
% L0=[6.73E10 2.88E10 2.88E10 0 0 0;2.88E10 6.73E10 2.88E10 0 0 0;2.88E10 2.88E10 6.73E10 0 0 0;0 0 0 1.92E10 0 0;0 0 0 0 1.92E10 0;0 0 0 0 0 1.92E10];

% L0 = stiffness matrix for eutectic Sn-Ag phase
L0=[7.39E10 5.97E10 3.67E10 0 0 0;5.97E10 7.4E10 3.67E10 0 0 0;3.64E10 3.66E10 9.03E10 0 0 0;0 0 0 2.26E10 0 0;0 0 0 0 2.26E10 0;0 0 0 0 0 2.45E10];

c11=L0(1,1);
c22=L0(2,2);
c33=L0(3,3);
c44=L0(4,4);
c55=L0(5,5);
c66=L0(6,6);
c12=L0(1,2);
c13=L0(1,3);

% Lattice constants of Sn
a=1;
c=1;
c1_3=sqrt(c11*c33);
neu3=sqrt(c66/c44);
```

```
D=1/4/pi()/c44/neu3;

neu1=((c1_3-c13)*(c1_3+c13+2*c44)/4/c33/c44)^0.5+((c1_3+c13)*(c1_3-c13-2*c44)/4/c33/c44)^0.5;
neu2=((c1_3-c13)*(c1_3+c13+2*c44)/4/c33/c44)^0.5-((c1_3+c13)*(c1_3-c13-2*c44)/4/c33/c44)^0.5;


A1=-(c44-c33*neu1^2)/(8*pi()*c33*c44*(neu1^2-neu2^2)*neu1^2);
A2=(c44-c33*neu2^2)/(8*pi()*c33*c44*(neu1^2-neu2^2)*neu2^2);

k1=(c11/neu1^2-c44)/(c13+c44);
k2=(c11/neu2^2-c44)/(c13+c44);
k3=(c11/neu3^2-c44)/(c13+c44);

if (neu1*c)<a
G_1=(a^2-neu1^2*c^2)^0.5;
F_1=atan(G_1/neu1/c);
I1_1=-(2*pi()*c/G_1^3)*(neu1*c*G_1-a^2*F_1);
I2_1=-(4*pi()*a^2*c/G_1^3)*(F_1-G_1/neu1/c);
else if (neu1*c)>a
    G_1=(neu1^2*c^2-a^2)^0.5;
    F_1=acosh(neu1*c/a);
    I1_1=(2*pi()*c/G_1^3)*(neu1*c*G_1-a^2*F_1);
    I2_1=(4*pi()*a^2*c/G_1^3)*(F_1-G_1/neu1/c);
   end
end

if (neu2*c)<a
G_2=(a^2-neu2^2*c^2)^0.5;
F_2=atan(G_2/neu2/c);
I1_2=-(2*pi()*c/G_2^3)*(neu2*c*G_2-a^2*F_2);
I2_2=-(4*pi()*a^2*c/G_2^3)*(F_2-G_2/neu2/c);
else if (neu2*c)>a
    G_2=(neu2^2*c^2-a^2)^0.5;
    F_2=acosh(neu2*c/a);
    I1_2=(2*pi()*c/G_2^3)*(neu2*c*G_2-a^2*F_2);
    I2_2=(4*pi()*a^2*c/G_2^3)*(F_2-G_2/neu2/c);
   end
end


if (neu3*c)<a
G_3=(a^2-neu3^2*c^2)^0.5;
F_3=atan(G_3/neu3/c);
I1_3=-(2*pi()*c/G_3^3)*(neu3*c*G_3-a^2*F_3);
I2_3=-(4*pi()*a^2*c/G_3^3)*(F_3-G_3/neu3/c);
else if (neu3*c)>a
    G_3=(neu3^2*c^2-a^2)^0.5;
    F_3=acosh(neu3*c/a);
    I1_3=(2*pi()*c/G_3^3)*(neu3*c*G_3-a^2*F_3);
    I2_3=(4*pi()*a^2*c/G_3^3)*(F_3-G_3/neu3/c);
   end
end



S1111=(2*((c44*(1+k1)*A1*neu1^3*I1_1)+(c44*(1+k2)*A2*neu2^3*I1_2)))-
(c66*((A1*neu1*I1_1)+(A2*neu2*I1_2)))+0.5*D*c66*I1_3
```

```
S1122=0.1*((2*((c44*(1+k1)*A1*neu1^3*I1_1)+(c44*(1+k2)*A2*neu2^3*I1_2)))-
(3*c66*((A1*neu1*I1_1)+(A2*neu2*I1_2)))+0.5*D*c66*I1_3)
S1133=2*((neu1*A1*(c13-c33*k1*neu1^2)*I1_1)+(neu2*A2*(c13-c33*k2*neu2^2)*I1_2))
S2211=S1122
S2222=S1111
S2233=S1133
S3311=2*((c44*neu1^5*k1*A1*(1+k1)*I2_1)+(c44*neu2^5*k2*A2*(1+k2)*I2_2))-
2*((c66*neu1^3*k1*A1*I2_1)+(c66*neu2^3*k2*A2*I2_2))
S3322=S3311
S3333=2*((neu1^3*k1*A1*(c13-c33*k1*neu1^2)*I2_1)+(neu2^3*k2*A2*(c13-
c33*k2*neu2^2)*I2_2))

S1212=c66*((A1*neu1*I1_1)+(A2*neu2*I1_2))+0.5*c66*D*I1_3
S1313=0.5*c44*((A1*neu1^3*(1+k1)*(I2_1-2*k1*I1_1))+(A2*neu2^3*(1+k2)*(I2_2-
2*k2*I1_2)))+0.25*D*c44*I2_3*neu3^2
S2323=S1313
```

A3. MATLAB code for second and fourth order tensor co-ordinate transformation

```
clc
clear all
close all

% % Euler angles from OIM data of Subhasis's specimen SAC305-1
% Grain no. 4
% phi1=33.947*pi()/180;
% PHI=69.553*pi()/180;
% phi2=358.62*pi()/180;

% Grain no. 2
% phi1=279.852*pi()/180;
% PHI=35.862*pi()/180;
% phi2=55.91*pi()/180;

% % Euler angles from OIM data of Subhasis's specimen SAC305-2
% % Grain no. 12
% phi1=17.52*pi()/180;
% PHI=18.844*pi()/180;
% phi2=304.94*pi()/180;

% % Grain no. 28
% phi1=225.892*pi()/180;
% PHI=28.907*pi()/180;
% phi2=96.00*pi()/180;

% Subhasis single crystal specimen
phi1=297.125*pi()/180;
PHI=41.375*pi()/180;
phi2=21.075*pi()/180;

% phi1=270*pi()/180; % rotated by x amount (90 degree - 90 180 270 360)
% PHI=41.375*pi()/180;
% phi2=21.075*pi()/180;

% % Gayatri single crystal specimen (Bulk of the specimen)
```

```
% phi1=52.69*pi()/180;
% PHI=50.38*pi()/180;
% phi2=24.78*pi()/180;

% % Euler angles from OIM data of Gayatri's single crystal specimen (Fillet region)

% % Green region (Fillet)
% phi1=162.21*pi()/180;
% PHI=68.13*pi()/180;
% phi2=75.01*pi()/180;

% % Blue region (Fillet)
% phi1=106.61*pi()/180;
% PHI=114.54*pi()/180;
% phi2=26.1*pi()/180;


% velocity of edge dislocation in Sn without impediment from forest dislocation and precipitates at shear stress of 10 MPa
% v0_ss1=102.69; %m/sec
% v0_ss2=59.69; %m/sec
% v0_ss3=106.15; %m/sec

a11=cos(phi2)*cos(phi1)-cos(PHI)*sin(phi1)*sin(phi2);
a12=cos(phi2)*sin(phi1)+cos(PHI)*cos(phi1)*sin(phi2);
a13=sin(PHI)*sin(phi2);
a21=-sin(phi2)*cos(phi1)-cos(PHI)*sin(phi1)*cos(phi2);
a22=-sin(phi2)*sin(phi1)+cos(PHI)*cos(phi1)*cos(phi2);
a23=sin(PHI)*cos(phi2);
a31=sin(PHI)*sin(phi1);
a32=-sin(PHI)*cos(phi1);
a33=cos(PHI);
sigma=[0 10 0;10 0 0;0 0 0];
a=[a11 a12 a13; a21 a22 a23; a31 a32 a33];
a*a'
sigmanew=a*sigma*a'

h1=sin(PHI)*sin(phi2);
k1=sin(PHI)*cos(phi2);
l1=cos(PHI);

u1=cos(phi1)*cos(phi2)-sin(phi1)*cos(PHI)*sin(phi2);
v1=-cos(phi1)*sin(phi2)-sin(phi1)*cos(PHI)*cos(phi2);
w1=sin(phi1)*sin(PHI);

a1=[h1 k1 l1];
b1=[u1 v1 w1];

h=(h1/min(abs(a1)));
k=(k1/min(abs(a1)));
l=(l1/min(abs(a1)));

u=(u1/min(abs(b1)));
v=(v1/min(abs(b1)));
w=(w1/min(abs(b1)));
```

```
t11=[k*w-v*l];
t12=-[h*w-u*l];
t13=[h*v-u*k];

c1=[t11 t12 t13];

t1=(t11/min(abs(c1)));
t2=(t12/min(abs(c1)));
t3=(t13/min(abs(c1)));

% coordinate system 1 (crystal coordinate system)
e1p =[h k l]; e2p = [t1 t2 t3]; e3p = [u v w];
e1p=e1p/norm(e1p);
e2p=e2p/norm(e2p);
e3p=e3p/norm(e3p)

% coordinate system 2 (slip system #1 coordinate system)
e11 =  [1 1 0]; e12  = [1 -1 0]; e13 = [0 0 1];
e11=e11/norm(e11);
e12=e12/norm(e12);
e13=e13/norm(e13);

%rotation matrix between crystal and slip system #1
Q1 = [ dot(e11,e1p) dot(e11,e2p) dot(e11,e3p)
     dot(e12,e1p) dot(e12,e2p) dot(e12,e3p)
     dot(e13,e1p) dot(e13,e2p) dot(e13,e3p) ];

% coordinate system 2 (slip system #2 coordinate system)
e21 =  [1 1 0]; e22  = [0.5 -0.5 -1]; e23 = [0.5 -0.5 0.5];
e21=e21/norm(e21);
e22=e22/norm(e22);
e23=e23/norm(e23);

%rotation matrix between crystal and slip system #1
Q2 = [ dot(e21,e1p) dot(e21,e2p) dot(e21,e3p)
     dot(e22,e1p) dot(e22,e2p) dot(e22,e3p)
     dot(e23,e1p) dot(e23,e2p) dot(e23,e3p) ];

% coordinate system 2 (slip system #3 coordinate system)
e31 =  [1 0 0]; e32  = [0 -1 -1]; e33 = [0 -1 1];
e31=e31/norm(e31);
e32=e32/norm(e32);
e33=e33/norm(e33);

%rotation matrix between crystal and slip system #1
Q3 = [ dot(e31,e1p) dot(e31,e2p) dot(e31,e3p)
     dot(e32,e1p) dot(e32,e2p) dot(e32,e3p)
     dot(e33,e1p) dot(e33,e2p) dot(e33,e3p) ];



% slip system SS1(110)[001]
Q1'*Q1
sigma_SS1=Q1*sigmanew*Q1'

% slip system SS2(110)0.5[1-11]
Q2'*Q2
```

```
sigma_SS2=Q2*sigmanew*Q2'

% slip system SS3(100)[0-11]
Q3'*Q3
sigma_SS3=Q3*sigmanew*Q3'



clear all;
clc;
% Euler Angles
phi1=297.125*pi()/180;
PHI=41.375*pi()/180;
phi2=21.075*pi()/180;

% Transformation matrices
a11=cos(phi2)*cos(phi1)-cos(PHI)*sin(phi1)*sin(phi2);
a12=cos(phi2)*sin(phi1)+cos(PHI)*cos(phi1)*sin(phi2);
a13=sin(PHI)*sin(phi2);
a21=-sin(phi2)*cos(phi1)-cos(PHI)*sin(phi1)*cos(phi2);
a22=-sin(phi2)*sin(phi1)+cos(PHI)*cos(phi1)*cos(phi2);
a23=sin(PHI)*cos(phi2);
a31=sin(PHI)*sin(phi1);
a32=-sin(PHI)*cos(phi1);
a33=cos(PHI);

a=[a11 a12 a13;a21 a22 a23;a31 a32 a33];

h1=sin(PHI)*sin(phi2);
k1=sin(PHI)*cos(phi2);
l1=cos(PHI);

u1=cos(phi1)*cos(phi2)-sin(phi1)*cos(PHI)*sin(phi2);
v1=-cos(phi1)*sin(phi2)-sin(phi1)*cos(PHI)*cos(phi2);
w1=sin(phi1)*sin(PHI);

a1=[h1 k1 l1];
b1=[u1 v1 w1];

h=round(h1/min(a1));
k=round(k1/min(a1));
l=round(l1/min(a1));

u=round(u1/min(b1));
v=round(v1/min(b1));
w=round(w1/min(b1));

t11=[k*w-v*l];
t21=-[h*w-u*l];
t31=[h*v-u*k];

c1=[t11 t21 t31];

t1=round(t11/min(c1));
t2=round(t21/min(c1));
t3=round(t31/min(c1));
```

```
b11=(u*0+v*0+w*1)/sqrt(0^2+0^2+1^2)/sqrt(u^2+v^2+w^2);
b12=(t1*0+t2*0+t3*1)/sqrt(0^2+0^2+1^2)/sqrt(t1^2+t2^2+t3^2);
b13=(h*0+k*0+l*1)/sqrt(0^2+0^2+1^2)/sqrt(h^2+k^2+l^2);

b21=(u*1+v*(-1)+w*0)/sqrt(1^2+(-1)^2+0^2)/sqrt(u^2+v^2+w^2);
b22=(t1*1+t2*(-1)+t3*0)/sqrt(1^2+(-1)^2+0^2)/sqrt(t1^2+t2^2+t3^2);
b23=(h*1+k*(-1)+l*0)/sqrt(1^2+(-1)^2+0^2)/sqrt(h^2+k^2+l^2);

b31=(u*1+v*1+w*0)/sqrt(1^2+1^2+0^2)/sqrt(u^2+v^2+w^2);
b32=(t1*1+t2*1+t3*0)/sqrt(1^2+1^2+0^2)/sqrt(u^2+v^2+w^2);
b33=(h*1+k*1+l*0)/sqrt(1^2+1^2+0^2)/sqrt(h^2+k^2+l^2);

c11=(u*0.5+v*(-0.5)+w*0.5)/sqrt(0.5^2+(-0.5)^2+0.5^2)/sqrt(u^2+v^2+w^2);
c12=(t1*0.5+t2*(-0.5)+t3*0.5)/sqrt(0.5^2+(-0.5)^2+0.5^2)/sqrt(t1^2+t2^2+t3^2);
c13=(h*0.5+k*(-0.5)+l*0.5)/sqrt(0.5^2+(-0.5)^2+0.5^2)/sqrt(h^2+k^2+l^2);

c21=(u*0.5+v*(-0.5)+w*(-1))/sqrt(0.5^2+(-0.5)^2+(-1)^2)/sqrt(u^2+v^2+w^2);
c22=(t1*0.5+t2*(-0.5)+t3*(-1))/sqrt(0.5^2+(-0.5)^2+(-1)^2)/sqrt(t1^2+t2^2+t3^2);
c23=(h*0.5+k*(-0.5)+l*(-1))/sqrt(0.5^2+(-0.5)^2+(-1)^2)/sqrt(h^2+k^2+l^2);

c31=(u*1+v*1+w*0)/sqrt(1^2+1^2+0^2)/sqrt(u^2+v^2+w^2);
c32=(t1*1+t2*1+t3*0)/sqrt(1^2+1^2+0^2)/sqrt(t1^2+t2^2+t3^2);
c33=(h*1+k*1+l*0)/sqrt(1^2+1^2+0^2)/sqrt(h^2+k^2+l^2);

d11=(u*0+v*(-1)+w*1)/sqrt(0^2+(-1)^2+1^2)/sqrt(u^2+v^2+w^2);
d12=(t1*0+t2*(-1)+t3*1)/sqrt(0^2+(-1)^2+1^2)/sqrt(t1^2+t2^2+t3^2);
d13=(h*0+k*(-1)+l*1)/sqrt(0^2+(-1)^2+1^2)/sqrt(h^2+k^2+l^2);

d21=(u*0+v*(-1)+w*(-1))/sqrt(0^2+(-1)^2+(-1)^2)/sqrt(u^2+v^2+w^2);
d22=(t1*0+t2*(-1)+t3*(-1))/sqrt(0^2+(-1)^2+(-1)^2)/sqrt(t1^2+t2^2+t3^2);
d23=(h*0+k*(-1)+l*(-1))/sqrt(0^2+(-1)^2+(-1)^2)/sqrt(h^2+k^2+l^2);

d31=(u*1+v*0+w*0)/sqrt(1^2+0^2+0^2)/sqrt(u^2+v^2+w^2);
d32=(t1*1+t2*0+t3*0)/sqrt(1^2+0^2+0^2)/sqrt(t1^2+t2^2+t3^2);
d33=(h*1+k*0+l*0)/sqrt(1^2+0^2+0^2)/sqrt(h^2+k^2+l^2);

b=[b11 b12 b13; b21 b22 b23;b31 b32 b33];
c=[c11 c12 c13; c21 c22 c23;c31 c32 c33];
d=[d11 d12 d13; d21 d22 d23;d31 d32 d33];

data= xlsread('input.xlsx');
c1 = 0.55; % Sn inclusion volume fraction
c0 = 1 - c1; % Eut. Sn-Ag phase volume fraction
c11 = 0.03; % Cu6Sn5 inclusion volume fraction

% Eshelby tensor for aspect ratio 2 (Sn inclusions)
% E =[0.3118 0.2031 -0.0756 0 0 0; 0.1877 0.3118 -0.0658 0 0 0; 0.1178 0.1219 0.8141 0 0 0;0 0 0 0.8141 0 0;0 0 0 0 0.6104 0;0 0 0 0 0 0.1717];  % Eshelby tensor for ellipsoidal Sn inclusion (aspect ratio = 5) embedded in anisotropic eut. Sn-Ag phase
%
S11=E(1,1);S12=E(1,2);S13=E(1,3);S21=E(2,1);S22=E(2,2);S23=E(2,3);S31=E(3,1);S32=E(3,2);S33=E(3,3);S44=E(4,4);S55=E(5,5);S66=E(6,6);
% Eshelby tensor for aspect ratio 10 (Sn inclusions)
E=[0.0215 0.0152 -0.0094 0 0 0;0.015 0.0215 -0.0093 0 0 0;0.3761 0.3762 0.9853 0 0 0;0 0 0 0.9853 0 0;0 0 0 0 0.9743 0;0 0 0 0 0 0.0106];
```

```
S11=E(1,1);S12=E(1,2);S13=E(1,3);S21=E(2,1);S22=E(2,2);S23=E(2,3);S31=E(3,1);S32=E(3,2);S33
=E(3,3);S44=E(4,4);S55=E(5,5);S66=E(6,6);
% Eshelby tensor for aspect ratio 50 (cylindrical Cu6Sn5 inclusions)
EC=[8.85E-4 6.28E-4 -3.99E-4 0 0 0;6.28E-4 8.85E-4 -3.99E-4 0 0 0;0.4049 0.4049 0.9994 0 0 0;0 0 0
0.9994 0 0;0 0 0 0 0.9989 0;0 0 0 0 0 4.35E-4];% Eshelby tensor for cylindrical Cu6Sn5 inclusion
(aspect ratio = 50) embedded in anisotropic eut. Sn-Ag phase
SC11=EC(1,1);SC12=EC(1,2);SC13=EC(1,3);SC21=EC(2,1);SC22=EC(2,2);SC23=EC(2,3);SC31=E
C(3,1);SC32=EC(3,2);SC33=EC(3,3);SC44=EC(4,4);SC55=EC(5,5);SC66=EC(6,6);

S(:,:,1,1)=[S11 0 0;0 S21 0;0 0 S31];
S(:,:,2,1)=[0 S66 0;S66 0 0;0 0 0];
S(:,:,3,1)=[0 0 S55;0 0 0;S55 0 0];
S(:,:,1,2)=[0 S66 0;S66 0 0;0 0 0];
S(:,:,2,2)=[S12 0 0;0 S22 0;0 0 S32];
S(:,:,3,2)=[0 0 0;0 0 S44;0 S44 0];
S(:,:,1,3)=[0 0 S55;0 0 0;S55 0 0];
S(:,:,2,3)=[0 0 0;0 0 S44;0 S44 0];
S(:,:,3,3)=[S13 0 0;0 S23 0;0 0 S33];

SC(:,:,1,1)=[SC11 0 0;0 SC21 0;0 0 SC31];
SC(:,:,2,1)=[0 SC66 0;SC66 0 0;0 0 0];
SC(:,:,3,1)=[0 0 SC55;0 0 0;SC55 0 0];
SC(:,:,1,2)=[0 SC66 0;SC66 0 0;0 0 0];
SC(:,:,2,2)=[SC12 0 0;0 SC22 0;0 0 SC32];
SC(:,:,3,2)=[0 0 0;0 0 SC44;0 SC44 0];
SC(:,:,1,3)=[0 0 SC55;0 0 0;SC55 0 0];
SC(:,:,2,3)=[0 0 0;0 0 SC44;0 SC44 0];
SC(:,:,3,3)=[SC13 0 0;0 SC23 0;0 0 SC33];

I(:,:,1,1)=eye(3);
I(:,:,2,1)=eye(3);
I(:,:,3,1)=eye(3);
I(:,:,1,2)=eye(3);
I(:,:,2,2)=eye(3);
I(:,:,3,2)=eye(3);
I(:,:,1,3)=eye(3);
I(:,:,2,3)=eye(3);
I(:,:,3,3)=eye(3);

for(i=1:length(data(:,1)))
row = data(i,:);
Mo_SS1= data(i,1:6); % transient viscosity data for eut.Sn-Ag phase for Slip system #1
M1_SS1= data(i,8:13); % transient viscosity data for Sn phase for Slip system #1
M0_SS1(:,:,1,1)=[Mo_SS1(1) 0 0;0 0 0;0 0 0];
M0_SS1(:,:,2,1)=[0 Mo_SS1(4) 0;Mo_SS1(4) 0 0;0 0 0];
M0_SS1(:,:,3,1)=[0 0 Mo_SS1(5);0 0 0;Mo_SS1(5) 0 0];
M0_SS1(:,:,1,2)=[0 Mo_SS1(4) 0;Mo_SS1(4) 0 0;0 0 0];
M0_SS1(:,:,2,2)=[0 0 0;0 Mo_SS1(2) 0;0 0 0];
M0_SS1(:,:,3,2)=[0 0 0;0 0 Mo_SS1(6);0 Mo_SS1(6) 0];
M0_SS1(:,:,1,3)=[0 0 Mo_SS1(5);0 0 0;Mo_SS1(5) 0 0];
M0_SS1(:,:,2,3)=[0 0 0;0 0 Mo_SS1(6);0 Mo_SS1(6) 0];
M0_SS1(:,:,3,3)=[0 0 0;0 0 0;0 0 Mo_SS1(3)];

MI_SS1(:,:,1,1)=[M1_SS1(1) 0 0;0 0 0;0 0 0];
MI_SS1(:,:,2,1)=[0 M1_SS1(4) 0;M1_SS1(4) 0 0;0 0 0];
MI_SS1(:,:,3,1)=[0 0 M1_SS1(5);0 0 0;M1_SS1(5) 0 0];
MI_SS1(:,:,1,2)=[0 M1_SS1(4) 0;M1_SS1(4) 0 0;0 0 0];
```

```
MI_SS1(:,:,2,2)=[0 0 0;0 M1_SS1(2) 0;0 0 0];
MI_SS1(:,:,3,2)=[0 0 0;0 0 M1_SS1(6);0 M1_SS1(6) 0];
MI_SS1(:,:,1,3)=[0 0 M1_SS1(5);0 0 0;M1_SS1(5) 0 0];
MI_SS1(:,:,2,3)=[0 0 0;0 0 M1_SS1(6);0 M1_SS1(6) 0];
MI_SS1(:,:,3,3)=[0 0 0;0 0 0;0 0 M1_SS1(3)];

M0T_SS1(:,:,1,1)=b'*b*(M0_SS1(:,:,1,1))*(b'*b);
M0T_SS1(:,:,2,1)=b'*b*(M0_SS1(:,:,2,1))*(b'*b);
M0T_SS1(:,:,3,1)=b'*b*(M0_SS1(:,:,3,1))*(b'*b);
M0T_SS1(:,:,1,2)=b'*b*(M0_SS1(:,:,1,2))*(b'*b);
M0T_SS1(:,:,2,2)=b'*b*(M0_SS1(:,:,2,2))*(b'*b);
M0T_SS1(:,:,3,2)=b'*b*(M0_SS1(:,:,3,2))*(b'*b);
M0T_SS1(:,:,1,3)=b'*b*(M0_SS1(:,:,1,3))*(b'*b);
M0T_SS1(:,:,2,3)=b'*b*(M0_SS1(:,:,2,3))*(b'*b);
M0T_SS1(:,:,3,3)=b'*b*(M0_SS1(:,:,3,3))*(b'*b);


M0T_SS1(:,:,1,1)=1./(M0T_SS1(:,:,1,1));
M0T_SS1(:,:,2,1)=1./(M0T_SS1(:,:,2,1));
M0T_SS1(:,:,3,1)=1./(M0T_SS1(:,:,3,1));
M0T_SS1(:,:,1,2)=1./(M0T_SS1(:,:,1,2));
M0T_SS1(:,:,2,2)=1./(M0T_SS1(:,:,2,2));
M0T_SS1(:,:,3,2)=1./(M0T_SS1(:,:,3,2));
M0T_SS1(:,:,1,3)=1./(M0T_SS1(:,:,1,3));
M0T_SS1(:,:,2,3)=1./(M0T_SS1(:,:,2,3));
M0T_SS1(:,:,3,3)=1./(M0T_SS1(:,:,3,3));

MIT_SS1(:,:,1,1)=b'*b*(MI_SS1(:,:,1,1))*(b'*b);
MIT_SS1(:,:,2,1)=b'*b*(MI_SS1(:,:,2,1))*(b'*b);
MIT_SS1(:,:,3,1)=b'*b*(MI_SS1(:,:,3,1))*(b'*b);
MIT_SS1(:,:,1,2)=b'*b*(MI_SS1(:,:,1,2))*(b'*b);
MIT_SS1(:,:,2,2)=b'*b*(MI_SS1(:,:,2,2))*(b'*b);
MIT_SS1(:,:,3,2)=b'*b*(MI_SS1(:,:,3,2))*(b'*b);
MIT_SS1(:,:,1,3)=b'*b*(MI_SS1(:,:,1,3))*(b'*b);
MIT_SS1(:,:,2,3)=b'*b*(MI_SS1(:,:,2,3))*(b'*b);
MIT_SS1(:,:,3,3)=b'*b*(MI_SS1(:,:,3,3))*(b'*b);

MIT_SS1(:,:,1,1)=1./(MIT_SS1(:,:,1,1));
MIT_SS1(:,:,2,1)=1./(MIT_SS1(:,:,2,1));
MIT_SS1(:,:,3,1)=1./(MIT_SS1(:,:,3,1));
MIT_SS1(:,:,1,2)=1./(MIT_SS1(:,:,1,2));
MIT_SS1(:,:,2,2)=1./(MIT_SS1(:,:,2,2));
MIT_SS1(:,:,3,2)=1./(MIT_SS1(:,:,3,2));
MIT_SS1(:,:,1,3)=1./(MIT_SS1(:,:,1,3));
MIT_SS1(:,:,2,3)=1./(MIT_SS1(:,:,2,3));
MIT_SS1(:,:,3,3)=1./(MIT_SS1(:,:,3,3));

MT_SS1(:,:,1,1)=M0T_SS1(:,:,1,1)+c1*(MIT_SS1(:,:,1,1)-
M0T_SS1(:,:,1,1))*inv(c0*S(:,:,1,1)*inv(M0T_SS1(:,:,1,1))*(MIT_SS1(:,:,1,1)-
M0T_SS1(:,:,1,1))+I(:,:,1,1))+c11*M0T_SS1(:,:,1,1)/(I(:,:,1,1)-c0*SC(:,:,1,1));
MT_SS1(:,:,2,1)=M0T_SS1(:,:,2,1)+c1*(MIT_SS1(:,:,2,1)-
M0T_SS1(:,:,2,1))*inv(c0*S(:,:,2,1)*inv(M0T_SS1(:,:,2,1))*(MIT_SS1(:,:,2,1)-
M0T_SS1(:,:,2,1))+I(:,:,2,1))+c11*M0T_SS1(:,:,2,1)/(I(:,:,2,1)-c0*SC(:,:,2,1));
MT_SS1(:,:,3,1)=M0T_SS1(:,:,3,1)+c1*(MIT_SS1(:,:,3,1)-
M0T_SS1(:,:,3,1))*inv(c0*S(:,:,3,1)*inv(M0T_SS1(:,:,3,1))*(MIT_SS1(:,:,3,1)-
M0T_SS1(:,:,3,1))+I(:,:,3,1))+c11*M0T_SS1(:,:,3,1)/(I(:,:,3,1)-c0*SC(:,:,3,1));
```

```
MT_SS1(:,:,1,2)=M0T_SS1(:,:,1,2)+c1*(MIT_SS1(:,:,1,2)-
M0T_SS1(:,:,1,2))*inv(c0*S(:,:,1,2)*inv(M0T_SS1(:,:,1,2))*(MIT_SS1(:,:,1,2)-
M0T_SS1(:,:,1,2))+I(:,:,1,2))+c11*M0T_SS1(:,:,1,2)/(I(:,:,1,2)-c0*SC(:,:,1,2));
MT_SS1(:,:,2,2)=M0T_SS1(:,:,2,2)+c1*(MIT_SS1(:,:,2,2)-
M0T_SS1(:,:,2,2))*inv(c0*S(:,:,2,2)*inv(M0T_SS1(:,:,2,2))*(MIT_SS1(:,:,2,2)-
M0T_SS1(:,:,2,2))+I(:,:,2,2))+c11*M0T_SS1(:,:,2,2)/(I(:,:,2,2)-c0*SC(:,:,2,2));
MT_SS1(:,:,3,2)=M0T_SS1(:,:,3,2)+c1*(MIT_SS1(:,:,3,2)-
M0T_SS1(:,:,3,2))*inv(c0*S(:,:,3,2)*inv(M0T_SS1(:,:,3,2))*(MIT_SS1(:,:,3,2)-
M0T_SS1(:,:,3,2))+I(:,:,3,2))+c11*M0T_SS1(:,:,3,2)/(I(:,:,3,2)-c0*SC(:,:,3,2));
MT_SS1(:,:,1,3)=M0T_SS1(:,:,1,3)+c1*(MIT_SS1(:,:,1,3)-
M0T_SS1(:,:,1,3))*inv(c0*S(:,:,1,3)*inv(M0T_SS1(:,:,1,3))*(MIT_SS1(:,:,1,3)-
M0T_SS1(:,:,1,3))+I(:,:,1,3))+c11*M0T_SS1(:,:,1,3)/(I(:,:,1,3)-c0*SC(:,:,1,3));
MT_SS1(:,:,2,3)=M0T_SS1(:,:,2,3)+c1*(MIT_SS1(:,:,2,3)-
M0T_SS1(:,:,2,3))*inv(c0*S(:,:,2,3)*inv(M0T_SS1(:,:,2,3))*(MIT_SS1(:,:,2,3)-
M0T_SS1(:,:,2,3))+I(:,:,2,3))+c11*M0T_SS1(:,:,2,3)/(I(:,:,2,3)-c0*SC(:,:,2,3));
MT_SS1(:,:,3,3)=M0T_SS1(:,:,3,3)+c1*(MIT_SS1(:,:,3,3)-
M0T_SS1(:,:,3,3))*inv(c0*S(:,:,3,3)*inv(M0T_SS1(:,:,3,3))*(MIT_SS1(:,:,3,3)-
M0T_SS1(:,:,3,3))+I(:,:,3,3))+c11*M0T_SS1(:,:,3,3)/(I(:,:,3,3)-c0*SC(:,:,3,3));

% M_extract100(i,:) = MT_SS1(1,1,1,1);
% M_extract010(i,:) = MT_SS1(2,2,2,2);
% M_extract001(i,:) = MT_SS1(3,3,3,3);

MTT_SS1=a'*a*MT_SS1(:,:,2,1)*a'*a;
M_sample_extractSS1(i,:) = MTT_SS1(1,2);


Mo_SS2= data(i,15:20); % transient viscosity data for eut.Sn-Ag phase for Slip system #1
M1_SS2= data(i,22:27); % transient viscosity data for Sn phase for Slip system #1
M0_SS2(:,:,1,1)=[Mo_SS2(1) 0 0;0 0 0;0 0 0];
M0_SS2(:,:,2,1)=[0 Mo_SS2(4) 0;Mo_SS2(4) 0 0;0 0 0];
M0_SS2(:,:,3,1)=[0 0 Mo_SS2(5);0 0 0;Mo_SS2(5) 0 0];
M0_SS2(:,:,1,2)=[0 Mo_SS2(4) 0;Mo_SS2(4) 0 0;0 0 0];
M0_SS2(:,:,2,2)=[0 0 0;0 Mo_SS2(2) 0;0 0 0];
M0_SS2(:,:,3,2)=[0 0 0;0 0 Mo_SS2(6);0 Mo_SS2(6) 0];
M0_SS2(:,:,1,3)=[0 0 Mo_SS2(5);0 0 0;Mo_SS2(5) 0 0];
M0_SS2(:,:,2,3)=[0 0 0;0 0 Mo_SS2(6);0 Mo_SS2(6) 0];
M0_SS2(:,:,3,3)=[0 0 0;0 0 0;0 0 Mo_SS2(3)];

MI_SS2(:,:,1,1)=[M1_SS2(1) 0 0;0 0 0;0 0 0];
MI_SS2(:,:,2,1)=[0 M1_SS2(4) 0;M1_SS2(4) 0 0;0 0 0];
MI_SS2(:,:,3,1)=[0 0 M1_SS2(5);0 0 0;M1_SS2(5) 0 0];
MI_SS2(:,:,1,2)=[0 M1_SS2(4) 0;M1_SS2(4) 0 0;0 0 0];
MI_SS2(:,:,2,2)=[0 0 0;0 M1_SS2(2) 0;0 0 0];
MI_SS2(:,:,3,2)=[0 0 0;0 0 M1_SS2(6);0 M1_SS2(6) 0];
MI_SS2(:,:,1,3)=[0 0 M1_SS2(5);0 0 0;M1_SS2(5) 0 0];
MI_SS2(:,:,2,3)=[0 0 0;0 0 M1_SS2(6);0 M1_SS2(6) 0];
MI_SS2(:,:,3,3)=[0 0 0;0 0 0;0 0 M1_SS2(3)];

M0T_SS2(:,:,1,1)=c*c'*(M0_SS2(:,:,1,1))*(c*c');
M0T_SS2(:,:,2,1)=c*c'*(M0_SS2(:,:,2,1))*(c*c');
M0T_SS2(:,:,3,1)=c*c'*(M0_SS2(:,:,3,1))*(c*c');
M0T_SS2(:,:,1,2)=c*c'*(M0_SS2(:,:,1,2))*(c*c');
M0T_SS2(:,:,2,2)=c*c'*(M0_SS2(:,:,2,2))*(c*c');
M0T_SS2(:,:,3,2)=c*c'*(M0_SS2(:,:,3,2))*(c*c');
M0T_SS2(:,:,1,3)=c*c'*(M0_SS2(:,:,1,3))*(c*c');
M0T_SS2(:,:,2,3)=c*c'*(M0_SS2(:,:,2,3))*(c*c');
```

```
M0T_SS2(:,:,3,3)=c*c'*(M0_SS2(:,:,3,3))*(c*c');

M0T_SS2(:,:,1,1)=(M0T_SS2(:,:,1,1))';
M0T_SS2(:,:,2,1)=(M0T_SS2(:,:,2,1))';
M0T_SS2(:,:,3,1)=(M0T_SS2(:,:,3,1))';
M0T_SS2(:,:,1,2)=(M0T_SS2(:,:,1,2))';
M0T_SS2(:,:,2,2)=(M0T_SS2(:,:,2,2))';
M0T_SS2(:,:,3,2)=(M0T_SS2(:,:,3,2))';
M0T_SS2(:,:,1,3)=(M0T_SS2(:,:,1,3))';
M0T_SS2(:,:,2,3)=(M0T_SS2(:,:,2,3))';
M0T_SS2(:,:,3,3)=(M0T_SS2(:,:,3,3))';

M0T_SS2(:,:,1,1)=1./(M0T_SS2(:,:,1,1));
M0T_SS2(:,:,2,1)=1./(M0T_SS2(:,:,2,1));
M0T_SS2(:,:,3,1)=1./(M0T_SS2(:,:,3,1));
M0T_SS2(:,:,1,2)=1./(M0T_SS2(:,:,1,2));
M0T_SS2(:,:,2,2)=1./(M0T_SS2(:,:,2,2));
M0T_SS2(:,:,3,2)=1./(M0T_SS2(:,:,3,2));
M0T_SS2(:,:,1,3)=1./(M0T_SS2(:,:,1,3));
M0T_SS2(:,:,2,3)=1./(M0T_SS2(:,:,2,3));
M0T_SS2(:,:,3,3)=1./(M0T_SS2(:,:,3,3));

MIT_SS2(:,:,1,1)=(c*c')*(MI_SS2(:,:,1,1))*(c*c');
MIT_SS2(:,:,2,1)=(c*c')*(MI_SS2(:,:,2,1))*(c*c');
MIT_SS2(:,:,3,1)=(c*c')*(MI_SS2(:,:,3,1))*(c*c');
MIT_SS2(:,:,1,2)=(c*c')*(MI_SS2(:,:,1,2))*(c*c');
MIT_SS2(:,:,2,2)=(c*c')*(MI_SS2(:,:,2,2))*(c*c');
MIT_SS2(:,:,3,2)=(c*c')*(MI_SS2(:,:,3,2))*(c*c');
MIT_SS2(:,:,1,3)=(c*c')*(MI_SS2(:,:,1,3))*(c*c');
MIT_SS2(:,:,2,3)=(c*c')*(MI_SS2(:,:,2,3))*(c*c');
MIT_SS2(:,:,3,3)=(c*c')*(MI_SS2(:,:,3,3))*(c*c');

MIT_SS2(:,:,1,1)=(MIT_SS2(:,:,1,1))';
MIT_SS2(:,:,2,1)=(MIT_SS2(:,:,2,1))';
MIT_SS2(:,:,3,1)=(MIT_SS2(:,:,3,1))';
MIT_SS2(:,:,1,2)=(MIT_SS2(:,:,1,2))';
MIT_SS2(:,:,2,2)=(MIT_SS2(:,:,2,2))';
MIT_SS2(:,:,3,2)=(MIT_SS2(:,:,3,2))';
MIT_SS2(:,:,1,3)=(MIT_SS2(:,:,1,3))';
MIT_SS2(:,:,2,3)=(MIT_SS2(:,:,2,3))';
MIT_SS2(:,:,3,3)=(MIT_SS2(:,:,3,3))';

MIT_SS2(:,:,1,1)=1./(MIT_SS2(:,:,1,1));
MIT_SS2(:,:,2,1)=1./(MIT_SS2(:,:,2,1));
MIT_SS2(:,:,3,1)=1./(MIT_SS2(:,:,3,1));
MIT_SS2(:,:,1,2)=1./(MIT_SS2(:,:,1,2));
MIT_SS2(:,:,2,2)=1./(MIT_SS2(:,:,2,2));
MIT_SS2(:,:,3,2)=1./(MIT_SS2(:,:,3,2));
MIT_SS2(:,:,1,3)=1./(MIT_SS2(:,:,1,3));
MIT_SS2(:,:,2,3)=1./(MIT_SS2(:,:,2,3));
MIT_SS2(:,:,3,3)=1./(MIT_SS2(:,:,3,3));

MT_SS2(:,:,1,1)=M0T_SS2(:,:,1,1)+c1*(MIT_SS2(:,:,1,1)-
M0T_SS2(:,:,1,1))*inv(c0*S(:,:,1,1)*inv(M0T_SS2(:,:,1,1))*(MIT_SS2(:,:,1,1)-
M0T_SS2(:,:,1,1))+I(:,:,1,1))+c11*M0T_SS2(:,:,1,1)/(I(:,:,1,1)-c0*SC(:,:,1,1));
```

```
MT_SS2(:,:,2,1)=M0T_SS2(:,:,2,1)+c1*(MIT_SS2(:,:,2,1)-
M0T_SS2(:,:,2,1))*inv(c0*S(:,:,2,1)*inv(M0T_SS2(:,:,2,1))*(MIT_SS2(:,:,2,1)-
M0T_SS2(:,:,2,1))+I(:,:,2,1))+c11*M0T_SS2(:,:,2,1)/(I(:,:,2,1)-c0*SC(:,:,2,1));
MT_SS2(:,:,3,1)=M0T_SS2(:,:,3,1)+c1*(MIT_SS2(:,:,3,1)-
M0T_SS2(:,:,3,1))*inv(c0*S(:,:,3,1)*inv(M0T_SS2(:,:,3,1))*(MIT_SS2(:,:,3,1)-
M0T_SS2(:,:,3,1))+I(:,:,3,1))+c11*M0T_SS2(:,:,3,1)/(I(:,:,3,1)-c0*SC(:,:,3,1));
MT_SS2(:,:,1,2)=M0T_SS2(:,:,1,2)+c1*(MIT_SS2(:,:,1,2)-
M0T_SS2(:,:,1,2))*inv(c0*S(:,:,1,2)*inv(M0T_SS2(:,:,1,2))*(MIT_SS2(:,:,1,2)-
M0T_SS2(:,:,1,2))+I(:,:,1,2))+c11*M0T_SS2(:,:,1,2)/(I(:,:,1,2)-c0*SC(:,:,1,2));
MT_SS2(:,:,2,2)=M0T_SS2(:,:,2,2)+c1*(MIT_SS2(:,:,2,2)-
M0T_SS2(:,:,2,2))*inv(c0*S(:,:,2,2)*inv(M0T_SS2(:,:,2,2))*(MIT_SS2(:,:,2,2)-
M0T_SS2(:,:,2,2))+I(:,:,2,2))+c11*M0T_SS2(:,:,2,2)/(I(:,:,2,2)-c0*SC(:,:,2,2));
MT_SS2(:,:,3,2)=M0T_SS2(:,:,3,2)+c1*(MIT_SS2(:,:,3,2)-
M0T_SS2(:,:,3,2))*inv(c0*S(:,:,3,2)*inv(M0T_SS2(:,:,3,2))*(MIT_SS2(:,:,3,2)-
M0T_SS2(:,:,3,2))+I(:,:,3,2))+c11*M0T_SS2(:,:,3,2)/(I(:,:,3,2)-c0*SC(:,:,3,2));
MT_SS2(:,:,1,3)=M0T_SS2(:,:,1,3)+c1*(MIT_SS2(:,:,1,3)-
M0T_SS2(:,:,1,3))*inv(c0*S(:,:,1,3)*inv(M0T_SS2(:,:,1,3))*(MIT_SS2(:,:,1,3)-
M0T_SS2(:,:,1,3))+I(:,:,1,3))+c11*M0T_SS2(:,:,1,3)/(I(:,:,1,3)-c0*SC(:,:,1,3));
MT_SS2(:,:,2,3)=M0T_SS2(:,:,2,3)+c1*(MIT_SS2(:,:,2,3)-
M0T_SS2(:,:,2,3))*inv(c0*S(:,:,2,3)*inv(M0T_SS2(:,:,2,3))*(MIT_SS2(:,:,2,3)-
M0T_SS2(:,:,2,3))+I(:,:,2,3))+c11*M0T_SS2(:,:,2,3)/(I(:,:,2,3)-c0*SC(:,:,2,3));
MT_SS2(:,:,3,3)=M0T_SS2(:,:,3,3)+c1*(MIT_SS2(:,:,3,3)-
M0T_SS2(:,:,3,3))*inv(c0*S(:,:,3,3)*inv(M0T_SS2(:,:,3,3))*(MIT_SS2(:,:,3,3)-
M0T_SS2(:,:,3,3))+I(:,:,3,3))+c11*M0T_SS2(:,:,3,3)/(I(:,:,3,3)-c0*SC(:,:,3,3));

% M_extract100(i,:) = MT_SS1(1,1,1,1);
% M_extract010(i,:) = MT_SS1(2,2,2,2);
% M_extract001(i,:) = MT_SS1(3,3,3,3);

MTT_SS2=a'*a*(MT_SS2(:,:,2,1))*a'*a;
M_sample_extractSS2(i,:) = MTT_SS2(1,2);

Mo_SS3= data(i,29:34); % transient viscosity data for eut.Sn-Ag phase for Slip system #1
M1_SS3= data(i,36:41); % transient viscosity data for Sn phase for Slip system #1
M0_SS3(:,:,1,1)=[Mo_SS3(1) 0 0;0 0 0;0 0 0];
M0_SS3(:,:,2,1)=[0 Mo_SS3(4) 0;Mo_SS3(4) 0 0;0 0 0];
M0_SS3(:,:,3,1)=[0 0 Mo_SS3(5);0 0 0;Mo_SS3(5) 0 0];
M0_SS3(:,:,1,2)=[0 Mo_SS3(4) 0;Mo_SS3(4) 0 0;0 0 0];
M0_SS3(:,:,2,2)=[0 0 0;0 Mo_SS3(2) 0;0 0 0];
M0_SS3(:,:,3,2)=[0 0 0;0 0 Mo_SS3(6);0 Mo_SS3(6) 0];
M0_SS3(:,:,1,3)=[0 0 Mo_SS3(5);0 0 0;Mo_SS3(5) 0 0];
M0_SS3(:,:,2,3)=[0 0 0;0 0 Mo_SS3(6);0 Mo_SS3(6) 0];
M0_SS3(:,:,3,3)=[0 0 0;0 0 0;0 0 Mo_SS3(3)];

MI_SS3(:,:,1,1)=[M1_SS3(1) 0 0;0 0 0;0 0 0];
MI_SS3(:,:,2,1)=[0 M1_SS3(4) 0;M1_SS3(4) 0 0;0 0 0];
MI_SS3(:,:,3,1)=[0 0 M1_SS3(5);0 0 0;M1_SS3(5) 0 0];
MI_SS3(:,:,1,2)=[0 M1_SS3(4) 0;M1_SS3(4) 0 0;0 0 0];
MI_SS3(:,:,2,2)=[0 0 0;0 M1_SS3(2) 0;0 0 0];
MI_SS3(:,:,3,2)=[0 0 0;0 0 M1_SS3(6);0 M1_SS3(6) 0];
MI_SS3(:,:,1,3)=[0 0 M1_SS3(5);0 0 0;M1_SS3(5) 0 0];
MI_SS3(:,:,2,3)=[0 0 0;0 0 M1_SS3(6);0 M1_SS3(6) 0];
MI_SS3(:,:,3,3)=[0 0 0;0 0 0;0 0 M1_SS3(3)];

M0T_SS3(:,:,1,1)=d'*d*(M0_SS3(:,:,1,1))*(d'*d);
M0T_SS3(:,:,2,1)=d'*d*(M0_SS3(:,:,2,1))*(d'*d);
M0T_SS3(:,:,3,1)=d'*d*(M0_SS3(:,:,3,1))*(d'*d);
```

```
M0T_SS3(:,:,1,2)=d'*d*(M0_SS3(:,:,1,2))*(d'*d);
M0T_SS3(:,:,2,2)=d'*d*(M0_SS3(:,:,2,2))*(d'*d);
M0T_SS3(:,:,3,2)=d'*d*(M0_SS3(:,:,3,2))*(d'*d);
M0T_SS3(:,:,1,3)=d'*d*(M0_SS3(:,:,1,3))*(d'*d);
M0T_SS3(:,:,2,3)=d'*d*(M0_SS3(:,:,2,3))*(d'*d);
M0T_SS3(:,:,3,3)=d'*d*(M0_SS3(:,:,3,3))*(d'*d);

M0T_SS3(:,:,1,1)=1./(M0T_SS3(:,:,1,1));
M0T_SS3(:,:,2,1)=1./(M0T_SS3(:,:,2,1));
M0T_SS3(:,:,3,1)=1./(M0T_SS3(:,:,3,1));
M0T_SS3(:,:,1,2)=1./(M0T_SS3(:,:,1,2));
M0T_SS3(:,:,2,2)=1./(M0T_SS3(:,:,2,2));
M0T_SS3(:,:,3,2)=1./(M0T_SS3(:,:,3,2));
M0T_SS3(:,:,1,3)=1./(M0T_SS3(:,:,1,3));
M0T_SS3(:,:,2,3)=1./(M0T_SS3(:,:,2,3));
M0T_SS3(:,:,3,3)=1./(M0T_SS3(:,:,3,3));

MIT_SS3(:,:,1,1)=d'*d*(MI_SS3(:,:,1,1))*(d'*d);
MIT_SS3(:,:,2,1)=d'*d*(MI_SS3(:,:,2,1))*(d'*d);
MIT_SS3(:,:,3,1)=d'*d*(MI_SS3(:,:,3,1))*(d'*d);
MIT_SS3(:,:,1,2)=d'*d*(MI_SS3(:,:,1,2))*(d'*d);
MIT_SS3(:,:,2,2)=d'*d*(MI_SS3(:,:,2,2))*(d'*d);
MIT_SS3(:,:,3,2)=d'*d*(MI_SS3(:,:,3,2))*(d'*d);
MIT_SS3(:,:,1,3)=d'*d*(MI_SS3(:,:,1,3))*(d'*d);
MIT_SS3(:,:,2,3)=d'*d*(MI_SS3(:,:,2,3))*(d'*d);
MIT_SS3(:,:,3,3)=d'*d*(MI_SS3(:,:,3,3))*(d'*d);

MIT_SS3(:,:,1,1)=1./(MIT_SS3(:,:,1,1));
MIT_SS3(:,:,2,1)=1./(MIT_SS3(:,:,2,1));
MIT_SS3(:,:,3,1)=1./(MIT_SS3(:,:,3,1));
MIT_SS3(:,:,1,2)=1./(MIT_SS3(:,:,1,2));
MIT_SS3(:,:,2,2)=1./(MIT_SS3(:,:,2,2));
MIT_SS3(:,:,3,2)=1./(MIT_SS3(:,:,3,2));
MIT_SS3(:,:,1,3)=1./(MIT_SS3(:,:,1,3));
MIT_SS3(:,:,2,3)=1./(MIT_SS3(:,:,2,3));
MIT_SS3(:,:,3,3)=1./(MIT_SS3(:,:,3,3));

MT_SS3(:,:,1,1)=M0T_SS3(:,:,1,1)+c1*(MIT_SS3(:,:,1,1)-
M0T_SS3(:,:,1,1))*inv(c0*S(:,:,1,1)*inv(M0T_SS3(:,:,1,1))*(MIT_SS3(:,:,1,1)-
M0T_SS3(:,:,1,1))+I(:,:,1,1))+c11*M0T_SS3(:,:,1,1)/(I(:,:,1,1)-c0*SC(:,:,1,1));
MT_SS3(:,:,2,1)=M0T_SS3(:,:,2,1)+c1*(MIT_SS3(:,:,2,1)-
M0T_SS3(:,:,2,1))*inv(c0*S(:,:,2,1)*inv(M0T_SS3(:,:,2,1))*(MIT_SS3(:,:,2,1)-
M0T_SS3(:,:,2,1))+I(:,:,2,1))+c11*M0T_SS3(:,:,2,1)/(I(:,:,2,1)-c0*SC(:,:,2,1));
MT_SS3(:,:,3,1)=M0T_SS3(:,:,3,1)+c1*(MIT_SS3(:,:,3,1)-
M0T_SS3(:,:,3,1))*inv(c0*S(:,:,3,1)*inv(M0T_SS3(:,:,3,1))*(MIT_SS3(:,:,3,1)-
M0T_SS3(:,:,3,1))+I(:,:,3,1))+c11*M0T_SS3(:,:,3,1)/(I(:,:,3,1)-c0*SC(:,:,3,1));
MT_SS3(:,:,1,2)=M0T_SS3(:,:,1,2)+c1*(MIT_SS3(:,:,1,2)-
M0T_SS3(:,:,1,2))*inv(c0*S(:,:,1,2)*inv(M0T_SS3(:,:,1,2))*(MIT_SS3(:,:,1,2)-
M0T_SS3(:,:,1,2))+I(:,:,1,2))+c11*M0T_SS3(:,:,1,2)/(I(:,:,1,2)-c0*SC(:,:,1,2));
MT_SS3(:,:,2,2)=M0T_SS3(:,:,2,2)+c1*(MIT_SS3(:,:,2,2)-
M0T_SS3(:,:,2,2))*inv(c0*S(:,:,2,2)*inv(M0T_SS3(:,:,2,2))*(MIT_SS3(:,:,2,2)-
M0T_SS3(:,:,2,2))+I(:,:,2,2))+c11*M0T_SS3(:,:,2,2)/(I(:,:,2,2)-c0*SC(:,:,2,2));
MT_SS3(:,:,3,2)=M0T_SS3(:,:,3,2)+c1*(MIT_SS3(:,:,3,2)-
M0T_SS3(:,:,3,2))*inv(c0*S(:,:,3,2)*inv(M0T_SS3(:,:,3,2))*(MIT_SS3(:,:,3,2)-
M0T_SS3(:,:,3,2))+I(:,:,3,2))+c11*M0T_SS3(:,:,3,2)/(I(:,:,3,2)-c0*SC(:,:,3,2));
```

```
MT_SS3(:,:,1,3)=M0T_SS3(:,:,1,3)+c1*(MIT_SS3(:,:,1,3)-
M0T_SS3(:,:,1,3))*inv(c0*S(:,:,1,3)*inv(M0T_SS3(:,:,1,3))*(MIT_SS3(:,:,1,3)-
M0T_SS3(:,:,1,3))+I(:,:,1,3))+c11*M0T_SS3(:,:,1,3)/(I(:,:,1,3)-c0*SC(:,:,1,3));
MT_SS3(:,:,2,3)=M0T_SS3(:,:,2,3)+c1*(MIT_SS3(:,:,2,3)-
M0T_SS3(:,:,2,3))*inv(c0*S(:,:,2,3)*inv(M0T_SS3(:,:,2,3))*(MIT_SS3(:,:,2,3)-
M0T_SS3(:,:,2,3))+I(:,:,2,3))+c11*M0T_SS3(:,:,2,3)/(I(:,:,2,3)-c0*SC(:,:,2,3));
MT_SS3(:,:,3,3)=M0T_SS3(:,:,3,3)+c1*(MIT_SS3(:,:,3,3)-
M0T_SS3(:,:,3,3))*inv(c0*S(:,:,3,3)*inv(M0T_SS3(:,:,3,3))*(MIT_SS3(:,:,3,3)-
M0T_SS3(:,:,3,3))+I(:,:,3,3))+c11*M0T_SS3(:,:,3,3)/(I(:,:,3,3)-c0*SC(:,:,3,3));

% % M_extract100(i,:) = MT_SS1(1,1,1,1);
% % M_extract010(i,:) = MT_SS1(2,2,2,2);
% % M_extract001(i,:) = MT_SS1(3,3,3,3);

MTT_SS3=a'*a*(MT_SS3(:,:,2,1))*a'*a;
M_sample_extractSS3(i,:) = MTT_SS3(1,2);

end

xlswrite('viscositySS1.xlsx', M_sample_extractSS1);
xlswrite('viscositySS2.xlsx', M_sample_extractSS2);
xlswrite('viscositySS3.xlsx', M_sample_extractSS3);

% xlswrite('crystal100.xlsx', M_extract100);
% xlswrite('crystal010.xlsx', M_extract010);
% xlswrite('crystal001.xlsx', M_extract001);


% Any order tensor transformation

function otr = transformation(itr,tmx)
% FUNCTION
% otr = transform(itr,tmx)
%
% DESCRIPTION
% transform 3D-tensor (Euclidean or Cartesion tensor) of any order (>0) to another coordinate system
%
% PARAMETERS
% otr = output tensor, after transformation; has the same dimensions as the input tensor
% itr = input tensor, before transformation; should be a 3-element vector, a 3x3 matrix, or a 3x3x3x...
multidimensional array, each dimension containing 3 elements
% tmx = transformation matrix, 3x3 matrix that contains the direction cosines between the old and the
new coordinate system
%

ne = numel(itr);            % number of tensor elements
nd = ndims(itr);            % number of tensor dimensions, i.e. order of tensor
if (ne==3), nd = 1; end      % order of tensor is 1 in case of a 3x1 or 1x3 vector

otr = itr;                % create output tensor
otr(:) = 0;                % fill output tensor with zeros; this way a symbolic tensor remains symbolic

iie = zeros(nd,1);          % initialise vector with indices of input tensor element
ioe = zeros(nd,1);          % initialise vector with indices of output tensor element
cne = cumprod(3*ones(nd,1))/3;  % vector with cumulative number of elements for each dimension
(divided by three)
```

```
for oe = 1:ne,                          % loop over all output elements
  ioe = mod(floor((oe-1)./cne),3)+1;        % calculate indices of current output tensor element
  for ie = 1:ne,                        % loop over all input elements
    pmx = 1;                            % initialise product of transformation matrices
    iie = mod(floor((ie-1)./cne),3)+1;      % calculate indices of current input tensor element
    for id = 1:nd,                      % loop over all dimensions
      pmx = pmx * tmx( ioe(id), iie(id) );  % create product of transformation matrices
    end
    otr(oe) = otr(oe) + pmx * itr(ie);      % add product of transformation matrices and input tensor element to output tensor element
  end
end
```

A4. Pile up stress calculations for Rosler's dislocation detachment model

In Rosler's dislocation detachment model, the dislocations are assumed to be randomly distributed in the crystal, so that their stress fields upon the dislocation overcoming the dispersoids are neglected. However, in most practical applications, resulting spatial distribution of lattice dislocations is not random and the stress fields from these pile-ups cannot anymore be assumed to cancel at all points within the material. These stress fields will affect the lead pile-up dislocation pinned by the dispersoid, and either aid or hinder the bypassing processes (Orowan climb or detachment process) by which the controlling dislocation overcomes its obstacle, and thus will increase or decrease the value of the threshold stress. Local number of dislocations (N) between each pair of dispersoid is calculated using closed form approximation [231] based on volume fraction and spacing of dispersoids and total saturated dislocation density.

$$N = (1-f_{Ag3Sn})\times\rho_{sat}\times\lambda^2 \qquad (A5.1)$$

where, f_{Ag3Sn} is the volume fraction of Ag_3Sn dispersoids in the eutectic Sn-Ag phase, ρ_{sat} is the saturated dislocation density; and λ is the interparticle spacing.

With the number of dislocations per pair of dispersoids known, we can assume that these dislocations form a single pileup against the dispersoid (refer to Figure A5.1). The spacing between dislocations within two dispersoids can be calculated assuming equal spacing between them. Then, number of pileup dislocations lying on a Ag_3Sn particle for different applied shear stress level is calculated based on the actual spacing between them and Ag_3Sn particle size.

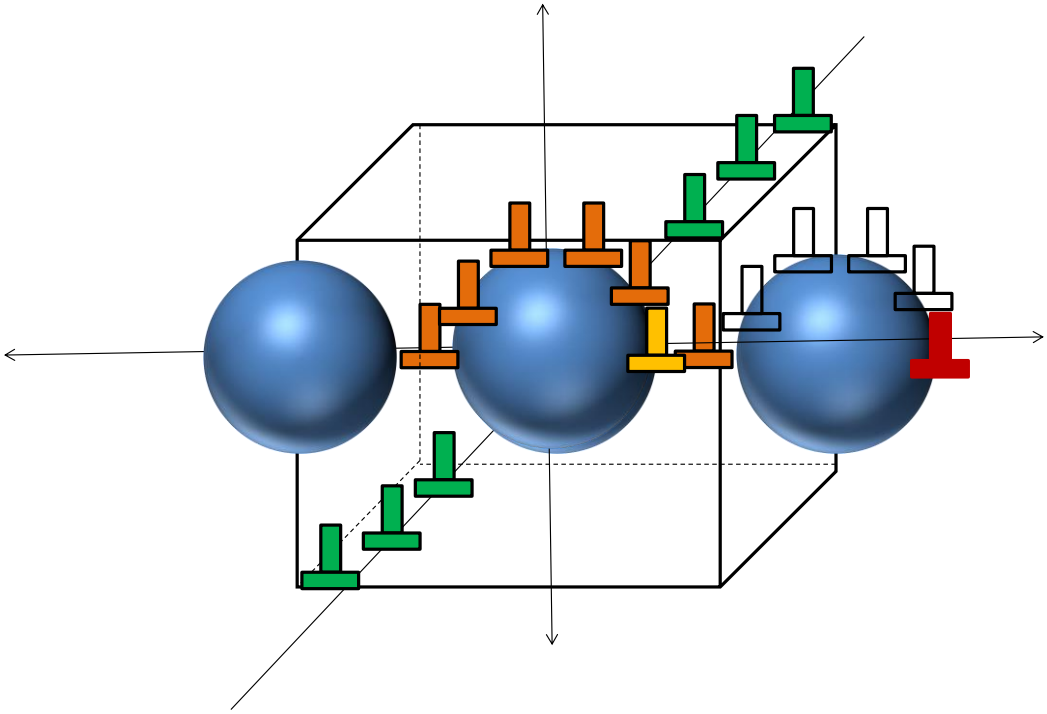

Figure A5.1: Pileup dislocation configuration near Ag_3Sn particles

Pileup stress on the detaching dislocation at the point of detachment due to the pileup dislocations surrounding the particle can be calculated and plotted in Figure A5.2. These stress fields will affect the lead pile-up dislocation pinned by the dispersoid, and either aid or hinder the bypassing processes (detachment stress) by which the controlling dislocation overcomes its obstacle, and thus will increase or decrease the value of the threshold stress (refer to Figure A5.3) for the particular applied shear stress level.

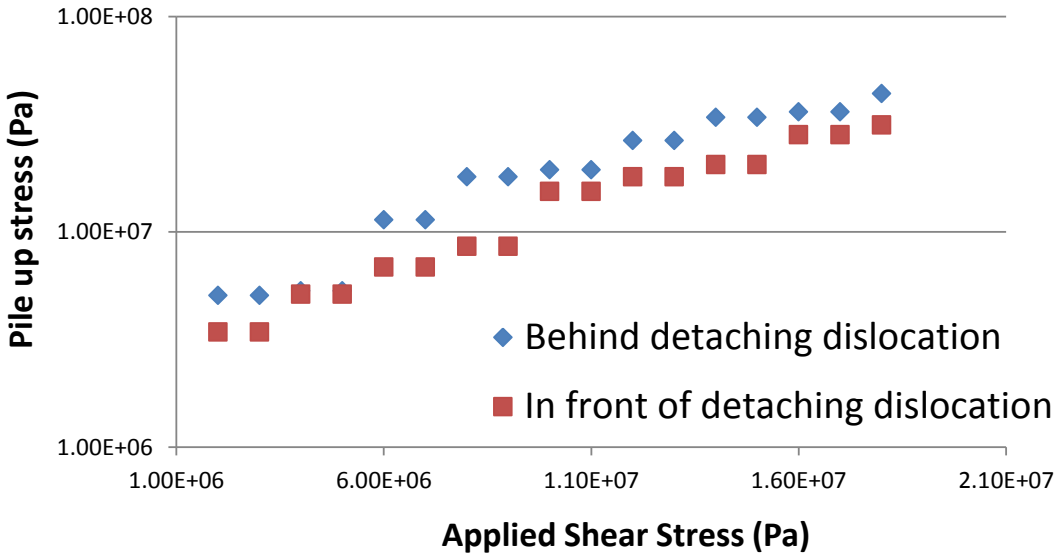

Figure A5.2: Pileup stress vs. applied shear stress

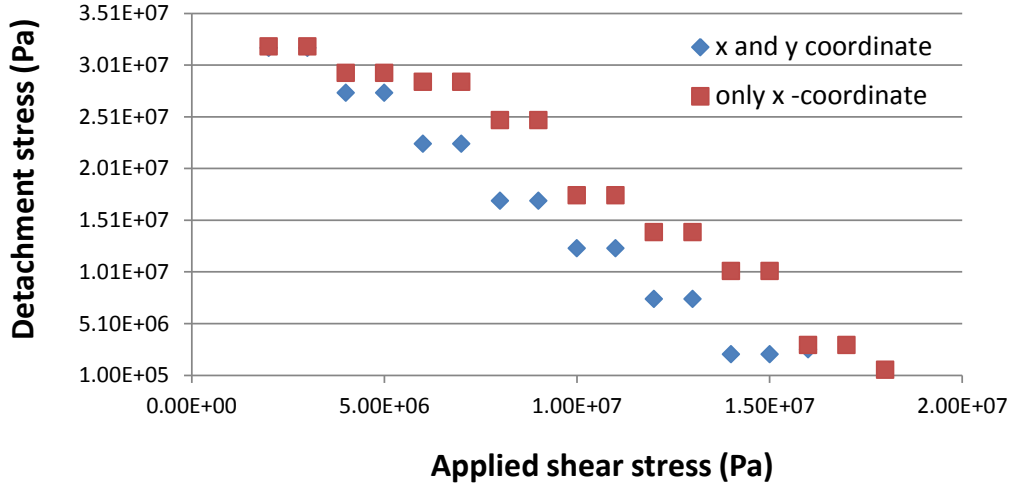

Figure A5.3: Detachment stress vs. applied shear stress

A5. Orientation Image Maps (OIM) for SAC specimens measured using Electron Backscatter (EBSD) detector

Orientation image maps (100 inverse pole figure maps) for SAC specimens along with the three Euler angles are given below:

5.1. SAC305-1

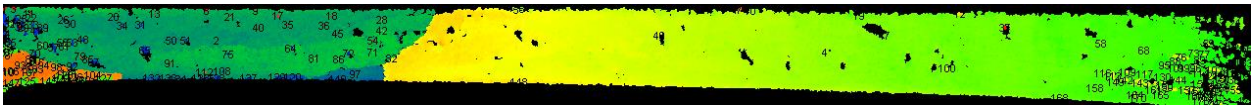

Grain no.	phi 1	PHI	phi2
4	33.947	69.553	358.62
2	279.852	35.862	55.91

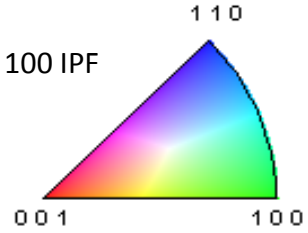

5.2. SAC305-2

Grain no.	phi 1	PHI	phi2
12	17.52	18.844	304.94
28	225.892	28.907	96
39	219.391	35.777	106.5
50	43.343	19.452	287.52

5.3. SAC105Sb-1

Grain no.	phi 1	PHI	phi2
17	270.026	82.081	100.93
3	321.816	73.608	40.39
39	331.53	83.759	7.19
20	299.788	91.376	70.56
38	143.032	86.673	174.38
41	135.75	88.699	193.94
2	312.918	76.454	46.96

5.4. SAC105Mn-1

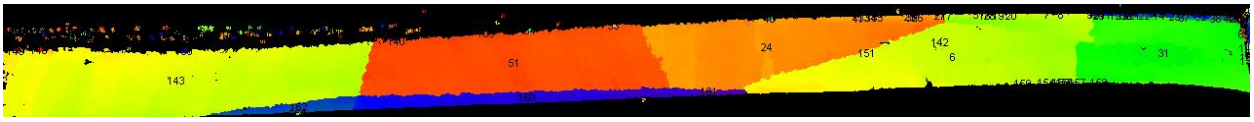

Grain no.	phi 1	PHI	phi2
143	330.395	61.987	39.57
51	276.377	6.929	70.11
6	27.524	85.987	9.53
24	197.622	46.417	197.88
31	272.721	43.531	105.98
160	259.124	77.823	135.99
162	109.215	68.276	213.91

5.5. SAC105Mn-2

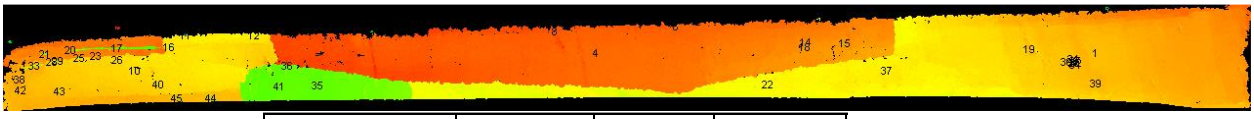

Grain no.	phi 1	PHI	phi2
4	344.708	38.411	58.45
1	196.838	82.689	127.06
10	201.897	54.196	125.42
22	308.639	30.096	41.79
35	321.001	69.4	82.63

5.6. SAC105Mn-3

Grain no.	phi 1	PHI	phi2
31	28.613	45.533	341.54
14	358.125	23.304	332.74
47	184.411	51.987	141.91
1	329.71	76.867	35.92
120	123.348	71.504	273.28

5.7. SAC105Mn-4

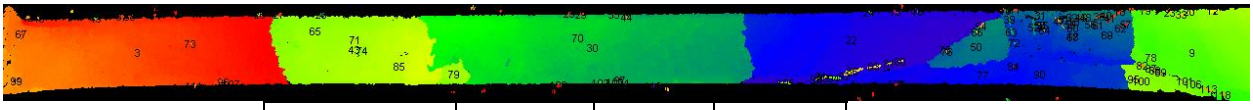

Grain no.	phi 1	PHI	phi2
30	111.525	55.699	212.9
3	186.282	75.507	154.77
22	287.988	93.756	92.02
43	220.468	50.731	142.84
9	39.613	68.962	295.04

A6. Discrete Dislocation Dynamics model for pure anisotropic BCT Sn lattice

6.1. Stress and strain fields of dislocations in anisotropic medium

Willis-Steeds-Lothe formula: The stress field of a finite segment can be obtained using Willis-Steeds-Lothe formula for the displacement gradient

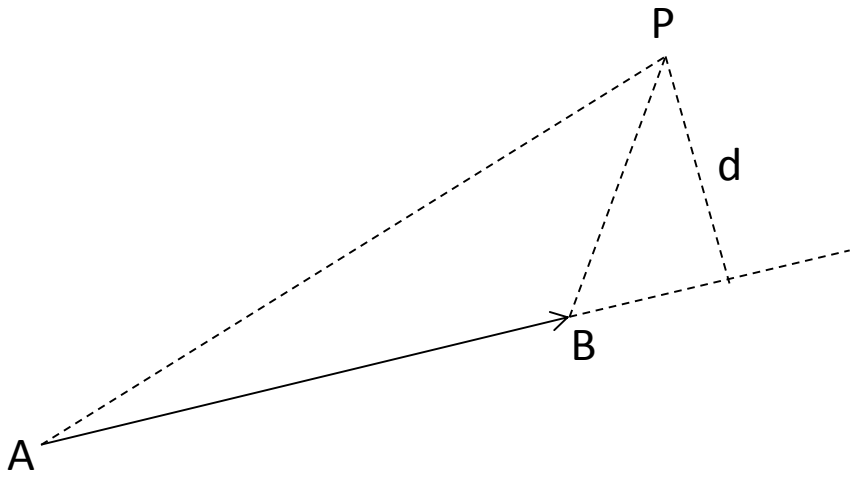

$$\frac{\partial u_m}{\partial x_s} = \frac{1}{4\pi d}\varepsilon_{jsn} b_i C_{ijkl} t_n \{-m_l Q_{mk} + n_l[(nn)^{-1}.(nm).Q]_{mk} + n_l[(nn)^{-1}.S^T]_{mk}\}\Big|_{BP}^{AP}$$

where, d is the shortest distance from field point x to the dislocation line along t,

$(mn)_{jk} = m_i C_{ijkl} n_l$

$$Q_{js} = -\frac{1}{2\pi}\int_0^{2\pi}(nn)^{-1}_{js}\,d\omega$$

$$S_{ij} = -\frac{1}{2\pi}\int_0^{2\pi}(nn)^{-1}_{ik}(nm)_{kj}\,d\omega$$

6.2. Stress and strain fields of pure edge dislocations in anisotropic medium

However, if we just consider the dislocation segments to be either pure edge or screw, the stress fields in anisotropic elasticity becomes much simpler, and we don't need to perform the integration for Q and S matrix at each step of computation.

For pure edge dislocation:

$$\sigma_{xx} = \frac{Mb_x}{2\pi\rho^4 c'_{22}}\{[(\bar{c}'_{11}-c'_{12})(\bar{c}'_{11}+c'_{12}+2c'_{66})-\bar{c}'_{11}c'_{66}]x^2y+\frac{\bar{c}'^2_{11}c'_{66}}{c'_{22}}y^3\}+\frac{Mb_y}{2\pi\rho^4}(\frac{\bar{c}'_{11}}{c'_{22}}xy^2-x^3)$$

$$\sigma_{yy} = \frac{Mb_x c'_{66}}{2\pi\rho^4}(\frac{\bar{c}'_{11}}{c'_{22}}y^3-x^2y)-\frac{Mb_y}{2\pi\rho^4\bar{c}'_{11}}\{[(\bar{c}'_{11}-c'_{12})(\bar{c}'_{11}+c'_{12}+2c'_{66})-\bar{c}'_{11}c'_{66}]xy^2+c'_{22}c'_{66}x^3\}$$

$$\sigma_{xy} = \frac{Mb_x c'_{66}}{2\pi\rho^4}(\frac{\bar{c}'_{11}}{c'_{22}}xy^2-x^3)+\frac{Mb_y c'_{66}}{2\pi\rho^4}(\frac{\bar{c}'_{11}}{c'_{22}}y^3-x^2y)$$

where, $M = (\bar{c}'_{11}+c'_{12})\left[\frac{\bar{c}'_{11}-c'_{12}}{c'_{22}c'_{66}(\bar{c}'_{11}+c'_{12}+2c'_{66})}\right]$

$$\rho^4 = (x^2+\frac{\bar{c}'_{11}}{c'_{22}}y^2)^2+\frac{(\bar{c}'_{11}+c'_{12})(\bar{c}'_{11}-c'_{12}-2c'_{66})}{c'_{22}c'_{66}}x^2y^2;$$

$$\bar{c}'_{11} = (c'_{11}c'_{22})^{1/2}$$

6.3. Stress and strain fields of pure screw dislocations in anisotropic medium

For pure screw dislocation:

$$\sigma_{xz} = -\frac{b_z}{2\pi}(c'_{44}c'_{55}-c'^2_{45})^{1/2}\frac{c'_{45}x-c'_{55}y}{c'_{44}x^2-2c'_{45}xy+c'_{55}y^2}$$

$$\sigma_{yz} = -\frac{b_z}{2\pi}(c'_{44}c'_{55}-c'^2_{45})^{1/2}\frac{c'_{44}x-c'_{45}y}{c'_{44}x^2-2c'_{45}xy+c'_{55}y^2}$$

$$\sigma_{zz} = -\frac{b_z}{2\pi}(c'_{44}c'_{55}-c'^2_{45})^{1/2}\frac{c'_{34}x-c'_{35}y}{c'_{44}x^2-2c'_{45}xy+c'_{55}y^2}$$

6.4. Stress and strain fields of a spherical particle in anisotropic medium

A particle which is misfitting with respect to the matrix, generates stress fields both within the particle and in the matrix. The dislocation interacts with the particle through these stress fields. The stress fields generated by a (dilatational) misfitting spherical particle were given by Eshelby [33]. The stress field at a point (x,y,z) outside a particle of radius R sitting at the origin of the co-ordinate system (0,0,0) is :

$$\sigma^{pt} = \frac{2\Delta G\varepsilon R^3}{r^5}\begin{Bmatrix} r^2-3x^2 & -3xy & -3xz \\ -3xy & r^2-3y^2 & -3yz \\ -3xz & -3yz & r^2-3z^2 \end{Bmatrix}$$

where, r is the distance from the point to the particle center, $r=\sqrt{(x-x_0)^2+(y-y_0)^2+(z-z_0)^2}$,

ΔG is difference in shear modulus between particle and matrix,

$\varepsilon=\varepsilon_0 (1+\nu)/3(1-\nu)$,

where ν is Poisson's ration, and ε_0 is dilatational misfit strain (ratio of difference in in-plane lattice constants to that of matrix lattice constant).

6.5. Cross-slip systems in BCT Sn lattice

Slip Systems		**Possible Cross-slip Systems**
SS1	(100)_[001]	(010); (110); (1-10)
	(010)_[001]	(100); (110); (1-10)
SS2	(110)_[001]	(100); (010); (1-10)
	(1-10)_[001]	(100); (010); (110)
SS4	(110)_[1-11]	-121
	(110)_[-111]	-211
	(1-10)_[111]	(1-21)
	(1-10)_[-1-11]	-112
SS7	(001)_[100]	(010); (011);(01-1)
	(001)_[010]	(100); (101);(10-1)
SS8	(001)_[110]	(1-10);
	(001)_[1-10]	(110);

Bibliography

[1] P. Sharma, *Micro-structural Modeling of Cyclic Creep Damage in Tin-lead Eutectic Solder*. University of Maryland, College Park, 2000.

[2] M. Kerr and N. Chawla, "Creep deformation behavior of Sn-3.5Ag solder at small length scales," *JOM J. Miner. Met. Mater. Soc.*, vol. 56, no. 6, pp. 50–54, 2004.

[3] S. K. Kang, P. A. Lauro, D.-Y. Shih, D. W. Henderson, and K. J. Puttlitz, "Microstructure and mechanical properties of lead-free solders and solder joints used in microelectronic applications," *IBM J Res Dev*, vol. 49, no. 4/5, pp. 607–620, Jul. 2005.

[4] A. Telang and T. Bieler, "The orientation imaging microscopy of lead-free Sn-Ag solder joints," *JOM J. Miner. Met. Mater. Soc.*, vol. 57, no. 6, pp. 44–49, 2005.

[5] W. Plumbridge, C. Gagg, and S. Peters, "The creep of lead-free solders at elevated temperatures," *J. Electron. Mater.*, vol. 30, no. 9, pp. 1178–1183, 2001.

[6] R. S. Sidhu and N. Chawla, "Microstructure Characterization and Creep Behavior of Pb-Free Sn-Rich Solder Alloys: Part I. Microstructure Characterization of Bulk Solder and Solder/Copper Joints," *Metall. Mater. Trans. A*, vol. 39, no. 2, pp. 340–348, 2008.

[7] J. G. Lee, A. Telang, K. N. Subramanian, and T. R. Bieler, "Modeling Thermomechanical Fatigue Behavior of Sn-Ag Solder Joints," *J. Electron. Mater.*, vol. 31, no. 11, pp. 1152–1159, 2002.

[8] G. Cuddalorepatta and A. Dasgupta, "Multi-scale modeling of the viscoplastic response of As-fabricated microscale Pb-free Sn3.0Ag0.5Cu solder interconnects," *Acta Mater.*, vol. 58, no. 18, pp. 5989–6001, 2010.

[9] P. Vianco, J. Rejent, and A. Kilgo, "Creep behavior of the ternary 95.5Sn-3.9Ag-0.6Cu solder—Part I: As-cast condition," *J. Electron. Mater.*, vol. 33, no. 11, pp. 1389–1400, 2004.

[10] H. Ma and J. Suhling, "A review of mechanical properties of lead-free solders for electronic packaging," *J. Mater. Sci.*, vol. 44, no. 5, pp. 1141–1158, 2009.

[11] M. A. Rist, W. J. Plumbridge, and S. Cooper, "Creep-constitutive behavior of Sn-3.8Ag-0.7Cu solder using an internal stress approach," *J. Electron. Mater.*, vol. 35, no. 5, pp. 1050–1058, May 2006.

[12] G. Cuddalorepatta, M. Williams, and A. Dasgupta, "Viscoplastic Creep Response and Microstructure of As-Fabricated Microscale Sn-3.0Ag-0.5Cu Solder Interconnects," *J. Electron. Mater.*, vol. 39, no. 10, pp. 2292–2309, 2010.

[13] G. Cuddalorepatta and A. Dasgupta, "Effect of primary creep behavior on fatigue damage accumulation rates in accelerated thermal cycling of Sn3.0Ag0.5Cu Pb-free interconnects," in *Thermal, Mechanical and Multi-Physics Simulation and Experiments in Microelectronics and Micro-Systems, 2008. EuroSimE 2008. International Conference on*, 2008, pp. 1 –8.

[14] P. Borgesen, T. Bieler, L. P. Lehman, and E. J. Cotts, "Pb-Free Solder: New Materials Considerations for Microelectronics Processing," *MRS Bull.*, vol. 32, no. April, pp. 360–365, 2007.

[15] T. R. Bieler, H. Jiang, L. P. Lehman, T. Kirkpatrick, E. J. Cotts, and B. Nandagopal, "Influence of Sn Grain Size and Orientation on the Thermomechanical Response and Reliability of Pb-free Solder Joints," *Compon. Packag. Technol. IEEE Trans. On*, vol. 31, no. 2, pp. 370 –381, Jun. 2008.

[16] L. Lehman, S. Athavale, T. Fullem, A. Giamis, R. Kinyanjui, M. Lowenstein, K. Mather, R. Patel, D. Rae, J. Wang, Y. Xing, L. Zavalij, P. Borgesen, and E. Cotts, "Growth of Sn and intermetallic compounds in Sn-Ag-Cu solder," *J. Electron. Mater.*, vol. 33, no. 12, pp. 1429–1439, 2004.

[17] S. Park, R. Dhakal, L. Lehman, and E. J. Cotts, "Grain Deformation and Strain in Board Level SnAgCu Solder Interconnects Under Deep Thermal Cycling," *Compon. Packag. Technol. IEEE Trans. On*, vol. 30, no. 1, pp. 178 –185, Mar. 2007.

[18] S. Wiese, M. Roellig, M. Mueller, and K.-J. Wolter, "The effect of downscaling the dimensions of solder interconnects on their creep properties," *Microelectron. Reliab.*, vol. 48, no. 6, pp. 843–850, Jun. 2008.

[19] C. Andersson, Z. Lai, J. Liu, H. Jiang, and Y. Yu, "Comparison of isothermal mechanical fatigue properties of lead-free solder joints and bulk solders," *Mater. Sci. Eng. A*, vol. 394, no. 1–2, pp. 20–27, Mar. 2005.

[20] K. S. Kim, "Effects of fourth alloying additive on microstructures and tensile properties of Sn-Ag-Cu alloy and joints with Cu," *Microelectron. Reliab.*, vol. 43, no. 2, pp. 259–267, 2003.

[21] S. K. Kang, D.-Y. Shih, D. Leonard, D. W. Henderson, T. Gosselin, S. Cho, J. Yu, and W. K. Choi, "Controlling Ag3Sn plate formation in near-ternary-eutectic Sn-Ag-Cu solder by minor Zn alloying," *Jom*, vol. 56, no. 6, pp. 34–38, 2004.

[22] I. Anderson, J. Foley, B. Cook, J. Harringa, R. Terpstra, and O. Unal, "Alloying effects in near-eutectic Sn-Ag-Cu solder alloys for improved microstructural stability," *J. Electron. Mater.*, vol. 30, no. 9, pp. 1050–1059, 2001.

[23] I. Anderson, B. Cook, J. Harringa, and R. Terpstra, "Sn-Ag-Cu solders and solder joints: Alloy development, microstructure, and properties," *JOM J. Miner. Met. Mater. Soc.*, vol. 54, no. 6, pp. 26–29, 2002.

[24] Y. Kariya, T. Hosoi, T. Kimura, S. Terashima, M. Tanaka, and T. Suga, "Fatigue life enhancement of low silver content Sn-Ag-Cu flip-chip interconnects by Ni addition," in *Thermal and Thermomechanical Phenomena in Electronic Systems, 2004. ITHERM '04. The Ninth Intersociety Conference on*, 2004, vol. 2, pp. 103 – 108 Vol.2.

[25] C.-M. Chuang and K.-L. Lin, "Effect of microelements addition on the interfacial reaction between Sn-Ag-Cu solders and the Cu substrate," *J. Electron. Mater.*, vol. 32, no. 12, pp. 1426–1431, 2003.

[26] J.-M. Song, Y.-R. Liu, C.-W. Su, Y.-S. Lai, and Y.-T. Chiu, "Intermetallic formation induced substrate dissolution in electroless Ni(P)-solder interconnections," *J. Mater. Res.*, vol. 23, no. 09, pp. 2545–2554, Jan. 2011.

[27] W. Liu, P. Bachorik, and N.-C. Lee, "The superior drop test performance of SAC-Ti solders and its mechanism," in *Electronic Manufacturing Technology Symposium (IEMT), 2008 33rd IEEE/CPMT International*, 2008, pp. 1 –9.

[28] H. Ma, J. C. Suhling, P. Lall, and M. J. Bozack, "Effects of aging on the stress-strain and creep behaviors of lead free solders," in *Thermal and Thermomechanical Phenomena in Electronics Systems, 2006. ITHERM '06. The Tenth Intersociety Conference on*, 2006, pp. 961 –976.

[29] H. Ma, J. C. Suhling, Y. Zhang, P. Lall, and M. J. Bozack, "The Influence of Elevated Temperature Aging on Reliability of Lead Free Solder Joints," in *Electronic Components and Technology Conference, 2007. ECTC '07. Proceedings. 57th*, 2007, pp. 653 –668.

[30] Y. Zhang, Z. Cai, J. C. Suhling, P. Lall, and M. J. Bozack, "The effects of aging temperature on SAC solder joint material behavior and reliability," in *Electronic Components and Technology Conference, 2008. ECTC 2008. 58th*, 2008, pp. 99 –112.

[31] Q. Xiao, L. Nguyen, and W. D. Armstrong, "Aging and creep behavior of Sn3.9Ag0.6Cu solder alloy," in *Electronic Components and Technology Conference, 2004. Proceedings. 54th*, 2004, vol. 2, pp. 1325 – 1332 Vol.2.

[32] N. Iosipescu, "New Accurate Procedure for Single Shear Testing of Metals," *Journal of Materials*, vol. 2, no. 3, pp. 537–566, 1967.

[33] J.-P. Clech, "An extension of the omega method to primary and tertiary creep of lead-free solders," in *Electronic Components and Technology Conference, 2005. Proceedings. 55th*, 2005, pp. 1261–1271 Vol. 2.

[34] W.J. Plumbridge, "The analysis of creep data for solder alloys," *Solder. Surf. Mt. Technol.*, vol. 15, no. 1, pp. 26–30, Apr. 2003.

[35] D. Bhate, D. Chan, G. Subbarayan, T. C. Chiu, V. Gupta, and D. R. Edwards, "Constitutive Behavior of Sn3.8Ag0.7Cu and Sn1.0Ag0.5Cu Alloys at Creep and Low Strain Rate Regimes," *IEEE Trans. Compon. Packag. Technol.*, vol. 31, no. 3, pp. 622–633, Sep. 2008.

[36] G. Cuddalorepatta and A. Dasgupta, "Effect of primary creep behavior on fatigue damage accumulation rates in accelerated thermal cycling of Sn3.0Ag0.5Cu Pb-free interconnects," in *International Conference on Thermal, Mechanical and Multi-Physics Simulation and Experiments in Microelectronics and Micro-Systems, 2008. EuroSimE 2008*, 2008, pp. 1–8.

[37] M. A. Matin, E. W. C. Coenen, W. P. Vellinga, and M. G. D. Geers, "Correlation between thermal fatigue and thermal anisotropy in a Pb-free solder alloy," *Scr. Mater.*, vol. 53, no. 8, pp. 927–932, Oct. 2005.

[38] J.-H. Zhao, P. Su, M. Ding, S. Chopin, and P. S. Ho, "Microstructure-Based Stress Modeling of Tin Whisker Growth," *Electron. Packag. Manuf. IEEE Trans. On*, vol. 29, no. 4, pp. 265 –273, Oct. 2006.
[39] K. N. Subramanian, "Role of anisotropic behaviour of Sn on thermomechanical fatigue and fracture of Sn-based solder joints under thermal excursions," *Fatigue Fract. Eng. Mater. Struct.*, vol. 30, no. 5, pp. 420–431, 2007.
[40] A. U. Telang and T. R. Bieler, "Characterization of microstructure and crystal orientation of the tin phase in single shear lap Sn–3.5Ag solder joint specimens," *Scr. Mater.*, vol. 52, no. 10, pp. 1027–1031, May 2005.
[41] R. L. J. M. Ubachs, P. J. G. Schreurs, and M. G. D. Geers, "Elasto-viscoplastic nonlocal damage modelling of thermal fatigue in anisotropic lead-free solder," *Mech. Mater.*, vol. 39, no. 7, pp. 685–701, Jul. 2007.
[42] S. Park, R. Dhakal, and J. Gao, "Three-Dimensional Finite Element Analysis of Multiple-Grained Lead-Free Solder Interconnects," *J. Electron. Mater.*, vol. 37, no. 8, pp. 1139–1147, 2008.
[43] A. Zamiri, T. R. Bieler, and F. Pourboghrat, "Anisotropic Crystal Plasticity Finite Element Modeling of the Effect of Crystal Orientation and Solder Joint Geometry on Deformation after Temperature Change," *J. Electron. Mater.*, vol. 38, no. 2, pp. 231–240, 2009.
[44] J. Rösler and M. Bäker, "A theoretical concept for the design of high-temperature materials by dual-scale particle strengthening," *Acta Mater.*, vol. 48, no. 13, pp. 3553–3567, Aug. 2000.
[45] S. Wiese and K.-J. Wolter, "Microstructure and creep behaviour of eutectic SnAg and SnAgCu solders," *Microelectron. Reliab.*, vol. 44, no. 12, pp. 1923–1931, Dec. 2004.
[46] T. Chen and I. Dutta, "Effect of Ag and Cu Concentrations on the Creep Behavior of Sn-Based Solders," *J. Electron. Mater.*, vol. 37, no. 3, pp. 347–354, 2008.
[47] I. Dutta, C. Park, and S. Choi, "Impression creep characterization of rapidly cooled Sn–3.5Ag solders," *Mater. Sci. Eng. A*, vol. 379, no. 1–2, pp. 401–410, Aug. 2004.
[48] M. Kerr and N. Chawla, "Creep deformation behavior of Sn–3.5Ag solder/Cu couple at small length scales," *Acta Mater.*, vol. 52, no. 15, pp. 4527–4535, Sep. 2004.
[49] M. Mathew, H. Yang, S. Movva, and K. Murty, "Creep deformation characteristics of tin and tin-based electronic solder alloys," *Metall. Mater. Trans. A*, vol. 36, no. 1, pp. 99–105, 2005.
[50] F. Ochoa, X. Deng, and N. Chawla, "Effects of cooling rate on creep behavior of a Sn-3.5Ag alloy," *J. Electron. Mater.*, vol. 33, no. 12, pp. 1596–1607, Dec. 2004.
[51] E. Arzt and E. Göhring, "A model for dispersion strengthening of ordered intermetallics at high temperatures," *Acta Mater.*, vol. 46, no. 18, pp. 6575–6584, Nov. 1998.
[52] J. Gong, C. Liu, P. P. Conway, and V. V. Silberschmidt, "Modelling of Ag3Sn coarsening and its effect on creep of Sn–Ag eutectics," *Mater. Sci. Eng. A*, vol. 427, no. 1–2, pp. 60–68, Jul. 2006.
[53] Chawla and R. S. Sidhu, "Microstructure-based modeling of deformation in Sn-rich (Pb-free) solder alloys," *J. Mater. Sci. Mater. Electron.*, vol. 18, no. 1–3, pp. 175–189, 2006.
[54] M. Pei and J. Qu, "Hierarchical Modeling of Creep Behavior of SnAg Solder Alloys," in *Electronic Components and Technology Conference, 2007. ECTC '07. Proceedings. 57th*, 2007, pp. 273 –277.
[55] J. Rösler and E. Arzt, "A new model-based creep equation for dispersion strengthened materials," *Acta Metall. Mater.*, vol. 38, no. 4, pp. 671–683, Apr. 1990.
[56] E. Arzt and J. Rösler, "The kinetics of dislocation climb over hard particles—II. Effects of an attractive particle-dislocation interaction," *Acta Metall.*, vol. 36, no. 4, pp. 1053–1060, Apr. 1988.
[57] E. Arzt and D. S. Wilkinson, "Threshold stresses for dislocation climb over hard particles: The effect of an attractive interaction," *Acta Metall.*, vol. 34, no. 10, pp. 1893–1898, Oct. 1986.
[58] J. Rosler, "Particle strengthened alloys for high temperature applications: strengthening mechanisms and fundamentals of design," *Int. J. Mater. Prod. Technol.*, vol. 18, no. 1, pp. 70–90, Jan. 2003.
[59] G. Cuddalorepatta and A. Dasgupta, "Multi-scale modeling of the viscoplastic response of As-fabricated microscale Pb-free Sn3.0Ag0.5Cu solder interconnects," *Acta Mater.*, vol. 58, no. 18, pp. 5989–6001, Oct. 2010.

[60] E. Arzt and J. Rösler, “The kinetics of dislocation climb over hard particles—II. Effects of an attractive particle-dislocation interaction,” *Acta Metall.*, vol. 36, no. 4, pp. 1053–1060, Apr. 1988.
[61] E. Arzt and J. Rösler, “The kinetics of dislocation climb over hard particles—II. Effects of an attractive particle-dislocation interaction,” *Acta Metall.*, vol. 36, no. 4, pp. 1053–1060, Apr. 1988.
[62] E. Arzt and D. S. Wilkinson, “Threshold stresses for dislocation climb over hard particles: The effect of an attractive interaction,” *Acta Metall.*, vol. 34, no. 10, pp. 1893–1898, Oct. 1986.
[63] S. Nemat-Nasser and M. Hori, *Micromechanics: Overall Properties of Heterogeneous Materials, Second Edition*, 2nd ed. North Holland, 1999.
[64] G. Y. Li, B. L. Chen, X. Q. Shi, S. C. K. Wong, and Z. F. Wang, “Effects of Sb addition on tensile strength of Sn–3.5Ag–0.7Cu solder alloy and joint,” *Thin Solid Films*, vol. 504, no. 1–2, pp. 421–425, May 2006.
[65] B. L. Chen and G. Y. Li, “An investigation of effects of Sb on the intermetallic formation in Sn-3.5Ag-0.7Cu solder joints,” *Compon. Packag. Technol. IEEE Trans. On*, vol. 28, no. 3, pp. 534 – 541, Sep. 2005.
[66] B. L. Chen and G. Y. Li, “Influence of Sb on IMC growth in Sn–Ag–Cu–Sb Pb-free solder joints in reflow process,” *Thin Solid Films*, vol. 462–463, pp. 395–401, Sep. 2004.
[67] C. Lee, C.-Y. Lin, and Y.-W. Yen, “The 260 °C phase equilibria of the Sn–Sb–Cu ternary system and interfacial reactions at the Sn–Sb/Cu joints,” *Intermetallics*, vol. 15, no. 8, pp. 1027–1037, Aug. 2007.
[68] Y.-S. Park, Y.-M. Kwon, H.-Y. Son, J.-T. Moon, B.-W. Jeong, K.-I. Kang, and K.-W. Paik, “Effect of sb addition in sn-ag-cu solder balls on the drop test reliability of BGA packages with electroless nickel immersion gold (ENIG) surface finish,” pp. 317–321, 2007.
[69] W. Liu, N.-C. Lee, A. Porras, M. Ding, A. Gallagher, A. Huang, S. Chen, and J. ChangBing Lee, “Achieving high reliability low cost lead-free SAC solder joints via Mn or Ce doping,” in *Electronic Components and Technology Conference, 2009. ECTC 2009. 59th*, 2009, pp. 994 – 1007.
[70] W. Liu, N.-C. Lee, A. Porras, M. Ding, A. Gallagher, A. Huang, S. Chen, and J. C.-B. Lee, “Shock resistant and thermally reliable low Ag SAC solders doped with Mn Or Ce,” in *Electronics Packaging Technology Conference, 2009. EPTC ’09. 11th*, 2009, pp. 49 –63.
[71] W. Liu and N.-C. Lee, “The effects of additives to SnAgCu alloys on microstructure and drop impact reliability of solder joints,” *Jom*, vol. 59, no. 7, pp. 26–31, 2007.
[72] Y.-R. Liu, J.-M. Song, Y.-S. Lai, and Y.-T. Chiu, “Effect of minor alloying additions on the BIT reliability of SnAgCu solder joints,” in *Microsystems, Packaging, Assembly and Circuits Technology Conference, 2009. IMPACT 2009. 4th International*, 2009, pp. 501 –504.
[73] I. Anderson and J. Harringa, “Suppression of void coalescence in thermal aging of tin-silver-copper-X solder joints,” *J. Electron. Mater.*, vol. 35, no. 1, pp. 94–106, 2006.
[74] L. Gao, S. Xue, L. Zhang, Z. Sheng, F. Ji, W. Dai, S. Yu, and G. Zeng, “Effect of alloying elements on properties and microstructures of SnAgCu solders,” *Microelectron. Eng.*, vol. 87, no. 11, pp. 2025–2034, Nov. 2010.
[75] L.-W. Lin, J.-M. Song, Y.-S. Lai, Y.-T. Chiu, and N.-C. Lee, “Alloying design of Sn-Ag-Cu solders for the improvement in drop test performance,” in *Electronic Materials and Packaging, 2008. EMAP 2008. International Conference on*, 2008, pp. 33 –36.
[76] P. Chauhan, “MICROSTRUCTURAL CHARACTERIZATION AND THERMAL CYCLING RELIABILITY OF SOLDERS UNDER ISOTHERMAL AGING AND ELECTRICAL CURRENT,” University of Maryland, College Park, Maryland, USA, 2012.
[77] I. Dutta, D. Pan, R. A. Marks, and S. G. Jadhav, “Effect of thermo-mechanically induced microstructural coarsening on the evolution of creep response of SnAg-based microelectronic solders,” *Mater. Sci. Eng. A*, vol. 410–411, pp. 48–52, Nov. 2005.
[78] Q. Zhang, “Isothermal Mechanical and Thermo-mechanical Durability Characterization of Selected Pb-Free Solders,” PhD Dissertation, University of Maryland, College Park, MD, USA, 2004.
[79] P. Haswell, “Durability Assessment and Microstructural Observations of Selected Solder Alloys,” PhD Dissertation, University of Maryland, College Park, MD, USA, 2001.
[80] N. Iosipescu, “New Accurate Procedure for Single Shear Testing of Metals,” *J. of Materials*, vol. 2, no. 3, pp. 537–566, Sep. 1967.

[81] M. P. T. Reinikainen, “A Finite-Element and Experimental Analysis of Stress Distribution in Various Shear Tests for Solder Joints,” *J. Electron. Packag. - J ELECTRON Packag.*, vol. 120, no. 1, 1998.
[82] G. Cuddalorepatta, “Evolution of the microstructure and viscoplatic behavior of microscale SAC305 solder joints as a function of mechanical fatigue damage,” PhD Dissertation, University of Maryland, College Park, MD, USA, 2010.
[83] T. R. Bieler, H. Jiang, L. P. Lehman, T. Kirkpatrick, and E. J. Cotts, “Influence of Sn grain size and orientation on the thermomechanical response and reliability of Pb-free solder joints,” in *Electronic Components and Technology Conference, 2006. Proceedings. 56th*, 2006.
[84] S. Terashima, T. Kohno, A. Mizusawa, K. Arai, O. Okada, T. Wakabayashi, M. Tanaka, and K. Tatsumi, “Improvement of Thermal Fatigue Properties of Sn-Ag-Cu Lead-Free Solder Interconnects on Casio’s Wafer-Level Packages Based on Morphology and Grain Boundary Character,” *J. Electron. Mater.*, vol. 38, no. 1, pp. 33–38, Oct. 2008.
[85] M. Lu, D.-Y. Shih, P. Lauro, C. Goldsmith, and D. W. Henderson, “Effect of Sn grain orientation on electromigration degradation mechanism in high Sn-based Pb-free solders,” *Appl. Phys. Lett.*, vol. 92, no. 21, pp. 211909–211909–3, May 2008.
[86] J. Li, T. T. Mattila, and J. K. Kivilahti, “Multiscale Simulation of Microstructural Changes in Solder Interconnections During Thermal Cycling,” *J. Electron. Mater.*, vol. 39, no. 1, pp. 77–84, Sep. 2009.
[87] Y. Wang, K. H. Lu, V. Gupta, L. Stiborek, D. Shirley, J. Im, and P. S. Ho, “Effect of Sn grain structure on electromigration reliability of Pb-free solders,” in *Electronic Components and Technology Conference (ECTC), 2011 IEEE 61st*, 2011, pp. 711–716.
[88] K. Lee, K.-S. Kim, K. Yamanaka, Y. Tsukada, S. Kuritani, M. Ueshima, and K. Suganuma, “Effects of the crystallographic orientation of Sn grain during electromigration test,” in *2010 IEEE CPMT Symposium Japan*, 2010, pp. 1–4.
[89] T. T. Mattila, E. Kaloinen, A. Syed, and J. K. Kivilahti, “Reliability of SnAgCu Interconnections with Minor Additions of Ni or Bi under Mechanical Shock Loading at Different Temperatures,” in *Electronic Components and Technology Conference, 2007. ECTC ’07. Proceedings. 57th*, 2007, pp. 381–390.
[90] H. Kim, M. Zhang, C. M. Kumar, D. Suh, P. Liu, D. Kim, M. Xie, and Z. Wang, “Improved Drop Reliability Performance with Lead Free Solders of Low Ag Content and Their Failure Modes,” in *Electronic Components and Technology Conference, 2007. ECTC ’07. Proceedings. 57th*, 2007, pp. 962–967.
[91] W. H. Zhu, L. Xu, J. H. L. Pang, X. R. Zhang, E. Poh, Y. F. Sun, A. Y. S. Sun, C. K. Wang, and H. B. Tan, “Drop reliability study of PBGA assemblies with SAC305, SAC105 and SAC105-Ni solder ball on Cu-OSP and ENIG surface finish,” in *Electronic Components and Technology Conference, 2008. ECTC 2008. 58th*, 2008, pp. 1667–1672.
[92] K. S. Kim, S. H. Huh, and K. Suganuma, “Effects of fourth alloying additive on microstructures and tensile properties of Sn–Ag–Cu alloy and joints with Cu,” *Microelectron. Reliab.*, vol. 43, no. 2, pp. 259–267, Feb. 2003.
[93] G. Y. Li, B. L. Chen, X. Q. Shi, S. C. K. Wong, and Z. F. Wang, “Effects of Sb addition on tensile strength of Sn–3.5Ag–0.7Cu solder alloy and joint,” *Thin Solid Films*, vol. 504, no. 1–2, pp. 421–425, 2006.
[94] B. L. Chen and G. Y. Li, “Influence of Sb on IMC growth in Sn–Ag–Cu–Sb Pb-free solder joints in reflow process,” *Thin Solid Films*, vol. 462–463, pp. 395–401, Sep. 2004.
[95] B. L. Chen and G. Y. Li, “An investigation of effects of Sb on the intermetallic formation in Sn-3.5Ag-0.7Cu solder joints,” *IEEE Trans. Compon. Packag. Technol.*, vol. 28, no. 3, pp. 534–541, Sep. 2005.
[96] M. Amagai, “A study of nanoparticles in Sn–Ag based lead free solders,” *Microelectron. Reliab.*, vol. 48, no. 1, pp. 1–16, Jan. 2008.
[97] G. Y. Li, B. L. Chen, and J. N. Tey, “Reaction of Sn-3.5Ag-0.7Cu-xSb solder with Cu metallization during reflow soldering,” *IEEE Trans. Electron. Packag. Manuf.*, vol. 27, no. 1, pp. 77–85, 2004.
[98] W. Liu, N.-C. Lee, A. Porras, M. Ding, A. Gallagher, A. Huang, S. Chen, and J. C.-B. Lee, “Shock resistant and thermally reliable low Ag SAC solders doped with Mn Or Ce,” in *Electronics Packaging Technology Conference, 2009. EPTC ’09. 11th*, 2009, pp. 49–63.

[99] W. Liu, N.-C. Lee, A. Porras, M. Ding, A. Gallagher, A. Huang, S. Chen, and J. C.-B. Lee, "Achieving high reliability low cost lead-free SAC solder joints via Mn or Ce doping," in *Electronic Components and Technology Conference, 2009. ECTC 2009. 59th*, 2009, pp. 994–1007.
[100] W. Liu and N.-C. Lee, "The effects of additives to SnAgCu alloys on microstructure and drop impact reliability of solder joints," *JOM*, vol. 59, no. 7, pp. 26–31, Jul. 2007.
[101] Y.-R. Liu, J.-M. Song, Y.-S. Lai, and Y.-T. Chiu, "Effect of minor alloying additions on the BIT reliability of SnAgCu solder joints," in *Microsystems, Packaging, Assembly and Circuits Technology Conference, 2009. IMPACT 2009. 4th International*, 2009, pp. 501–504.
[102] L.-W. Lin, J.-M. Song, Y.-S. Lai, Y.-T. Chiu, and N.-C. Lee, "Alloying design of Sn-Ag-Cu solders for the improvement in drop test performance," in *International Conference on Electronic Materials and Packaging, 2008. EMAP 2008*, Oct., pp. 33–36.
[103] Q. Zhang, A. Dasgupta, and P. Haswell, "Partitioned viscoplastic-constitutive properties of the Pb-free Sn3.9Ag0.6Cu solder," *J. Electron. Mater.*, vol. 33, no. 11, pp. 1338–1349, Nov. 2004.
[104] N. Iosipescu, "New Accurate Procedure for Single Shear Testing of Metals," *J. of Materials*, vol. 2, no. 3, pp. 537–566, Sep. 1967.
[105] T. Reinikainen, M. Poech, M. Krumm, and J. Kivilahti, "A Finite-Element and Experimental Analysis of Stress Distribution in Various Shear Tests for Solder Joints," *J. Electron. Packag.*, vol. 120, no. 1, pp. 106–113, Mar. 1998.
[106] G. Cuddalorepatta, M. Williams, and A. Dasgupta, "Viscoplastic Creep Response and Microstructure of As-Fabricated Microscale Sn-3.0Ag-0.5Cu Solder Interconnects," *J. Electron. Mater.*, vol. 39, no. 10, pp. 2292–2309, Oct. 2010.
[107] S. Mukherjee, T. T. Mattila, and A. Dasgupta, "Effect of addition of manganese and antimony on viscoplastic properties and cyclic mechanical durability of low silver Sn-Ag-Cu solder," in *2012 13th IEEE Intersociety Conference on Thermal and Thermomechanical Phenomena in Electronic Systems (ITherm)*, 2012, pp. 888–895.
[108] G. Cuddalorepatta and A. Dasgupta, "Multi-scale modeling of the viscoplastic response of As-fabricated microscale Pb-free Sn3.0Ag0.5Cu solder interconnects," *Acta Mater.*, vol. 58, no. 18, pp. 5989–6001, Oct. 2010.
[109] L. P. Lehman, Y. Xing, T. R. Bieler, and E. J. Cotts, "Cyclic twin nucleation in tin-based solder alloys," *Acta Mater.*, vol. 58, no. 10, pp. 3546–3556, Jun. 2010.
[110] J. Rösler and M. Bäker, "A theoretical concept for the design of high-temperature materials by dual-scale particle strengthening," *Acta Mater.*, vol. 48, no. 13, pp. 3553–3567, Aug. 2000.
[111] N. Hamada, M. Hamada, T. Uesugi, Y. Takigawa, and K. Higashi, "Effect of Small Addition of Zinc on Creep Behavior of Tin," *Mat. Trans.*, vol. 51, no. 10, pp. 1747–1752, 2010.
[112] S. N. Nasser and M. Hori, *Micromechanics: Overall Properties of Heterogeneous Materials*. North-Holland, 1993.
[113] M. Pei and J. Qu, "Hierarchal Modeling of Creep Behavior of SnAg Solder Alloys," *J. Electron. Packag.*, vol. 130, no. 3, p. 031004, 2008.
[114] A. Syed, "Accumulated creep strain and energy density based thermal fatigue life prediction models for SnAgCu solder joints," in *Electronic Components and Technology Conference, 2004. Proceedings. 54th*, 2004, vol. 1, pp. 737–746 Vol.1.
[115] R. Dudek, R. Döring, and B. Michel, "Reliability Prediction of Area Array Solder Joints," *J. Electron. Packag.*, vol. 125, no. 4, pp. 562–568, Dec. 2003.
[116] D. W. Henderson, J. J. Woods, T. A. Gosselin, J. Bartelo, D. E. King, T. M. Korhonen, M. A. Korhonen, L. P. Lehman, E. J. Cotts, S. K. Kang, P. Lauro, D.-Y. Shih, C. Goldsmith, and K. J. Puttlitz, "The microstructure of Sn in near-eutectic Sn–Ag–Cu alloy solder joints and its role in thermomechanical fatigue," *J. Mater. Res.*, vol. 19, no. 06, pp. 1608–1612, Jun. 2004.
[117] L. P. Lehman, S. N. Athavale, T. Z. Fullem, A. C. Giamis, R. K. Kinyanjui, M. Lowenstein, K. Mather, R. Patel, D. Rae, J. Wang, Y. Xing, L. Zavalij, P. Borgesen, and E. J. Cotts, "Growth of Sn and intermetallic compounds in Sn-Ag-Cu solder," *J. Electron. Mater.*, vol. 33, no. 12, pp. 1429–1439, Dec. 2004.
[118] L. P. L. R. Kinyanjui, "Effect of Sample Size on the Solidification Temperature and Microstructure of SnAgCu Near Eutectic Alloys," *J. Mater. Res.*, vol. 20, no. 11, pp. 2914 – 2918, 2005.

[119] A. U. Telang, T. R. Bieler, J. P. Lucas, K. N. Subramanian, L. P. Lehman, Y. Xing, and E. J. Cotts, "Grain-boundary character and grain growth in bulk tin and bulk lead-free solder alloys," *J. Electron. Mater.*, vol. 33, no. 12, pp. 1412–1423, Dec. 2004.
[120] K. N. Subramanian and J. G. Lee, "Effect of anisotropy of tin on thermomechanical behavior of solder joints," *J. Mater. Sci. Mater. Electron.*, vol. 15, no. 4, pp. 235–240, Apr. 2004.
[121] M. S. Shawkret Ahat, "Effects of static thermal aging and thermal cycling on the microstructure and shear strength of Sn95.5Ag3.8Cu0.7 solder joints," *J. Mater. Res.*, vol. 16, no. 10, pp. 2914 – 2921, 2001.
[122] J. A. Rayne and B. S. Chandrasekhar, "Elastic Constants of β Tin from 4.2°K to 300°K," *Phys. Rev.*, vol. 120, no. 5, pp. 1658–1663, Dec. 1960.
[123] J. G. Lee, F. Guo, S. Choi, K. N. Subramanian, T. R. Bieler, and J. P. Lucas, "Residual-mechanical behavior of thermomechanically fatigued Sn-Ag based solder joints," *J. Electron. Mater.*, vol. 31, no. 9, pp. 946–952, Sep. 2002.
[124] M. A. Matin, E. W. C. Coenen, W. P. Vellinga, and M. G. D. Geers, "Correlation between thermal fatigue and thermal anisotropy in a Sn-rich solder alloy," in *Proceedings of the 6th International Conference on Thermal, Mechanical and Multi-Physics Simulation and Experiments in Micro-Electronics and Micro-Systems, 2005. EuroSimE 2005*, 2005, pp. 497–501.
[125] A. U. Telang and T. R. Bieler, "Characterization of microstructure and crystal orientation of the tin phase in single shear lap Sn–3.5Ag solder joint specimens," *Scr. Mater.*, vol. 52, no. 10, pp. 1027–1031, May 2005.
[126] A. U. Telang, T. R. Bieler, and M. A. Crimp, "Grain boundary sliding on near-7°, 14°, and 22° special boundaries during thermomechanical cycling in surface-mount lead-free solder joint specimens," *Mater. Sci. Eng. A*, vol. 421, no. 1–2, pp. 22–34, Apr. 2006.
[127] A. U. Telang and T. R. Bieler, "The orientation imaging microscopy of lead-free Sn-Ag solder joints," *JOM*, vol. 57, no. 6, pp. 44–49, Jun. 2005.
[128] T. R. Bieler, H. Jiang, L. P. Lehman, T. Kirkpatrick, and E. J. Cotts, "Influence of Sn grain size and orientation on the thermomechanical response and reliability of Pb-free solder joints," in *Electronic Components and Technology Conference, 2006. Proceedings. 56th*, 2006, pp. 370–381.
[129] A. U. Telang, T. R. Bieler, D. E. Mason, and K. N. Subramanian, "Comparisons of experimental and computed crystal rotations caused by slip in crept and thermomechanically fatigued dual-shear eutectic Sn-Ag solder joints," *J. Electron. Mater.*, vol. 32, no. 12, pp. 1455–1462, Dec. 2003.
[130] S. Park, R. Dhakal, L. Lehman, and E. J. Cotts, "Grain Deformation and Strain in Board Level SnAgCu Solder Interconnects Under Deep Thermal Cycling," *IEEE Trans. Compon. Packag. Technol.*, vol. 30, no. 1, pp. 178 –185, Mar. 2007.
[131] J. Weertman, "Compressional Creep of Tin Single Crystals," *J. Appl. Phys.*, vol. 28, no. 2, pp. 196–197, Feb. 1957.
[132] F. Yang and J. C. M. Li, "Deformation behavior of tin and some tin alloys," *J. Mater. Sci. Mater. Electron.*, vol. 18, no. 1–3, pp. 191–210, Oct. 2006.
[133] J. Sylvestre and A. Blander, "Large-Scale Correlations in the Orientation of Grains in Lead-Free Solder Joints," *J. Electron. Mater.*, vol. 37, no. 10, pp. 1618–1623, Oct. 2008.
[134] S. N. G. Chu and J. C. M. Li, "Pencil slip in beta-tin single crystals," *J. Mater. Sci.*, vol. 15, no. 11, pp. 2733–2742, Nov. 1980.
[135] A. LaLonde, D. Emelander, J. Jeannette, D. Swenson, and D. W. Henderson, "Quantitative Metallography of beta-Sn Dendrites in Sn-3.8Ag-0.7Cu Ball Grid Array Solder Balls via Electron Backscatter Diffraction and Polarized Light Microscopy," *Journal of Electronic Materials*, vol. 33, no. 12, pp. 1545–49, 2004.
[136] J. J. W. Donald W. Henderson, "The microstructure of Sn in near-eutectic Sn–Ag–Cu alloy solder joints and its role in thermomechanical fatigue," *J. Mater. Res.*, vol. 19, no. 06, pp. 1608 – 1612, 2004.
[137] B. Arfaei, Y. Xing, J. Woods, J. Wolcott, P. Tumne, P. Borgesen, and E. Cotts, "The effect of Sn grain number and orientation on the shear fatigue life of SnAgCu solder joints," in *Electronic Components and Technology Conference, 2008. ECTC 2008. 58th*, 2008, pp. 459 –465.
[138] P. Borgesen, T. Bieler, L. P. Lehman, and E. J. Cotts, "Pb-Free Solder: New Materials Considerations for Microelectronics Processing," *MRS Bull.*, vol. 32, no. 04, pp. 360–365, 2007.

[139] H. Ma and J. C. Suhling, “A review of mechanical properties of lead-free solders for electronic packaging,” *J. Mater. Sci.*, vol. 44, no. 5, pp. 1141–1158, Mar. 2009.
[140] G. Cuddalorepatta, M. Williams, and A. Dasgupta, “Viscoplastic Creep Response and Microstructure of As-Fabricated Microscale Sn-3.0Ag-0.5Cu Solder Interconnects,” *J. Electron. Mater.*, vol. 39, no. 10, pp. 2292–2309, Oct. 2010.
[141] T.-K. Lee, B. Zhou, L. Blair, K.-C. Liu, and T. R. Bieler, “Sn-Ag-Cu Solder Joint Microstructure and Orientation Evolution as a Function of Position and Thermal Cycles in Ball Grid Arrays Using Orientation Imaging Microscopy,” *J. Electron. Mater.*, vol. 39, no. 12, pp. 2588–2597, Dec. 2010.
[142] N. C. M. Kerr, “Creep deformation behavior of Sn3.5Ag solder at small length scales,” *Jom*, vol. 56, no. 6, pp. 50–54, 2004.
[143] I. Dutta, “A constitutive model for creep of lead-free solders undergoing strain-enhanced microstructural coarsening: A first report,” *J. Electron. Mater.*, vol. 32, no. 4, pp. 201–207, Apr. 2003.
[144] M. Besterci and J. Čadek, “Creep in Dispersion Strengthened Materials on Al Basis Prepared by Powder Metallurgy,” *High Temp. Mater. Process.*, vol. 23, no. 1, Jan. 2004.
[145] B. . Han and D. . Dunand, “Creep of magnesium strengthened with high volume fractions of yttria dispersoids,” *Mater. Sci. Eng. A*, vol. 300, no. 1–2, pp. 235–244, Feb. 2001.
[146] E. Arzt and D. S. Wilkinson, “Threshold stresses for dislocation climb over hard particles: The effect of an attractive interaction,” *Acta Metall.*, vol. 34, no. 10, pp. 1893–1898, Oct. 1986.
[147] G. S. Ansell and J. Weertman, “Creep of a dispersion-hardened aluminium alloy,” *Trans. of the Mettalurgical Society of AIME*, vol. 215, p. 838, Oct. 1959.
[148] E. Arzt and E. Göhring, “A model for dispersion strengthening of ordered intermetallics at high temperatures,” *Acta Mater.*, vol. 46, no. 18, pp. 6575–6584, Nov. 1998.
[149] J. H. Schröder and E. Arzt, “Weak beam studies of dislocation/dispersoid interaction in an ods superalloy,” *Scr. Metall.*, vol. 19, no. 9, pp. 1129–1134, Sep. 1985.
[150] N. S. Brar and W. R. Tyson, “Elastic and Plastic Anisotropy of White Tin,” *Can. J. Phys.*, vol. 50, no. 19, pp. 2257–2264, Oct. 1972.
[151] R. . Weeks, S. . Pati, M. . Ashby, and P. Barrand, “The elastic interaction between a straight dislocation and a bubble or a particle,” *Acta Metall.*, vol. 17, no. 12, pp. 1403–1410, Dec. 1969.
[152] R. R. Chromik, R. P. Vinci, S. L. Allen, and M. R. Notis, “Nanoindentation measurements on Cu–Sn and Ag–Sn intermetallics formed in Pb-free solder joints,” *J. Mater. Res.*, vol. 18, no. 09, pp. 2251–2261, 2003.
[153] J. P. Poirier, “On the symmetrical role of cross-slip of screw dislocations and climb of edge dislocations as recovery processes controlling high-temperature creep,” *Rev. Phys. Appliquée*, vol. 11, no. 6, pp. 731–738, 1976.
[154] R. J. McCabe and M. E. Fine, “Creep of tin, Sb-solution-strengthened tin, and SbSn-precipitate-strengthened tin,” *Metall. Mater. Trans. A*, vol. 33, no. 5, pp. 1531–1539, May 2002.
[155] “Rate Equations, ‘http://engineering.dartmouth.edu/defmech/chapter_2.htm.’” .
[156] B. Zhou, T. R. Bieler, T.-K. Lee, and K.-C. Liu, “Methodology for Analyzing Slip Behavior in Ball Grid Array Lead-Free Solder Joints After Simple Shear,” *J. Electron. Mater.*, vol. 38, no. 12, pp. 2702–2711, Dec. 2009.
[157] T. R. Bieler and A. U. Telang, “Analysis of Slip Behavior in a Single Shear Lap Lead-Free Solder Joint During Simple Shear at 25°C and 0.1/s,” *J. Electron. Mater.*, vol. 38, no. 12, pp. 2694–2701, Dec. 2009.
[158] J. D. Eshelby, W. T. Read, and W. Shockley, “Anisotropic elasticity with applications to dislocation theory,” *Acta Metall.*, vol. 1, no. 3, pp. 251–259, May 1953.
[159] D. M. Barnett, R. J. Asaro, S. D. Gavazza, D. J. Bacon, and R. O. Scattergood, “The effects of elastic anisotropy on dislocation line tension in metals,” *J. Phys. F Met. Phys.*, vol. 2, no. 5, pp. 854–864, Sep. 1972.
[160] A. N. Stroh, “Dislocations and Cracks in Anisotropic Elasticity,” *Philos. Mag.*, vol. 3, no. 30, pp. 625–646, 1958.
[161] J. Chang, W. Cai, V. V. Bulatov, and S. Yip, “Molecular dynamics simulations of motion of edge and screw dislocations in a metal,” *Comput. Mater. Sci.*, vol. 23, pp. 111–115, 2002.
[162] J. P. Hirth and J. Lothe, *Theory of Dislocations*, vol. Chapter 7, Dislocation Dynamics. Krieger, 1982.

[163] J. Preußner, Y. Rudnik, H. Brehm, R. Völkl, and U. Glatzel, “A dislocation density based material model to simulate the anisotropic creep behavior of single-phase and two-phase single crystals,” *Int. J. Plast.*, vol. 25, no. 5, pp. 973–994, May 2009.
[164] B. Düzgün and İ. Karaman, “The Relation Between Dislocation Density and Crystal Crosscut in b-Sn Grown by Modified Bridgman Method,” *Turk. J. Phys.*, vol. 22, no. 8, pp. 803–810, 1998.
[165] A. N. Gulluoglu, C. T. Tsai, C. S. Hartley, and A. Chait, “Dislocation generation in GaAs crystals grown by the Bridgman method using a crystallographic model,” *Model. Simul. Mater. Sci. Eng.*, vol. 2, no. 1, p. 67, Jan. 1994.
[166] H. Ma, J. C. Suhling, P. Lall, and M. J. Bozack, “Effects of aging on the stress-strain and creep behaviors of lead free solders,” in *The Tenth Intersociety Conference on Thermal and Thermomechanical Phenomena in Electronics Systems, 2006. ITHERM ’06*, 2006, pp. 961–976.
[167] T. Mura, *Micromechanics of Defects in Solids*, 2nd edition. Dordrecht, Netherlands ; Boston : Hingham, MA, USA: Springer, 1987.
[168] J. D. Eshelby, W. T. Read, and W. Shockley, “Anisotropic elasticity with applications to dislocation theory,” *Acta Metall.*, vol. 1, no. 3, pp. 251–259, May 1953.
[169] A. N. Stroh, “Dislocations and cracks in anisotropic elasticity,” *Philosophical Magazine*, vol. 3, no. 30, p. 625, 1958.
[170] D. M. Barnett, R. J. Asaro, S. D. Gavazza, D. J. Bacon, and R. O. Scattergood, “The effects of elastic anisotropy on dislocation line tension in metals,” *J. Phys. F Met. Phys.*, vol. 2, no. 5, pp. 854–864, Sep. 1972.
[171] D. M. Barnett and L. A. Swasger, “The elastic energy of a straight dislocation in an infinite anisotropic elastic medium,” *Phys. Status Solidi B*, vol. 48, no. 1, pp. 419–428, 1971.
[172] A. N. Stroh, “Dislocations and Cracks in Anisotropic Elasticity,” *Philos. Mag.*, vol. 3, no. 30, pp. 625–646, 1958.
[173] D. G. House and E. V. Vernon, “Determination of the elastic moduli of tin single crystals, and their variation with temperature,” *Br. J. Appl. Phys.*, vol. 11, no. 6, p. 254, Jun. 1960.
[174] D. B. S. V. T. Deshpande, “Thermal expansion of tin in the β–γ transition region,” *Acta Crystallogr.*, vol. 15, no. 3, pp. 294–295, 1962.
[175] L. P. Lehman, Y. Xing, T. R. Bieler, and E. J. Cotts, “Cyclic twin nucleation in tin-based solder alloys,” *Acta Mater.*, vol. 58, no. 10, pp. 3546–3556, Jun. 2010.
[176] J. Weertman, “CREEP OF INDIUM, LEAD, AND SOME OF THEIR ALLOYS WITH VARIOUS METALS,” *Trans Met Soc AIME*, vol. Vol: 218, 1960.
[177] J. Weertman and J. E. Breen, “Creep of Tin Single Crystals,” *J. Appl. Phys.*, vol. 27, no. 10, pp. 1189–1193, Oct. 1956.
[178] T. R. Bieler, B. Zhou, L. Blair, A. Zamiri, P. Darbandi, F. Pourboghrat, T.-K. Lee, and K.-C. Liu, “The Role of Elastic and Plastic Anisotropy of Sn in Recrystallization and Damage Evolution During Thermal Cycling in SAC305 Solder Joints,” *J. Electron. Mater.*, vol. 41, no. 2, pp. 283–301, Feb. 2012.
[179] T.-K. Lee, B. Zhou, and T. R. Bieler, “Impact of Isothermal Aging and Sn Grain Orientation on the Long-Term Reliability of Wafer-Level Chip-Scale Package Sn #x2013;Ag #x2013;Cu Solder Interconnects,” *IEEE Trans. Compon. Packag. Manuf. Technol.*, vol. 2, no. 3, pp. 496–501, Mar. 2012.
[180] J. D. Eshelby, “The Determination of the Elastic Field of an Ellipsoidal Inclusion, and Related Problems,” *Proc. R. Soc. Math. Phys. Eng. Sci.*, vol. 241, no. 1226, pp. 376–396, Aug. 1957.
[181] J. D. Eshelby, “The Elastic Field Outside an Ellipsoidal Inclusion,” *Proc. R. Soc. Lond. Ser. Math. Phys. Sci.*, vol. 252, no. 1271, pp. 561–569, Oct. 1959.
[182] H. Y. Yu and S. C. Sanday, “Elastic Inhomogeneous Inclusion and Inhomogeneity in Bimaterials,” *Proc. Math. Phys. Sci.*, vol. 439, no. 1907, pp. 659–667, Dec. 1992.
[183] A. C. Gavazzi and D. C. Lagoudas, “On the numerical evaluation of Eshelby’s tensor and its application to elastoplastic fibrous composites,” *Comput. Mech.*, vol. 7, no. 1, pp. 13–19, Jan. 1990.
[184] P. J. Withers, “The determination of the elastic field of an ellipsoidal inclusion in a transversely isotropic medium, and its relevance to composite materials,” *Philos. Mag. A*, vol. 59, no. 4, pp. 759–781, Apr. 1989.
[185] L. C. C. E. W. Kammer, “The elastic constants for single-crystal bismuth and tin from room temperature to the melting point,” *J. Phys. Chem. Solids*, no. 10, pp. 1891–1898, 1972.

[186] K. Suganuma, “Advances in lead-free electronics soldering,” *Curr. Opin. Solid State Mater. Sci.*, vol. 5, no. 1, pp. 55–64, Jan. 2001.
[187] A. Z. Miric and A. Grusd, “Lead-free alloys,” *Solder. Surf. Mt. Technol.*, vol. 10, no. 1, pp. 19–25, Apr. 1998.
[188] M. R. Harrison, J. H. Vincent, and H. A. H. Steen, “Lead-free reflow soldering for electronics assembly,” *Solder. Surf. Mt. Technol.*, vol. 13, no. 3, pp. 21–38, Dec. 2001.
[189] J. C. Suhling, H. S. Gale, R. W. Johnson, M. N. Islam, T. Shete, P. Lall, M. J. Bozack, J. L. Evans, P. Seto, T. Gupta, and J. R. Thompson, “Thermal cycling reliability of lead free solders for automotive applications,” in *The Ninth Intersociety Conference on Thermal and Thermomechanical Phenomena in Electronic Systems, 2004. ITHERM ’04*, 2004, vol. 2, pp. 350–357 Vol.2.
[190] L. P. Lehman, S. N. Athavale, T. Z. Fullem, A. C. Giamis, R. K. Kinyanjui, M. Lowenstein, K. Mather, R. Patel, D. Rae, J. Wang, Y. Xing, L. Zavalij, P. Borgesen, and E. J. Cotts, “Growth of Sn and intermetallic compounds in Sn-Ag-Cu solder,” *J. Electron. Mater.*, vol. 33, no. 12, pp. 1429–1439, Dec. 2004.
[191] B. Salam, C. Virseda, H. Da, N. N. Ekere, and R. Durairaj, “Reflow profile study of the Sn-Ag-Cu solder,” *Solder. Surf. Mt. Technol.*, vol. 16, no. 1, pp. 27–34, Apr. 2004.
[192] S. L. Allen, M. R. Notis, R. R. Chromik, and R. P. Vinci, “Microstructural evolution in lead-free solder alloys: Part I. Cast Sn–Ag–Cu eutectic,” *J. Mater. Res.*, vol. 19, no. 05, pp. 1417–1424, 2004.
[193] M. R. N. Sarah L. Allen, “Microstructural evolution in lead-free solder alloys: Part II. Directionally solidified Sn-Ag-Cu, Sn-Cu and Sn-Ag,” *J. Mater. Res.*, vol. 19, no. 05, pp. 1425 – 1431, 2004.
[194] M. Amagai, M. Watanabe, M. Omiya, K. Kishimoto, and T. Shibuya, “Mechanical characterization of Sn–Ag-based lead-free solders,” *Microelectron. Reliab.*, vol. 42, no. 6, pp. 951–966, Jun. 2002.
[195] F. Guo, J. P. Lucas, and K. N. Subramanian, “Creep behavior in Cu and Ag particle-reinforced composite and eutectic Sn-3.5Ag and Sn-4.0Ag-0.5Cu non-composite solder joints,” *J. Mater. Sci. Mater. Electron.*, vol. 12, no. 1, pp. 27–35, Jan. 2001.
[196] H. J. B. Qiang Xiao, “Aging Effects on Microstructure and Tensile Property of Sn3.9Ag0.6Cu Solder Alloy,” *J. Electron. Packag. - J ELECTRON Packag.*, vol. 126, no. 2, 2004.
[197] J. H. L. Pang, T. H. Low, B. S. Xiong, X. Luhua, and C. C. Neo, “Thermal cycling aging effects on Sn–Ag–Cu solder joint microstructure, IMC and strength,” *Thin Solid Films*, vol. 462–463, pp. 370–375, Sep. 2004.
[198] W. J. Plumbridge, C. R. Gagg, and S. Peters, “The creep of lead-free solders at elevated temperatures,” *J. Electron. Mater.*, vol. 30, no. 9, pp. 1178–1183, Sep. 2001.
[199] D. Q. Yu, J. Zhao, and L. Wang, “Improvement on the microstructure stability, mechanical and wetting properties of Sn–Ag–Cu lead-free solder with the addition of rare earth elements,” *J. Alloys Compd.*, vol. 376, no. 1–2, pp. 170–175, Aug. 2004.
[200] T.-M. K. Korhonen, P. Turpeinen, L. P. Lehman, B. Bowman, G. H. Thiel, R. C. Parkes, M. A. Korhonen, D. W. Henderson, and K. J. Puttlitz, “Mechanical properties of near-eutectic Sn-Ag-Cu alloy over a wide range of temperatures and strain rates,” *J. Electron. Mater.*, vol. 33, no. 12, pp. 1581–1588, Dec. 2004.
[201] J.-W. Kim and S.-B. Jung, “Experimental and finite element analysis of the shear speed effects on the Sn–Ag and Sn–Ag–Cu BGA solder joints,” *Mater. Sci. Eng. A*, vol. 371, no. 1–2, pp. 267–276, Apr. 2004.
[202] J. Lau, W. Dauksher, J. Smetana, R. Horsley, D. Shangguan, T. Castello, I. Menis, D. Love, and B. Sullivan, “Design for lead-free solder joint reliability of high-density packages,” *Solder. Surf. Mt. Technol.*, vol. 16, no. 1, pp. 12–26, Apr. 2004.
[203] P. S. ME Erinç, “Characterization and fatigue damage simulation in SAC solder joints,” *Microelectron. Reliab.*, vol. 44, no. 9, pp. 1287–1292, 2004.
[204] M. A. Matin, E. W. C. Coenen, W. P. Vellinga, and M. G. D. Geers, “Correlation between thermal fatigue and thermal anisotropy in a Pb-free solder alloy,” *Scr. Mater.*, vol. 53, no. 8, pp. 927–932, Oct. 2005.
[205] K. N. Subramanian and J. G. Lee, “Effect of anisotropy of tin on thermomechanical behavior of solder joints,” *J. Mater. Sci. Mater. Electron.*, vol. 15, no. 4, pp. 235–240, Apr. 2004.

[206] A. U. Telang, T. R. Bieler, J. P. Lucas, K. N. Subramanian, L. P. Lehman, Y. Xing, and E. J. Cotts, "Grain-boundary character and grain growth in bulk tin and bulk lead-free solder alloys," *J. Electron. Mater.*, vol. 33, no. 12, pp. 1412–1423, Dec. 2004.
[207] T. T. B. A. A. Telang, "Orientation imaging studies of Sn-based electronic solder joints," *J. Mater. Res.*, vol. 17, no. 09, pp. 2294 – 2306, 2002.
[208] C. R. Chen and S. X. Li, "Distribution of stresses and elastic strain energy in an ideal multicrystal model," *Mater. Sci. Eng. A*, vol. 257, no. 2, pp. 312–321, Dec. 1998.
[209] J. A. Rayne and B. S. Chandrasekhar, "Elastic Constants of β Tin from 4.2°K to 300°K," *Phys. Rev.*, vol. 120, no. 5, pp. 1658–1663, Dec. 1960.
[210] G. Cuddalorepatta, M. Williams, and A. Dasgupta, "Viscoplastic Creep Response and Microstructure of As-Fabricated Microscale Sn-3.0Ag-0.5Cu Solder Interconnects," *J. Electron. Mater.*, vol. 39, no. 10, pp. 2292–2309, Oct. 2010.
[211] H. Ma and J. C. Suhling, "A review of mechanical properties of lead-free solders for electronic packaging," *J. Mater. Sci.*, vol. 44, no. 5, pp. 1141–1158, Mar. 2009.
[212] G. Cuddalorepatta and A. Dasgupta, "Multi-scale modeling of the viscoplastic response of As-fabricated microscale Pb-free Sn3.0Ag0.5Cu solder interconnects," *Acta Mater.*, vol. 58, no. 18, pp. 5989–6001, Oct. 2010.
[213] J. Keller, D. Baither, U. Wilke, and G. Schmitz, "Mechanical properties of Pb-free SnAg solder joints," *Acta Mater.*, vol. 59, no. 7, pp. 2731–2741, Apr. 2011.
[214] G. S. Ansell, J. Weertman, N. R. L. (U.S.), and N. P. S. (U.S.), *Creep of a Dispersion-hardened Aluminum Alloy*. Naval Research Laboratory, 1958.
[215] E. Arzt and J. Rösler, "The kinetics of dislocation climb over hard particles—II. Effects of an attractive particle-dislocation interaction," *Acta Metall.*, vol. 36, no. 4, pp. 1053–1060, Apr. 1988.
[216] T. Mura, *Micromechanics of Defects in Solids*. Springer Science & Business Media, 1987.
[217] S. N. G. Chu and J. C. M. Li, "Pencil slip in beta-tin single crystals," *J. Mater. Sci.*, vol. 15, no. 11, pp. 2733–2742, Nov. 1980.
[218] P. Kumar, B. Talenbanpour, U. Sahaym, C. H. Wen, and I. Dutta, "Microstructural evolution and some unusual effects during thermo-mechanical Cycling of Sn-Ag-Cu alloys," in *2012 13th IEEE Intersociety Conference on Thermal and Thermomechanical Phenomena in Electronic Systems (ITherm)*, 2012, pp. 880–887.
[219] M. R. N. Sarah L. Allen, "Microstructural evolution in lead-free solder alloys: Part I. Cast Sn–Ag–Cu eutectic," *J. Mater. Res.*, vol. 19, no. 05, pp. 1417 – 1424, 2004.
[220] D. D. P. L. Snugovsky, "Experiments on the aging of Sn–Ag–Cu solder alloys," *Mater. Sci. Technol.*, vol. 20, no. 8, pp. 1049–1054, 2004.
[221] T. Y. Lee, W. J. Choi, K. N. Tu, J. W. Jang, S. M. Kuo, J. K. Lin, D. R. Frear, K. Zeng, and J. K. Kivilahti, "Morphology, kinetics, and thermodynamics of solid-state aging of eutectic SnPb and Pb-free solders (Sn–3.5Ag, Sn–3.8Ag–0.7Cu and Sn–0.7Cu) on Cu," *J. Mater. Res.*, vol. 17, no. 02, pp. 291–301, 2002.
[222] T. Chen and I. Dutta, "Effect of Ag and Cu Concentrations on the Creep Behavior of Sn-Based Solders," *J. Electron. Mater.*, vol. 37, no. 3, pp. 347–354, Mar. 2008.
[223] I. Dutta and P. Kumar, "Microstructural coarsening in Sn-Ag-based solders and its effects on mechanical properties," vol. 61, no. 6, pp. 29–38.
[224] H. Ma, J. C. Suhling, Y. Zhang, P. Lall, and M. J. Bozack, "The Influence of Elevated Temperature Aging on Reliability of Lead Free Solder Joints," in *Electronic Components and Technology Conference, 2007. ECTC '07. Proceedings. 57th*, 2007, pp. 653–668.
[225] T. G. Dw. Henderson, "Ag3Sn plate formation in the solidification of near ternary eutectic Sn-Ag-Cu alloys," *J. Mater. Res. - J MATER RES*, vol. 17, no. 11, pp. 2775–2778, 2002.
[226] Q. Xiao, L. Nguyen, and W. D. Armstrong, "Aging and creep behavior of Sn3.9Ag0.6Cu solder alloy," in *Electronic Components and Technology Conference, 2004. Proceedings. 54th*, 2004, vol. 2, pp. 1325–1332 Vol.2.
[227] V. Venkatadri, L. Yin, Y. Xing, E. Cotts, K. Srihari, and P. Borgesen, "Accelerating the effects of aging on the reliability of lead free solder joints in a quantitative fashion," in *Electronic Components and Technology Conference, 2009. ECTC 2009. 59th*, 2009, pp. 398–405.
[228] Y. Zhang, Z. Cai, J. C. Suhling, P. Lall, and M. J. Bozack, "The effects of aging temperature on SAC solder joint material behavior and reliability," in *Electronic Components and Technology Conference, 2008. ECTC 2008. 58th*, 2008, pp. 99–112.

[229] S. Mukherjee, T. T. Mattila, and A. Dasgupta, “Effect of addition of manganese and antimony on viscoplastic properties and cyclic mechanical durability of low silver Sn-Ag-Cu solder,” in *2012 13th IEEE Intersociety Conference on Thermal and Thermomechanical Phenomena in Electronic Systems (ITherm)*, 2012, pp. 888–895.
[230] J. Rösler and M. Bäker, “A theoretical concept for the design of high-temperature materials by dual-scale particle strengthening,” *Acta Mater.*, vol. 48, no. 13, pp. 3553–3567, Aug. 2000.
[231] D. C. Dunand and A. M. Jansen, “Creep of metals containing high volume fractions of unshearable dispersoids—Part I. Modeling the effect of dislocation pile-ups upon the detachment threshold stress,” *Acta Mater.*, vol. 45, no. 11, pp. 4569–4581, Nov. 1997.